Annual reports on
NMR Spectroscopy

Volume 64

Annual Reports on

NMR SPECTROSCOPY

VOLUME **64**

This page intentionally left blank

Annual Reports on
NMR SPECTROSCOPY

VOLUME **64**

Edited by

GRAHAM A. WEBB
Royal Society of Chemistry
Burlington House
Piccadilly, London, UK

ELSEVIER

Amsterdam • Boston • Heidelberg • London • New York • Oxford
Paris • San Diego • San Francisco • Singapore • Sydney • Tokyo
Academic Press is an imprint of Elsevier

Academic Press is an imprint of Elsevier
84 Theobald's Road, London WC1X 8RR, UK
Radarweg 29, PO Box 211, 1000 AE Amsterdam, The Netherlands
Linacre House, Jordan Hill, Oxford OX2 8DP, UK
30 Corporate Drive, Suite 400, Burlington, MA 01803, USA
525 B Street, Suite 1900, San Diego, CA 92101-4495, USA

First edition 2008

ISBN: 978-0-12-374337-4
ISSN: 0066-4103

Printed and bound in Great Britain

08 09 10 11 12 10 9 8 7 6 5 4 3 2 1

CONTENTS

CONTRIBUTORS

Michael Bühl
Max-Planck Institut für Kohlenforschung, Kaiser-Wilhelm-Platz 1, D-45470 Mülheim an der Ruhr, Germany; Present address: School of Chemistry, North Haugh, University of St. Andrews, St. Andrews, Fife, KY16 9ST, UK

J.T. Gerig
Department of Chemistry and Biochemistry, University of California, Santa Barbara, CA 93106, USA

E. Guichard
UMR1129 FLAVIC, ENESAD, INRA, Université de Bourgogne, 17 rue Sully, B.P. 86510, 21065 Dijon, France

Daniel Huster
Institute of Medical Physics and Biophysics, Härtelstr. 16–18, D-04107 Leipzig, Germany

J. Kidrič
National Institute of Chemistry, Hajdrihova 19, 1000 Ljubljana, Slovenia

C. Moreau
UMR1129 FLAVIC, ENESAD, INRA, Université de Bourgogne, 17 rue Sully, B.P. 86510, 21065 Dijon, France

L. Tavel
UMR1129 FLAVIC, ENESAD, INRA, Université de Bourgogne, 17 rue Sully, B.P. 86510, 21065 Dijon, France

J.A. Tossell
Department of Chemistry and Biochemistry, University of Maryland, College Park, MD 20742, USA

Marcin Wachowicz
Deparment of Chemistry, Oklahoma State University, Stillwater, Oklahoma 74078

Jeffery L. White
Department of Chemistry, Oklahoma State University, Stillwater, Oklahoma 74078

This page intentionally left blank

PREFACE

It is my great pleasure to introduce Volume 64 of Annual Reports on NMR. As is usual with this series of cutting edge reports the great importance of NMR in many areas of scientific research is highlighted.

The volume commences with a chapter on Theoretical and Experimental Studies on ^{19}F NMR Shieldings in Mineral Glasses, Zeolites and Related Silsequioxanes by J.A. Tossell. Chapter 2 is on NOE Studies of Solvent–Solute Interactions by G.T. Gerig. Chapter 3 is a state-of-the-art account of DFT Computations of Transition Metal Chemical Shifts by M. Bühl; this is followed by a contribution from D. Huster on Solid-State NMR Studies of Collagen Structure and Dynamics in Isolated Fibrils and in Biological Tissues; J. Kidrič reports on NMR Studies of Beverages; the Contribution of NMR Spectroscopy to Flavour Release and Perception is covered by L. Tavel, E. Guichard and C. Moreau; the final contribution by J.L. White is on Polymer Blend Miscibility.

My gratitude for their very interesting reports is due to all of these contributors. My thanks also go to the production staff at Elsevier for their help in the timely appearance of volumes of Annual Reports on NMR Spectroscopy.

G.A. Webb
Royal Society of Chemistry
Burlington House
Piccadilly
London, UK

This page intentionally left blank

CHAPTER 1

Theoretical and Experimental Studies on ^{19}F NMR Shieldings in Mineral Glasses, Zeolites and Related Silsesquioxanes

J.A. Tossell

Contents

Abstract

While much attention has been devoted to the measurement and calculation of O NMR shieldings in solid oxides and silicates, F has been seriously neglected. This is because, except for the metal fluorides, F enters most solids as a low-concentration impurity or defect. Yet, the presence of only small amounts of F can exercise enormous influence upon physical properties, such as phase relations and viscosity, and upon chemical reactivity and mechanism of formation. Since the 1990s a number of studies have shown that F NMR shieldings in solids can be calculated quite accurately using quantum methods, which use large flexible basis sets and partially incorporate electron correlation, so long as the cluster model for the solid is adequate. Studies directed toward the assignment of particular unexpected peaks in specific glasses or disordered solids, as well as more general studies of trends in F NMR shifts have both been performed. We now have a good general understanding of the effect of local and mid-range structure about F on its NMR shift. However, for any given site trends often

Department of Chemistry and Biochemistry, University of Maryland, College Park, MD 20742, USA

Annual Reports on NMR Spectroscopy, Volume 64
ISSN 0066-4103, DOI 10.1016/S0066-4103(08)00001-X

compete. For example, F sites can differ both in the number of other ligands in the coordination sphere and in the degree of oligomerization, so that considerably different F sites could give the same shift. Nonetheless, for many different classes of solids conclusions about both structures and energetics can now be drawn from the F NMR shieldings observed.

Keywords: quantum calculations; ^{19}F NMR; amorphous solids; disordered solids; silsesquioxanes; zeolites

1. INTRODUCTION

There are relatively few minerals (naturally occurring inorganic crystalline solids) that have F-rich compositions. One unusual one, rosenbergite, will be discussed at the end of this paper. However, F can occur at low concentration in a number of oxide, silicate and aluminosilicate mineral solid solutions and glasses. Since the valence of F is one (rather than the two of O, more commonly found in minerals) it usually forms either a strong single bond or a moderate number of weak bonds to high-coordination-number cations. The decrease in overall bond number and bond strength caused by F substitution for O within an oxide, silicate or aluminosilicate mineral weakens the strength of the network, decreasing its melting point. Dissolved "volatile components" such as F in melts of mineral composition, or magmas, can strongly influence their physical properties and eruptive behavior. F is one of the most important such volatile components, significantly influencing phase relations,[1] lowering viscosity[2] and increasing diffusion coefficients of cations. F is also an important additive to industrial silicate glasses, in which it is primarily used to lower the refractive index.[3] These effects are very important in ceramic sciences and geosciences. ^{19}F NMR has also been used to determine the positions and to help understand the energetics and mechanisms for incorporation of F into open aluminosilicate cage molecules, such as zeolites[4] and silsesquioxanes,[5] important in catalysis and materials science.

In fact the main focus of ^{19}F NMR studies is to obtain structural information which will allow us to understand the effects of substitution of small amounts of F on physical properties such as viscosities of magmas, refractive indexes of doped aluminosilicate glass or the stabilities of low-defect, low-density, large-pore structures for mesoporous or microporous aluminosilicates.

Identification of the species produced can sometimes be made by comparison of observed NMR shifts with those in well-characterized crystalline solids. However, an important characteristic of Al oxides, silicates, aluminosilicates and hydroxyfluorides is their tendency to form amorphous solids and/or oligomeric solution complexes. For characterization of amorphous materials and solution complexes multinuclear NMR can be a very powerful approach, particularly if coupled with cross-polarization techniques to determine connectivity of different atoms. For example, we might anticipate that for a F-bearing aluminosilicate glass a combination of highly resolved F, Na, Si and Al NMR (with perhaps a bit of anion–cation cross-polarization information) would allow us to construct a

detailed picture of the medium-range structure of the glass from information about the local structure around each atom. This procedure is sometimes effective but suffers from the problem that the local geometries involved may not exist in any well-studied crystalline material so that a fingerprinting approach is not adequate.

The NMR shielding range of F in solids is substantial and is strongly influenced by nearest neighbor environment. In many cases, details of the environment such as bond distance are important. Since F often occupies impurity or partially occupied sites characterization of its environment with X-rays is fraught with difficulty. Since NMR is inherently a local probe it can sometimes give a more accurate and detailed information on the F environment rather than the averaged picture sometimes given by X-ray diffraction. Since many of the F environments are not well characterized by X-ray, establishing a relationship between structure and spectra is difficult.

In this respect calculation of the NMR shielding of cations or anions for models with different local structures can be very valuable.[6] Such calculations can be done from different perspectives, namely concentrating on accurate reproduction of experimental data for a particular F structural site or focusing on uncovering general trends in F NMR shielding with changes in structural parameters. While the identity of the cations bonded to the F will always exercise an important influence on its shielding, the number and identity of other ligands within the coordination sphere may also be important. In many cases both the atoms of a bond may show shifts in the same direction due to changes in the local energy spectrum, with a lowering of occupied–unoccupied orbital energy differences or decrease in bond gap increasing the magnitude of the deshielding, paramagnetic contributions for both atoms.

2. RECOMMENDED COMPUTATIONAL METHODS

NMR calculations for solids can be done using both local cluster methods and periodic methods.[7] All calculations on fluorides to date have utilized a cluster approach, partly because much of the experimental interest has been in amorphous materials, more difficult to treat within a periodic approach. In many cases certain atoms distant from the F have been replaced by point charges.[8] This is consistent with the expectation that many fluorine compounds are quite ionic in nature. Ionic crystals, in general, will have larger numbers of weak interactions and relatively high F coordination numbers. Thus, the number of atoms or ions even in the first coordination shell can be fairly large and calculations incorporating several shells can be quite demanding. For the viewpoint of interpreting the computational results, large clusters may also make qualitative interpretations somewhat dubious. The basis set and quantum method requirements for accurate shielding calculations are much like those for the more studied oxygen.[9] Difficulties in obtaining accurate local geometries using cluster methods must now be considered the most important factor limiting the accuracy of calculated F NMR shieldings for most cases of

disordered materials or those which are incompletely characterized on a local scale. We have found that to accurately describe the full range of ^{19}F shifts in solids requires large bases (e.g., 6−311+*G*(3df,2p) or the equivalent) and methods which treat at least some aspects of correlation (e.g., at least at the hybrid Hartree–Fock–density functional techniques (HF–DFT) B3LYP level or the MP2 level). We typically average the HF and B3LYP as described originally in Liu and Nekvasil.[10] This procedure gives improved agreement with the experimental shifts for both molecules and solids. A similar scaling procedure has been developed by Chesnut.[11]

Experimental findings indicate that broad trends in F shieldings can be understood using rather modest cluster models of solids, even without neutralizing counterions or point charges. Body et al.[12] have used minimal cluster models some of which are shown in Figure 1 for a range of metal fluorides and find quite reasonable overall trends of calculated shielding vs. experimental

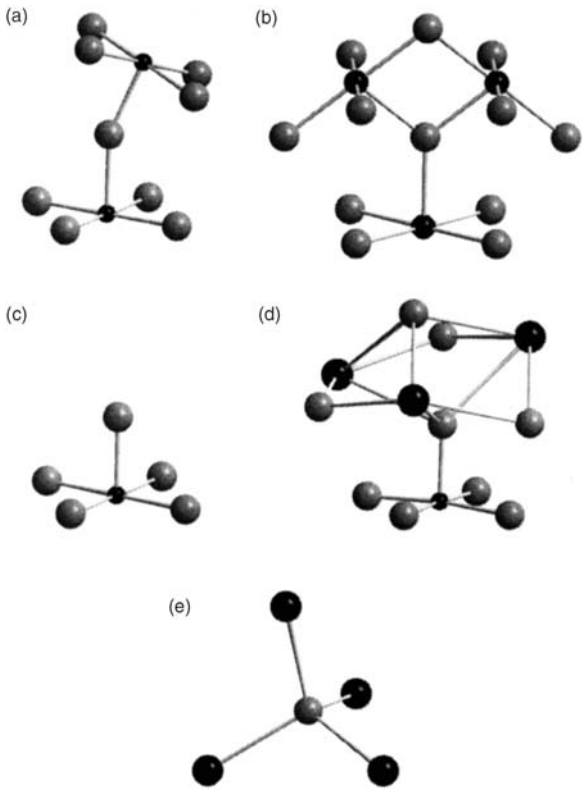

Figure 1 Example of clusters used in calculation. (a) $[FAl_2F_8]^{3-}$cluster for AlF_3, (b) $[FMg_3F_{11}]^{3-}$ cluster for MgF_2, (c) $[FAlF_4]^{2-}$ cluster for the unshared fluorine atom of $KAlF_4$, (d) $[FAlF_4FBaFBa_2F_2]$ retained cluster for the unshared fluorine atom F7 in $Ba_3Al_2F_{12}$ and (e) $[FBa_4]^{7+}$ cluster for BaF_2. Gray and black spheres represent fluorine and metal atoms, respectively. (Adapted from ref. 12.)

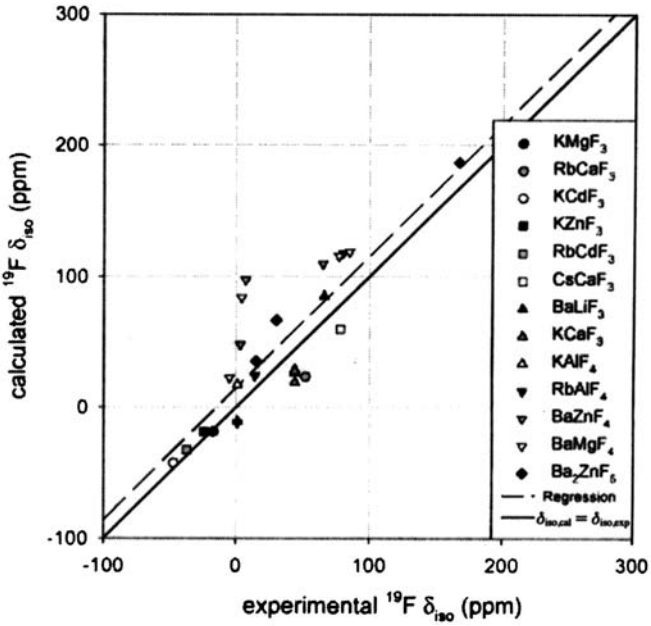

Figure 2 Calculated isotropic chemical shift values vs. experimental values for some fluoride compounds. The solid line corresponds to $\delta_{iso,cal} = \delta_{iso,exp}$. The dashed line corresponds to the linear regression. (Adapted from ref. 12.)

as shown in Figure 2. Given adequate computer resources one can construct appropriate clusters and apply reliable quantum methodologies to them.

3. FLUORINE IN ALUMINOSILICATE GLASSES

It is generally acknowledged that in F-bearing aluminosilicate glasses the F bonds mainly with Al, and that much of the Al is in 4-coordination and is highly polymerized, just as in the F-free case. However, much interest attaches to the identification of that small number of defect or unusual sites, F replacing O at 4- or 5-coordinate Al sites, which may influence the properties of the glass greatly out of proportion to their number, i.e., the sites most effective in determining the physical or chemical properties of the glass.

It is always sobering to look back over one's previous work and assess problems of concern then which have now been solved and assumptions, implicit or explicit, since shown to be false. In ref. 13 the overall goal was actually to assign both major and minor peaks in the ^{27}Al NMR spectra of some F-containing aluminosilicate glasses. This study was prompted by the ^{27}Al and $^{19}F \Rightarrow {}^{27}Al$ cross-polarization study of Kohn et al.[14] and the ^{19}F NMR

study of Schaller et al.[15] on F-bearing aluminosilicate glasses. Schaller et al.[15] was the first to apply ^{19}F NMR to determination of the local structure about F in F-doped aluminosilicate glasses. The overall intent of these NMR studies (and related studies on F-bearing aluminosilicate glasses using Raman and X-ray absorption spectroscopies) was to understand the enormous lowering of viscosity caused by even small amount of F. In Tossell,[13] a single species $AlF_3(O^-)_2$ was identified which had ^{27}Al and ^{19}F NMR spectra (including the quadrupole coupling constant observed for ^{27}Al) as well as IR spectra and energetics which seemed most consistent with experiment. Methods were used for the NMR calculations which are now obsolete (core-corrected common origin HF and RPA-LORG,[16] both with polarized double-zeta basis sets). In addition, the quantum methods employed could not even really give accurate geometries for gas-phase molecules of this size and no corrections could be made for the effects of the external environment on structures or shieldings. Nonetheless, such methods could yield important insights into trends in shielding. For example, it was found that ^{19}F NMR trends paralleled trends in central atom (Al or Si) shieldings – increases in coordination number of the central polyhedra increased the shielding for both Al (or Si) and F. Some results are shown in Table 1.

It is observed that the shielding for F atoms bonded to Al increases with the Al coordination number, and therefore with the Al NMR shielding. Substitution of –OH for F shields the remaining F's and the F shielding is smaller for F bound to Si, an atom which shows a significantly larger paramagnetic deshielding than does Al. These qualitative results have stood the test of time and of other better calculations. Although it has never been proven, there appears to be a general correlation between the shieldings of the two atoms of a bond, causing them to generally shift together, as expected from naive arguments based on the eigenvalue spectrum.

On the other hand, the precise identification of species may be illusory (even when several properties are considered) since several species may exist which fit

Table 1 Calculated F isotropic NMR shieldings using a 3–21G* basis and 3–21G* optimized geometries

Species, symmetry	CHF	Core-corrected CHF
AlF_4^-	533	476
AlF_5^{2-}, C_{4v}	540(eq), 549(ap)	487 av
AlF_5^{2-}, D_{3n}	543(eq), 541(ap)	488 av
AlF_6^{3-}	577	505
$AlF(OH)_3^-$	527	471
$AlF_2(OH)_2^-$	522	465
$AlF_3(OH)_2^{2-}$	532, 530	477, 476
SiF_6^{2-}	528	472

Source: Adapted from ref. 13.

the data equally well, particularly if structural effects arising from thermal motion or medium effects are taken into account. Also, an inability to treat an effect (such as that of the surrounding medium) unfortunately does not in itself ensure that such effects are small. However, this study did establish that the fairly simple methods which at that time were yielding good results for the NMR shieldings of cations could be readily extended to anions and that there were interesting, simple trends in F shielding associated with the local environment. At this time only trends associated with a single-coordination polyhedron could be explored, because of method and computer limitations. As noted at the beginning of this manuscript, F may be weakly bonded to more than one cation, i.e., it may be involved in various types of oligomerization or polymerization in which it bridges coordination polyhedra at their corners or their edges. Study of the effects of such environments on the shielding had to wait for bigger and faster computers and better methodologies for calculating shieldings.

When Liu and Nekvasil[10] returned to this problem a decade later, such improvements had been made and they were able to study much larger systems, using methods that yielded much more accurate geometries as well as more accurate NMR shieldings. In particular, they used geometries calculated using hybrid HF–DFT and they used a scaling procedure for the NMR shifts based on both HF and hybrid HF–DFT calculations which has been previously mentioned, along with much larger basis sets. Even using these better, yet more computationally demanding methods, advances in software and computer environments allowed them to study larger systems in which F was in a bridging environment between polyhedra as well as to examine the effects of inclusion of counterions, like Na^+, and variation of structural parameters, such as Si–O–Si angles. They examined a range of Si- and Al-centered polyhedra, attempting to assign a ^{19}F NMR resonance at −147 ppm, which had been tentatively assigned to a Si–F species.

Later studies of F in amorphous SiO_2[17] yielded a major peak at −146 ppm that was consistent with their calculations for $SiF(OSiH_3)_3$ (their model for $SiO_{3/2}F$) groups at −146 ppm. However, there is yet no explanation for a minor peak at −135 ppm, since calculations on models for the $SiF(O^-)_4$ group suggested by Youngman and Sen[17] give F shifts around 40 ppm deshielded from those for $SiO_{3/2}F$ (Tossell, unpublished results).

Both the Tossell[13] and the Liu and Nekvasil[10] papers followed an approach quite common in the application of quantum techniques to problems in material and mineral sciences: focus on new experimental data, which has been interpreted in terms of unexpected and broadly interesting species and attempt to test the assignment. This assures interest within the experimental community in a way that a general theoretical paper, focusing on overall trends in properties, does not. However, it may tempt us to do more with the calculations that we safely can.

At this time there were also no comprehensive experimental studies of F as impurity in either SiO_2, Al_2O_3 and its hydrated forms or aluminosilicate minerals. Although ^{19}F is rather a good NMR nuclide, since it is 100% abundant and has a spin of 1/2, the lack of understanding of details of the local structure in

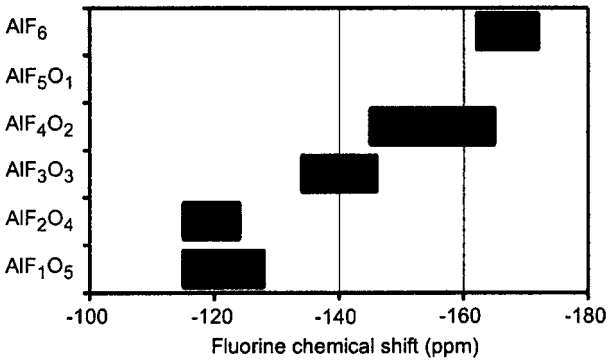

Figure 3 Typical ^{19}F chemical shifts of octahedral aluminum environments with oxygen and fluorine in the first coordination sphere, $AlO_{6-x}F_x$, vs. *x*. (Adapted from ref. 18.)

materials inherently poorly crystalline or amorphous had prevented the development of a general framework for interpreting F NMR shifts, as explained by Chupas et al.[18] However, in that work the literature was scrutinized sufficiently to produce a very useful correlation of F NMR shift with number of F and O within the local octahedral environment for F bonded to 6-coordinate Al, as seen in Figure 3.[18] Again, increased shielding for F was correlated with increased numbers of F within the local octahedral, which in turn correlated with increased shielding for the Al.

Partly to provide more systematic data Liu and Tosell,[19] used the same hybrid HF–DFT methods with large basis sets as in Liu and Nekvasil,[10] to examine much larger Al-centered polyhedral oligomeric clusters. Some of these polyhedra are shown in Figure 4.[19] The cluster method and quantum methodology were tested by calculating the shielding for some well-characterized crystalline fluorides, obtaining the excellent agreement with experiment shown in Table 2 from Liu and Tossell[19]. Perhaps inevitably, as more species were considered the number of distinct species that could be fitted to any given ^{19}F NMR peak generally increased, the opposite of the desired result. However, at the same time interesting patterns began to emerge. Figure 5[19] shows such patterns, with ^{19}F NMR shifts becoming less negative as central polyhedron coordination numbers increase and also as the linkage of the polyhedral elements increases, e.g., from corner to edge-shared linkages. Substitution of Si for Al invariably leads to a deshielding of the F adjacent to the substitution site. Thus, there were a number of factors determining the F NMR shift: (1) the identity of the cation to which it was bound, (2) the coordination number of its local polyhedron, (3) the ligand composition of that polyhedron and (4) the degree and type of polymeric linkage of the polyhedra.

Thus, it became apparent that some general principles could be formulated to predict the ^{19}F NMR shift from its the local and mid-range geometry about F, but that competition between trends could lead to a considerable spread of shielding

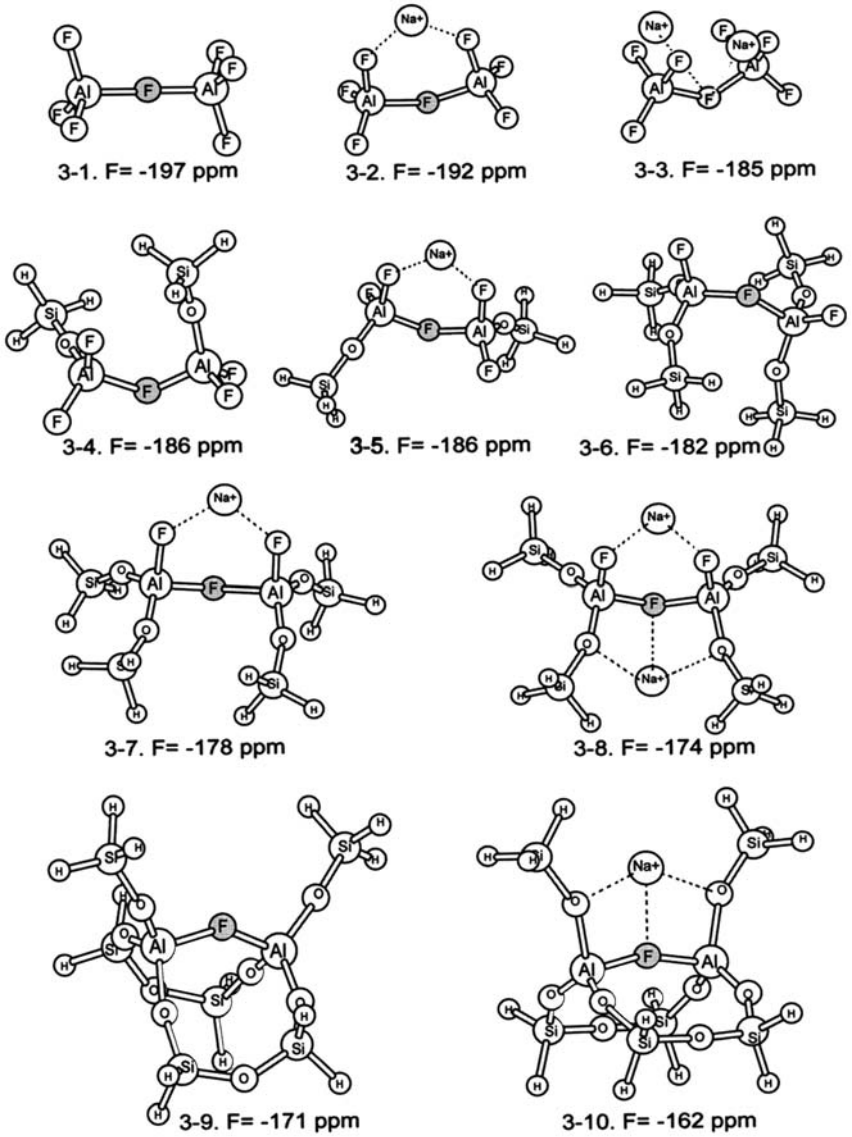

Figure 4 Cluster models used for corner-shared bridging F atoms in 4-coordinated Al species, and their chemical-shift values. (Adapted from ref. 19.)

for each of the different local structures. For example, a corner shared F bonded to a 4-coordinate Al could have the same shift as a terminal, nonbridging F bonded to a 5-coorinate Al. There was some suggestion in the calculations of Liu and Tossell[19] that such F species could also be distinguished on the basis of their chemical-shift anisotropy (CSA) values. Invariably the CSA is much greater for

Table 2 Calculated and experimental ^{19}F NMR results for crystalline phases

Phase	^{19}F NMR result (ppm)			
	HF	B3LYP	Scaled	Experimental (chemical shift)
$Na_5Al_3F_{14}$ (chiolite, 151.2°)	−141.6	−179.2	−160.4	−165
Na_2SiF_6	−129.6	−177.0	−153.3	−152
K_2SiF_6	−117.6	−156.1	−136.9	−136
LiF	−178.0	−220.0	−199.0	−204
NaF	−193.3	−250.9	−222.1	−225
KF	−126.1	−142.8	−134.5	−132.4

Source: Adapted from ref. 19.

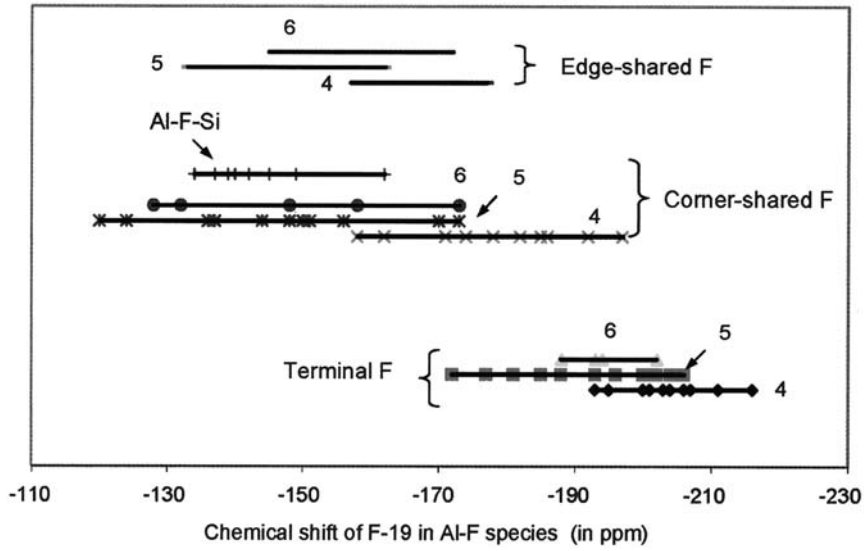

Figure 5 Diagram of the distribution of calculated ^{19}F chemical shifts for terminal, corner-shared, and edge-shared F atoms in various aluminum-containing species. Numbers in the figure specify 4-, 5- or 6-coordinated Al species. (Adapted from ref. 19.)

Si–F than for Al–F bonds and it seems to decrease somewhat with increase in Al coordination number. However, for comparison of terminal vs. bridging F's changes in CSA are subtle and show no obvious uniformity and the presence and position of counterions like Na^+ have surprisingly large effects.

The study of Liu and Tossell was used to assist the assignment of the ^{19}F NMR spectra of Na_2O–Al_2O_3–SiO_2 aluminosilicate glasses by Mysen et al.[20] They

assigned peaks to four different fluoride complexes: (1) Na–F complexes (NF); (2) Na–Al–F complexes with Al in fourfold coordination (NAF); (3) Na–Al–F complexes with Al in sixfold coordination with F(CF); and (4) Al–F complexes with Al in sixfold, and possibly also fourfold coordination (TF, for tourmaline-like F). The latter three complexes could be linked to the aluminosilicate network via Al–O–Si bridges. Raman spectra along the mineral series were also examined and equilibrium constants were evaluated for a number of different reactions affecting the silicate network polymerization. One of the main conclusions was that the dissolution of F in aluminosilicate melts was highly composition dependent and changed greatly with the proportion of bridging O (or degree of polymerization) of the melt.

4. FLUORINE IN ZEOLITES (LOW-DENSITY, LARGE-PORE ALUMINOSILICATES) AND IN SILSESQUIOXANES

Zeolites are used as catalysts for a number of organic reactions, both as formed, and with additional catalytic species added, usually to enhance their acidity. Although they have been wildly successful as heterogeneous catalysts there is still room for improvement, i.e., there are many useful acid-catalyzed reactions for which there are no zeolite catalysts or for which their activity tends to be short and unstable. Attention is constantly focused upon producing zeolite-type materials which retain stability and have even larger pore spaces, increased acidity and increased ease and yield in their synthesis. It was observed early that the structures of zeolites could be modified by introducing ''structure directing agents'' (SDA) and ''mineralizers'' (principally OH^- and F^-) into the reaction mixture . The structure directing agents change the ring structures of the zeolites, or more generally the class of ''microporous and mesoporous materials'' now being employed (with P, Ge and other elements in addition to the basic O, Al and Si). It may well be that the SDA and the mineralizers actually work together to produce the final product structure.[22,23] There is enormous activity in this field, both experimental and theoretical.

In general, F could have at least three potentially different types of location in zeolites, as discussed by Attfield et al.[24] It could be close to the SDA cation, essentially an ion-pair, it could be at or near the middle of an aluminosilicate cage or it could bond to a Si of an aluminosilicate cage to produce a 5-coordinate Si. These possibilities are shown in Figure 6.[24] The particular cage chosen for display in the figure is what is variously called a double 4-ring (D4R) or a 4^6, a cage bounded by six square sides, i.e., a cube. Attfield et al. found for two all-silica zeolite structures that the 5-coordinate form was energetically preferred and they were able to calculate an accurate S–F bond length around 1.76 Å. They also explained why the X-ray crystallographic studies on these compounds obtained a much longer erroneous bond length due to structural averaging. Another possibility (but one never observed in crystalline zeolites) is that the F might

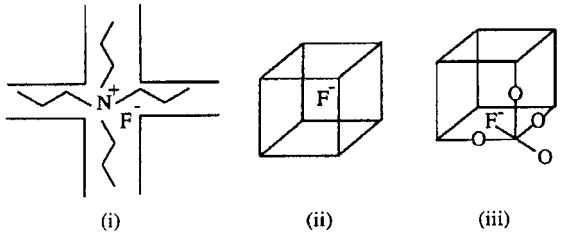

Figure 6 A schematic representation of the three types of F^- ion environments found in siliceous zeolites: (i) as part of an ion pair, (ii) in the center of a small cage far from any Si atoms and (iii) coordinated to a Si atom to form part of a pentacoordinated SiO_4F^- unit. (Adapted from ref. 24.)

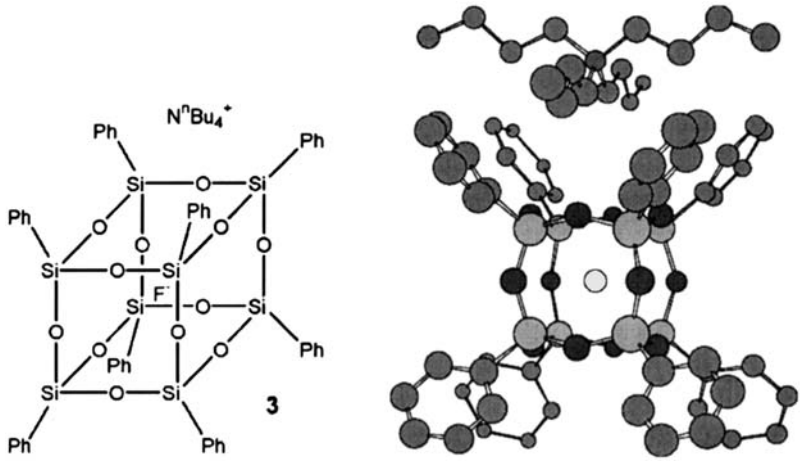

Figure 7 Structure of tetrabutylammonium octaphenyloctasilsesquioxane fluoride (3). (Adapted from ref. 5.)

replace one of the O bonded to Si, retaining the 4-coordinate Si and reducing the degree of polymerization.

Such structural possibilities can be more readily explored by focusing on a slightly less complicated group of materials often used to model zeolites, the silsesquioxanes, which can be readily synthesized from trisilanolchloride reactants in aqueous solution. Some silsesquioxane molecules, with general formula $(RSiO_{1.5})_n$ and D4R cage structures, have been found to encapsulate F^- ions at their centers.[5] One such structure is shown in Figure 7 above, taken from ref. 5. In zeolites and mesoporous silicas F^- are found either at the centers of D4R cages as in octadecasil[25] or near one of the apical Si atoms in larger cages.[26] For slightly different reaction systems, encapsulated F^- has not been

characterized but the yield of D4R cages in the synthesized zeolite or mesoporous silica is greatly increased by the presence of fluorides in the reaction mixture.[4] The presence of such D4R is correlated with low density, large void space, and consequently high internal surface area of the mesoporous solid, increasing their capabilities as catalysts. In order to design such low-density mesoporous solids it is important to understand which types of silsesquioxane cages can incorporate F^-, how the properties of the F^- are affected and how the internal and external properties of the silsesquioxane cages are influenced by the entrapped F^-.

A particularly interesting study of ^{19}F shieldings for F^- in D4R-mixed Si/Ge zeolites was performed by Pulido et al.[27] They initially optimized geometries using empirical force field techniques but also refined the local geometries using DFT methods. They calculated the shieldings at the DFT level using several different potentials and basis sets and for models of the D4R of two different sizes. Their optimized geometries showed that F invariably bonded to Ge when it was present to form a 5-coordinate species, while for the pure Si end member the equilibrium F position was at the center of the D4R. The existence of 5-coordinate Ge had been indicated by a preliminary study,[28] the first computational study of ^{19}F NMR shifts in zeolites. Their calculated F NMR shifts were in quite good agreement with experiment for the 8Si/0Ge, 7Si/1Ge and 0Si/Ge8 members, the only ones studied experimentally (see Table 3 of ref. 27 for details). The 8Si/0Ge species, with the F^- in the center of the cage, had the most negative F shift (−31 to −36 depending upon the details of model and method) compared to −38 obtained experimentally.[25]

In our own studies[29] we used similar DFT methodology to obtain equilibrium geometries and the combined HF–DFT methodology, discussed earlier, to calculate F NMR shieldings for a series of D*n*R species, with $n = 3-6$, as well as for the 5-coordinate monomer and a series of single-ring compounds, *n*RF^-, with both –H and –OH terminating groups on the Si. Some very clear trends emerged. The shift of F^- in $Si(OH)_4F^-$ was about –115 ppm, but it became more positive for the *n*RF^- rings (in which the optimized position of F^- was over the ring) with the effect largest for the smallest rings. As the rings became larger the F shift approached that in free monomeric $Si(OH)_4F^-$. For F^- inside the D*n*R, when the F^- was bonded to a single F ($n = 5-6$) the shifts were like those in the single-ring species, but when the equilibrium position for F^- was at the center of the ring ($n = 3-4$) the shifts were much more positive, even reaching +40 ppm (vs. the CCl_3F reference) for $n = 3$. However, when we constrained the F^- to be at the center of the large D*n*R, $n = 5-6$, the F shifts became very negative, with the value of −170.8 ppm for D6R(H) central F^-, beginning to approach that we calculated for a free F^- anion (−276.4 ppm). The simplest qualitative explanation is that the F shift is determined at least partly by the bond strength received at F, with the free ion value around −280 ppm for no bonds and values around −115 ppm for a single bond from Si. Of course, some of these structures we considered

Table 3 Calculated ^{19}F NMR shieldings, isotropic shifts and spans (in ppm, average of HF and B3LYP GIAO calculations using 6−311+*G*(2d,p) bases evaluated at 6−31*G** HF geometries) for reference species and for ring and double ring silsesquioxane species with −H or −OH termination

Type	Formula	$1/2(\sigma_{HF}+\sigma_{B3LYP})$	δ^F shift	Ω^F span
Reference	CCl_3F	203.8	0	90.1
Free F^-	F^-	480.2	−276.4	0
M(OH)	$Si(OH)_4F^-$	318.6	−114.8	109.5
3R(OH)	$Si_3O_9H_6F^-$	271.6	−67.5	81.9
4R(OH)	$Si_4O_{12}H_8F^-$	291.1	−87.3	92.4
5R(OH)	$Si_5O_{15}H_{10}F^-$	291.4	−87.7	110.2
6R(OH)	$Si_6O_{18}H_{12}F^-$	294.0	−90.2	111.3
D3R(H)	$Si_6O_9H_6F^-$	163.8	+40.0	55.8
D4R(H)	$Si_8O_{12}H_8F^-$	242.2	−38.4 exp = −26 R = Ph	6.8
D5R(H)	$Si_{10}O_{15}H_{10}F^-$	258.0	−54.2	87.9
D5R(H) central F	$Si_{10}O_{15}H_{10}F^-$	317.0	−112.6	22.6
D6R(H)	$Si_{12}O_{18}H_{12}F^-$	272.5	−68.7	104.7
D6R(H) central F	$Si_{12}O_{18}H_{12}F^-$	374.1	−170.8	27.8
D3R(OH)	$Si_6O_{15}H_6F^-$	173.7	+30.0	45.1
D4R(OH)	$Si_8O_{20}H_8F^-$	263.1	−59.3 exp = −38 silicalite	0.7
D5R(OH)	$Si_{10}O_{25}H_{10}F^-$	265.2	−61.4	79.7
Opened D5R(OH)	$Si_{10}O_{27}H_{14}F^-$			101.5
	opt. R(Si–F) = 1.749	276.5	−72.7	
	X-ray R(Si–F) = 1.916	252.8	−49.0 exp = −64 silicalite = −1	

Source: Adapted from ref. 29.

may be hypothetical, with such low bond strength to F^- that they cannot exist. For example, the central F position in D6R(H) ($Si_{12}O_{18}H_{12}F^-$) is calculated to be about 26 kcal/mol less stable than the apex position bonding to a single Si at a distance around 1.75 Å. Results of these calculations are shown in Table 3.[29]

A particularly interesting case is the $Si_{10}O_{27}H_{14}F^-$ cluster, which can be derived from a D5R(OH) cluster by hydrolyzing two Si–O–Si linkages, thus converting five 4-rings into one 4-ring and two 6-rings. We call this an "opened" D5R(OH). This cluster occurs in silicalite 1 and we calculate for it an F shift of −72.7 ppm, which agrees well with the experimental value of −64 ppm.[30]

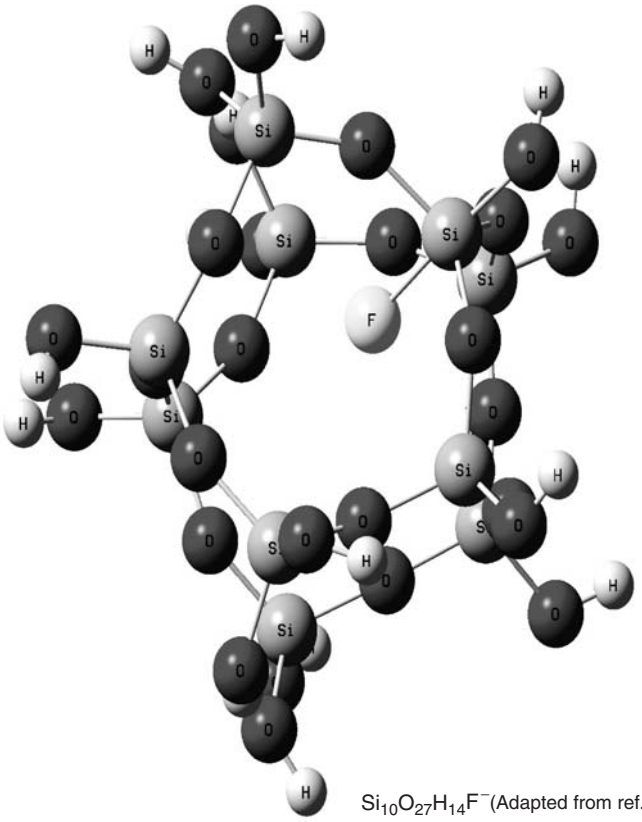

$Si_{10}O_{27}H_{14}F^-$ (Adapted from ref. 29)

It should also be anticipated that similar changes in coordination and F shielding will be found for D*n*Rs involving other elements like Ge and element combinations like Al and P. For example, we have found that for the D3R(H) species $Ge_6O_9H_6F^-$ the equilibrium F position is in the center of the cage, as shown below (rather than singly bonded to Ge as in the D4R) and the F shift, evaluated in

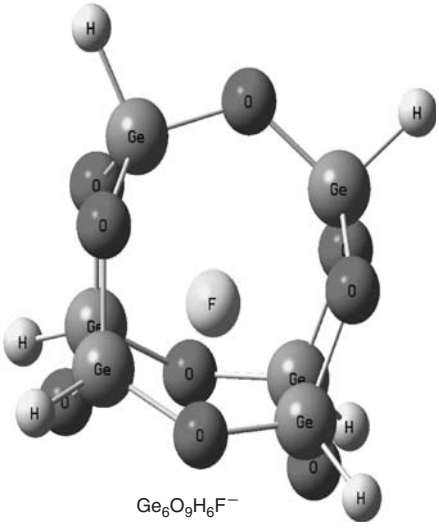

$Ge_6O_9H_6F^-$

the same way as in ref. 29 is −34.0 ppm, i.e., substantially deshielded from that seen in the all Ge species of D4R type, in which F^- is apex bonded to a single Ge.

Thus, there are large and systematic changes in both the ^{19}F NMR shift and span, depending upon the size of the cage. Therefore, with a sufficient database of experimental ^{19}F NMR and crystal structures and/or calculated ^{19}F NMR and structures, it would be possible to determine the location of the F^- from its NMR alone in silsesquioxanes and related mesoporous compounds. When the F^- is at the center of a smaller D*n*R it can be strongly deshielded and its NMR span is substantially reduced.

In ref. 29 the formation of the D4RF^- species $Si_8O_{12}H_8F^-$ is correctly predicted to be thermodynamically favorable in toluene, but not in aqueous solution. The favorability of encapsulation is greatest for the D4R, although the encapsulation of F^- in the double 5- and 6-rings is only 5–6 kcal less favorable. Energetics for encapsulation of F^- and OH^- are very similar for the D4R so that F^- and OH^- will compete for this location. The mechanism for the formation of low-density mesoporous silicas using F^- as mineralizer has been discussed by Corma and Davis[21] and Zones et al.[31] We hope that the energetics calculated in this paper will help to refine the proposed mechanisms.

The favorability of the encapsulation process is primarily a result of a stabilizing electrostatic interaction between the (strained) $Si_8O_{12}H_8$ cage and F^-. Qualitatively, interaction of the F^- with the cage is responsible for the deshielding of the ^{19}F NMR.

5. AL IN HYDROXYFLUORIDES: ROSENBERGITE

In their study of aluminum hydroxyfluorides Chupas et al.[18] determined ^{19}F and ^{27}Al NMR spectra for the mineral rosenbergite, $AlF[F_{0.5}(H_2O)_{0.5}]_4$. H_2O (one polymorph of $AlF_3 \cdot 3H_2O$), unusual because it has a large and fixed percentage of F. The crystal structure of this mineral consists of infinite chains of F corner sharing octahedral units. It thus gave us a chance to test more stringently the prediction in Liu and Tossell[19] that corner sharing fluorines were systematically deshielded compared to terminal fluorines. The experimental F NMR showed a major peak at about −145 ppm and additional weak peaks up to about –160 ppm. Chupas et al. attributed this range to *cis*/*trans* ordering of fluorines with diverse H-bonding arrangements, but our results suggested some breakdown of order with the creation of terminal, as well as bridging F's. In ref. 32 we used two different experimental X-ray geometries to construct a $Al_2F_3(OH_2)_8^{+3}$ geometry cluster and calculated bridging F shifts of −147 and nonbridging or terminal F shifts of −155 to −158 ppm. We also considered a larger cluster of Al_3F_4 type, obtaining essentially the same value for the F shifts (but slightly different values for central and terminal Al shifts). The various clusters considered are shown in Figure 8.

This study thus confirmed some of the systematics we have previously predicted but it also showed some limitations to our approach. Optimizing the geometries of the $Al_2F_3(OH_2)_8^{+3}$, whether as a free ion or within a polarizable

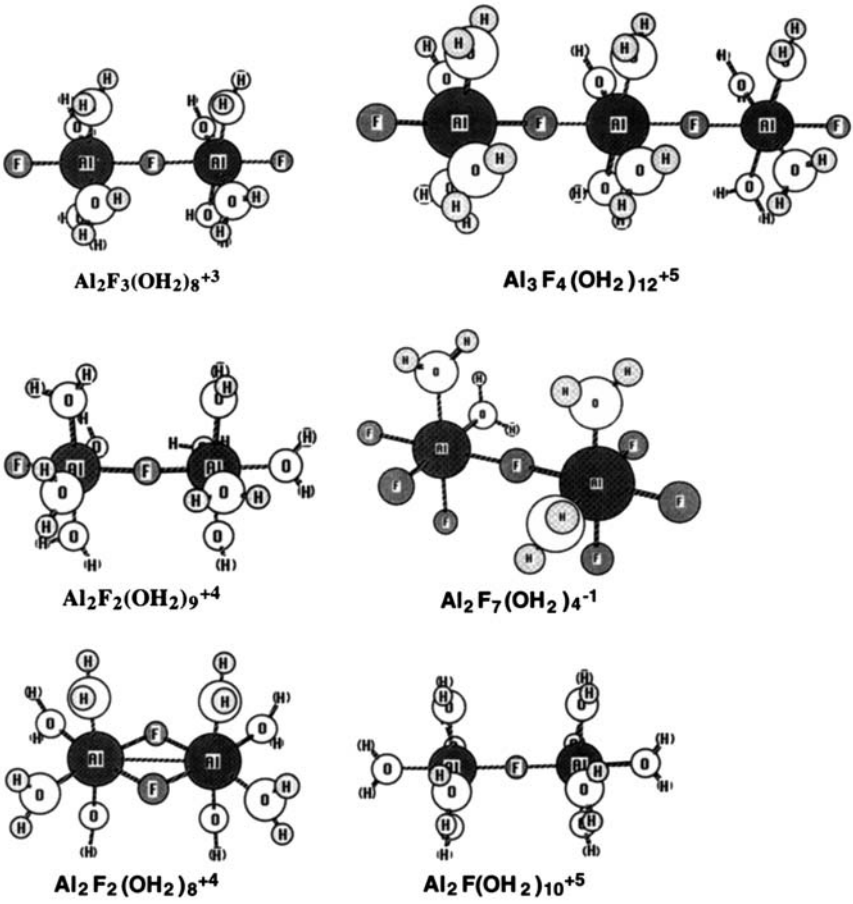

Figure 8 Ball-and-stick drawings of some of the molecules considered. (Adapted from ref. 32.)

continuum, gave Al–F bond distances and shifts for bridging and terminal F's that were in much poorer agreement with experiment. The observed value of the main F NMR peak in rosenbergite (−146 ppm) is also very close to the values around −147 ppm observed for a minor peak in F-bearing anhydrous Na aluminosilicate glasses, as discussed in ref. 19. Thus, such a corner-shared bridging F bonded to 6-coordinate Al is a possibility for assigning this feature in the glasses (in which the OH_2 grounds would presumably be replaced by OSi groups). We also speculated that species like that in rosenbergite could be present in Al hydroxyfluoride aqueous solutions giving F NMR peaks around −154 to −157 ppm. When the geometry of the cluster $Al_2F_3(OH_2)_8^{+3}$ is optimized in a PCM appropriate to water the Al–terminal F distance is reduced and the Al–bridging F distance increases, so that the bridging F becomes more shielded, with a calculated shift around −153. This thus provides a speculative means for adapting polymeric structures observed in solids to smaller oligomeric species

anticipated in solution, which will have slightly different local geometries and therefore slightly different NMR shifts. We also established that the monomeric unit like $Al(OH_2)_5F^{2+}$ had a F shift around −174 (since its F is terminal) and therefore could not explain deshielded peaks around −153 to −157 observed in solution.

6. CONCLUSION

F is an uncommon element in aluminosilicate minerals, mineral glasses and inorganic materials such as zeolites and silsesquioxanes, but it can strongly influence their physical and chemical properties and reactivities. Since many of these materials are amorphous, disordered or have complex crystal structures, the local environment of the F is hard to determine with X-ray crystallography. In such a case, multinuclear NMR might seem an ideal technique to determine local and some aspects of mid-range structure. However, recovering structure from F NMR has been difficult since the shielding systematics were poorly understood. In recent-year theoretical studies, directed either at the identification of particular unassigned or puzzling peaks in F NMR spectra or toward elucidation of general trends, have given us enhanced ability to recover structure from the F NMR spectra. For small molecules or well-characterized solids, a methodology going somewhat beyond HF theory, incorporating electron correlation at the MP2 or B3LYP level, along with the use of large (at least local) basis sets, seems to yield accurate agreement with experiment. The main difficulty for less well-characterized materials seems to be obtaining accurate geometries. The general trends we see are (1) less negative shifts when F is bonded to Si rather than its more common partner Al, (2) less negative shifts as the coordination number of the central atom decreases, e.g., from 6 to 5 to 4 for Al, (3) less negative shifts as other F's in the coordination environment are replaced by –OH or –O-Si, (4) less negative shifts as F's became part of shared polyhedral elements, i.e., as they form shared corners or edges and (5) a range of shifts from highly negative to positive when F^- occupies the centers of D*n*R cages in silsesquioxanes or zeolites.

ACKNOWLEDGMENT

This work was supported by NSF Grant EAR-0001031 and 0539109 and DOE Grant DE-FG02-94ER14467.

REFERENCES

1. D. A. C. Manning, *Contrib. Mineral. Petrol*, 1981, **76**, 206–2165.
2. D. B. Dingwell, *Am. Mineral*., 1989, **74**, 333–338.
3. T. M. Duncan, D. C. Douglas, R. Csencsits and K. L. Walker, *J. Appl. Phys*., 1986, **60**, 130–136.
4. P. Caullet, J.-L. Paillaurd, A. Simon-Masseron, M. Soulard and J. Patarin, *Comp. Rendu. Chimie*., 2005, **8**, 245–266.
5. A. R. Bassindale, D. J. Parker, M. Pourny, P. G. Taylor, P. N. Horton and M. B. Hursthouse, *Organometallics*, 2004, **23**, 4400–4405.

6. J. A. Tossell, Using quantum mechanical calculations of NMR properties to elucidate local and min-range structures in amorphous oxides, nitrides and aluminosilicates, in: *Computational Materials Chemistry: Methods and Applications*, L. A. Curtiss and M. S. Gordon, eds., Kluwer, Boston, MA, 2004, pp. 1–34.
7. M. Profeta, F. Mauri and C. J. Pickard, *J. Am. Chem. Soc*., 2003, **125**, 541–548.
8. D. Solis, *J. Mol. Struct*., 2002, **602–603**, 159–164.
9. J. R. Cheeseman, G. W. Trucks, T. A. Keith and M. J. Frisch, *J. Chem. Phys*., 1996, **104**, 5497–5509.
10. Y. Liu and H. Nekvasil, *Am. Mineral*., 2002, **87**, 339–346.
11. D. B. Chesnut, *Chem. Phys. Lett*., 2003, **380**, 251–257.
12. M. Body, G. Silly, C. Legein and J.-Y. Buzare, *J. Phys. Chem*., 2005, **109**, 10270–10278.
13. J. A. Tossell, *Am. Mineral*, 1993, **78**, 16–22.
14. S. C. Kohn, R. Dupree, M. G. Mortuza and C. M. B. Henderson, *Am. Mineral*., 1991, **76**, 309–312.
15. T. Schaller, D. B. Dingwell, H. Keppler, W. Knoller, L. Merwin and A. Sebald, *Geochim. Cosmochim. Acta*, 1991, **56**, 701–707.
16. A. E. Hansen and T. D. Bouman, *J. Chem. Phys*., 1985, **82**, 5033–5047.
17. R. E. Youngman and S. Sen, *J. Non-Cryst. Solids*, 2004, **337**, 182–186.
18. P. J. Chupas, D. R. Corbin, V. N. M. Rao, J. C. Hanson and C. P. Grey, *J. Phys. Chem. B*, 2003, **107**, 8327–8336.
19. Y. Liu and J. Tossell, *J. Phys. Chem. B*, 2003, **107**, 11280–11289.
20. B. O. Mysen, G. D. Cody and A. Smith, *Geochim. Cosmochim. Acta*, 2004, **68**, 2745–2769.
21. A. Corma and M. E. Davis, *Chem. Phys. Chem*., 2004, **5**, 304–313.
22. A. Pulido, A. Corma and G. Sastre, *J. Phys. Chem. B*, 2006, **110**, 23951–23961.
23. G. Sastre, *Phys. Chem. Chem. Phys*., 2007, **9**, 1052–1058.
24. M. P. Attfield, C. R. A. Catlow and A. A. Sokol, *Chem. Mater*., 2001, **13**, 4708–4713.
25. P. Caullet, J. L. Guth, J. Hazm, J. M. Lamblin and H. Gies, *Eur. J. Solid State Inorg. Chem*., 1991, **28**, 345–361.
26. H. Koller, A. Wolker, L. A. Vallaescusa, M. J. Diaz-Cabanas, S. Valencia and M. A. Camblor, *J. Am. Chem. Soc*., 1999, **121**, 3368–3376.
27. A. Pulido, G. Sastre and A. Corma, *Chem. Phys. Chem*., 2006, **7**, 1092–1099.
28. G. Sastre, A. Pulido and A. Corma, *Chem. Comm*., 2005, 2357–2359.
29. J. A. Tossell, *J. Phys. Chem. C*, 2007, **111**, 3584–3590.
30. L. Delmotte, F. Soulard, A. Guth, A. Seive, A. Lopez and J. L. Guth, *Zeolites*, 1990, **10**, 778–783.
31. S. I. Zones, R. J. Darton and S. J. Hwang, *J. Phys. Chem. B*, 2005, **109**, 652–661.
32. J. A. Tossell and Y. Liu, *Magn. Res. Chem*., 2004, **42**, S34–S40.

This page intentionally left blank

CHAPTER 2

NOE Studies of Solvent–Solute Interactions

J.T. Gerig

Contents

Department of Chemistry & Biochemistry, University of California, Santa Barbara, CA 93106, USA

Annual Reports on NMR Spectroscopy, Volume 64
ISSN 0066-4103, DOI 10.1016/S0066-4103(08)00002-1

Abstract

Intermolecular Overhauser effects resulting from interactions of solvent molecules with a solute are readily detected with modern instrumentation. After a discussion of how these effects arise, applications of intermolecular Overhauser effects in studies of solute–solvent and other interactions in solution are reviewed. Observed effects may reflect (a) a local concentration of solvent molecules near the solute that is different from the concentration of the bulk, (b) kinematic behavior of solvent molecules near the solute that is different from that characteristic of the bulk solvent, or (c) formation of solute–solvent complexes that are long-lived relative to the time associated with diffusive encounters of solute and solvent. In mixed solvents, a solute–solvent Overhauser effect may indicate preferential association of one solvent component with the solute; such interactions may be regiospecific. Determination of solvent–solute intermolecular Overhauser effects have been done in systems that range from solutions of monoatomic gases to proteins. It is shown that additional experimental developments are needed to enable unambiguous interpretation of observed effects.

Keywords: overhauser effect; solvent interactions; NOE; intermolecular NOE; solvent effects; cross-relaxation; intermolecular dipole-dipole interaction; selective solvation; complex formation

1. INTRODUCTION

Beginning chemistry students are taught that a solution is a homogenous mixture of two or more materials. The component in highest concentration is called the solvent while the lesser component is the solute. The student's instructor tries to make clear that a solution will not form unless there is a net favorable free energy change resulting from interactions between the solvent and solute molecules within the mixture, as compared to interactions present in the separated solvent and solute. These simple concepts, of course, hide a world of complexity, for understanding the interactions between and within molecules lies at the heart of all chemistry and biochemistry. Further, the intrinsic disorder characteristic of the liquid state presents a huge experimental challenge to defining the structure, and structural fluctuations, present in a solution.

Sufficiently strong non-covalent interactions are central to the existence of condensed phases of pure materials and solutions.[1] These interactions can be the result of hydrogen-bond formation, electrostatic effects arising between dipoles and ions, dispersion effects resulting from electron behavior of atoms and molecules at short range, charge-transfer interactions and entropy-driven (solvophobic, hydrophobic) effects.[1–3] All interactions would preferably be described in quantum mechanical terms,[2] but empirical or classical approaches can often be adequate for the purpose at hand.

A change of solvent can alter the dominant conformation of a dissolved molecule,[4–6] change the rate of a reaction,[7,8] shift the position of an equilibrium,[8] or modify the interaction of a species with electromagnetic radiation. The influence of solvent on reaction rates can be dramatic. For example, the rate constant for the S_N2

nucleophilic displacement reaction of bromide from methyl bromide by hydroxide ion is reduced by about 20 orders of magnitude when the reaction takes place in aqueous solution compared to the gas phase. A significant portion of this effect is probably related to the hydration of hydroxide ion[8,9] and the gas phase reaction is likely more complex mechanistically than the usual picture of an S_N2 reaction.[10,11]

A number of empirical ''solvent scales'' have been developed to correlate observed solvent effects on reactivity with some physical or chemical property of the solvent or solvent mixture. Such correlates include the polarity or ''ionizing power'' of the solvent and the solvatochromic effect of solvent on a spectroscopic probe molecule.[8,12–15]

Successful completion of a chemical reaction in solution may require a mixture of solvents. An extensive literature indicates that it is usually possible to construct mixtures of liquids that have desired physical and chemical properties, such as density or viscosity, in addition to possessing the ability to dissolve the materials of interest.[16] Use of a solvent mixture raises questions about which solvent component or components interact with a particular solute. The notion of selective interactions of solutes with solvent components in mixed systems has been extant in the chemical community for at least 50 years, and a variety of experimental methods have been developed to explore the composition and dynamics of the critical layer(s) of solvent molecules adjacent to a solute in a mixed solvent. These have included (a) spectroscopic studies of dye molecules whose transition energies are dependent on solvent composition and solvent molecule dynamics,[17–20] (b) examination of chemical reactivity,[21,22] (c) mass spectrometry,[23,24] (d) molecular dynamics (MD) simulations,[25] and (e) various theoretical/thermodynamic approaches.[26,27]

A challenge to theoretical chemistry is a reliable prediction of the effect of a given solvent or solvent mixture on the rate of a reaction in solution. Early theoretical studies of solvent effects on chemical processes viewed the solute as occupying a cavity in a continuum of solvent molecules, typically characterized by a set of bulk solvent molecule properties. However, theory based on continuum models probably cannot reveal subtle effects such as the difference between the effects of ethanol and acetonitrile, two liquids which have similar molecular weights and bulk dielectric constants. Continuum theories for mixed solvents are rarely successful due to selective solvation and microscopic dielectric constants that differ from the dielectric constant of the bulk medium.

Theoretical descriptions of solvent–solute interactions that recognize to some extent the discrete nature of solvent molecules include various quantum chemical approaches and MD calculations.[2,28–30] Molecular dynamics simulations of solvent–solute systems rely on descriptions of the interactions of a limited number of solute and solvent molecules constrained by some procedure to a space of defined shape and volume. The interactions between entities within that volume are described by a potential energy function that may contain some combination of empirical or semi-empirical terms, usually based in some manner on experimental information. The potential energy function describing the interaction of solvent molecules with each other is important to the success of these approaches. It is noteworthy that a potential energy function (force field) for

the interaction of water molecules obtained using only quantum mechanical methods has been recently described.[31] When used in MD simulations, this function predicts spectroscopic and thermodynamic properties of liquid water that are in agreement with experiment. Computational (and experimental) methods have developed to the extent that it is possible to achieve detailed understandings, for example, of reactivity of conformations differing only by rotation around a single carbon–carbon bond[32] or of multi-reagent processes such as water catalysis of the reaction between hydroxyl radicals and acetaldehyde in the gas phase.[33]

It is natural that understanding a subject as broad and important as the roles of solvent molecules in defining chemical reactivity has produced a large literature. It would be impossible and inappropriate to survey that literature for this article. However, to provide some context for the discussions which follow the following works should be mentioned.

An early monograph by Amis summarizes treatments of solvent effects on rates of reactions involving an ion and a dipolar reactant, two dipolar reactants, or electron exchange.[34] A multi-author series of volumes presents the status of theoretical and experimental approaches to examination of ion–solvent interactions through 1984.[35] The volume ''Molecular Theory of Solvation'', edited by Hirata[36], provides an indication of the current status of statistical mechanical theories of the liquid state based on reference interaction site models. The indispensable ''Handbook of Solvents'' is a comprehensive collection of short chapters on a wide variety of topics, including theoretical and empirical descriptions of solvents and solute–solvent interactions, solvent effects on reactions, practical information on the industrial uses of solvents, and biological and environmental considerations in the use of solvents.[37] The third edition of Reichardt's ''Solvents and Solvent Effects in Organic Chemistry'' offers extensive coverage of the literature through 2001 on topics related to solute–solvent interactions, solvent effects of chemical equilibria and chemical reactivity, and solvent effects on various spectroscopies of organic molecules.[8] Egelstaff[38] has provided an introduction to descriptions of the liquid state; a contemporaneous volume by Balucani and Zoppi[39] focuses on dynamics of the liquid state. Older introductory texts provide useful introductions to theories of the liquid state and experimental methods for study of this state.[40,41]

2. METHODS USED TO EXAMINE SOLVENT–SOLUTE INTERACTIONS

Infrared, Raman, ultraviolet-visible, NMR, ESR, microwave, and ultra-sound spectroscopic experiments have been applied to the study of solute–solvent interactions. A survey of spectroscopic methods that have contributed to understanding the nature of electrolyte solutions is provided by a volume edited by Dogonadze et al.[35] Muller-Dethlefs and Hobza[1] describe the application of these and other spectroscopic methods to study of non-covalent interactions in condensed media. Reichardt[8] provides a chapter on solvent effects on ultraviolet-visible, fluorescence, CD, infrared, ESR, and NMR spectra.

Various scattering experiments, particularly neutron scattering, provide valuable information about the microstructure of solutions.[39,42]

Electrospray and other ionization techniques enable mass spectrometric examination of solute–solvent clusters in the gas phase. These clusters presumably are reflective of species present in the solution from which they are formed and their study provides clues about the stoichiometry and energetics of solvent–solute interaction. Self-association in binary solvent mixtures[23,24,43–45] and selective solvation of solutes[23,44,45] have been examined recently by these techniques.

Kirkwood–Buff integrals are related to pair correlation functions for solution components and can be obtained from such data as isothermal compressibilities, molar volumes, and vapor composition.[46,47] They can provide a direct, quantitative measure of the preferential solvation of solution components. Kirkwood–Buff integrals for a number of completely miscible aqueous binary mixtures have been provided by Marcus.[48,49]

NMR techniques have proven to be especially revealing of solute–solvent interactions.[50] Indeed, the first chapter of the first volume of Annual Reviews of NMR Spectroscopy in 1968 included discussion of hydrogen bonding and other solvent effects on NMR spectra[51] and this topic has been a staple of such reviews ever since. The solvent used for liquid state NMR influences chemical shielding parameters, scalar and dipolar coupling constants, and relaxation behavior. Bagno et al.[52] provide a recent survey of results that indicate how these quantities respond to a solvent change. Solvent effects on chemical shifts and scalar coupling constants are also discussed by Reichardt.[8] An early review considered NMR relaxation studies of solute–solvent interactions.[53] NMR methods readily provide information about translational and rotational diffusion in solutions;[54] these properties are tightly linked to molecular shape and volume and can give indications of solute-solvent interactions, aggregation behavior, and the binding of ligands to large molecules.

Nuclear Overhauser effects (NOEs) and the related rotating frame nuclear Overhauser effects (ROEs) result from magnetic interactions between spin dipoles that produce nuclear spin-lattice and transverse relaxation.[55–57] Intramolecular NOEs and ROEs are familiar to most chemists and biochemists – these are effects that arise from interactions between nuclear spins that are present within the same molecule. Intramolecular spin dipolar interactions are strongly dependent on internuclear distance, to the extent that intramolecular NOEs and ROEs are not detectable if the distance between the interacting spins is greater than 5–6 Å. It is the strong internuclear distance dependence that makes determinations of intramolecular NOEs and ROEs such powerful tools for deducing three-dimensional (3D) structures.

Spin dipoles on different molecules may also interact, produce spin relaxation and, therefore, lead to *intermolecular* Overhauser effects. Intermolecular NOEs were first reported by Kaiser[58] who used c.w. techniques to observe an approximately 30% increase in the intensity of the chloroform proton signal from a 2 : 9 mixture of chloroform and cyclohexane when the cyclohexane proton resonance was saturated. In other early work, Homer and Cedeno[59] determined intermolecular NOEs in mixtures of organic solvents and demonstrated that intermolecular interactions with protons may contribute to carbon-13 relaxation in these systems. Using c.w. experiments, Pitner et al.[60,61] provided evidence that

intermolecular NOEs could be used to explore the interaction of water and organic solvents with peptides.

Detection of the chloroform–cyclohexane NOE in Kaiser's system was realized by a two-dimensional (2D) NMR experiment by Macura and Ernst[62,63] in 1980. Subsequent improvements in instrumentation, particularly the introduction of stable, self-shielded pulsed field gradient technologies, have facilitated detection of solvent–solute and other intermolecular NOEs and ROEs.[52,54,64] In the process, it has become clear that determination of intermolecular NOEs can be a useful experiment for the study of selective solvation and the time-scales for solvent–solute interactions.

3. SCOPE OF THIS CHAPTER

An effort has been made to include citations of all papers from the 10 years prior to June 2007 that describe results of intermolecular NOE experiments directed toward understanding solute–solvent and other intermolecular interactions. Sufficient citations of earlier reports are included so that the reader can find other relevant papers using contemporary searching techniques. The author readily acknowledges that the chapter is probably not exhaustive and apologizes in advance to those whose work should have been mentioned but was not. The goal has been to provide a digestible and didactic summary of emerging NMR techniques that provide information about the strength and duration of interactions of dissolved molecules with solvent molecules or other species in solution.

4. THEORETICAL BACKGROUND

Overhauser effects are the result of those processes in a solution that produce spin–lattice (T_1) and spin–spin (T_2) nuclear spin relaxation. The relaxation times characterizing these processes are measurable (bulk) properties of the sample. The populations of allowed nuclear spin states in a macroscopic collection of spins (the ^1H spins in a 0.01 M solution of chloroform in CCl_4, for example) are specified by the Boltzmann distribution law. After any perturbation of these populations, the system returns to the Boltzmann populations by exchanging energy with its surroundings. The rate at which equilibrium is re-established is quantified by a spin–lattice relaxation time T_1.

Relaxation requires the presence of magnetic fields within or near the molecules of interest that change at frequencies near the frequencies that correspond to the energy of transitions between the allowed spin energy states. Thus, relaxation of the protons in the chloroform sample mentioned will be driven by magnetic fields within or near individual chloroform molecules that change at a frequency of $\sim$500 MHz if the sample is in a magnetic field of 14.74 T. The spacing between allowed nuclear spin energy levels depends on the laboratory magnetic field in which the sample resides. As a result, relaxation

processes and measured relaxation times may be dependent on the magnetic field of the spectrometer used to measure T_1 or T_2.

In what follows, we limit the discussion of relaxation and NOEs to collections of spin 1/2 nuclei in an isotropic medium. Nuclei that have spin $>1/2$, or are in situations where molecular motions are anisotropic due to orientational or positional ordering, need somewhat more complex treatments.[65–68]

Consider a spin system containing two spin 1/2 nuclei, A and X. The two spins could be of the same spin type, say both ^{1}H nuclei, but characterized by different chemical shifts, or could be different species, perhaps A $\equiv ^1$H and X $\equiv ^{19}$F. The spins A and X could be in the same molecule or in different molecules. When in the same molecule, spins A and X may be spin coupled to each other, or not.

A system consisting of two spin 1/2 nuclei has four allowed nuclear spin energy states.[69–71] Taking into account all of the possible transitions between the allowed states as avenues for relaxation leads to the Solomon equations for spin–lattice relaxation (Equations (1) and (2))

$$\frac{dA_Z(t)}{dt} = -\rho_A(A_Z(t) - A_Z^\infty) - \sigma_{AX}(X_Z(t) - X_Z^\infty) \quad (1)$$

$$\frac{dX_Z(t)}{dt} = -\rho_X(X_Z(t) - X_Z^\infty) - \sigma_{XA}(A_Z(t) - A_Z^\infty) \quad (2)$$

Here $A_Z(t)$ and $X_Z(t)$ are components at time t of the sample magnetizations associated with spin A and spin X along the direction of the laboratory magnetic field (taken to be the z-axis in a Cartesian reference frame), and A_Z^∞ and X_Z^∞ are these magnetizations at equilibrium (i.e., $t = \infty$). The coefficients ρ_A and ρ_X are sums of transition probabilities between the allowed states, such that $\rho_A = 1/T_{1A}$, the spin–lattice relaxation rate for spin A that would be observed in an experiment in which the populations of energy levels associated with spin A are inverted, with a similar meaning for ρ_X. The term $\sigma_{AX}(\equiv \sigma_{XA})$ is commonly called the cross relaxation rate; it has the same units as $1/T_{1A}(s^{-1})$. The cross relaxation rate depends on the difference between the probabilities of transition between the lowest and highest allowed energy states of the AX system and the probabilities of transition between the two intermediate allowed energy states of this two-spin system.

The mutual interaction of the nuclear spin dipole of spin X with the nucleus of spin A, and vice versa, leads to relaxation of both spins and potentially contributes to a non-zero value of σ_{AX}. There are other mechanisms or processes by which spin A and spin X can be relaxed but most of these do not contribute to the cross relaxation term σ_{AX}.

Two ingredients determine the contribution of a nuclear spin dipole–nuclear spin dipole interaction to relaxation. One is the strength of the interaction or, more correctly, the Hamiltonian that describes the interaction. The dipolar Hamiltonian for the A–X interaction is discussed in many texts.[69,72–74] The second component is a description of the time dependence of the A–X interaction. That is, how rapidly and in what manner the magnetic field created by a dipole–dipole interaction changes. This second aspect will be fundamentally different when

both spin A and spin X are covalently bound to the same molecule, producing an *intramolecular* dipolar interaction between the spins, compared to the situation where A and X are parts of different molecules, leading to an *intermolecular* A–X relaxation interaction.

4.1 Intramolecular dipole–dipole cross relaxation

Spin coupling between spins A and X has been neglected in the discussion that follows. Neuhaus and Williamson,[56] Kowalewski and Maier,[75] and Ghalebani et al.,[76] among others, have considered the complications introduced by such coupling.

Assuming that the distance between them (r_{AX}) is invariant, the dipolar interaction between two interacting spins A and X present in the same molecule is modulated by the rotational motions of the molecule. As an approximation, it is often assumed that the spins are fixed in a spherical molecule that has radius r_{AX}. The sphere reorients randomly and isotropically due to collisions with solvent molecules. In this simplified but often useful description, a rotational correlation time (τ_R) is used to describe the random tumbling of the AX-containing molecule, where the time τ_R corresponds roughly to the average time it takes the molecule to rotate through 1 rad in any direction.

A molecule of volume $V(= 4\pi r_{AX}^3/3)$ within a solvent of bulk viscosity η at temperature T has a rotational correlation time given by the Stokes–Einstein–Debye equation (Equation (3)), where k_B is Boltmann's constant and f_R is a microviscosity factor defined by Gierer and Wirtz.[77]

$$\tau_R = \frac{V\eta f_R}{k_B T} \tag{3}$$

Equation (3) agrees with one's intuition, showing that the rotational correlation time increases as the size of the molecule holding A and X increases, and decreases as the sample temperature is increased. An increase in solution viscosity is expected to slow the rate of molecular tumbling, leading to an increase in τ_R. The viscosity of the solution likely decreases as a sample is warmed, thereby also contributing to the reduction of τ_R when temperature is increased.

The NOE cross relaxation term σ_{AX}^{NOE} in Equation (1) is given by

$$\sigma_{AX}^{NOE} = \frac{K_{AX}}{10}\frac{1}{r_{AX}^6}\left(\frac{6\tau_R}{1+(\omega_A+\omega_X)^2\tau_R^2} - \frac{\tau_R}{1+(\omega_A-\omega_X)^2\tau_R^2}\right) \tag{4}$$

where

$$K_{AX} = \left(\frac{\mu_0}{4\pi}\right)^2(\gamma_A\gamma_X\hbar)^2 \tag{5}$$

γ_A and γ_X are the gyromagnetic ratios of the interacting spins, and ω_A and ω_X are the Larmor frequencies of these spins. The factor K_{AX} is referred to as the dipolar coupling constant and has the value 5.66×10^{11} Å^{6}s^{-2} when the interspin distance is expressed in Angstrom units and both spins are ^{1}H nuclei.

In the rotating frame Overhauser experiment the cross relaxation term σ_{AX}^{ROE} is given by

$$\sigma_{AX}^{ROE} = \frac{K_{AX}}{10}\frac{1}{r_{AX}^6}\left(\frac{3\tau_R}{1+(\omega_A)^2\tau_R^2}+\frac{2\tau_R}{1+(\omega_A-\omega_X)^2\tau_R^2}\right) \tag{6}$$

The cross relaxation term σ_{AX}^{ROE} is always positive, while σ_{AX}^{NOE} can be positive, zero or negative depending on the values of the terms within the parentheses of Equation (4). It should be mentioned that σ_{AX}^{ROE} can only be experimentally determined if spin A and spin X are of the same nuclear type. Typically both are ^{1}H nuclei. In practice, the σ_{AX}^{NOE} and σ_{AX}^{ROE} terms are only detectable if the interspin distance r_{AX} is less than $\sim$5.5 Å.

Equations (4) and (6) assume that reorientation of the A–X spin pair in solution is isotropic. This is clearly a simplification. Real molecules have asymmetric shapes and undergo rotational diffusion more readily in some directions than others. Further, the spin pair of interest may be able to undergo local motions that are not reflected in the overall correlation time. Treatments of intramolecular relaxation in which reorientation is anisotropic, or in which the A–X spin pair has mobility relative to the molecule in which the spin pair resides, are available.[55,57,78]

4.2 Intermolecular dipole–dipole cross relaxation

When spin A and spin X are on different molecules, the time dependence of their mutual interaction is defined by the diffusion of the molecules containing them relative to each other. Various models have been proposed to describe diffusion and interaction of molecules in solution.[79–82] One approach posits that A and X are at the centers of separate hard (impenetrable) spheres of radius r_A and r_X, respectively. The spheres diffuse due to Brownian motion with characteristic translational self-diffusion coefficients D_A and D_X; the two spins cannot come closer than r_A+r_X, the ''distance of closest approach''. A correlation time (τ_D) for the interaction of A and X is usually taken as the time required to diffuse the distance r_A+r_X, with τ_D given by[80,83,84]

$$\tau_D = \frac{(r_A+r_X)^2}{(D_A+D_X)} \tag{7}$$

The cross relaxation rate σ_{AX}^{NOE} for the intermolecular interaction of the spins A and X when the signal for spin A is observed is[84]

$$\sigma_{AX}^{NOE} = \frac{6K'_{AX}\pi N_X}{5(D_A+D_X)(r_A+r_X)}(6J_2(\omega_A+\omega_X)-J_2(\omega_A-\omega_X)) \tag{8}$$

while

$$\sigma_{AX}^{ROE} = \frac{6K'_{AX}\pi N_X}{5(D_A+D_X)(r_A+r_X)}(3J_2(\omega_A)+2J_2(\omega_A-\omega_X)) \tag{9}$$

The spectra density function $J_2(\omega)$ in these equations is

$$J_2(\omega) = \left(\frac{\omega\tau_D + \frac{5}{\sqrt{2}}(\omega\tau_D)^{1/2} + 4}{(\omega\tau_D)^3 + 4\sqrt{2}(\omega\tau_D)^{5/2} + 16(\omega\tau_D)^2 + 27\sqrt{2}(\omega\tau_D)^{3/2} + 81(\omega\tau_D) + 81\sqrt{2}(\omega\tau_D)^{1/2} + 81} \right) \tag{10}$$

In Equations (8) and (9), N_X is the number of X spins per mL of solution, (r_A+r_X) is expressed in Å, the diffusion coefficients (D_A+D_X) given in units of cm^2s^{-1} and $K'_{AX} = K_{AX} \times 10^{-40}$.[1]

Equations (8) and (9) convey the important qualitative information that the cross relaxation of spin A due to intermolecular interactions with molecules containing spin X depends on the *concentration* of the X-containing molecules, the *mutual diffusion* of the A and X molecules and the *distance* of closest approach of A and X.

The model used to obtain Equations (8) and (9) is not very realistic for reasons that include the following:

(a) It neglects any interactions between solute molecules (containing spin A) and solvent molecules (having the X spin) or the effects of any interactions between solvent molecules. Such interactions in real systems produce local organization of molecules and may lead to diffusive motions that are not completely random.[38,39,47] Moreover, the surfaces of real molecules are not electrically homogeneous so that the strength of interactions of dipoles and ions with these surfaces will vary across them.

(b) Real molecules are not spherical but rather have ''lumpy'' surfaces with bumps and depressions following the outlines of their van der Waals surface. A method that seems to give reliable results has been developed to extend Equations (8) and (9) to take into account the shape of the molecule containing spin A as it interacts with a spherical molecule containing spin X.[85] Another approach to this problem has been reported by Teng, Martini, and Bryant.[86]

(c) In real molecules the spin of interest is likely not in the center of the sphere chosen to represent the molecule. If interacting spins are not located at the center of their representative spheres, rotation of the molecules will have the effect of altering the A–X interaction distance as the molecules approach each other. Further elaborations of the theory for the intermolecular dipole–dipole interaction take into account modulation of the A–X internuclear distance by the rotational motions of the molecules containing spins A and X.[81,82,84,87,88]

(d) Due to intermolecular interactions, it is unlikely that diffusion of an X-containing molecule when near an A-spin molecule will be exactly the same as its diffusion in the bulk of a solution. That is, the quantity D_A+D_X may be a function of the distance r_A+r_X. Halle has presented theory for a

[1]The Stokes–Einstein relation ($D = k_BT/6\pi\eta r$, where k_B is the Boltzmann constant, T the absolute temperature, η the shear viscosity, and r the radius) gives a reasonable estimate of the translational diffusion coefficient of a species that can be represented by a sphere of radius r.

model in which a layer of solvent molecules of a given thickness around an A-containing molecule is allowed to have D_A+D_X different from the value that is characteristic of the solution beyond this layer. The ''special layer'' presumably would have a thickness corresponding to one or a few molecules of the type bearing spin X.[82]

(e) The potential energy of interaction of A and X molecules envisioned in the development of Equations (8) and (9) is a ''hard wall'' potential – the energy of interaction is infinitely large when the molecules are at the distance of closest approach but otherwise is zero. Frezzato et al.[88] have extended this treatment to several somewhat more realistic interaction potentials between the A and X molecules.

Khazanovich and Skrynnikov[89] have discussed errors that may arise when solute spin A is spin coupled to another species.

4.3 Intermolecular dipole–dipole cross relaxation in the presence of long-lived association

The model used to obtain Equations (8) and (9) assumed that molecules containing spin A and spin X are undergoing force-free translation. Some extensions of this model were indicated in the previous section. But it may be that X-containing molecules interact strongly enough with molecules containing spin A that an A–X complex is formed. Halle has shown that this kind of ''sticky'' interaction leads to a contribution to the σ_{AX}^{NOE} cross relaxation parameter that is given by[82]

$$\sigma_{AX\ \mathrm{complex}}^{NOE} = \frac{K_{AX}}{10}(6J_2'(\omega_A+\omega_X) - J_2'(\omega_A-\omega_X)) \tag{11}$$

with the spectral density function J_2' defined as

$$J_2'(\omega) = \sum_{k=1}^{N} \frac{n_k}{r_k^6} \frac{\tau_{C,k}}{1+\omega^2\tau_{C,k}^2} \tag{12}$$

The summation in Equation (12) is over N classes of X-containing molecules, with each class having n_k solvent spins at a distance r_k from the A spin of interest. Interactions of each class of solvent molecules are characterized by the correlation time $\tau_{C,k}$, given by

$$\frac{1}{\tau_{C,k}} = \frac{1}{\tau_R} + \frac{1}{\tau_{M,k}} \tag{13}$$

where τ_R is the rotational correlation time of the complex and $\tau_{M,k}$ is the mean residence time of the spins in the complex. As the mean residence time of X molecules in the complex increases, the A–X interaction comes to resemble more and more an intramolecular interaction, with $\sigma_{AX\ \mathrm{complex}}^{NOE}$ approaching the value predicted by Equation (4).

To have an appreciable influence on an observed cross relaxation term, a ''sticky'' solute–solvent collision must persist for a time of the order of the rotation correlation time of the complex, reasonably assumed to be

approximately the same as τ_R for the solute molecule. The duration of ''non-sticky'' solvent–solute interactions at normal temperatures appears to be of the order of 10 ps,[90,91] although this time is dependent on the nature of the solute and solvent and surely varies over the chemically and electrically heterogeneous surface of the solute. Small molecules could have rotational correlation times of this order and thus may have cross relaxation terms that may depend on the contributions represented by both Equations (8) and (11).

4.4 Molecular dynamics simulations

Calculation of intramolecular cross relaxation rates from molecular dynamics (MD) simulations has a long history, particularly in the area of biological structure determination.[92] The random intermolecular interactions of molecules that lead to intermolecular dipole–dipole cross relaxation should also be correctly represented in a reliable MD simulation of a solute–solvent system. It has been shown that intermolecular relaxation phenomena, calculated from a simulation of a collection of soft spheres or of Lennard–Jones atoms, reproduces the results predicted from the model used for the derivation of Equations (8) and (9).[93,94] Grivet[93] and Odelius et al.[94] have emphasized that the details of MD simulations intended to explore intermolecular relaxation must use a sufficiently large simulation model in terms of the number of molecules present and must be allowed to run for a sufficiently long time.

Molecular dynamics studies of intermolecular ^1H–^1H interactions in acetonitrile,[95] water,[96] and a lipid bilayer model of a biological membrane[97] have been reported. Intermolecular relaxation of xenon dissolved in liquid benzene by the solvent protons was confirmed by a MD simulation.[98] MD simulations of selective (preferential) solvent interaction in water–organic solvent mixtures, motivated by the goal of understanding NOE observations, have been reported.[99–101]

4.5 Some calculations

Calculations using the equations in the previous sections can provide some feeling for the magnitudes of Overhauser effects to be anticipated for real systems. Table 1 presents results for a solution of glucose (MW = 180) in a solution of 90%

Table 1 Calculated small molecule cross relaxation parameters

Proton frequency (MHz)	σ_{HH}^{NOE} (s^{-1})	σ_{HH}^{ROE} (s^{-1})	σ_{HH}^{NOE} (s^{-1})	σ_{HH}^{ROE} (s^{-1})
	Intramolecular	Intramolecular	Intermolecular	Intermolecular
200	0.138	0.147	0.0451	0.0503
400	0.112	0.143	0.0418	0.0490
600	0.083	0.137	0.0393	0.0481
800	0.059	0.130	0.0372	0.0473
1000	0.039	0.123	0.0354	0.0467

$H_2O/10\%$ D_2O.[102] The water proton concentration in this mixture is 99 M, corresponding to $N_H = 5.96 \times 10^{22}$ spins mL^{-1} in Equations (8) and (9). The experimental rotational correlation time (τ_R) of glucose in this system is 0.1 ns and the translational diffusion coefficients for water and glucose are 4.9×10^{-5} cm^2s^{-1} and 5.6×10^{-6} cm^2s^{-1}, respectively.[102] The interproton distance (r_{HH} in Equations (4) and (6) or (r_H+r_H) in Equations (8) and (9)) was set to 2.4 Å, the van der Waals contact distance for two hydrogen atoms.[103] The intermolecular cross relaxation terms in Table 1 correspond to Overhauser effects of 3–5% at a mixing time of 1 s and should be representative of effects on systems of small molecules at room temperature in solvents of typical viscosities.

The calculated intramolecular and intermolecular cross relaxation contributions are of the same magnitude in this example. Although the contribution of an individual intramolecular proton–proton interaction to cross relaxation is larger than that of a single proton–proton intermolecular interaction, there are many more (N_H) intermolecular interactions. The distance dependence in Equations (8) and (9) is weak, and spins at molecular separations greater than 8 Å still contribute appreciably to the intermolecular σ_{HH}^{NOE} and σ_{HH}^{ROE} .

The ''extreme narrowing'' limit ($\omega\tau_c \rightarrow 0$) for Equations (4) and (6) under the conditions of this calculation is 0.148 s^{-1} and it is seen that the intramolecular cross relaxation terms (σ_{HH}^{NOE} and σ_{HH}^{ROE}) approach this limit at the lowest proton frequency. The ''extreme narrowing'' limit for intermolecular relaxation (Equations (8) and (9)) requires $(\omega\tau_D)^{1/2} \rightarrow 0$. In this limit, the intermolecular σ_{HH}^{NOE} and σ_{HH}^{ROE} terms for the glucose–water system are 0.0532 s^{-1}. The intermolecular terms do not approach the extreme narrowing limit as closely as do the intramolecular terms, even at 200 MHz. Nordstierna et al.[104] have most recently reaffirmed the conclusion reached by several authors that ''there is no (experimentally accessible) extreme narrowing regime for intermolecular cross relaxation''.

A second set of calculations (Table 2) was done with a rotational correlation time (τ_R) of 5 ns and translational diffusion coefficients of 2.3×10^{-5} cm^2s^{-1} and 4.2×10^{-6} cm^2s^{-1} respectively. These parameters are characteristic of the small protein lysozyme (MW = 14,313) in aqueous solution.[105,106] Again, the interproton distance (r_{HH} in Equations (4) and (6) or (r_H+r_H) in Equations (8)

Table 2 Calculated large molecule cross relaxation parameters

Proton frequency (MHz)	σ_{HH}^{NOE} (s^{-1})	σ_{HH}^{ROE} (s^{-1})	σ_{HH}^{NOE} (s^{-1})	σ_{HH}^{ROE} (s^{-1})
	Intramolecular	Intramolecular	Intermolecular	Intermolecular
200	−1.425	3.071	0.0457	0.0511
400	−1.467	2.989	0.0424	0.0498
600	−1.474	2.973	0.0398	0.0489
800	−1.476	2.967	0.0377	0.0481
1000	−1.477	2.963	0.0358	0.0474

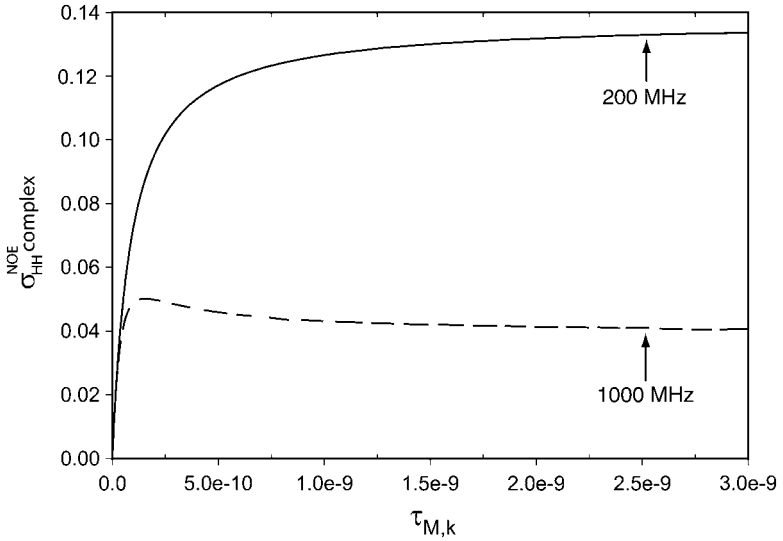

Figure 1 Calculated contributions to observed intermolecular NOE cross relaxation terms when a complex of mean lifetime $\tau_{M,k}$ forms between the species bearing spin A and spin X. The parameters used in the calculations were for the glucose–water solution described in the text (Table 1).

and (9)) was set to 2.4 Å and it was assumed that the protein is dissolved in 90% H_2O/10% D_2O.

The NOE intramolecular cross relaxation rate is negative for molecules the size of this protein since the second term in Equation (4) becomes dominant when τ_R is large. Diffusion coefficients decrease as molecular size increases but the sum of the diffusion coefficients for water and the protein solute is not massively different from the sum characteristic of the glucose-water system. The result is that computed intermolecular cross relaxation terms are similar for the large molecule and small molecule examples.

Equation (11) indicates that an additional contribution to an intermolecular σ^{NOE}_{HH} or σ^{ROE}_{HH} cross relaxation term can arise if the species containing spin X (the solvent) forms a complex with the molecule containing spin A (the solute) such that the two species are together for a mean time $\tau_{M,k}$. Experimental data indicate that the time scale for such interactions may range from picoseconds[90] to nanoseconds.[107,2] Application of Equation (11) requires knowledge of the number of spins (n_k) interacting with spin A at a distance of r_k with the mean lifetime of $\tau_{M,k}$. Figure 1 shows the calculated contribution ($\sigma^{NOE}_{HH\,complex}$) to the observed small

[2]Otting[108] gives a procedure for estimating the mean lifetime of a water molecule–protein interaction. Assuming that the mean life time of a solvent molecule interacting with the solute is the time it takes for the solvent molecule to translate a distance corresponding to its diameter and the applicability of the Einstein–Smoluchowski equation ($\tau_{M,k} = x^2/6D$) where x is a displacement in any direction and D is the translational diffusion, the mean life time for a water–solute interaction would be about 10 ps if the water diffusion coefficient is 2×10^{-5} cm^2s^{-1}.

molecule intermolecular cross relaxation term when $n_k = 1$ and $r_k = 2.4$ Å, for a range of $\tau_{M,k}$ when τ_R is 0.1 ns. As the mean lifetime increases, the dynamics of the complex more and more resemble those of a single molecule containing spins A and X. Thus, the contribution $\sigma^{NOE}_{HH\ complex}$ approaches the value of the intramolecular σ^{NOE}_{HH} at long mean lifetimes. The calculations shown in Figure 1 also emphasize that this contribution to cross relaxation is expected to be strongly dependent on spectrometer frequency.

Figure 2 provides results of similar calculations for the large molecule ($\tau_R = 5$ ns) intermolecular $\sigma^{NOE}_{HH\ complex}$ term when $n_k = 1$ and $r_k = 2.4$ Å over the same range of $\tau_{M,k}$. At small values of $\tau_{M,k}$ the overall dynamics of the interaction between solute and solvent molecules within the complex resemble those for a small molecule and $\sigma^{NOE}_{HH\ complex}$ is calculated to increase in a spectrometer frequency-dependent way when the mean life time of the interaction is less that ~1 ns. For longer life times, the A–X interaction is dominated by the dynamics of the large molecule and $\sigma^{NOE}_{HH\ complex}$ approaches the negative value characteristic of the intramolecular A–X interaction shown in Table 2.

Figures 1 and 2 suggest a potentially fruitful way to diagnose the effects of complex formation on intermolecular Overhauser effects would be studies of the spectrometer frequency dependence of σ^{NOE}_{HH} and σ^{ROE}_{HH}. Such experiments have been reported,[104,109] but are rare. However, a reliable interpretation of results in terms of complex formation may be difficult since various combinations of $\tau_{C,k}$, n_k, and r_k in Equation (11) can give the same value for $\sigma^{NOE}_{HH\ complex}$.

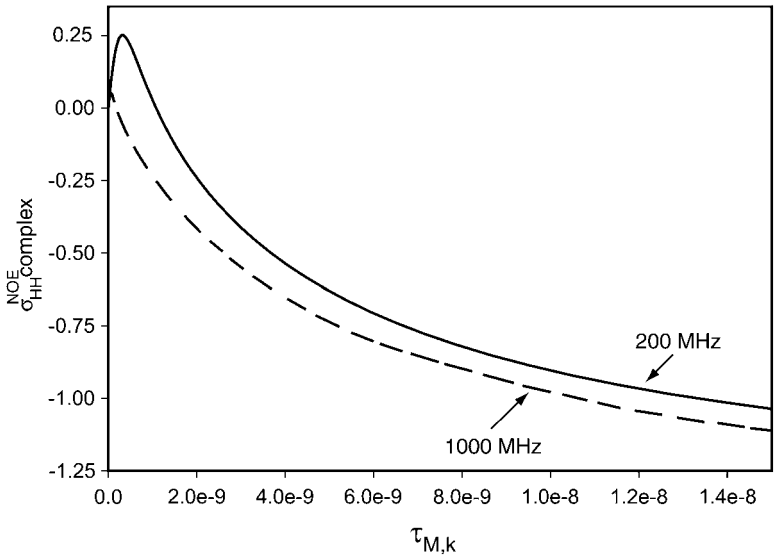

Figure 2 Calculated contributions to observed intermolecular NOE cross relaxation terms when a complex of mean lifetime $\tau_{M,k}$ forms between the species bearing spin A and spin X. The parameters used in the calculations were for the lysozyme–water solution described in the text (Table 2).

5. EXPERIMENTAL CONSIDERATIONS

The calculated intermolecular cross relaxation terms in Tables 1 and 2 suggest that solvent–solute Overhauser effects should be reliably detected with current instrumentation. However, the calculations were done with a solvent having a high molar concentration of solvent spins (99 M); the concentration of protons in an organic solvent will be less than this, with a concomitant reduction in the cross relaxation term. In practice one will usually want to use a mixing time shorter than 1 s to ensure initial rate behavior of the NOE, so the ability to detect an intensity effect as small as a few tenths of a per cent will be needed.

Neglecting spin coupling, the intensity of a solute NMR signal (spin A) in a one-dimensional NMR experiment depends on the z-component of the A magnetization prior to application of the RF pulse that leads to the detected signal of A. Suppose that a NOE experiment with the A–X system starts with all spins at equilibrium, so that at $t = 0$, $A_Z(t) = A_Z^\infty$. Transverse magnetization components are zero. The Solomon equations (Equations (1) and (2)) are used to describe the components of magnetization along the laboratory magnetic field direction after an instantaneous perturbation of the z-magnetization of spin X.

The change in $A_Z(t)$, and, thus the A signal intensity over time, is described initially by Equation (4)

$$\frac{dA_Z(t)}{dt} = -\sigma_{AX}^{NOE}(X_Z(0) - X_Z^\infty) \tag{14}$$

where the subscript Z indicates the magnitude of the z-magnetization of the A and X spins. The quantity $X_Z(0)$ is the initial value of the solvent spin z-magnetization created by the perturbation, X_Z^∞ is the solvent spin magnetization when the system is fully relaxed, and σ_{AX}^{NOE} is the cross-relaxation rate due to the dipolar interactions of the solvent (X) and solute (A) spins. The initial change of intensity of the A signal after inversion of the X (solvent) magnetization ($X_Z(0) \equiv -X_Z^\infty$) is given by

$$A_Z(t) = 2\sigma_{AX}^{NOE}X_Z^\infty t + A_Z(0) \tag{15}$$

Given a mixing time (t) that is of duration much less than T_{1A}, the calculations in the previous section indicate that the first term in Equation (15) will likely be small relative to the initial A signal intensity. That is, detecting $2\sigma_{AX}^{NOE}X_Z^\infty t$ will involve finding a small difference between two large numbers $A_Z(t)$ ($\approx A_Z^\infty$) and $A_Z(0)$ ($\approx A_Z^\infty$) as a function of the mixing time t.

A better strategy for determining a small intermolecular NOE is to devise an experiment in which the initial A signal intensity is zero. In that case, Equation (15) becomes

$$A_Z(t) = 2\sigma_{AX}^{NOE}X_Z^\infty t + \rho_A A_Z^\infty t \tag{16}$$

A second experiment in which the X spin is unperturbed ($X_Z(0) = X_Z^\infty$) and the initial A signal intensity is again zero will produce an initial change

in the A signal that is given by

$$A_Z(t) = \rho_A A_Z^{\infty} t \tag{17}$$

Subtraction of the results of the second experiment from those of the first will give $2\sigma_{AX}^{NOE} X_Z^{\infty} t$ as the difference between small numbers. Plotting the result of the difference experiment against the mixing time will be linear initially, with a slope proportional to $2\sigma_{AX}^{NOE}$.

5.1 Pulse sequences

Bagno et al.[52] and Brand et al.[54] have discussed pulse sequences for detecting intermolecular NOEs. Use of magic angle pulsed field gradients is preferable in homonuclear experiments,[110] particularly when water is present in high concentrations. Figure 3 shows a pulse sequence used for heteronuclear NOE experiments in the author's group.

NOE experiments to detect solvent interactions usually involve determining the solute spin–solvent spin cross relaxation rate after perturbation of the magnetization of the solvent spins. If one is willing to sacrifice information about the site specificity of these interactions, the inverse experiment (detect signals of solvent spins, perturb solute spins) can also be used to investigate preferential solvation in a multi-component solvent. Thus, Bagno et al.[111] demonstrated selective interactions between the protons of dissolved glucose and the protons of

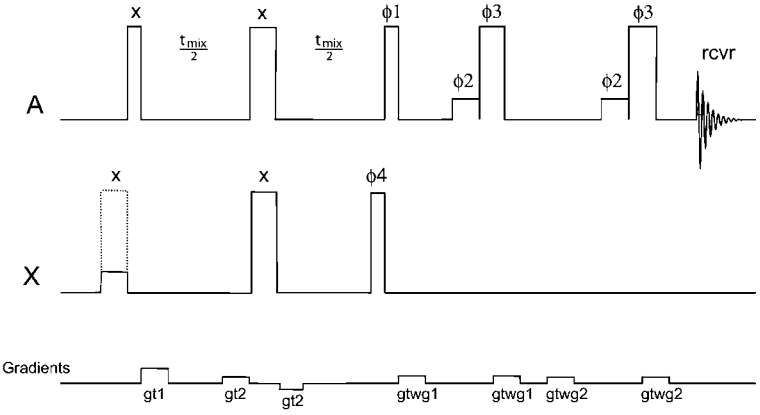

Figure 3 Pulse sequence for determination of heteronuclear NOEs. The narrow rectangles indicate 90° pulses. The wide rectangles indicate 180° pulses. The phases are $\phi1$ = x, x, y, y, -x, -x, -y, -y; $\phi2$ = -x, -x, -y, -y, x, x, y, y; $\phi3$ = x, x, y, y, -x, -x, -y, -y; $\phi4$ = x, -x, x, -x, x, -x, x, -x; rcvr = -x, x, -y, y, x, -x, y, -y; all other phases = x. The first 180° X pulse alternates *on* and *off* in alternate scans. This pulse may be made selective. Typical gradient levels and durations are gt1 = 19 Gcm^{-1}, 3 ms; gt2 = $\pm$8 Gcm^{-1}, 1 ms; gtwg1 = 11 Gcm^{-1}, 1ms and gtwg2 = 7 Gcm^{-1}, 1 ms. Gradients during the mixing period may be on at a low level for most of the mixing period ($gt2 \sim \frac{t_{mix}}{2}$). The 90° X pulse with phase $\phi4$ is for control of the dipolar field produced by the X spins. The sequence ends with the DPFGSE sequence for suppression of the solvent signal.

water in water–acetonitrile and water–dimethylsulfoxide mixtures by perturbing the magnetizations of the glucose molecules and observing intermolecular NOEs on the proton signals of the components of the solvent mixture.

5.2 Other details

Some attention must be paid to experimental details when determining cross relaxation terms arising from intermolecular solvent–solute interactions. These include the following:

(a) The molar concentration of solvent spins is typically high and X_Z^∞ is large relative to the solute magnetization. Thus, suppression of the solvent signal by a method that does not involve pre-saturation is usually required when collecting spectral data.
(b) Radiation damping effects can be present and can lead to unexpected recovery behavior of the solvent magnetization during the mixing time.[112,113]
(c) Difference (subtraction) methods place a premium on instrument stability, particularly phase stability, and the linearity of the detection system. Neuhaus and Williamson[56] discuss minimizing artifacts in NOE experiments. Certainly, a sharp, stable lock signal and good sample temperature control are essential for obtaining good difference spectra.[56,116]
(d) Control of the dipolar field associated with the solvent spins is important in getting good difference spectra.[114,115]
(e) Shaped or selective pulses are often used to invert the magnetization of interest. These have small effects on resonances at frequencies quite distant from the intended bandwidth of the pulse and can create effects that can be mistaken for NOEs.
(f) Corrections to experimentally determined cross relaxation terms should be applied to account for incomplete inversion of spin X; see the Supplementary Material of ref. 117 for the appropriate equations.

6. APPLICATIONS

6.1 Interactions between solvent molecules

Furó, Mutzenhardt, and Canet[117] have presented an experiment for detecting intermolecular dipolar interactions between identical molecules and applied it to examination of self-interactions of potassium octanoate molecules in a lyotropic liquid crystal. Their method relies on the low natural abundance of carbon-13 to distinguish molecules. They note that this and similar experiments could be used to study contacts between identical small solvent molecules. Such experimental results could provide useful tests of MD simulations.

6.2 Dissolved xenon

Xenon gas is soluble in most liquids and porous solids at high enough concentrations that NMR experiments with both NMR-active isotopes are feasible. Xenon-131 is a spin 3/2 nucleus with a substantial quadrupole moment. Relaxation of ^{131}Xe is dominated by the quadrupole mechanism, being driven by the electric field gradient at the nucleus arising from the electron distribution of the atom and from electric fields associated with surrounding solvent molecules.[118] Studies of quadrupolar relaxation in ^{131}Xe have provided insight into interactions of the monoatomic gas with solvents.[119,120]

All aspects of the NMR spectroscopy of ^{129}Xe, a spin 1/2 nucleus, have been reviewed recently.[121] Chemical shifts of ^{129}Xe are highly sensitive to local environment, with observed shifts spanning a range of nearly 250 ppm. Pioneering work by Stengle and co-workers[122] related the sensitivity of xenon shifts to the properties of its solvent. These and more recent authors typically have considered solvent effects on shifts in terms of empirical correlations with expected electric fields and/or van der Waals interactions. Recent efforts by the Jameson group[123] have put these considerations on a firmer theoretical foundation.

Spin-lattice relaxation times of ^{129}Xe in solution are typically of the order of 100 s.[124,125] As noted by Luhmer et al.,[98] determination of spin-lattice relaxation times for ^{129}Xe can be subject to errors arising from the effects of dissolved paramagnetic impurities and diffusion. Careful work has shown that relaxation of ^{129}Xe is primarily due to a transient spin-rotation mechanism involving complexes of gas atoms with solvent molecules and, in the case of proton-bearing solvents, intermolecular dipole–dipole interactions with the spins of the solvent molecules. The role of intermolecular proton–xenon relaxation has been confirmed by MD simulations.[98] Intermolecular ^{129}Xe{^{1}H} NOEs are typically negative due to the negative gyromagnetic ratio of ^{129}Xe.

Xenon is clinically useful as a general anesthetic. The mechanism of anesthesia remains poorly defined but likely involves dissolution of xenon in hydrophobic sites of neuronal membranes. Xu and Tang have used ^{129}Xe{^{1}H} Overhauser effects to probe the interactions of xenon with phosphatidylcholine vesicles, intended to be a model for cellular membranes.[126] Xenon–proton cross relaxation rates (σ_{XeH}) were largest for the choline methyl groups, indicating preferential interaction of the anesthetic with the amphiphilic head groups of the phospholipids.

Samples of ^{129}Xe can be hyperpolarized to levels as high as 65% by laser techniques, potentially producing orders of magnitude enhancement in sensitivity to detection.[127,128] Medical imaging applications using the hyperpolarized gas are feasible and are of growing importance.[121,129] Song et al.[130] have reported enhancement of proton signals of 4-nitrotoluene and α-cyclodextrin by hyperpolarized ^{129}Xe dissolved in organic solvents. However, attempts to detect enhancement of proton signals from several other solutes dissolved in D_2O were unsuccessful.[131] Dimitrov, Reddy, and Leigh[132] showed that solvent–solute dipole–dipole interactions provide the dominant relaxation mechanism for ^{129}Xe dissolved in water. The cross relaxation rate σ_{XeH} was found to be $3.2 \times 10^{-3}\,s^{-1}$ at 20°C; analysis indicated that the distance of closest approach of

water molecules to xenon was about 2.7 Å. Although proton–xenon cross relaxation exists, the authors concluded that, at reasonable concentrations, little net enhancement ($^{1}H\{^{129}Xe\}$ NOE) of the water proton signal by hyperpolarized xenon would be expected.

6.3 Ion–ion and ion–solvent interactions

Many experimental approaches can be used to estimate the number of solvent molecules associated with a dissolved ion and to characterize the energetics of ion–solvent interactions.[133] These interactions may be highly dynamic, with solvent molecules entering and leaving the solvent shell of an ion at rates that cover a wide range. Association of ions into ion pairs or higher aggregates can complicate any picture that emerges from such studies.[134] Selective solvation of ions, especially transition metal ions, in mixed organic–water solutions is amenable to study by NMR methods.[50,64,135]

Mo and Pochapsky[64] have reviewed the use of intermolecular NOEs to characterize ion–solvent interactions. A comprehensive review by Bagno, Rastrelli, and Saielli[52] covers various NMR observations that can be used to probe solvation of ionic species, including NOEs. Pregosin[136] has reviewed the use of NMR-based diffusion measurements for examining ion pairing and the effects of solvents on ion pairing.

An early example of the use of NMR to assess ion–solvent interactions is the detection of $^{113}Cd\{^{1}H\}$ NOEs in cadmium complexes of ethylenediaminetetraacetate (EDTA) and cyclohexanediaminetetraacetate (**1**).[137,138] A water–proton/metal–ion NOE was present in the first complex but absent in the second, indicating that solvent water molecules enter at least one inner sphere coordination site in the EDTA complex but probably do not coordinate to cadmium in the cyclohexanediaminetetraacetate complex.

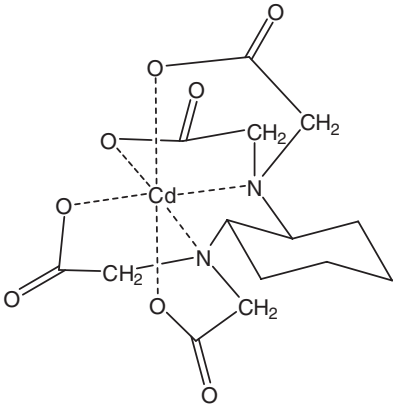

1

Interactions between complexed transition metals, their counterions and solvent molecules can be important in defining chemical properties of these materials, especially when they participate in reactions as catalysts or have a role

in reactions for synthesis of asymmetric compounds. NOE determinations and diffusion measurements have provided essential information for characterization of these systems, including their aggregation.[139–143] For example, hydrogen bonding of BF_4^- with a hydride (H_1, H_2) was the expected point of interaction of the 2,2′-bipyridyl iridium cation (**2**) with its counter ion. However, $^1H\{^{19}F\}$ NOE experiments in solution showed the presence of fluorine–proton dipolar interactions between the fluorines of BF_4^- and protons H_3 and $H_{3'}$, indicating that in solution the BF_4^- anion resides near these protons.[144] The observed anion–cation pairing in solution is consistent with the calculated electrostatic potential of **2**.

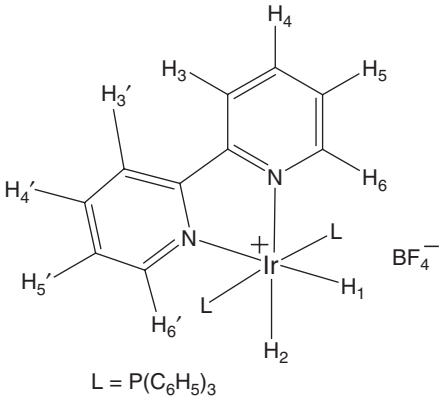

2

6.4 Ionic liquids

Ionic liquids are air-stable salts, typically composed of bulky organic cations and a variety of anions, that have the property of being liquid at convenient temperatures. These materials are thermally stable and have no detectable vapor pressure. Their unique properties have led to much interest in their use as solvents for chemical reactions, particularly in industrial processes where the handling of toxic or photochemically reactive conventional organic solvents is of concern. Many reviews and monographs covering the history, chemistry, and applications of ionic liquids are available and have been summarized in articles by Pandey;[145] Xue, Verma, and Shreeve;[146] and Rooney and Seddon.[147] Solute–solvent interactions of compounds dissolved in ionic liquids have been investigated by ultraviolet-visible spectroscopy of dye molecules used as probes[148] and through changes in proton chemical shifts.[149]

A typical ionic liquid is 1-*n*-butyl-3-methylimidazolium tetrafluoroborate (**3**), a material that is fluid above 15°C and has been used as a solvent for hydrogenation reactions. Mass spectrometric studies have shown that ionic liquids, including this one, aggregate in solution. The 1-*n*-butyl-3-methylimidazolium cation can associate head-to-head (contacts of charged imidazolium rings) or head-to-tail (contacts of the imidazolium ring and the *n*-butyl side chain).

Interactions between the anion and cation components of **3**, and between these components and materials dissolved in the ionic liquid, have been examined through $^{1}H\{^{1}H\}$ NOESY and ROESY intermolecular Overhauser effects.[150,151] (Rotating frame experiments may be preferable for such efforts since the viscosity of an ionic liquid may lead to correlation times that correspond to small or zero NOEs.[152]) NOESY spectra showed cross peaks indicative of both head-to-head and head-to-tail contacts. Consideration of the observed proton–proton cross relaxation rates led to estimated inter-proton distances that were similar to the distances found in crystals of the 1-*n*-butyl-3-methylimidazolium cation where head-to-head interactions predominate.[151] NOE data also provided evidence for formation of aggregates of the cations in which the *n*-butyl tail of one interacts with the polar head of an adjacent cation.

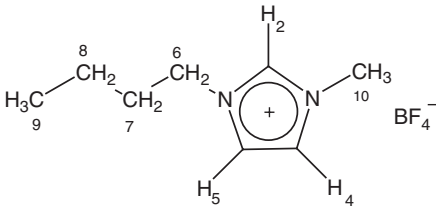

3

Intermolecular $^{1}H\{^{19}F\}$ NOE determinations showed that in neat samples of **3** there are proton–fluorine interactions between BF_4 counterions and all of the 1-*n*-butyl-3-methylimidazolium protons.[153] When the ionic liquid is diluted with methanol the intensity of all of the intermolecular NOEs decrease as the concentration of methanol increases, although some cross peaks appear to decrease more slowly than others. These observations have been taken to show that strong interactions of the ions of **3** with methanol reduce anion–cation contacts present in the neat liquid. By contrast, dilution of **3** with dichloromethane had little effect on the $^{1}H\{^{19}F\}$ NOE cross peaks, even at dilutions as high as 1 : 59. Strong cation–anion interactions present in the neat ionic liquid apparently are retained when this less polar, low dielectric constant co-solvent is added.

Proton–proton Overhauser effects have been used to study the influences of added water on the structure of **3**.[150] As water content of the mixture increases, intermolecular ROEs between imidazolium protons H_2, H_4, and H_5 decrease, while ROEs between the methyl protons (H_{10}) and the *n*-butyl protons increase. ROE cross peaks between the water and protons of the cation were also observed. At low water content the interaction of water molecules appears to be specific for the imidazolium protons, while higher amounts of water lead to detectable interactions of water molecules with all components of the material. At high water content, proton–fluorine NOEs were observed only between the imidazolium ring protons and the fluorines of the counterion. Mele and co-workers[150] interpreted these observations as indicating that hydrogen bonds exist in the neat liquid between the imidazolium ring protons and the

fluorines of BF_4. These are progressively displaced by hydrogen bonding interactions with water as water content of the mixture is increased. Evidence thus indicates that ion pairing of the components of **3** obtains under all solution conditions, although the nature of the interactions of added solvents with the ionic components of **3** depends on the nature and amount of the co-solvent present.

6.5 Cyclodextrin complexes

Cyclodextrins are cyclic oligomers of α-D-glucose (**4**) in which six, seven, or eight glucose units (α-, β- γ-cyclodextrins) typically are present. Due to their cyclic structure and the lack of free rotation about the glycosidic bonds, cyclodextrins have a toroidal shape, with a pronounced, largely hydrophobic cavity in the center. As illustrated in **5**, protons H_3 and H_5 of each glucose unit are within the cavity while protons H_1, H_2, H_6, and $H_{6'}$ are found on the surface of the toroid. Interest in these molecules derives from their abilities to form inclusion complexes with a very wide variety of small molecules and ions. There are experimental indications that flexibility of the cyclodextrin partner is important in optimizing the weak, non-bonded interactions favoring formation of complexes.[154]

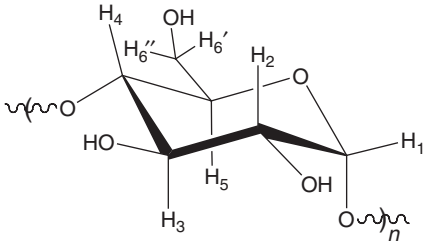

4

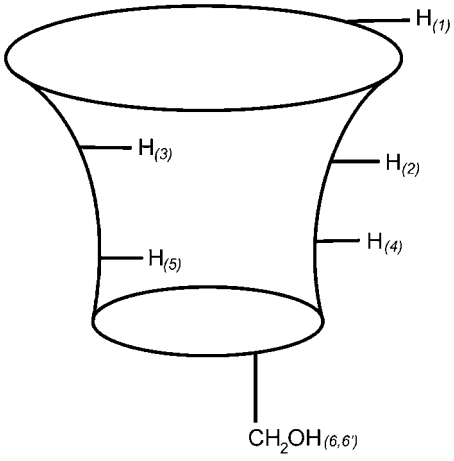

5

The literature related to the cyclodextrins is extensive. An early multi-authored volume shows the scope of the applications of these materials,[155] while more recent reviews,[156–158]including an entire issue of Chemical Reviews,[159] indicate their expanding importance.

NMR spectroscopy has played a useful role in characterizing the host–guest complexes formed with cyclodextrins. Changes in chemical shifts and relaxation times can be used to determine the stoichiometry of complexes. Intermolecular Overhauser effects, particularly rotating frame NOEs, between protons of the host cyclodextrin and the guest molecule, in conjunction with molecular modeling and MD simulations, provide indications of the 3D structure of complexes. Typically, intermolecular NOEs between protons of the guest species and interior protons H_3 and H_5 of the cyclodextrin show the extent to which the guest molecule has been bound inside the cyclodextrin structure. Examples of such studies include structure determinations of the complexes formed with β-cyclodextrin by 1-bromo-adamantane,[160] flurbiprofen,[161] cholesterol,[162] prednisolone,[163] ethinyloestradiol,[163] estriol,[163] noradrenalin,[164] and 2-dibenzofuran carboxylate.[165]

Cyclodextrins are inherently chiral and the formation of complexes is enantiospecific.[166] Chiral discrimination has been studied in cyclodextrin complexes formed with α-pinene,[167] where NOE and ROE results indicated different mobilities of the guest optical isomers within α-cyclodextrin complexes. Cyclodextrin structures have been chemically modified to alter their charges or hydrophobicity, with the goal of increasing the enantioselectivity of complex formation.[168,169]

Both the interior and exterior surfaces of cyclodextrins afford multiple sites for hydrogen bonding interactions with water; about 7 water molecules are sufficently immobilized within the cavity of the β-cyclodextrin toroid that they become detectable by X-ray crystallography.[170] Interior solvent molecules must be displaced when solute enters the toriod to form a complex forms and understanding solvent interactions with liganded and unliganded forms of a cyclodextrin is important to understanding the specificity and stability of complexes.

Guerrero-Martinez et al.[171] have investigated solvent–α-cyclodextrin interactions in water and a mixtures of trifluoroethanol in water. Proton chemical shift effects produced by adding fluoroalcohol led to the conclusion that a 1:1 complex of trifluoroethanol and α-cyclodextrin is formed. Homonuclear $^1H\{^1H\}$ ROESY and heteronuclear $^1H\{^{19}F\}$ NOE experiments confirmed that addition of the trifluoroethanol results in the displacement of the water molecules that interact with the interior protons H_3 and H_5, consistent with the fluoroalcohol taking up a position within the toroid. $^1H\{^{19}F\}$ NOEs develop at other sites on the cyclodextrin but these are weaker and appear to be site specific, with variations in the (weak) degree of water displacement and possibly local diffusive behavior.

6.6 Solvation of small organic molecules

The evolution of experimental capabilities for detecting $^1H\{^1H\}$ solvent–solute NOEs and ROEs since the pioneering work of Kaiser[58] and Macura and Ernst[62,63] is illustrated by studies of the solvation of small molecules by water and

dimethylsulfoxide reported by Angulo et al.[100] As indicated by Equation (8), solvent–solute cross relaxation at a particular solute proton should depend on the population of solvent molecules in the vicinity of the solute proton of interest. Comparing cross relaxation rates, it was shown that the protons of the CH–OH group of 2-butanol (**6**) probably have a somewhat higher number of nearby DMSO molecules compared to the hydrogens of the remainder of this molecule, all of which seem to have similar interactions with the protons of the solvent. These results are consistent with development of hydrogen bonds between the hydroxyl group of **6** and DMSO solvent molecules.

Molecular dynamics simulations of 2-butanol in water were done to obtain atom pair distribution functions which were integrated to obtain estimates of the number of water molecules localized on average about each hydrogen of the alcohol.[100] Experimental water–alcohol $^1H\{^1H\}$ cross relaxation rates correlated with the number of interacting solvent molecules so identified.

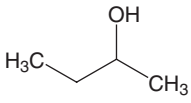

6

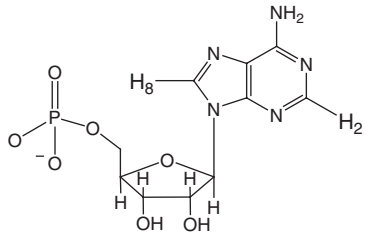

7

Solvent–proton/solute–proton NOEs will be reduced by any conformational or structural aspect that limits access of solvent molecules to the solute proton of interest. Thus, study of solvent interactions may help elucidate structural details of the solute. An example of this is provided by studies of water interactions with adenosine and adenosine 5′-monophosphate (**7**).[100] The adenine ring in these molecules may be found in *syn* or *anti* orientations. In the *anti* conformation (shown in **7**) the bulk of the ribose ring is expected to reduce the number of solvent molecule contacts at proton H_8 on the adenine ring, relative to the number of contacts at the more exposed proton H_2. In the *syn* conformation, obtained by 180° rotation about the glycosidic bond, the opposite situation should obtain. Experimental results show that the cross relaxation rates for water interactions at proton H_2 are larger than those at proton H_8 in both adenosine and the corresponding 5′-phosphate, supporting the conclusion that the *anti* orientation of the adenine ring is favored in both compounds.[100]

The regiochemical dependence of solvent–solute NOEs is also apparent in studies of the interactions of tetramethylsilane (**8**) (as a solvent) with the protons of 1,3-di-*t*-butylbenzene (**9**).[85] Molecular models suggest that aromatic proton H_2 of **9** will be sheltered from interactions with the solvent spins, in qualitative agreement with the observation that the solute–solvent cross relaxation rate for proton H_2 is smaller than the cross relaxation rates for protons H_4–H_6. Procedures described earlier for prediction of intermolecular solvent–solute NOEs, were applied to this system, with the result that the observed cross

relaxation rates for all protons of **9** were correctly estimated to within an average error of about 15%.

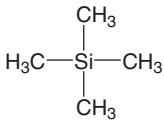

8

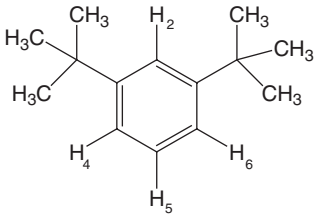

9

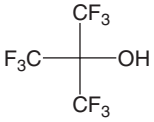

10

Similar studies of **9** dissolved in perfluoro-*t*-butanol (**10**), a solvent molecule outwardly similar in structure to tetramethylsilane, gave experimental $^{1}H\{^{1}H\}$ and $^{1}H\{^{19}F\}$ cross relaxation rates that were much larger than predicted. The enhanced NOEs are probably the result of formation of long-lived solute–solvent complexes, a notion consistent with the acidity of **10** and the expected π-basicity of **9**.[85]

The hydrogens of organic molecules are on the "surface" of the molecule where encounters with solvent molecules will be maximally effective in producing relaxation. Carbon and other elements that form the "backbone" of organic molecules are somewhat shielded from solvent molecules by the atoms on the surface. Given the distance dependence of intermolecular Overhauser effects (Equations (8) and (9)), it may be somewhat surprising that NOEs arising from the interaction of solvent protons with the carbon-13 atoms of a molecule are detectable. The first reported $^{13}C\{^{1}H\}$ intermolecular NOE experiments appear to be those of Seba and Ancian[172] in which NOEs were found with carbon-13 enriched CCl_4 and CS_2 dissolved in hydrocarbon solvents. Using a number of approximations, these authors showed that the cross relaxation parameter σ_{CH} was about $0.5 \times 10^{-3} s^{-1}$ for CS_2 in *n*-hexane. An earlier report of a $^{13}C\{^{1}H\}$ intermolecular NOE[173] was subsequently shown to be likely due to an experimental error.[174]

Solute–solvent $^{13}C\{^{1}H\}$ intermolecular NOEs have been observed for the fullerenes C_{60} and C_{70} dissolved in *o*-dichlorobenzene.[175] The NOEs show that solvent molecules tend to be oriented so that their protons are adjacent to the C_{60} and C_{70} carbon atoms. Solvent NOEs observed at the carbons of C_{70} (**11**) suggest site-specific interactions of *o*-dichlorobenzene with this solute.

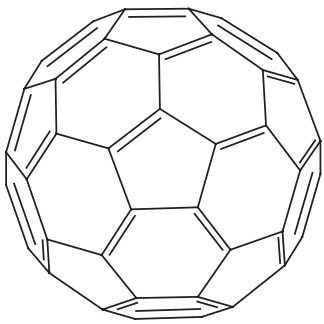

11

Other work of Seba and Ancian has focused on the interactions of water molecules with 2(1*H*)-pyridone and 1-methyl-2(1*H*)-pyridone,[176] uracil,[177] and uridine.[178] The studies of uracil included detection of $^{15}N\{^1H\}$ water–solute NOEs; these NOEs arise via both an intermolecular solute–solvent contribution and through a slow exchange of nitrogen-bound hydrogens with water. Water–proton/solute–carbon intermolecular NOEs observed by these workers have been interpreted in terms of the number of water molecules in the first solvation shell of the solute and the lifetimes of these relative to the rotational correlation time of the water–solute complexes. Similarly, preferential interaction of water molecules with dissolved pyridine is suggested by water–proton/pyridine–proton intermolecular NOEs.[179]

Water interactions with the phosphate groups of ATP (**12**) have been examined through $^{31}P\{^1H\}$ intermolecular NOEs.[180,181] All three phosphates show substantial dipolar interactions with water-derived protons, with the strength of these interactions varying in the order $\gamma > \alpha > \beta$. Apparently the terminal γ-phosphorus is most accessible to solvent molecules. It is unclear to what extent exchange of phosphate-bound protons with solvent protons are reflected in these results.

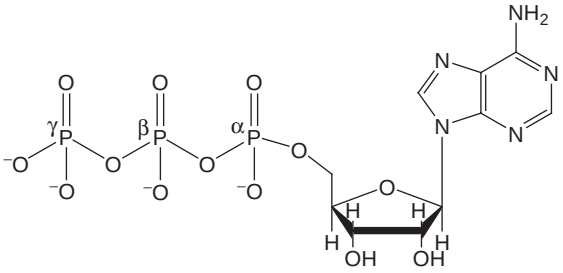

12

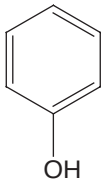

13

Nordstierna, Yushmanov, and Furo[104] examined the interaction of trifluoroacetate ion and non-micellized ammonium perfluorooctanoate with water. An unusual aspect of their work is the determination of the frequency dependence of the fluorine–proton cross relaxation parameters σ_{FH}. These were found to change about 8% for trifluoroacetate over the frequency range 188 to 470 MHz, emphasizing that for intermolecular NOEs the ''extreme narrowing'' limit is not achieved even for small molecules dissolved in low-viscosity solvents. A model for the dynamics of water–fluorinated-solute interactions was developed and shown to be consistent with the observed frequency dependence. The results suggest that layers of water molecules closest to the solute have translational and rotational dynamics that are slower than those that characterize bulk water. Interestingly, interactions between water and the CF_3 group of the detergent producing these effects appear to be stronger than the corresponding interactions with the CF_3 group of trifluoroacetate.

6.7 Selective solvation of small organic molecules

It may be desirable or necessary to use a mixture of miscible liquids as a solvent for a chemical process. For example, solubility considerations may dictate that a mixture of water and ethanol be used for a particular reaction. A description of solute–solvent interactions in a mixed solvent is substantially more difficult than for a single solvent system since interactions between the different solvent molecules must also be considered in addition to the interactions between the solute and each solvent component.[8] Complicating any such description is the possibility that the solute interacts more extensively with one of the components in the mixture or that solvation complexes are formed in which the ratio of solvent components in the solvation shell is different from the concentration ratio characteristic of the bulk mixture.[182] The groups of Bagno[52] and of Berger[54] have been especially productive in exploring preferential solvation by NMR methods, largely through studies of diffusion and intermolecular Overhauser effects.

Many organic solvent molecules dissolved in water tend to exist as clusters surrounded by clusters of water molecules, rather than being homogeneously (randomly) distributed throughout the sample.[47,183,184] Interpretation of experimental results for water–organic solvent mixtures thus may be made more difficult by the tendency of the components of an apparently miscible mixture of solvents to be incompletely mixed when considered at the microscopic level.

Selective interactions of phenol (**13**) with mixtures of water and various alcohols have been examined by Bagno and collaborators,[185,186] primarily using 2D intermolecular NOE experiments. For a solution composed of a solute in a mixture of two solvents, they showed that the ratio of the intensities of intermolecular NOE cross peaks arising from individual solute–solvent interactions is expected to be proportional to the relative concentrations of solvent species. Deviation of the experimental ratio from the value calculated provides evidence that the one type of solvent molecule is preferentially solvating a given solute proton. It should be noted that this approach tacitly assumes that the solvent mixture is homogeneous throughout and that solvent–solute interactions with all solvent species leading to NOEs are solely diffusive in nature.

Intermolecular NOE data indicate that phenol is preferentially solvated by the organic component in solvents composed of acetonitrile–water, dimethylsulfoxide–water, ethanol–water and *n*-propanol–water,[185–187] with the local concentration of water about phenol molecules being decreased about 25% relative to the concentration of water in the bulk solvent. These results are consistent with mass spectrometric studies of the systems[188] and MD simulations.[99]

A similar study of several nitroanilines dissolved in a mixture of cyclohexane and tetrahydrofuran (THF) indicated that THF preferentially solvates these materials. Tetramethyl ammonium ion is selectively solvated by water in

Table 3 Solvent cross relaxation rates ($\times 10^3\,s^{-1}$) for adenine protons of adenosine in 25% trifluoroethanol-water at 25°C (Data from ref. 100.)

pH	H_2		H_8	
	σ_{HH}	σ_{HF}	σ_{HH}	σ_{HF}
4	0.03	3.1	0.05	1.1
7	0.3	3.1	0.2	1.2
10	4.1	2.7	2.1	0.8

acetonitrile–water but tetrabutyl ammonium ion in the same solvent is solvated preferentially by acetonitrile.[185,186]

Angulo and Berger[189] have explored the preferential solvation of adenosine and adenosine monophosphate (**7**) in a solvent composed of 25% trifluoroethanol-d3 and 75% water. The cross relaxation terms σ_{HH} and σ_{HF} were measured for interaction of water and the fluorines of trifluoroethanol with aromatic protons H_2 and H_8 of the adenosine ring in each compound. Some of their results are shown in Table 3. All cross relaxation rates for interaction of water with these adenine ring protons are significantly reduced relative to their values in pure water, implying that water molecules in the solvation shell around protons H_2 and H_8 have been replaced by trifluoroethanol molecules. This is confirmed by the substantial values of σ_{HF} found for interactions of TFE with these spins. Interestingly, water appears to become a better solvent for the adenine ring under alkaline conditions, with σ_{HH} greatly increased at pH 10 while interactions with TFE, as indicated by σ_{HF}, appear to recede. A degree of regiospecificity is also present, with the more solvent-accessible proton H_2 showing larger interactions with both water and TFE compared to the more solvent-shielded proton H_8, confirming conclusions about the preferred conformation of the adenine ring mentioned earlier.

Although liquid perfluorocarbons generally are immiscible with hydrocarbons, some fluorocarbon–hydrocarbon systems become miscible at elevated temperatures conveniently achieved in the laboratory. The ability of such non-aqueous systems to exist as two phases at low temperature, but as a single phase at higher temperature, has led to development of strategies for doing chemical synthesis that rely on the temperature-dependent phase behavior to achieve separation of reactants from products and reaction catalysts. These so-called ''fluorous'' methodologies have received much attention and have been reviewed by a number of authors.[190,191] This author's laboratory has used intermolecular NOEs to investigate the interactions of solvent components with the protons and fluorines of 3-heptafluorobutyrylcamphor (**14**) in both phases of a biphasic system derived from chloroform and perfluoro(methylcyclohexane).[192] Chloroform is the most polar component of this system (solvent polarity index $P_s = 7.93$[15]) while perfluoro(methylcyclohexane) is essentially non-polar ($P_s = 0.46$). The solvent system exists as two phases at 25°, with the heavier

layer being rich in perfluorocarbon ([perfluoro(methylcyclohexane)]/[chloroform] ≈ 2) and the lighter layer rich in chloroform ([perfluoro(methylcyclohexane)]/[chloroform] ≈ 0.08). The system becomes a single phase at 54°.

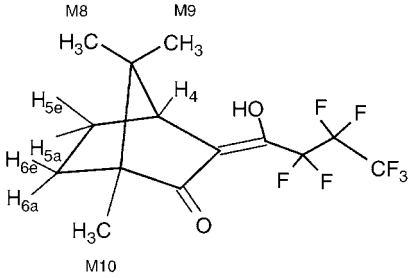

14

Observed cross relaxation rates were compared to those predicted from molecular shapes and diffusion coefficients of the solute and solvent species using Equation (8). There are no indications of unusual solute interactions with either solvent component in the chloroform-rich layer at 25° and only weak suggestions of such interactions in the high-temperature phase. NOE results at 25° indicate that in the perfluorocarbon-rich layer both solvent components interact with the solute more strongly than expected. Various mechanisms for the enhancement of solute–solvent cross relaxation rates in the perfluoro(methylcyclohexane)-rich phase were considered. It was suggested that the solvation layer around the solute has a different composition and possibly different hydrodynamic properties than those characteristic of the bulk solution. In this phase, the chloroform of the solvent mixture accumulates near the hydrogens of the solute while the perfluoro(methylcyclohexane) accumulates near the heptafluorobutyryl group.[192] There were indications of appreciable regioselectivity of chloroform interactions with the hydrocarbon part of the solute in all phases.

6.8 Selective solvation of peptides

The catalytic action, selective binding abilities and conformational properties of peptides and proteins can potentially be useful in industrial and pharmacological contexts. A major focus has been the development of enzyme systems that will be stable and catalytically active in non-polar solvents, at high temperatures, or absorbed to solid materials.[193–195] These uses may require that the biomaterial be introduced into a low-water environment.[193] Most native peptides and protein molecules are designed to operate in an aqueous environment and the effects of transfer of these materials to a less aqueous milieu have to be appreciated to foster these applications.

Addition of a soluble aliphatic alcohol to a water solution of a peptide may produce a change in the conformation of the peptide.[196] Aliphatic alcohols added to a water solution of a protein will, upon reaching a certain concentration, typically induce unfolding of the protein, with a concomitant loss of biological activity. Both effects can be accentuated when a fluorinated alcohol is used;

trifluoroethanol (TFE, **15**) and hexafluoroisopropanol (HFIP, **16**) have been known for 50 years to induce formation of helical and other structures in peptides and produce structural transformations in proteins.[197] A variety of possible reasons for the conformation-altering effects of organic solvents, particularly fluoroalcohols, have been advanced, including the notion that the organic component of a mixed solvent system preferentially interacts with the dissolved peptide.[198]

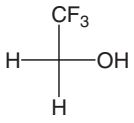

15

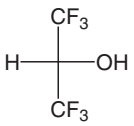

16

Interaction of the fluoroalcohol component in mixtures of water with trifluoroethanol, hexafluoroisopropanol, hexafluoroacetone hydrate, and perfluoro-*t*-butanol, with the cyclic dipeptide *cyclo*-alanylglycine (**17**) have been studied by $^{1}H\{^{19}F\}$ NOE experiments.[199] The observed cross relaxation parameters (σ_{HF}) were two to three times larger than those predicted by using the assumption that solvent–solute encounters take place solely by translational diffusion of these molecules (Equation (8)). A possible explanation of these observations is that the concentration of fluoroalcohol near the peptide is higher than the nominal concentration of the bulk solution. The tendency of peptides to accumulate fluoroalcohols near their surfaces, leading to an increase in local concentration, has been proposed by several groups.[101,200] Large solute–fluoroalcohol cross relaxation terms were observed in perfluoro-*t*-butanol–water. This alcohol is more acidic than the other fluoroalcohols examined[85] and the large $^{1}H\{^{19}F\}$ inter-molecular NOEs observed in this instance may be due to formation of long-lived complexes with the cyclic dipeptide stabilized by strong hydrogen bonds to this alcohol.

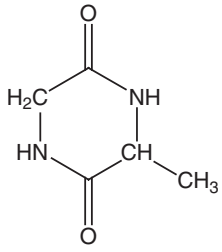

17

Intermolecular solvent–solute Overhauser effects have been used to explore solvent interactions of the small peptide **18** with water and with the components of water–ethanol and water–trifluoroethanol solvent mixtures.[101,200] In pure water, $^{1}H\{^{1}H\}$ water proton–peptide proton NOEs show appreciable regioselectivity, suggesting that the order of solvation by water molecules of the protons of **18** is CH_2(Phe) > aromatic H (Phe) ≈ CH_3(Acetyl) ≈ Hβ(Val) > CH_3(Val). The water NOEs are decreased by the addition of TFE to the solvent (Figure 4),

to the extent that these NOEs appear to be essentially absent when the concentration of TFE exceeds about 30%. The implication is that TFE molecules replace water molecules in the near-neighbor solvation structures of the peptide; intermolecular $^{1}H\{^{19}F\}$ NOEs between peptide protons and co-solvent fluorines were readily detected, supporting this conclusion. Interestingly, the $^{1}H\{^{19}F\}$ NOEs suggest a relative lack of regioselectivity in the TFE–peptide interactions.

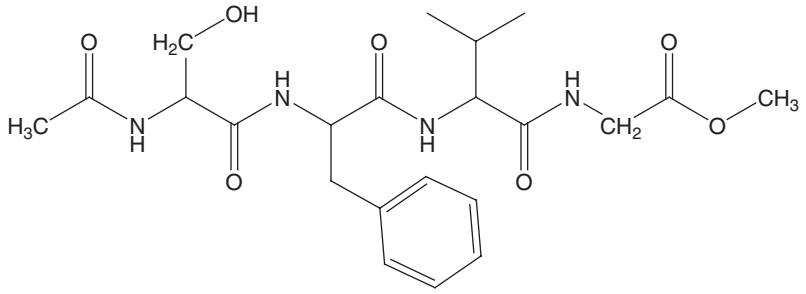

18

As shown in Figure 4, water NOEs on the protons of **18** are *increased* when ethanol is added to the solution, presumably because interactions of water with the peptide are enhanced when ethanol is present as a co-solvent.

Diffusion constants for peptide **18** in various solvent mixtures were determined and analyzed for indications of the hydrodynamic radius of the peptide.[101] The radius of **18** is not changed significantly when ethanol is added

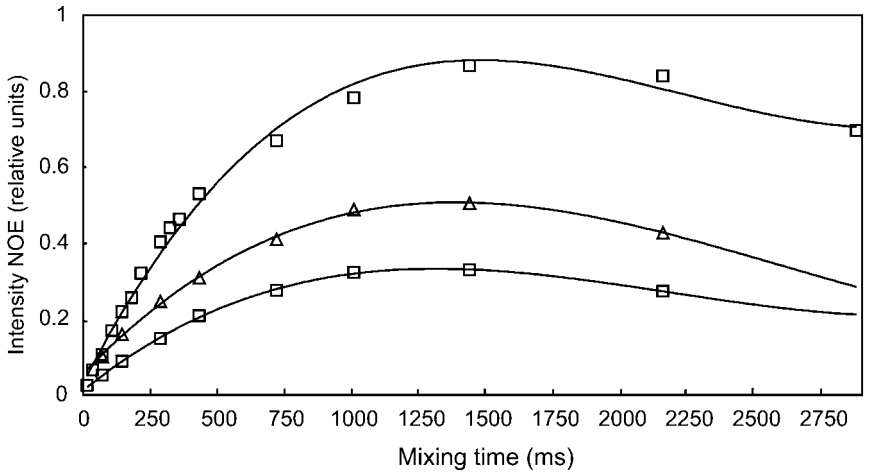

Figure 4 Experimental intermolecular NOEs between water and the aromatic side chain protons of peptide **18** in pure water (triangles), 1% ethanol–water (open squares) and 1% trifluoroethanol–water (filled squares) as a function of mixing time. The initial slope of each curve defines the cross relaxation parameter σ_{HH}^{NOE}. The figure is redrawn from ref. 101 and is used with permission of the authors and the American Chemical Society.

to the solution. However, the apparent hydrodynamic radius of the peptide increases progressively as the amount of trifluoroethanol in the solution is increased. In accord with FTIR evidence for other peptides[201] and the NMR observations mentioned, peptide **18** appears to be preferentially solvated by TFE, to the extent that water molecules are excluded from near-neighbor contacts with the surface of the peptide and a ''coating'' of TFE molecules is sufficiently strongly attracted to the peptide that some of the TFE molecules diffuse with the peptide, thereby increasing the apparent hydrodynamic radius of the peptide. Ethanol, by contrast, appears not to interact with the peptide significantly and appears to have only minor effects on the interactions of the peptide with water.

Molecular dynamics simulations of **18** in ethanol–water and trifluoroethanol–water solutions have been done.[101] Trifluoroethanol was observed to accumulate preferentially near the peptide in these simulations, while there was little tendency for ethanol to so accumulate.

Bombesin (**19**) is a tetradecapeptide with sequence Glp–QR LGN QWA VGH LM-NH_2 (Glp ≡ pyroglutamic acid) isolated from the skin of frogs. Homologs of the peptide are found in neural and endocrine cells of mammals and may be involved in the regulation of food intake. The peptide is unstructured in water but adopts a helical conformation from residues Asn6 to Met14 in the presence of trifluoroethanol.[202]

Diaz et al.[203] have examined the solvation of bombesin in trifluoroethanol–water mixtures. Similar to the observations reported for peptide **18**, intermolecular water–proton/peptide–proton NOEs were reduced by increasing the amount of TFE present in the solvent while $^{1}H\{^{19}F\}$ NOEs indicated enhanced interactions of the solute with the fluoroalcohol. Molecular dynamics simulations again showed preferential accumulation of TFE near the peptide surface, with the local concentration of TFE about twice the nominal concentration in the bulk solvent mixture.

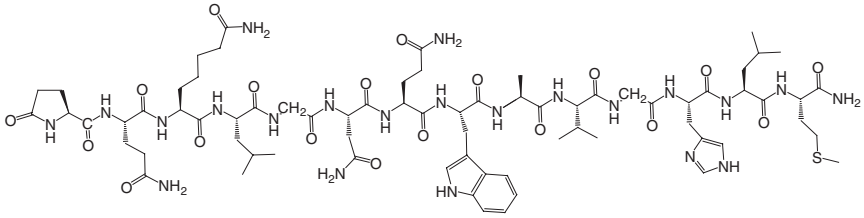

19

The ''Trp-cage'' peptide (NLY IQW LKD GGP SSG RPP PS), a 20-amino acid peptide designed by Neidigh et al.,[204] rapidly folds to a compact structure.[205] The conformation of Trp-cage in 42% trifluoroethanol–water, shown in Figure 5, is essentially the same as that observed in pure water.

Figure 6 indicates $^{1}H\{^{19}F\}$ NOEs produced by interaction of the trifluoroethanol component of a 42% trifluoroethanol–water mixture with Trp-cage.[206] Making the assumption that cross relaxation interactions between Trp-cage

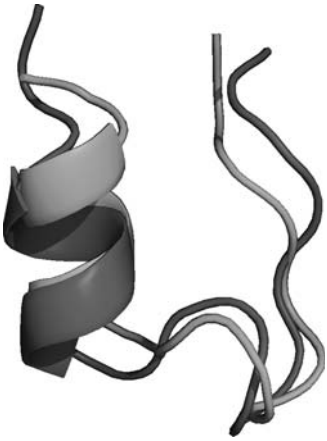

Figure 5 Comparison of structures found for Trp-cage peptide at 5°C (cyan) and 45°C (red) in 42% trifluoroethanol–water[206] (see color plate section at the end of this chapter).

protons and the solvent fluorines are modulated only by the relative diffusion of the peptide solute and the trifluoroethanol co-solvent (Equation (8)), it can be calculated that all peptide–TFE NOEs at temperatures from 5°C to 45°C should be positive. However, at 5°C the only positive intermolecular NOE is the one arising from interaction of TFE with the TSP reference compound in the sample (Figure 6). Negative $^{1}H\{^{19}F\}$ NOEs on the signals of the tyrosine (Y) and tryptophan (W) side chains of the peptide were observed, while peptide N–H spins and the methyl protons of the leucine and isoleucine residue show weaker, but still negative TFE NOEs. At 45°C, all $^{1}H\{^{19}F\}$ NOEs are positive, but often are substantially larger than expected on the basis of Equation (8).

Experimental cross relaxation terms (σ_{HF}^{NOE}) for this system are not consistent with values of σ_{HF}^{NOE} anticipated on the basis of diffusive encounters between TFE and the peptide at 5° or 45°C. These observations were taken to indicate formation of complexes of Trp-cage with the fluoroalcohol that persist for times of the order of 1 ns (Equation (15)).[206]

Hexafluoroisopropanol is substantially more effective than trifluoroethanol in stabilizing selected conformations of peptides.[196,207] Cross relaxation parameters (σ_{HF}^{NOE}) for interactions of the fluorines in a 30% HFIP–water mixture with protons of Trp-cage determined from intermolecular $^{1}H\{^{19}F\}$ NOE experiments indicated that this fluoroalcohol also forms long-lived complexes with the peptide.[107] At both 5° and 45°C, the HFIP cross relaxation parameter for any given interaction was found to be appreciably more negative than σ_{HF}^{NOE} found with TFE. This is consistent with an increase in the lifetimes of peptide–HFIP complexes compared to peptide–TFE complexes. Stronger hydrogen-bonding interactions of HFIP would be expected due to the greater acidity of HFIP compared to TFE, and stronger hydrophobic interactions with HFIP would be expected due to the greater fluorination of HFIP. Compared to trifluoroethanol, both considerations

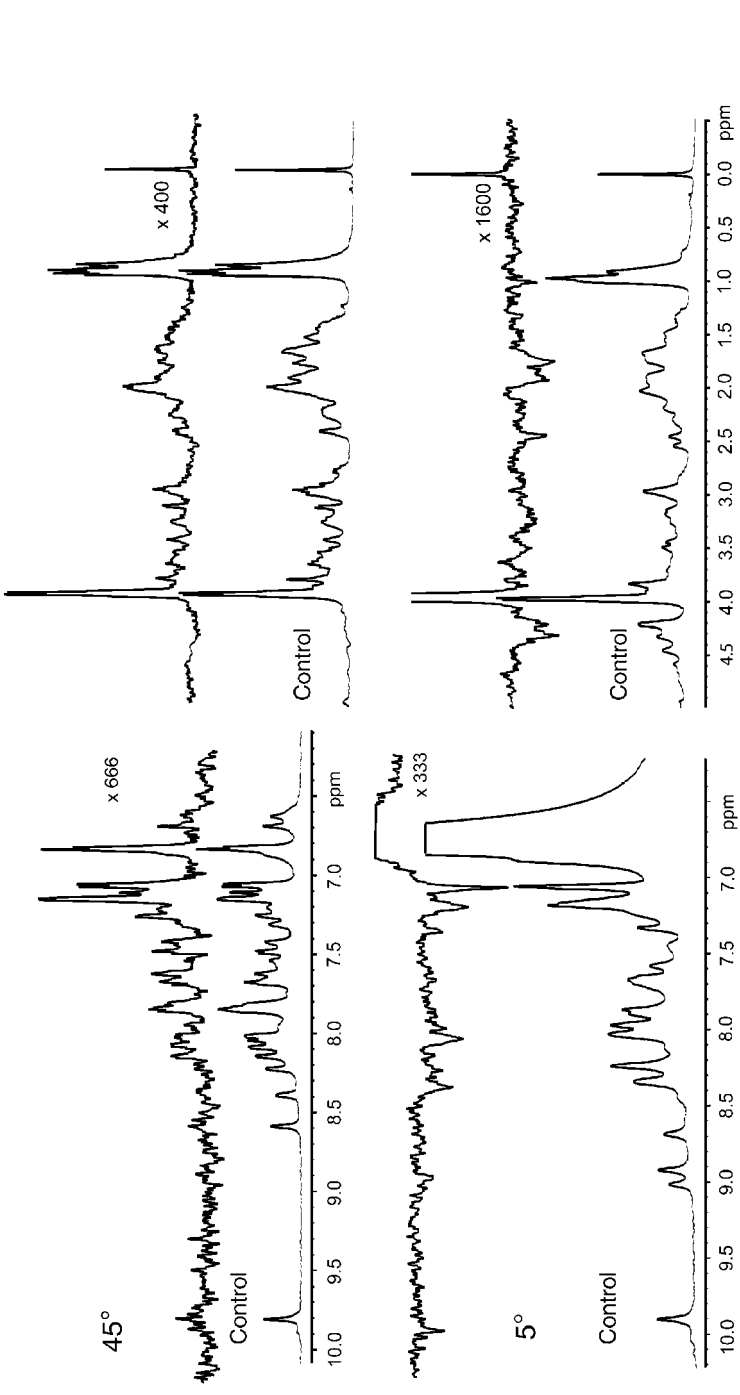

Figure 6 $^{1}H(^{19}F)$ Intermolecular NOE and control spectra of Trp-cage in 42%TFE-d_2 at 5°C and 45°C. The mixing times for the NOE data were 400 and 500 ms. Vertical scales of the sets of spectra vary. The strong feature near 6.7 ppm arises from the hydroxyl proton of trifluoroethanol which is in intermediate exchange with the protons of water at 5°C. The only positive σ_{HF}^{NOE} observed at 5°C arises from interaction of TFE with the TSP reference compound. The positive NOE at ~3.9 ppm is the result of intramolecular hydrogen-fluorine interactions in molecules of TFE-d_2 where protons remain due to incomplete deuteration.[206]

would tend to increase the lifetime of HFIP–peptide complexes relative to the life times of similar TFE–peptide interactions.

Peptide melittin (GIG AVL KVL TTG LPA LIS WIK RKR QQ) is a principal component of the venom of the honeybee, *Apis mellifera*. The N-terminal end of the peptide is hydrophobic while the C-terminal is hydrophilic. Melittin has many biological effects which seem to be mediated by its interaction(s) with cell membranes.[208]

An intermolecular $^{1}H\{^{19}F\}$ NOE study of the interactions of HFIP with melittin in 35% HFIP–water was carried out at a sample temperature of 25°C.[209] Residues 2 through 8 and residues 13 through 25 of melittin are in α-helical conformations under these conditions, with an angle of about 73° between the axes of the two helices (Figure 7). Many cross relaxation parameters (σ_{HF}) for interactions of the fluoroalcohol with side chain and backbone protons are approximately those expected from the random collisions of spheres model (Equation (8)). However, values of σ_{HF}^{NOE} for interactions of HFIP with the backbone N–H protons were not in agreement with those expected (Figure 8). The negative $^{1}H\{^{19}F\}$ NOEs observed for these protons in the bend region between the two helices probably indicates that the fluoroalcohol binds strongly enough to this part of the peptide that, like the Trp-cage peptide discussed earlier, peptide–solvent interactions can no longer be described as diffusive. A subsequent MD simulation showed that the two α-helical segments of melittin are highly dynamic, sampling a range of angular orientations that, on average, gives an inter-helix angle within experimental error of the value found in the

Figure 7 Alpha carbon backbone plots of ten low-energy conformations of melittin in 30% hexafluoroisopropanol-d_2–water found by analysis of intramolecular NOESY data.[209]

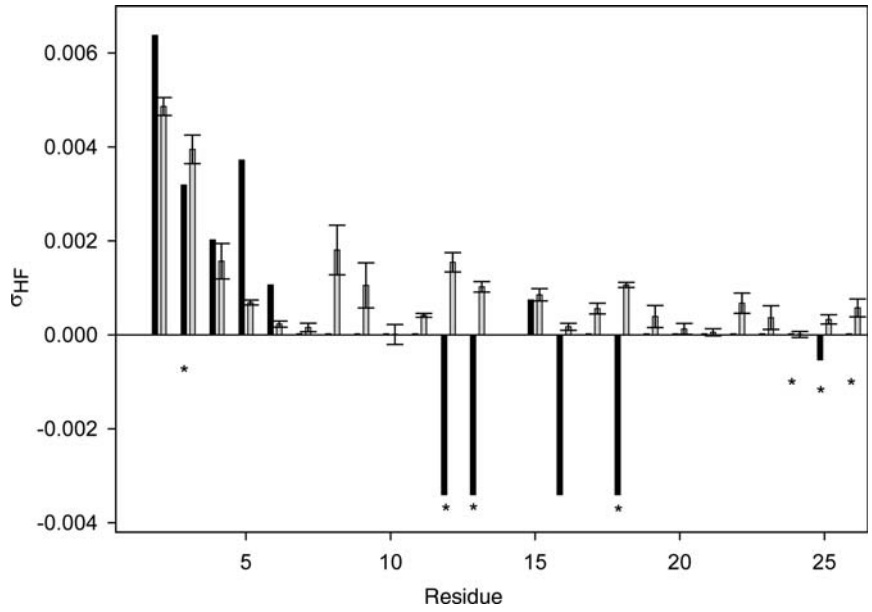

Figure 8 Comparisons of observed (dark bars) and calculated (light bars) values of σ_{HF} of the peptide backbone N–H signals in melittin in 35% HFIP–water. Error bars represent standard deviations of calculated data for the 10 low energy conformations found in the structure determination. Asterisks indicate ambiguous assignments. The signals for glycine-12, leucine-13, and serine-18 are overlapped; one or more of the experimental NOEs for any of these could be zero. The signals for glycine-3 and arginine-24 are overlapped; based on the calculations it has been assumed that the observed NOE signal arises from glycine-3. Experimental values of σ_{HF} indistinguishable from 0 have been set to 2×10^{-5} in the plot to provide indications of the positions of these data. Figure taken from ref. 209 and used with the permission of the author and the Biophysical Society.

NMR study. The simulations also confirmed that HFIP tends to aggregate around the peptide, increasing the local co-solvent to more than twice the concentration of the bulk solvent.[210]

Intermolecular $^1H\{^{19}F\}$ and $^1H\{^1H\}$ NOEs were used to explore interaction of solvent components with melittin dissolved in 50% hexafluoroacetone trihydrate (HFA)–water.[211] In this solvent mixture the peptide is α-helical from residues Ala4 to Thr11 and from Leu13 to Arg24 with an inter-helix angle of 144°. Intermolecular NOEs arising from interactions between spins of the solvent and the solute indicate that both fluoroalcohol and water molecules are bound strongly enough to the peptide that solvent–solute complexes persist for $\geqslant 2$ ns. Preferential interactions of HFA with many hydrophobic side chains of the peptide are apparent while water protons appear to be localized near hydrophilic side chains. These results show that interactions of both HFA and water with melittin are qualitatively different from solvent–solute interactions present when the peptide is dissolved in 35% HFIP.

Overall, observed $^{1}H\{^{19}F\}$ intermolecular NOEs for peptides dissolved in mixtures of fluoroalcohols and water appear to arise from some combination of the effects of locally increased concentrations of TFE, altered diffusive behavior of TFE in the vicinity of the solute surface and the formation of solute–fluoroalcohol complexes that exist for times at least as long as the order of the rotational correlation time of the solute. Reliable experimental methods for disentangling these effects are needed.

Intermolecular NOEs between the methyl group protons of ethanol-d2 (CH_3CD_2OH) and Trp-cage dissolved in 35% ethanol-d2–water are strikingly different from the $^{1}H\{^{19}F\}$ NOEs found in trifluoroethanol–water. The observed $^{1}H\{^{1}H\}$ intermolecular NOEs are positive and somewhat larger than the effects expected for peptide–alcohol interactions on the basis of only diffusive encounters at 5°C and higher temperatures. Only side chain protons of the peptide show appreciable NOEs to the methyl protons of ethanol (Gerig, J. T., work in progress). The concordance between these observations and the conclusions of the Berger group regarding the interactions of ethanol with peptide **18**[101] are currently under study.

It should be noted that ethanol and other aliphatic alcohols as well as trifluoroethanol and other fluorinated alcohols form aggregates in mixtures with water.[184,196,207] What is the relation of alcohol aggregation to the interaction or non-interaction of these compounds with peptide solutes remains to be determined.[212]

6.9 Chiral interactions

The NMR properties of a pair of enantiomeric molecules are identical in an achiral environment. However, if the enantiomers are derivatized or complexed with a chiral material, the NMR properties of the resulting diastereomeric systems become distinguishable. In practice, the property examined is usually a chemical shift, with the proton shift differences between the diastereomeric systems being of the order of 0.05 ppm.

It was demonstrated over 40 years ago that the components of a racemic mixture dissolved in a chiral solvent can show differential chemical shifts due to the formation of solute–solvent complexes that are diastereomeric. Thus, racemic 2,2,2-trifluoro-1-phenylethanol (**20**) dissolved in nearly optically pure α-phenethylamine shows two fluorine signals separated by 0.04 ppm for this reason.[213]

Methods for producing enantiomerically pure materials and for analyzing enantiomeric composition have burgeoned in the intervening years,[214,215] with development of ''chiral solvating agents'' being one focus of such efforts. Such agents typically are small molecules which have been designed to form reasonably stable diasteromeric complexes with enantiomers and to produce large chemical shift effects. A number of workers have used intermolecular NOEs arising from dipolar interactions between the spins of the chiral solvating agent

and spins of the analyte to explore the intermolecular contacts between solvent and analyte.[213,216–220]

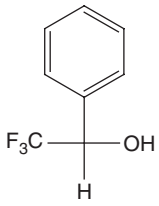

20

As indicated earlier, cyclodextrins and modified cyclodextrins can function effectively as chiral solvating agents. Micelles formed from chiral surfactant molecules may interact selectively with a pair of enantiomers and allow discrimination of these isomers through chemical shift effects, intermolecular NOEs, or differences in diffusivity.[221]

An emerging technique for analysis of enantiomeric composition that does not rely exclusively on chemical shift differences is the use of residual dipolar couplings in chiral liquid crystals.[222–224] Interactions of solutes with chiral liquid crystal molecules are, on average, different for the members of a pair of enantiomers. The result is that homonuclear and heteronuclear residual dipolar couplings between spins in each molecule are distinguishable. Differential averaging of the chemical shift anisotropies of each molecule under these conditions can also be used to augment discrimination of the enantiomers. Buckingham has suggested it may be possible to detect chirality directly by NMR experiments without the need for a chiral auxilliary.[225,226]

6.10 Micelles and aggregated systems

Molecules having strongly solvophilic and solvophobic aspects of their structures tend to aggregate. An example mentioned earlier is trifluoroethanol. In this molecule a polar, hydrogen-bonding part of the structure interacts favorably with solvent water molecules while its hydrophobic (and fluorophilic) CF_3 group preferentially interacts with other trifluoromethyl groups. Trifluoroethanol and water are miscible in all proportions, but the mixtures are inhomogeneous at the molecular level as a result of the formation of aggregates or clusters of trifluoroethanol.[184,196,207]

Surfactant molecules have hydrophilic and hydrophobic parts and tend to self-assemble into a variety of structures when exposed to water. Such structures are highly dynamic, with their properties defined by the rates of association and dissociation of the surfactants and their counterions, if present, as well as the rates of conformational changes in both the aggregated and non-aggregated states. The effects of micelles on chemical reactions have suggested that water at the interface between a micelle and the bulk solution has special properties, apparently being less polar[227] and less mobile[228–230] than bulk water.

A variety of NMR methods, discussed in recent reviews,[64,231–233] have been used to address questions related to details of the structure and dynamics of aggregates.

Heteronuclear $^{13}C\{^1H\}$ intermolecular Overhauser effects have been observed between carboxylate carbons of the surfactants sodium octanoate and sodium dodecanoate and water.[234,235] The carboxyl–carbon/water–proton cross relaxation parameter σ_{CH} was of the order 0.4 to $4.3 \times 10^{-4}\,s^{-1}$ and was interpreted to indicate an average distance between water molecules and the carboxylate carbon of 3–4 Å.

Water contact with the perfluorinated surfactant cesium perfluorooctanoate has been explored by $^{19}F\{^1H\}$ intermolecular NOE experiments.[109,236] The fluorine spectrum of this surfactant is well-resolved and NOEs for the CF_3 and each CF_2 group are readily obtained. Appreciable water–CF_2 interactions are detected for the CF_2 group adjacent to the carboxylate head group of the surfactant. This was initially interpreted to mean that water molecules could approach to within about 2 Å of these spins. A more detailed analysis made possible by the determination of cross relaxation parameters as a function of spectrometer frequency show that translational motions of water molecules near the head group are retarded by about a factor of 3 relative to what is observed for bulk water. One or two layers of water molecules at the head group are so affected. While some water contacts with the next CF_2 group are possible, Nordstierna, Yushmanov, and Furo[109] concluded the minor water–fluorine NOEs observed for the remainder of the surfactant molecule are largely the result of long-range intermolecular dipolar interactions with the solvent spins.

The surfactant cetyltimethylammonium bromide (CTAB) forms micellar structures in non-aqueous solvents such as formamide. Belmajdoub et al.[237] have reported the observation of $^{13}C\{^1H\}$ intermolecular NOEs between the H–C=O proton of the solvent and carbon atoms at the end of the C_{16} chain of CTAB. Curiously, these NOEs were negative in sign whereas a positive NOE would be anticipated. The authors argue that spin-diffusion effects are involved in producing the observations and conclude that their results imply that solvent formamide molecules ''penetrate'' aggregates formed by CTAB in this system.

Sodium-bis(2-ethylhexyl)sulfosuccinate (**21**), known as ''aerosol OT'' or AOT, is a surfactant able to form reversed micelles in apolar solvents. In reversed micelles, the polar head groups of the surfactant aggregate to form the interior of the micellar structure(s) while the hydrophobic parts of the surfactant interact with the solvent.

Micelles that form when urea and AOT are dispersed in carbon tetrachloride or benzene were examined by several techniques, including intermolecular $^1H\{^1H\}$ NOE experiments.[238] NOEs were found between the protons of urea and the head group protons (labeled 1, 1′, and 3 in **21**), implying that urea molecules are localized in the vicinity of the head groups.[238] Substantial intermolecular NOEs were also detected between the urea and protons of the CH_3 and CH_2 groups. These may be the result of spin diffusion or may

indicate a highly dynamic structure that brings the alkyl groups into contact with urea over time.

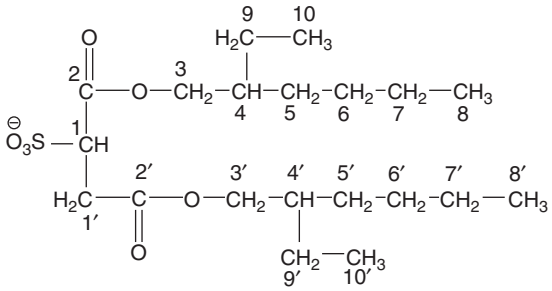

21

Shapiro et al.[239] have studied the conformation of a tripeptide analog (PYG-NH_2) of melanotrophic inhibiting factor solubilized in AOT micelles. The observation of intermolecular NOEs between the protons of the proline ring of the tripeptide and protons 1, 1′, and 3 of **21** are consistent with the peptide being located near the interior surface of the AOT reversed micelles.

Band-selective 2D and 3D $^1H\{^1H\}$ Overhauser experiments have been used to examine the state of the peptide gramicidin when it is solubilized in sodium dodecylsulfate micelles.[240] Under these conditions, the peptide forms a dimer with a distinct channel through the dimer center, consistent with the anticipated behavior of the peptide in biological membranes. Over 80 NOEs between detergent and hydrophobic residues on the surface of the dimer were observed, supporting the expected 3D structure of the dimer.

Colipase is a small protein which acts as a cofactor for the digestive enzyme pancreatic lipase. Formation of a ternary complex of lipase, colipase, and micelles formed from bile salts is necessary for its biological activity. Dominguez et al.[241] have shown through intermolecular NOEs that micelles of sodium taurodeoxycholate, a model bile salt, interact with aromatic amino acids on the surface of colipase.

Dendrimers are monodisperse macromolecules in which repeated structural units emanate radially from a structural core (Figure 9). Like globular proteins, they have a ''surface'' and an interior ''core''. Dendritic structures designed to be biocompatible are of interest for selective delivery of drug molecules to target sites. Morgan et al.[242] have reported detection of $^1H\{^1H\}$ intermolecular NOEs between protons of dye molecules encapsulated in a dendrimer prepared from glycerol and succinic acid. The results indicate localization of dye molecules near the glycerol methylene protons and are consistent with dye molecules being held sufficiently strongly in the polymeric structure that they tumble on approximately the same time scale as the macromolecule.

Intermolecular NOEs can be used to demonstrate interaction of small molecules to form complexes and aggregates. Proton NMR spectra of caffeine show intermolecular $^1H\{^1H\}$ NOEs that are consistent with formation of dimers.[243] One-dimensional intermolecular $^1H\{^1H\}$ NOEs were observed for charge-transfer complexes of 2,4,6-trinitrotoluene and several aromatic

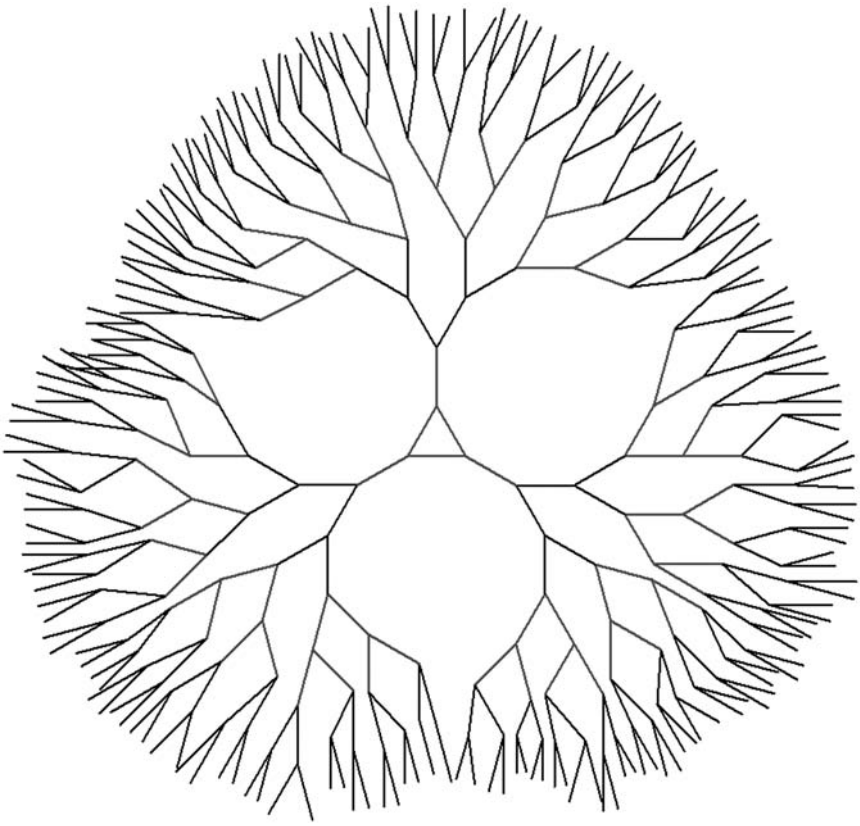

Figure 9 Schematic representation of a dendrimeric molecule. The image is taken from the site http://en.wikipedia.org/wiki/Image:DendrimerOverview.png and used in accord with the license granted there (see color plate section at the end of this chapter).

hydrocarbons.[244] Intermolecular NOE experiments, often in conjunction with studies of diffusion coefficients, have been used to indicate aggregation of organometallics.[52,64,142]

Intermolecular hydrogen-bonding interactions, responsible for the miscibility of poly(4-vinylphenol) and poly(methylacrylate) in tetrahydrofuran solutions, have been examined by 2D $^{1}H\{^{1}H\}$ NOEs.[245] Interpolymer proton NOEs have been observed for solutions of polystyrene, poly(vinyl methyl ether) and polycaprolactone.[246]

6.11 Protein–small molecule interactions

Macromolecules such as proteins and nucleic acids interact with water, other small molecules, and with other macromolecules, in the course of performing their biological roles. These interactions can involve conformational changes of the interacting molecules and are characterized by a wide range of dissociation constants and time scales. Crystallographic methods can provide structural

details at atomic resolution of complexes formed but supply little information about the time scales for the process of complex formation. It has become apparent that NMR is uniquely capable of providing detailed information regarding the structure and dynamics of ligand–receptor complexes.[247] A wide variety of NMR methods are used, including detection of chemical shift and relaxation time differences produced by complex formation, changes in the rates of diffusion of the interacting partners,[248,249] and detection of NOEs that arise from dipolar interactions between spins of interacting partners. The type of NOE experiment done and interpretation of the observations made in such an experiment depend on the magnitude of the binding constant for the interaction and time scales for formation and dissociation of the ligand–receptor complex.

While studies of this nature are somewhat beyond the purview of this article, experimental techniques for detecting the NOEs and interpreting them share commonalities with studies of solvent–solute interactions. A number of excellent reviews cover protein–ligand experiments, particularly in the context of protein–small molecule interactions.[247,250–252] Effective drug molecules must be involved in ligand–receptor interactions and much effort, including NOE experiments of various types, has been useful in detecting these interactions.[253–256]

Timethylamine N-oxide (TMAO) is one of a group of organic molecules known collectively as osmolytes. Osmolytes are found in cells, often at high concentrations, and function to enable cells to withstand extremes of temperature or loss of water. TMAO has the ability to enhance the formation of folded peptide and protein structures and is present to counteract the effects of other osmolytes which tend to be denaturing. As a step in exploring the interactions between TMAO and peptides that lead to these structural effects, an intermolecular $^{1}H\{^{1}H\}$ NOE study of the interactions of TMAO with cycloalanylglycine (**16**) was untertaken.[257] It was concluded that the observed NOEs result from the formation of long-lived complexes of the peptide and hydrated TMAO.

6.11.1 Peptide and protein hydration

Liquid water is indispensable to the generation of the biologically active 3D shapes of proteins and other biomolcules, to the interactions between these species, and to their interactions with small molecules.[4,42,258,259] The ubiquity of liquid water in the human experience tends to conceal its complexity. An excellent website (http://www.lsbu.ac.uk/water/index.html) indicates that there are at least 63 properties of water that are anomalous and provides up-to-date literature references to all aspects of the chemistry of water.

Interactions between water molecules and proteins has been of interest since the polymeric nature of proteins became known. Many methods have been applied in the study of these interactions, including determination of transport properties, dielectric relaxation, various scattering experiments, and NMR experiments.[108,260,261] Magnetic field dependence of relaxation (MRD, magnetic relaxation dispersion) and NOEs have been important NMR tools. Computer

simulations play an increasingly important role in interpretation of experimental results.[4]

Some protein-associated water molecules are integral parts of the 3D structure of the protein and are revealed to be so by crystallographic experiments. These ''internal'' water molecules can exchange with bulk water, typically on a time scale of microseconds, but sometimes much longer.[260] Intramolecular NOEs between the protons of internal water molecules and nearby protons of the protein are readily detected.[262–264] Interpretation of these NOEs needs to include consideration of the rates of the exchange of the interior molecules with the bulk solvent.

Most NOE studies of protein–water interactions are concerned with water molecules at the surface of the protein. Timasheff has described these molecules as a ''fluctuating cloud'', asserting that there is no rigid shell of water molecules around a protein but rather a collection of molecules that are affected by interactions with the protein which influence their rotational and translational dynamics.[265] The surface of a protein is highly heterogeneous, with side chains of hydrophilic and hydrophobic amino acids exposed to bulk water to about the same extent,[259] and with a unique ''roughness'' that includes invaginations that may favor water molecule interactions. Water–protein surface interactions that persist for times of the order of nanoseconds are revealed by ^{17}O and ^{2}H MRD experiments.[260,266] These experiments show that rotational and translational diffusion of waters in direct contact with the protein surface are typically slowed by a factor of 2–5 relative to their behavior in bulk water. These conclusions are generally supported by neutron scattering experiments.[261,267,268]

Intermolecular $^{1}H\{^{1}H\}$ NOE experiments used to study protein or peptide interactions with solvent water usually involve inversion of the magnetization associated with the bulk water protons. An NOE or ROE on the proton signals of the solute can then arise because water in the hydration layer has become inverted through chemical exchange with the bulk water. NOEs or ROEs may also result because protons such as those of –OH or –NH groups on the surface of the protein are exchangeable with water protons under the conditions of the experiment and thus can also become inverted. Finally, all protons of the solute are subject to intermolecular effects that arise from dipolar interactions with the bulk solvent protons. Halle reminds that these latter interactions are proportional to $1/d$, where d is the distance from the protein proton to bulk solvent protons and that this contribution does not necessarily reflect local hydration of a solute spin but rather the properties of the bulk solvent.[260] Given the difficulty of separating the various effects mentioned, it is perhaps not surprising that conclusions regarding the nature of water on the surface of a protein that rely exclusively on intermolecular NOE and ROE data have been at variance with the indications of MRD and other experiments. Halle and his group[260,266] have discussed the origins of these disagreements in more detail.

A complication in determination of reliable intermolecular water–solute Overhauser effects is the fact that the chemical shifts of the Cα-H protons can be so close to the chemical shift of the bulk water that it is impossible to selectively

invert only the bulk water magnetization. Schemes for selectively perturbing the bulk water that rely on differences in diffusion coefficients, scalar coupling constants, and differential relaxation rates have been developed.[269,270]

6.11.2 Proteins and organic solvents

In the laboratory or production plant, proteins, particularly enzymes, may be placed into solvents that are mixtures of water and some water-soluble component such as acetone. The non-water solvent components present in the solution may compete with the protein for available water or may preferentially interact with the protein, thus displacing some of the water present in its hydration shell.[271–277]

Proteins can form stable complexes with organic solvents that are present as part of a water–co-solvent mixture. Intramolecular $^{1}H\{^{1}H\}$ NOEs that arise from interactions between the protons of hen egg white lysozyme and protons of acetone, acetonitrile, dimethylsulfoxide, methanol, isopropanol, and *t*-butanol,[278] as well as $^{1}H\{^{19}F\}$ NOEs that result from interactions of the enzyme and trifluoroethanol,[279] have been reported. The assignment of proton signals of lysozyme are available, leading to identification of binding sites on the lysozyme surface for these organic solvents. Similarly, intermolecular $^{1}H\{^{1}H\}$ NOEs between acetonitrile and several hydrocarbons with the hydrophobic binding site of a lipid transfer protein from wheat have been reported.[280] Protein binding sites for organic solvents can also be identified through $^{1}H\{^{15}N\}$ HSQC spectra.[281] It has been suggested that identified interaction sites for organic solvent molecules on protein surfaces can provide useful starting points for the design of new drugs.[278,281,282]

6.12 Models of biological membranes

A defining characteristic of living systems is separation. A complex structure, the cell membrane, separates the interior of a cell from its surroundings. Membranes are composed of proteins and other molecules inserted in some manner into bilayered assemblies of lipidic molecules. The structures formed are complex and highly dynamic. A variety of liquid state and solid state NMR experiments have been developed to examine the structure and dynamics of biological membranes and models of these membranes.[283]

Studies of proton–proton cross relaxation in lipid bilayer structures often show intense interactions between protons that are apparently quite distant from each other in the structures, such as those of the methyl groups of the choline headpiece and those of the lipid hydrocarbon chains in a phosphatidylcholine bilayer. The observed interactions could be the result of mobile, highly disordered structure for the bilayer or could be the result of spin diffusion. Work by Huster and Gawrisch[284] demonstrate that the observed cross relaxation does not arise from spin diffusion but rather is the result of direct contacts (with ~ 5 Å) of the headgroup and lipid protons.

Anesthetics, some drugs and biologically active peptides produce their effects by binding to membranes. The interactions involved typically are studied in

membrane–mimetic systems such as micelles or lipid bilayer structures. The location of the bound material can be assessed through detection of intermolecular NOEs that arise from interactions between components of the model membrane and spins of the interacting small molecule.

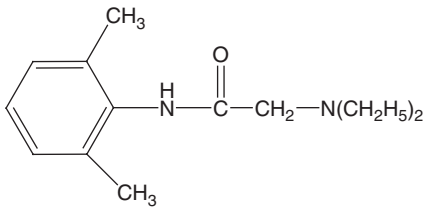

22

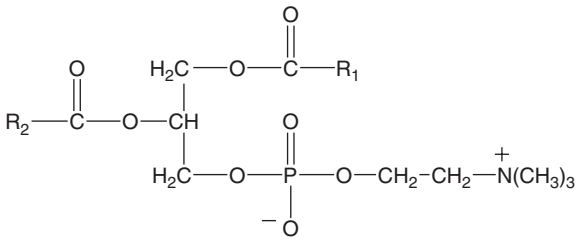

R1, R2 derived from stearic, palmitic, oleic acids

23

Fraceto et al.[285] have used $^{1}H\{^{1}H\}$ ROE experiments to show that the aromatic protons of the anesthetic lidocane (**22**) are in close proximity to the protons of the choline methyl groups in unilamellar vesicles of phosphatidyl choline (**23**). Glover et al.[286] have studied the interaction of a model transmembrane peptide (Acetyl-KKG LLL ALL LLA LLL ALL LKK A-NH_2) with phospholipid bicelles. The central 16 amino acids of this peptide have hydrophobic side chains and are expected to take up a helical conformation. Intermolecular NOEs showed that the peptide preferentially interacts with the bilayer portion of the bicelle structure rather than at the surface. Wang[283] describes similar experiments with several antimicrobial peptides.

$^{1}H\{^{19}F\}$ intermolecular NOEs indicate that the anesthetic halothane (2-bromo-2-chloro-1,1,1-trifluoroethane) interacts with micelles of sodium dodecylsulfate near the surface of the micelle.[287]

Small, water soluble organic solvents such as dimethylsulfoxide and ethanol present in aqueous solutions distribute to some extent into biological membranes.[288,289] Binding of ethanol within the lipid matrix of membranes is thought to be an essential aspect of anesthesia produced by this molecule. Proton–proton NOE experiments have been used to determine cross relaxation rates between the protons of ethanol and those of phospholipid side chains in bilayer structures.[290] The results were compared to cross relaxation terms predicted from a MD simulation. Both experiment and simulations indicate that

the strongest interaction of ethanol takes place at protons near the lipid–water interface.[290]

6.13 Probing molecular surfaces

The surface of any molecule larger than a single atom potentially presents an anisotropic ''face'' to the molecule's environment. Interactions with surrounding molecules will be dependent on the electronic and steric properties of this surface. Surface characteristics are especially important for biological molecules since it is the surface of such molecules that is responsible for guiding the intermolecular interactions which define the molecule's *raison d'etre*. Nuclear spin dipole–dipole interactions between spins of the molecule of interest and spins of other molecules in a solution should provide a means to probe the degree to which a solute spin is ''exposed'' to interactions with the solution by giving rise to intermolecular NOEs. This would provide a means of distinguishing parts of a molecule that are on the exterior (solvent exposed) or interior (protected from interactions with solvent) of the solute. The cross relaxation parameter for such a situation would depend on the concentration of the interacting spins, the relative diffusion of the solute and the species holding the interacting spins, and their distance of closest approach, as discussed earlier (Equation (8)). Unfortunately, it appears rarely to be the case that a surface-probing molecule is without specific (non-random) interactions with the solute. The upshot is that observed intermolecular NOEs often arise from complex formation (Equation (11)), reflecting a different aspect of the solute's surface than simply its ''exposure''.

The spins of the solvent molecules are the most likely to be those used in probing the surface of a molecule of interest. For proteins and other biomolecules, this would usually mean determining intermolecular NOEs with solvent water protons. As has been discussed earlier, water–solute NOEs can arise in a variety of ways and observed cross relaxation is often larger than would be expected from diffusive, intermolecular interactions of the type envisioned in the derivation of Equation (8). Surface accessibility of biomolecules *can* be probed in this way,[291] but care in the interpretation of the data is required, and it is probably best to confirm any conclusions by using several chemically different probes.

Paramagnetic species provide alternate means of potentially obtaining solvent exposure information. The effects observed in these cases are due to electron dipole–nuclear dipole interactions of the paramagnet with solute spins. Molecular oxygen (O_2) has been demonstrated to be useful in this regard,[292–295] although it appears that even this simple species can have site-specific interactions with proteins.[293] Water-soluble nitroxides are another possible type of paramagnetic probe molecule that could have utility[291,296] but there is evidence of selective interactions of these molecules at the surfaces of proteins as well.[296,297]

6.14 Toward the future

Equations (8) and (9) indicate dependence of intermolecular Overhauser effects on properties of the sample that include the concentration of spins of type X (N_X) that interact with the spin of interest (A), the intermolecular distance of closest approach (r_A+r_X) and the sum of the translational diffusion coefficients (D_A+D_X). In attempting to interpret an experimental cross relaxation term (σ_{AX}) in terms of these quantities, it is essential to keep several considerations in mind.

(a) Most important is that the model behind the derivation of these equations is only an approximation; the shapes and electrical anisotropy of solute and solvent molecules have been ignored along with the ''granularity'' or local organization of molecules in the liquid state.

(b) It may be that preferential solvation effects lead to a local accumulation of solvent spins (X) near solute spins (A). Thus the local N_X may not be the bulk value assigned to the solution and may well be a function of the distance away from the solute molecule.

(c) Because real molecules have definite 3D shapes, internuclear separations (r_A+r_X) in real systems will depend on the approach path taken as the A and X molecules interact. The shapes of the interacting molecules thus have to be considered.

(d) Measured diffusion coefficients represent the collective behavior of all species in the sample. Complexes formed between solute and solvent will have different diffusion properties than either component when separated and an experimental D may be the average result for a number of species that are in rapid exchange. Clustering of solute or solvent molecules may take place; each cluster may have different diffusive behavior. It is likely that the rates of diffusion leading to (D_A+D_X) are not constant but are functions of intermolecular distances (r_A+r_X), especially when molecules are close to one another.

(e) Complex formation can augment or decrease an intermolecular cross relaxation term (Equation (11)) and any interpretation exclusively in terms of Equation (8) or (9) or the like may be misleading. Thus, a value for σ_{AX} larger than anticipated based on Equation (8) may mean that the local concentration of X spins N_X is higher than the nominal value for the solution, may mean that the diffusion behavior appropriate for use in Equation (8) is not the same as the diffusive behavior of species in the bulk of the solutions, or may mean that complex formation takes place and is contributing to the observed σ_{AX}.

It is not clear that MD simulations have reached a state of reliability such that these can be the final arbiters of what effects or interactions are producing an observed cross relaxation parameter. Clearly, more research that provides methods and theory for unambiguous interpretation of experimental values of σ_{AX} is justified.

A major part of current efforts to develop chemical processes that have reduced environmental impacts (''green chemistry'') have focused on new solvent systems.[8] Among such solvents are the room temperature ionic liquids which were alluded to in Section 6.4. Other solvent systems employ carbon

dioxide or other gases in liquid or supercritical states.[298] Primarily through chemical shift studies, NMR observations have indicated selective interactions of various alcohols and hydrocarbons with CO_2 solvent molecules.[299,300] Interactions of CO_2 with fluorine-containing materials appear to be highly site specific.[299–304]A so-called carbon dioxide-expanded solvent is a mixture of subcritical but liquid CO_2 and an organic solvent.[305] These mixtures have a higher capacity to dissolve polar materials than does pure liquid CO_2 and appear to be particularly effective media for catalytic reactions.[306]

IR spectroscopy has demonstrated selective interactions of solutes with solvent components in liquid CO_2-containing systems.[307,308] While the experimental considerations in dealing with samples under high pressure in an NMR spectrometer have to be dealt with,[299,309] intermolecular NOE experiments could be useful in examining solvent clustering and solvent–solute interactions in supercritical CO_2 and CO_2-expanded solvents. An advantage of using supercritical fluids in NMR experiments is the low viscosity of these media which may lead to better resolution due to a reduction of line widths in quadrupolar[310] or macromolecular systems.[311]

Application of magnetic field gradients during certain experiments can lead to detected signals that arise from intermolecular multiple quantum coherences.[312–314] Such signals originate from long range dipole–dipole interactions between molecules. The interacting molecules may be a single type[315] or pairs of chemically distinct molecules.[316] The intensity of such signals are typically weak, appearing when the molar concentrations of interacting molecules are high, and are dependent on experimental details, including such considerations as rates of diffusion.[317] Development of this phenomenon in the future may afford new tools for examining the various solvent–solute interactions described in this chapter.

The examples cited in this chapter show that new, useful information about the nature of solutions and intermolecular interactions can be obtained by intermolecular Overhauser effect experiments. This information may prove useful in validating results of MD simulations, particularly as regards solvent structure and local solvent–solute interactions. As with any vibrant research field, new systems continue to emerge where the basic ideas behind the NMR experiments can be applied to new systems or in new ways.

ACKNOWLEDGMENTS

Work in the author's laboratory discussed in this article has been supported by the UCSB Committee on Research, the Petroleum Research Fund (ACS-PRF # 36776-AC4), and the National Science Foundation (CHE-0408415). The author thanks these sponsors, his spouse, and Dr. T. B. Woliver and his staff, for their contributions in making preparation of the article possible.

REFERENCES

1. K. Muller-Dethlefs and P. Hobza, *Chem. Rev.*, 2000, **100**, 143.
2. J. Tomasi, B. Mennucci and C. Cappelli, in: *Handbook of Solvents*, G. Wypych, ed., William Andrew, Toronto, 2001, p. 419.

3. R. Schmid, in: *Highlights in Solute–Solvent Interactions*, W. Linert, ed., Springer-Verlag, New York, 2002, p. 59.
4. N. Prabhu and K. Sharp, *Chem. Rev.*, 2006, **106**, 1616.
5. K. B. Wiberg, W. Hinz, R. M. Jarrett and K. B. Aubrecht, *J. Org. Chem.*, 2005, **70**, 8381.
6. R. Urbani and A. Cesaro, in: *Handbook of Solvents*, G. Wypych, ed., William Andrew, Toronto, 2001, p. 706.
7. J. Gao, M. Garcia-Viloca, T. D. Poulsen and Y. Mo, *Adv. Phys. Org. Chem.*, 2003, **38**, 161.
8. C. Reichardt, *Solvents and Solvent Effects in Organic Chemistry,* Wiley-VCH, Weinheim, 2003.
9. D. K. Bohme and G. I. Mackay, *J. Am. Chem. Soc.*, 1981, **103**, 978.
10. L. Sun, K. Song and W. L. Hase, *Science*, 2002, **296**, 875.
11. S. Gronert, L. M. Pratt and S. Mogali, *J. Am. Chem. Soc.*, 2001, **123**, 3081.
12. J. Catalan, in: *Handbook of Solvents*, G. Wypych, ed., William Andrew, Toronto, 2001, p. 583.
13. M. Karelson, in: *Handbook of Solvents*, G. Wypych, ed., William Andrew, Toronto, 2001, p. 639.
14. R. Schmid, in: *Handbook of Solvents*, G. Wypych, ed., William Andrew, Toronto, 2001, p. 737.
15. B. K. Freed, J. Biesecker and W. J. Middleton, *J. Fluorine Chem.*, 1990, **48**, 63.
16. Y. Y. Fialkov and V. L. Chumak, in: *Handbook of Solvents*, G. Wypych, ed., William Andrew, Toronto, 2001, p. 505.
17. N. Agmon, *J. Phys. Chem. A*, 2002, **106**, 7256.
18. M. Jozefowicz and J. R. Heldt, *Chem. Phys.*, 2003, **294**, 105.
19. S. Park, B. N. Flanders, X. M. Shang, R. A. Westervelt, J. Kim and N. F. Scherer, *J. Chem. Phys.*, 2003, **118**, 3917.
20. T. Bevilaqua, T. F. Goncalves, C. D. G. Venturini and V. G. Machado, *Spectrochim. Acta A*, 2006, **65**, 535.
21. T. W. Bentley, D. N. Ebdon, E.-J. Kim and I. S. Koo, *J. Org. Chem.*, 2005, **70**, 1647.
22. T. W. Bentley and I. S. Koo, *Org. Biomol. Chem.*, 2004, **2**, 2376.
23. D. N. Shin, J. W. Wijnen, J. B. F. N. Engberts and A. Wakisaka, *J. Phys. Chem. B*, 2001, **105**, 6759.
24. K. Yoshida, T. Yamaguchi, T. Adachi, T. Otomo, D. Matsuo, T. Takamuku and N. Nishi, *J. Chem. Phys.*, 2003, **119**, 6132.
25. R. Gratias and H. Kessler, *J. Phys. Chem. B*, 1998, **102**, 2027.
26. T. J. F. Day and G. N. Patey, *J. Chem. Phys.*, 1997, **106**, 2782.
27. A. Perera, F. Sokolic, L. Almasy and Y. Koga, *J. Chem. Phys.*, 2006, **124**, 124515/1.
28. N. Rega, G. Brancato and V. Barone, *Chem. Phys. Lett.*, 2006, **422**, 367.
29. E. Cubero, F. J. Luque, M. Orozco and J. Gao, *J. Phys. Chem. B*, 2003, **107**, 1664.
30. H. Hu, M. Elstner and J. Hermans, *Proteins Struct. Funct. Bioinform.*, 2003, **50**, 451.
31. R. Bukowski, K. Szalewicz, G. C. Groenenboom and A. van der Avoird, *Science*, 2007, **315**, 1249.
32. M. H. Kim, L. Shen, H. Tao, T. J. Martinez and A. G. Suits, *Science*, 2007, **315**, 1561.
33. E. Vohringer-Martinez, B. Hansmann, H. Hernandez, J. S. Francisco, J. Troe and B. Abel, *Science*, 2007, **315**, 497.
34. E. Amis, *Solvent Effects on Reaction Rates and Mechanisms*, Academic, New York, 1966.
35. R. R. Dogonadze, E. Kalman, A. A. Kornyshev and J. Ulstrup, eds., *The Chemical Physics of Solvation*, Elsevier, Amsterdam, 1985.
36. F. Hirata ed., *Molecular Theory of Solvation*, Kluwer, Dordrecht, 2003.
37. G. Wypych ed., *Handbook of Solvents*, William Andrew, Toronto, 2001.
38. P. A. Egelstaff, *An Introduction to the Liquid State*, Oxford, New York, 1994.
39. U. Balucani and M. Zoppi, *Dynamics in the Liquid State*, Oxford, New York, 1994.
40. P. Kruss, *Liquids and Solutions*, Dekker, New York, 1977.
41. J. N. Murrell and E. A. Boucher, *Properties of Liquids and Solutions,* Wiley, Chichester, 1982.
42. R. B. Gregory*Protein–Solvent Interactions,* Dekker, New York, 1995.
43. A. Wakisaka and K. Matsuura, *J. Mol. Liq.*, 2006, **129**, 25.
44. F. Rastrelli, G. Saielli, A. Bagno and A. Wakisaka, *J. Phys. Chem. B*, 2004, **108**, 3479.
45. A. Wakisaka, S. Komatsu and Y. Usui, *J. Mol. Liq.*, 2001, **90**, 175.
46. A. Perera, F. Sokolic, L. Almasy, P. Westh and Y. Koga, *J. Chem. Phys.*, 2005, **123**, 024503.
47. Y. Marcus, *Solvent Mixtures: Properties and Selective Solvation*, Marcel Dekker, New York, 2002.

48. Y. Marcus, in: *Highlights in Solute–Solvent Interactions*, W. Linert, ed., Springer-Verlag, New York, 2002, p. 151.
49. Y. Marcus, *Monatsh. Chem*., 2001, **132**, 1387.
50. J.-J. Delpuech, *Analyst*, 1992, **117**, 267.
51. R. A. Y. Jones, *Ann. Rev. NMR Spectrosc*., 1968, **1**, 1.
52. A. Bagno, F. Rastrelli and G. Saielli, *Prog. NMR Spectrosc*., 2005, **47**, 41.
53. R. G. Bryant, *Annu. Rev. Phys. Chem*., 1978, **29**, 167.
54. T. Brand, E. J. Cabrita and S. Berger, *Prog. NMR Spectrosc*., 2005, **46**, 159.
55. V. I. Baskhmutov, *Practical NMR Relaxation for Chemists*, Wiley, Chichester, 2004.
56. D. Neuhaus and M. P. Williamson, *The Nuclear Overhauser Effect in Structural and Conformational Analysis*, Wiley, New York, 2000.
57. R. Lenk, *Brownian Motion and Spin Relaxation*, Elsevier, Amsterdam, 1977.
58. R. Kaiser, *J. Chem. Phys*., 1965, **42**, 1838.
59. J. Homer and E. R. V. Cedeno, *J. Chem. Soc. Faraday Trans. 2*, 1980, **80**, 375.
60. T. P. Pitner, J. D. Glickson, J. Dadok and G. R. Marshall, *Nature*, 1974, **250**, 582.
61. T. P. Pitner, J. D. Glickson, R. Rowan, J. Dadok and A. A. Bothner-By, *J. Am. Chem. Soc*., 1975, **97**, 5917.
62. S. Macura and R. R. Ernst, *Mol. Phys*., 1980, **41**, 95.
63. S. Macura and R. R. Ernst, *Mol. Phys*., 2002, **100**, 135.
64. H. Mo and T. C. Pochapsky, *Prog. NMR Spectrosc*., 1997, **30**, 1.
65. V. Domenici, M. Geppi and C. A. Veracini, *Prog. NMR Spectrosc*., 2007, **50**, 1.
66. J. Garcia de la Torre, P. Bernado and M. Pons, *Methods Enzymol*., 2005, **394**, 419.
67. R. Y. Dong, *Annu. Rep. NMR Spectrosc*., 2004, **53**, 67.
68. J. H. Freed, *J. Chem. Phys*., 1977, **66**, 4183.
69. J. Keeler, *Understanding NMR Spectroscopy*, Wiley, Chichester, 2005.
70. D. Canet, *NMR Concepts and Methods*, Wiley, Chichester, 1996.
71. J. H. Noggle and R. E. Schirmer, *The Nuclear Overhauser Effect*, Academic, New York, 1971.
72. M. H. Levitt, *Spin Dynamics*, Wiley, Chichester, 2001.
73. J. W. Hennel and J. Klinowski, *Fundamentals of NMR*, Longman, Harlow, 1993.
74. R. K. Harris, *Nuclear Magnetic Resonance Spectroscopy*, Pitman, London, 1983.
75. J. Kowalewski and L. Maier, *Nuclear Spin Relaxation in Liquids*, Taylor & Francis, Boca Raton, 2006.
76. L. Ghalebani, P. Bernatowicz, S. N. Aski and J. Kowalewski, *Concepts Magn. Reson*., 2007, **30A**, 100.
77. A. Geirer and K. Wirtz, *Z. Naturforsch. A*, 1953, **8**, 532.
78. R. E. London, in: *Magnetic Resonance in Biology*, J. S. Cohen, ed., Vol. 1, Wiley, New York, 1980.
79. C. A. Sholl, *J. Phys. C Solid State Phys*., 1981, **14**, 447.
80. L.-P. Hwang and J. H. Freed, *J. Chem. Phys*., 1975, **63**, 4017.
81. P. S. Hubbard, *Phys. Rev*., 1963, **131**, 275.
82. B. Halle, *J. Chem. Phys*., 2003, **119**, 12372.
83. B. Cowan, *Nuclear Magnetic Resonance and Relaxation*, Cambridge, Cambridge, 1997.
84. Y. Ayant, E. Belorizky, P. Fries and J. Rossett, *J. Phys. (Paris)*, 1977, **38**, 325.
85. J. T. Gerig, *J. Org. Chem*., 2003, **68**, 5244.
86. C.-L. Teng, S. Martini and R. G. Bryant, *J. Am. Chem. Soc*., 2004, **126**, 15253.
87. N. R. Skrynnikov, T. N. Khazanovich and B. C. Sanctuary, *Mol. Phys*., 1997, **91**, 977.
88. D. Frezzato, F. Rastrelli and A. Bagno, *J. Phys. Chem. B*, 2006, **110**, 5676.
89. T. N. Khazanovich and N. R. Skrynnikov, *J. Phys. Soc. Japan*, 1995, **64**, 631.
90. J. R. Zheng, K. Kwak, J. Asbury, X. Chen, I. R. Piletic and M. D. Fayer, *Science*, 2005, **309**, 1338.
91. S. Woutersen, Y. Mu, G. Stock and P. Hamm, *Chem. Phys*., 2001, **266**, 137.
92. C. Peter, X. Daura and W. F. van Gunsteren, *J. Biomol. NMR*, 2001, **20**, 297.
93. J.-P. Grivet, *J. Chem. Phys*., 2005, **123**, 034503.
94. M. Odelius, A. Laaksonen, M. H. Levitt and J. Kowalewski, *J. Magn. Reson. A*, 1993, **105**, 289.
95. P. O. Westland and R. M. Lynden-Bell, *J. Magn. Reson*., 1987, **72**, 522.
96. G. Lippens, D. van Belle, S. J. Wodak and J. Jeener, *Mol. Phys*., 1993, **80**, 1469.
97. S. E. Feller, D. Huster and K. Gawrisch, *J. Am. Chem. Soc*., 1999, **121**, 8963.
98. M. Luhmer, A. Moschos and J. Reisse, *J. Magn. Reson. A*, 1995, **113**, 164.

99. M. Dahlberg and A. Laaksonen, *J. Phys. Chem. A*, 2006, **110**, 2253.
100. M. Angulo, C. Hawat, H. J. Hofmann and S. Berger, *Org. Biomol. Chem.*, 2003, **1**, 1049.
101. M. Fioroni, M. D. Diaz, K. Burger and S. Berger, *J. Am. Chem. Soc.*, 2002, **124**, 7737.
102. C. Monteiro and C. H. du Penhoat, *J. Phys. Chem. A*, 2001, **105**, 9827.
103. A. J. Gordon and R. A. Ford, *The Chemist's Companion*, Wiley-Interscience, New York, 1972.
104. L. Nordstierna, P. V. Yushmanov and I. Furo, *J. Chem. Phys.*, 2006, **125**, 074704.
105. W. S. Price, F. Tsuchiya, C. Suzuki and Y. Arata, *J. Biomol. NMR*, 1999, **13**, 113.
106. L. T. Kakalis and I. D. Baianu, *Arch. Biochem. Biophys.*, 1988, **267**, 829.
107. C. Chatterjee and J. T. Gerig, *Biochemistry*, 2006, **45**, 14665.
108. G. Otting, *Prog. NMR Spectrosc.*, 1997, **31**, 259.
109. L. Nordstierna, P. V. Yushmanov and I. Furo, *J. Phys. Chem. B*, 2006, **110**, 25775.
110. C. Dalvit, *J. Biomol. NMR*, 1998, **11**, 437.
111. A. Bagno, F. Rastrelli and G. Scorrano, *J. Magn. Reson.*, 2004, **167**, 31.
112. D. Wu and C. S. Johnson Jr, *J. Magn. Reson. A*, 1994, **110**, 113.
113. X. Mao, J. Guo and C. Ye, *Chem. Phys. Lett.*, 1994, **222**, 417.
114. B. Lix, F. D. Sonnichsen and B. D. Sykes, *J. Magn. Reson. A*, 1996, **121**, 83.
115. H. T. Edzes, *J. Magn. Reson.*, 1990, **86**, 293.
116. T. D. W. Claridge, *High-Resolution NMR Techniques in Organic Chemistry*, Pergamon, Amsterdam, 1999.
117. I. Furo, P. Mutzenhardt and D. Canet, *J. Am. Chem. Soc.*, 1995, **117**, 10405.
118. A. Dejaegere, M. Luhmer, M.-L. Stein and J. Reisse, *J. Magn. Reson.*, 1991, **91**, 362.
119. T. R. Stengle, N. V. Reo and K. L. Williamson, *J. Phys. Chem.*, 1984, **88**, 3225.
120. M. Luhmer and J. Reisse, *J. Magn. Reson. A*, 1995, **115**, 197.
121. D. Raftery, *Annu. Rep. NMR Spectrosc.*, 2006, **57**, 206.
122. T. R. Stengle, N. V. Reo and K. L. Williamson, *J. Phys. Chem.*, 1981, **85**, 3772.
123. C. J. Jameson, D. N. Sears and S. Murad, *J. Chem. Phys.*, 2004, **121**, 9581.
124. P. Diehl and J. Jokisaari, *J. Magn. Reson.*, 1990, **88**, 660.
125. A. Moschos and J. Reisse, *J. Magn. Reson.*, 1991, **95**, 603.
126. Y. Xu and P. Tang, *Biochim. Biophys. Acta*, 1997, **1323**, 154.
127. G. Navon, Y.-Q. Song, T. Room, S. Appelt, R. E. Taylor and A. Pines, *Science*, 1996, **271**, 1848.
128. A. L. Zook, B. B. Adhyaru and C. R. Bowers, *J. Magn. Reson.*, 2002, **159**, 175.
129. A. M. Oros and N. J. Shah, *Phys. Med. Biol.*, 2004, **49**, R105.
130. Y.-Q. Song, B. M. Goodson, R. E. Taylor, D. D. Laws, G. Navon and A. Pines, *Angew. Chem. Int. Ed.*, 1997, **36**, 2368.
131. A. Stith, T. K. Hitchens, D. P. Hinton, S. S. Berr, B. Driehuys, J. R. Brookeman and R. G. Bryant, *J. Magn. Reson.*, 1999, **139**, 225.
132. I. E. Dimitrov, R. Reddy and J. S. Leigh, *J. Magn. Reson.*, 2000, **145**, 302.
133. H. Ohtaki, in: *Highlights in Solute–Solvent Interactions*, W. Linert, ed., Springer-Verlag, New York, 2002, p. 1.
134. P. M. Stone, T. C. Pochapsky and E. Callegari, *J. Chem. Soc. Chem. Commun.*, 1992, 178.
135. W. von Phillipsborn, *Chem. Soc. Rev.*, 1999, **28**, 95.
136. P. S. Pregosin, *Prog. NMR Spectrosc.*, 2006, **49**, 261.
137. C. F. Jensen, S. Deshmukh, H. J. Jakobsen, R. R. Inners and P. D. Ellis, *J. Am. Chem. Soc.*, 1981, **103**, 3659.
138. C. C. Bryden and C. N. Reilley, *J. Am. Chem. Soc.*, 1982, **104**, 2697.
139. E. Martinez-Viviente, P. S. Pregosin, L. Vial, C. Herse and J. Lacour, *Chem. Eur. J.*, 2004, **10**, 2912.
140. B. Binotti, A. Macchioni, C. Zuccaccia and D. Zuccaccia, *Comments Inorg. Chem.*, 2002, **23**, 417.
141. A. Macchioni, *Eur. J. Inorg. Chem.*, 2003, 195.
142. D. Zuccaccia, S. Sabatini, G. Bellachioma, G. Cardaci, E. Clot and A. Macchioni, *Inorg. Chem.*, 2003, **42**, 5465.
143. I. Fernandez and P. S. Pregosin, *Magn. Reson. Chem.*, 2006, **44**, 76.
144. A. Macchioni, C. Zuccaccia, E. Clot, K. Gruet and R. H. Crabtree, *Organometallics*, 2001, **20**, 2367.
145. S. Pandey, *Anal. Chim. Acta*, 2006, **556**, 38.
146. H. Xue, R. Verma and J. M. Shreeve, *J. Fluorine Chem.*, 2006, **127**, 159.

147. D. W. Rooney and K. R. Seddon, in: *Handbook of Solvents*, G. Wypych, ed., William Andrew, Toronto, 2001, p. 1459.
148. A. Sarkar and S. Pandey, *J. Chem. Eng. Data*, 2006, **51**, 2051.
149. A. D. Headley, S. Kotti, J. Nam and K. Y. Li, *J. Phys. Org. Chem.*, 2005, **18**, 1018.
150. A. Mele, C. D. Tran and S. H. De Paoli Lacerda, *Angew. Chem. Int. Ed.*, 2003, **42**, 4364.
151. A. Mele, G. Romano, M. Giannone, E. Ragg, G. Fronza, G. Raos and V. Marcon, *Angew. Chem. Int. Ed.*, 2006, **45**, 1123.
152. R. A. Mantz, P. C. Trulove, R. A. Carlin and R. A. Osteryoung, *Inorg. Chem.*, 1995, **34**, 3846.
153. D. Nama, P. G. A. Kumar, P. S. Pregosin, T. J. Geldbach and P. J. Dyson, *Inorg. Chim. Acta*, 2006, **359**, 1907.
154. H. Dodziuk, *J. Mol. Struct.*, 2002, **614**, 33.
155. J. Szejtli, *Cyclodextrin Technology*, Kluwer, Dordrecht, 1988.
156. E. M. M. Del Valle, *Process Biochem.*, 2004, **39**, 1033.
157. B. Chankvetadze, *Chem. Soc. Rev.*, 2004, **33**, 337.
158. F. Hapiot, S. Tilloy and E. Monflier, *Chem. Rev.*, 2006, **106**, 767.
159. V. T. D'Souza and K. B. Lipkowitz, *Chem. Rev.*, 1998, **98**, 1741.
160. C. Jaime, J. Redondo, F. Sanchez-Ferrando and A. Virgili, *J. Org. Chem.*, 1990, **55**, 4772.
161. P. Salvadori, G. Uccello-Barretta, F. Balzano, C. Bertucci and C. Chiavacci, *Chirality*, 1996, **8**, 423.
162. R. Ravichandran and S. Divakar, *J. Inclusion Phenom. Macrocyclic Chem.*, 1998, **30**, 253.
163. E. Bednarek, W. Bocian, J. Poznanski, J. Sitkowski, N. Sadlej-Sosnowska and L. Kozerski, *J. Chem. Soc. Perkin Trans. 2*, 2002, **2**, 999.
164. S. Lee, D.-H. Yi and S. Jung, *Bull. Korean Chem. Soc.*, 2004, **25**, 216.
165. G. Gonzalez-Gaitano, P. R. Sainz-Rozas, J. R. Isasi, A. Guerrero-Martinez and G. Tardajos, *J. Phys. Chem. B*, 2004, **108**, 14154.
166. H. Dodziuk, W. Kozminski and A. Ejchart, *Chirality*, 2004, **16**, 90.
167. H. Dodziuk, W. Kozminski, O. Lukin and D. Sybilska, *J. Mol. Struct.*, 2000, **523**, 205.
168. C. F. Dignam, L. A. Randall, R. D. Blacken, P. R. Cunningham, S.-K. G. Lester, M. J. Brown, S. C. French, S. E. Aniagyei and T. J. Wenzel, *Tetrahedron Asymmetry*, 2006, **17**, 1199.
169. Q. Liu, L. M. V. Tillekeratne, Y.-W. Kim, J. R. Kirchhoff and R. A. Hudson, *Chirality*, 2005, **17**, 570.
170. K. Lindner and W. Saenger, *Carbohydr. Res.*, 1982, **99**, 103.
171. A. Guerrero-Martinez, S. Berger and G. Tardajos, *ChemPhysChem*, 2006, **7**, 2074.
172. H. B. Seba and B. Ancian, *J. Magn. Reson.*, 1989, **84**, 177.
173. D. P. Miller, B. Ternai and G. B. Maciel, *J. Am. Chem. Soc.*, 1972, **95**, 1336.
174. J. C. Vandenbosch, D. Zimmermann and J. Reisse, *Org. Magn. Reson.*, 1976, **8**, 436.
175. A. Troganis, I. P. Gerothanassis and D. K. Papademitriou, *J. Magn. Reson.*, 1998, **130**, 149.
176. H. B. Seba and B. Ancian, *J. Chem. Soc. Chem. Commun.*, 1990, 996.
177. M. Chahinian, H. B. Seba and B. Ancian, *Chem. Phys. Lett.*, 1998, **285**, 337.
178. H. B. Seba, P. Thureau, B. Ancian and A. Thevand, *Magn. Reson. Chem.*, 2006, **44**, 1109.
179. G. R. Smith and B. Ternai, *Aust. J. Chem.*, 1983, **36**, 493.
180. C. Yu and G. C. Levy, *J. Am. Chem. Soc.*, 1983, **105**, 6994.
181. C. Yu and G. C. Levy, *J. Am. Chem. Soc.*, 1984, **106**, 6533.
182. R. Ta-shma and Z. Rappoport, *Advan. Phys. Org. Chem.*, 1992, **27**, 239.
183. S. Dixit, J. Crain, W. C. K. Poon, J. L. Finney and A. K. Soper, *Nature*, 2002, **416**, 829.
184. T. Takamuku, T. Kumai, K. Yoshida, T. Otomo and T. Yamaguchi, *J. Phys. Chem. A*, 2005, **109**, 7667.
185. A. Bagno, M. Campulla, M. Pirana, G. Scorrano and S. Stiz, *Chem. Eur. J.*, 1999, **5**, 1291.
186. A. Bagno, *J. Phys. Org. Chem.*, 2002, **15**, 790.
187. A. Bagno, G. Scorrano and S. Stitz, *J. Am. Chem. Soc.*, 1997, **119**, 2299.
188. A. Wakisaka, S. Takahashi and N. Nishi, *J. Chem. Soc. Faraday Trans.*, 1995, **91**, 4063.
189. M. Angulo and S. Berger, *Anal. Bioanal. Chem.*, 2004, **378**, 1555.
190. J. A. Gladysz, D. P. Curran and I. T. Horvath, *Handbook of Fluorous Chemistry*, Wiley, Somerset, 2004.
191. W. Zhang, *Chem. Rev.*, 2004, **104**, 2531.
192. J. T. Gerig, *J. Am. Chem. Soc.*, 2005, **127**, 9277.
193. A. Gomez-Puyou, A. Darszon and M. T. de Gomez-Puyou, *Biomolecules in Organic Solvents*, CRC Press, Boca Raton, 1992.

194. JD. L. Williams Jr, I. Rapanovich and A. J. Russell, in: *Protein–Solvent Interactions*, R. B. Gregory, ed., Dekker, New York, 1995, p. 327.
195. F. H. Arnold, *Trends Biotechnol*., 1990, **8**, 244.
196. D.-P. Hong, M. Hoshino, R. Kuboi and Y. Goto, *J. Am. Chem. Soc*., 1999, **121**, 8427.
197. M. Buck, *Q. Rev. Biophys*., 1998, **31**, 297.
198. R. Rajan, S. K. Awasthi, S. Bhattacharjya and P. Balaram, *Biopolymers*, 1997, **42**, 125.
199. M. A. Strickler and J. T. Gerig, *Biopolymers*, 2002, **64**, 227.
200. M. D. Diaz and S. Berger, *Magn. Reson. Chem*., 2001, **39**, 369.
201. A. Starzyk, W. Barber-Armstrong, M. Sridharan and S. M. Decatur, *Biochemistry*, 2005, **44**, 369.
202. J. A. Carver and J. G. Collins, *Eur. J. Biochem*., 1990, **187**, 645.
203. M. D. Diaz, M. Fioroni, K. Burger and S. Berger, *Chem. Eur. J*., 2002, **8**, 1663.
204. J. W. Neidigh, R. M. Fersinmeyer and N. H. Anderson, *Nat. Struct. Biol*., 2002, **9**, 425.
205. L. Qiu, S. A. Pabit, A. E. Roitberg and S. J. Hagen, *J. Am. Chem. Soc*., 2002, **124**, 12952.
206. C. Chatterjee and J. T. Gerig, *Biopolymers*, 2007, **87**, 115–123.
207. K. Gast, A. Siemer, D. Zirwer and G. Damaschun, *Eur. Biophys. J*., 2001, **30**, 273.
208. C. E. Dempsey, *Biochim. Biophys. Acta Rev. Biomembr.*, 1990, **1031**, 143.
209. J. T. Gerig, *Biophys. J*., 2004, **86**, 3166.
210. D. Roccatano, M. Fioroni, M. Zacharias and G. Colombo, *Protein Sci*., 2005, **14**, 2582.
211. J. T. Gerig, *Biopolymers*, 2004, **74**, 240.
212. A. Berkessel, J. A. Adrio, D. Huettenhain and J. M. Neudorfl, *J. Am. Chem. Soc*., 2006, **128**, 8421.
213. W. H. Pirkle, *J. Am. Chem. Soc*., 1966, **88**, 1837.
214. D. Parker, *Chem. Rev*., 1991, **91**, 1441.
215. A. F. Casy, *Trends Anal. Chem*., 1993, **12**, 185.
216. W. H. Pirkle, P. G. Murray, D. J. Rausch and S. T. McKenna, *J. Org. Chem*., 1996, **61**, 4769.
217. W. H. Pirkle and T. C. Pochapsky, *J. Am. Chem. Soc*., 1987, **109**, 5975.
218. W. H. Pirkle and S. R. Selness, *J. Org. Chem*., 1995, **60**, 3252.
219. M. de Moragas, E. Cervello, A. Port, C. Jaime, A. Virgili and B. Ancian, *J. Org. Chem*., 1998, **63**, 8689.
220. A. Port, A. Virgili, A. Alvarez-Larena and J. F. Piniella, *Tetrahedron Asymmetry*, 2000, **11**, 3747.
221. K. F. Morris, B. A. Becker, B. C. Valle, I. M. Warner and C. K. Larive, *J. Phys. Chem. B*, 2006, **110**, 17359.
222. L. Beguin, J. Courtieu, L. Ziani and D. Merlet, *Magn. Reson. Chem*., 2006, **44**, 1096.
223. M. Sugiura, A. Kimura and H. Fujiwara, *Magn. Reson. Chem*., 2006, **44**, 121.
224. W. Hu and L. Wang, *Annu. Rep. NMR Spectrosc*., 2006, **58**, 232.
225. A. D. Buckingham, *Chem. Phys. Lett*., 2004, **398**, 1.
226. A. D. Buckingham and P. Fischer, *Chem. Phys*., 2006, **324**, 111.
227. K. A. Zachariasse, B. Kozankiewicz and W. Kuhnle, *Surfactants in Solution*Vol. 1, Plenum, New York, 1984
228. S. Vass, H. Grimm, I. Banyai, G. Meier and T. Gilanyi, *J. Phys. Chem. B*, 2005, **109**, 11870.
229. B. Halle and C. Goeran, *J. Phys. Chem*., 1981, **85**, 2142.
230. P. G. Nilsson and B. Lindman, *J. Phys. Chem*., 1983, **87**, 4756.
231. I. Furo, *J. Mol. Liq*., 2005, **117**, 117.
232. O. Soderman, P. Stilbs and W. S. Price, *Concepts Magn. Reson. A*, 2004, **23A**, 121.
233. Y. R. Du, S. Zhao and L. F. Shen, *Annu. Rep. NMR Spectrosc*., 2002, **48**, 145.
234. D. Canet, N. Mahieu and P. Tekely, *J. Am. Chem. Soc*., 1992, **114**, 6190.
235. N. Mahieu, P. Tekely and D. Canet, *J. Phys. Chem*., 1993, **97**, 2764.
236. R. Raulet, I. Furo, J. Brondeau, B. Diter and D. Canet, *J. Magn. Reson*., 1998, **133**, 324.
237. A. Belmajdoub, N. Mahieu, P. Tekely and D. Canet, *J. Phys. Chem*., 1992, **96**, 1011.
238. L. Ceraulo, E. Dormond, A. Mele and V. T. Liveri, *Colloids Surf. A*, 2003, **218**, 255.
239. Y. E. Shapiro, V. Y. Gorbatyuk, A. A. Mazurov and S. A. Andronati, *Analyst*, 1994, **119**, 647.
240. M. Seigneuret and C. Le Guerneve, *J. Biomol. NMR*, 1999, **13**, 31.
241. C. Dominquez, C. Sebban-Kreuzer, O. Bornet, B. Kerfelec, C. Chapus and F. Guerlesquin, *FEBS Lett*., 2000, **482**, 109.

242. M. T. Morgan, M. A. Carnahan, C. E. Immoos, A. A. Riberio, S. Finkelstein, S. J. Lee and M. W. Grinstaff, *J. Am. Chem. Soc*., 2003, **125**, 15485.
243. M. Falk, W. Chew, J. A. Walter, W. Kwiatkowski, K. D. Barclay and G. A. Klassen, *Can. J. Chem*., 1998, **76**, 48.
244. R. E. Hoffman and M. Rabinowitz, *Magn. Reson. Chem*., 1993, **31**, 1031.
245. X. Zhang, K. Takegoshi and K. Hikichi, *Macromolecules*, 1992, **25**, 4871.
246. P. J. Mirau, H. Tanaka and F. A. Bovey, *Macromolecules*, 1988, **21**, 2929.
247. T. Stangler, R. Hartmann, D. Willbold and B. W. Koenig, *Z. Phys. Chem*., 2006, **220**, 567.
248. Y. Cohen, L. Avram and L. Frish, *Angew. Chem. Int. Ed*., 2005, **44**, 520.
249. K. I. Momot and P. W. Kuchel, *Concepts Magn. Reson. A*, 2006, **28A**, 249.
250. C. B. Post, *Curr. Opin. Struct. Biol*., 2003, **13**, 581.
251. J. Clarkson and I. D. Campbell, *Biochem. Soc. Trans*., 2003, **31**, 1006.
252. F. Ni, *Prog. NMR Spectrosc*., 1994, **26**, 517.
253. T. Carlomagno, *Annu. Rev. Biophys. Biomol. Struct*., 2005, **34**, 245.
254. W. Jahnke and H. Widmer, *Cell. Mol. Life Sci*., 2004, **61**, 580.
255. B. J. Stockman and C. Dalvit, *Prog. NMR Spectrosc*., 2002, **41**, 187.
256. M. Pellecchia, D. J. Sem and K. Wuthrich, *Nat. Rev. Drug Discov*., 2002, **11**, 211.
257. K. G. Hovagimyan and J. T. Gerig, *J. Phys. Chem. B*, 2005, **109**, 24142.
258. M. Chaplin, *Nat. Rev. Mol. Cell Biol*., 2006, **7**, 861.
259. J. Janin, *Structure*, 1999, **7**, R277.
260. B. Halle, *Philos. Trans. R. Soc. Lond. B*, 2004, **359**, 1207.
261. D. Russo, R. K. Murarka, J. R. D. Copley and T. Head-Gordon, *J. Phys. Chem. B*, 2005, **109**, 12966.
262. G. Otting and K. Wuthrich, *Acc. Chem. Res*., 1995, **28**, 171.
263. V. A. Likic, N. Juranic, S. Macura and F. G. Predergast, *Protein Sci*., 2000, **9**, 497.
264. I. Bertini, K. Ghosh, A. Rosato and P. R. Vasos, *Biochemistry*, 2003, **42**, 3457.
265. S. N. Timasheff, *Biochemistry*, 2002, **41**, 13473.
266. K. Modig, E. Liepinsh, G. Otting and B. Halle, *J. Am. Chem. Soc*., 2004, **126**, 102.
267. I. Michalarias, X. Gao, R. C. Ford and J. Li, *J. Mol. Liq*., 2005, **117**, 107.
268. D. Russo, G. Hura and T. Head-Gordon, *Biophys. J*., 2004, **86**, 1852.
269. G. Wider, R. Riek and K. Wuthrich, *J. Am. Chem. Soc*., 1996, **118**, 11629.
270. H. Huang and G. Melacini, *Anal. Chim. Acta*, 2006, **564**, 1.
271. K. E. S. Tang and V. Bloomfield, *Biophys. J*., 2002, **82**, 2876.
272. S. Kumar, K. Modig and B. Halle, *Biochemistry*, 2003, **42**, 13708.
273. R. K. Eppler, R. S. Komor, J. Huynh, J. S. Dordick, J. A. Reimer and D. S. Clark, *Proc. Natl. Acad. Sci*., 2006, **103**, 5706.
274. M. C. A. Donkersloot, *J. Solution Chem*., 1979, **8**, 293.
275. B. M. Baynes and B. L. Trout, *J. Phys. Chem. B*, 2003, **107**, 14058.
276. I. L. Shulgin and E. Ruckenstein, *Biophys. Chem*., 2005, **118**, 128.
277. I. L. Shulgin and E. Ruckenstein, *Biophys. J*., 2006, **90**, 704.
278. E. Liepinsh and G. Otting, *Nat. Biotechnol*., 1997, **15**, 264.
279. D. Martinez and J. T. Gerig, *J. Magn. Reson*., 2001, **152**, 269.
280. E. Liepinsh, P. Sodano, S. Tassin, D. Marion, F. Vovelle and G. Otting, *J. Biomol. NMR*, 1999, **15**, 213.
281. D. W. Byerly, C. A. McElroy and M. P. Foster, *Protein Sci*., 2002, **11**, 1850.
282. C. Dlavit, *J. Biomol. NMR*, 1998, **11**, 437.
283. G. Wang, *Curr. Org. Chem*., 2006, **10**, 569.
284. D. Huster and K. Gawrisch, *J. Am. Chem. Soc*., 1999, **121**, 1992.
285. L. F. Fraceto, L. de Alves Pinto, L. Franzoni, A. A. C. Braga, A. Spisni, S. Schreier and E. de Paula, *Biophys. Chem*., 2002, **99**, 229.
286. K. J. Glover, J. A. Whiles, R. R. Vold and G. Melacini, *J. Biomol. NMR*, 2002, **22**, 57.
287. A. Yoshino, T. Yoshida, H. Okabayashi, H. Kamaya and I. Ueda, *J. Colloid Interface Sci*., 1998, **198**, 319.
288. P. Westh, *Biochim. Biophys. Acta Biomembr*., 2004, **1664**, 217.
289. B. W. Koenig and K. Gawrisch, *J. Phys. Chem. B*, 2005, **109**, 7540.

290. S. E. Feller, C. A. Brown, D. T. Nizza and K. Gawrisch, *Biophys. J.*, 2002, **82**, 1396.
291. N. Niccolai, A. Ciutti, O. Spiga, M. Scarselli, A. Bernini, L. Bracci, D. Di Maro, C. Dalvit, H. Molinari, G. Esposito and P. A. Temussi, *J. Biol. Chem.*, 2001, **276**, 42455.
292. J. J. Delpuech, *Analyst*, 1992, **117**, 267.
293. C.-L. Teng, B. Hinderliter and R. G. Bryant, *J. Phys. Chem. A*, 2006, **110**, 580.
294. F. Evanics, I. Bezsonova, J. Marsh, J. L. Kitevski, J. D. Forman-Kay and R. S. Prosser, *Biochemistry*, 2006, **45**, 14120.
295. F. Evanics, P. M. Hwang, Y. Cheng, L. E. Kay and R. S. Prosser, *J. Am. Chem. Soc.*, 2006, **128**, 8256.
296. N. Niccolai, R. Spadaccini, M. Scarselli, A. Bernini, O. Crescenzi, O. Spiga, A. Ciutti, D. di Maro, L. Bracci, C. Dalvit and P. A. Temussi, *Protein Sci.*, 2001, **10**, 1498.
297. C.-L. Teng and R. G. Bryant, *J. Magn. Reson.*, 2006, **179**, 199.
298. A. K. Sunol and S. G. Sunol, in: *Handbook of Solvents*, G. Wypych, ed., William Andrew, Toronto, 2001, p. 1419.
299. M. Kanakubo, T. Aizawa, T. Kawakami, O. Sato, Y. Ikushima, K. Hatakeda and N. Saito, *J. Phys. Chem. B*, 2000, **104**, 2749.
300. M. Kanakubo, T. Umecky, C. C. Liew, T. Aizawa, K. Hatakeda and Y. Ikushima, *Fluid Phase Equilibria*, 2002, **194**, 859.
301. M. Temtem, T. Casimiro, A. G. Gil Santos, A. L. Macedo, E. J. Cabrita and A. Aguiar-Ricardo, *J. Phys. Chem. B*, 2007, **111**, 1318.
302. M. Kanakubo, T. Umecky, P. Raveendran, T. Ebina and Y. Ikushima, *J. Solution Chem.*, 2004, **33**, 863.
303. M. Kanakubo, T. Umecky, H. Kawanami, T. Aizawa, Y. Ikushima and Y. Masuda, *Chem. Phys. Lett.*, 2001, **338**, 95.
304. A. Dardin, J. M. DeSimone and E. T. Samulski, *J. Phys. Chem. B*, 1998, **102**, 1775.
305. Y. Houndonougbo, H. Jin, B. Rajagopalan, K. Wong, K. Kuczera, B. Subramaniam and B. Laird, *J. Phys. Chem. B*, 2006, **110**, 13195.
306. F. Zhao, S. Fujita, J. Sun, Y. Ikushima and M. Arai, *Chem. Commun.*, 2004, 2326.
307. S. Sala, T. Tassaing, N. Ventosa, Y. Danten, M. Besnard and J. Veciana, *ChemPhysChem*, 2004, **5**, 243.
308. S. Sala, Y. Danten, N. Ventosa, T. Tassaing, M. Besnard and J. Veciana, *J. Supercrit. Fluids*, 2006, **38**, 295.
309. R. W. Peterson and A. J. Wand, *Rev. Sci. Inst.*, 2005, **76**, 094101/1.
310. S. Gaemers, J. Groenevelt and C. J. Elsevier, *Eur. J. Inorg. Chem.*, 2001, **2001**, 829.
311. R. W. Peterson, M. S. Pometun, Z. Shi and A. J. Wand, *Protein Sci.*, 2005, **14**, 2919.
312. W. Richter and W. S. Warren, *Concepts Magn. Reson. A*, 2000, **12**, 396.
313. J. Jeener, *Concepts Magn. Reson. A*, 2002, **14**, 79.
314. R. T. Branca, S. Capuani and B. Maraviglia, *Concepts Magn. Reson. A*, 2004, **21**
315. Z. Chen, S. K. Zheng and J. Zhong, *Chem. Phys. Lett.*, 2001, **347**, 143.
316. Z. Chen, Z.-W. Chen, D. W. Hwang, J. H. Zhong and L. P. Hwang, *J. Magn. Reson.*, 2004, **171**, 244.
317. Z. Chen, Z. Chen and J. Zhong, *J. Chem. Phys.*, 2001, **115**, 10769.

CHAPTER 3

DFT Computations of Transition-Metal Chemical Shifts

Michael Bühl

Contents

Max-Planck Institut für Kohlenforschung, Kaiser-Wilhelm-Platz 1, D-45470 Mülheim an der Ruhr, Germany; Present address: School of Chemistry, North Haugh, University of St. Andrews, St. Andrews, Fife, KY16 9ST, UK

Annual Reports on NMR Spectroscopy, Volume 64
ISSN 0066-4103, DOI 10.1016/S0066-4103(08)00003-3

Abstract Probing the central metal with NMR can provide a wealth of information on the geometrical and electronic structure of transition-metal compounds. Accurate quantum-chemical computations of the salient metal NMR parameters can be a valuable complement to experiments, which are frequently plagued by low sensitivity, poor resolution or other fundamental problems, in particular for quadrupolar nuclei. Current computational approaches are mainly rooted in density functional theory and face different challenges, namely the proper choice of the exchange-correlation functional, and the treatment of relativistic, solvation and dynamical effects. This review summarizes the present state-of-the art of first-principles approaches for computation of transition-metal NMR parameters, calling special attention to the isotropic chemical shifts. Typical accuracies that can be reached for different classes of compounds are given, and illustrative chemical applications are highlighted. Corresponding results are also discussed for the full magnetic shielding and nuclear quadrupole coupling tensors, relevant for solid-state NMR spectroscopy, as well as for indirect spin–spin coupling constants involving transition-metal nuclei. In many cases, the computations can lead to a deeper understanding of the factors influencing the NMR parameters.

Keywords: transition metal NMR; density functional computations; chemical shifts; shielding tensor; spin-spin coupling

1. INTRODUCTION

Computational transition-metal chemistry remains a stronghold of DFT with all its merits and problems. While it appears to be difficult with all modern flavours of DFT to achieve quantitative accuracy for this important branch of chemistry in a systematic manner, reliable qualitative results can very often be obtained. Thus, DFT computations are being used to complement experimental studies at an increasing rate.[1,2] A huge amount of experience is now available on the ever-growing number of specific XC functionals, and on their performance in reproducing (and, thus, predicting) geometries, energies, vibrational frequencies and NMR properties of transition-metal complexes.[3] Occasionally, newly developed exchange-correlation functionals are even assessed by their performance in reproducing chemical shifts of transition-metal nuclei.[4]

Chemical shifts have been said to be sensitive to everything,[5] implying that they can depend significantly on molecular structure, temperature and solvation on the experimental side, and, in addition, to the quantum-chemical model and basis set used in computations from first-principles. Transition-metal nuclei are intriguing in that respect because their chemical shifts can be extremely sensitive to all of these factors. While typical $\delta(^{1}H)$ and $\delta(^{13}C)$ values cover just a few dozen or a few hundreds of ppm, respectively, transition-metal chemical shifts can easily span many thousands of ppm. These metals thus can act as strong looking glasses, magnifying not only the effects one wishes to study, but also the problems in computing the corresponding NMR properties.

This sensitivity can make transition-metal NMR a powerful analytical probe for diamagnetic complexes.[6,7] Widespread applications, however, are often hampered by technical problems in the acquisition of spectra for many of the NMR-active metal nuclei, problems that are typically rooted in low receptivity, low abundance and/or large quadrupole moments in cases of $I > ½$. In particular the latter issue can be a major obstacle, as signals in solution can become undetectably broad. Methodological progress and advances in spectrometer hardware continue unabated, however.[8] For instance, the use of low-viscosity solvents such as supercritical fluids has been shown to be beneficial for 'difficult' transition-metal nuclei,[9] and with the advent of high-field spectrometers it can even be possible to record and evaluate solid-state transition-metal NMR spectra in cases where detection in solution is very problematic if not impossible (see refs. 10, 11, for recent examples). It is to be expected that these and other ways to expand the current limits of transition-metal NMR spectroscopy will further the usefulness of this technique in many areas of chemistry. As a consequence, there will be a steady need for reliable tools to compute the salient NMR parameters in order to complement, interpret or precede such experiments.

Theoretical NMR properties of transition-metal complexes have been addressed in several reviews,[3,12–14] most of which are, however, rather limited in scope or in the time frame that is covered. The present review is intended to give a broad overview of the state-of-the-art in present-day DFT computations of such properties.

This review is organized as follows: First, a brief, non-technical methodological part is given, intended to familiarize the reader with the basic concepts and models involved in DFT and NMR computations, with some of the jargon that is being used by theoreticians and with the interrelation of computed quantities and observed NMR parameters. In the main body of the text, salient data from the literature are presented and discussed, selected so as to give a broad overview of the performance of the various methods for the NMR properties of all transition elements. Where available, illustrative chemical applications will be highlighted, in order to give an impression of the amount of 'extra' information (i.e., in addition to that from experiment) that can be provided by such computations. The results are ordered by rows in the periodic table, rather than by groups (i.e., by chemical similarity), because the computational requirements tend to be fairly similar within each row. For example, the necessity to take relativistic effects into account rises more steeply when going down in the periodic table than when moving across. In each section, the emphasis will be on

the isotropic chemical shifts, encompassing tensorial quantities and SSCCs where available. Finally, a brief assessment and some concluding remarks are given.

2. METHODOLOGICAL ASPECTS

Methods for computing NMR properties are relatively young players in the quantum-chemistry team. As the details of the underlying theoretical machinery have been often summarized and documented,[15,16] only some of the basic aspects of chemical-shift computations in the framework of Kohn–Sham DFT will be briefly touched. For details, the reader is referred to the original papers describing the implementations into various quantum-chemistry program packages (for instance, deMon,[17] ADF,[18] Gaussian[19] or Dalton[20]).

2.1 Shielding

Formally, and in the non-relativistic limit, the magnetic shielding tensor if a nucleus I, σ_I, is obtained as second derivative of the total quantum-mechanical energy E of a system with respect to the external magnetic field $\boldsymbol{B}$ and the magnetic momenta $\boldsymbol{\mu}_I$ of the nuclei present:[21]

$$\sigma_{I_{\alpha\beta}} = \left.\frac{\partial^2 E}{\partial \mu_{I_\alpha} \partial B_\beta}\right|_{\partial \boldsymbol{\mu}_I, \partial B = 0} \tag{1}$$

(where α and β denote the x, y or z component of the corresponding vector, and $\alpha\beta$ the xx, xy, xz etc. components of the corresponding tensor). This derivative is conveniently evaluated by means of double perturbation theory, and can in principle be formulated for any desired quantum-mechanical approximation. In order to circumvent the so-called gauge problem, one usually employs sets of gauge origins for the magnetic perturbations that are distributed over the molecular system, either at the MO level (in the IGLO or LORG approaches), or, more commonly, at the level of the atomic basis set, in the GIAO framework.[15,16,21] The tensor components of σ are obtained as sum of two parts, a diamagnetic (shielding) part, which depends only on the ground-state wave function, and a paramagnetic (deshielding) part, which depends, in addition, on the excited states, expressed in terms of the virtual (unoccupied) MOs. As with lighter nuclei, it is usually the paramagnetic part that is decisive for the actual δ(metal) value and the considerable range frequently observed for such nuclei. Individual matrix elements to these paramagnetic contributions contain integrals of the type

$$-\frac{1}{\varepsilon_\mathrm{i} - \varepsilon_\mathrm{a}} \left\langle \phi_\mathrm{i} | \hat{\mathbf{M}}_\beta | \phi_\mathrm{a} \right\rangle \left\langle \phi_\mathrm{a} | \hat{\mathbf{M}}_\alpha \boldsymbol{r}^{-3} | \phi_I \right\rangle \tag{2}$$

(where ϕ_i and ϕ_a are occupied and virtual MOs with orbital energies ε_i and ε_a, respectively, $\hat{\mathbf{M}}$ the angular operator of the magnetic perturbation in α, $\beta = x, y$ or z direction and $\boldsymbol{r}$ the position of the nth electron), which become important when the MOs involved have the proper symmetry (i.e., when they can mix upon action of $\hat{\mathbf{M}}$) and a small energetic separation (*cf.* the denominator in Equation (2)). Trends in

chemical shifts of lighter nuclei can often be rationalized on this basis, for instance for ^{13}C chemical-shift tensors in organometallic compounds,[22] but a comprehensive interpretation of metal shielding tensors is difficult, because there is usually a plethora of significant MO contributions, quite often unique to a particular structure. The occurrence of matrix elements as in Equation (2) is related to the simplified expressions derived by Ramsey in a crystal-field formalism.[23]

In standard Kohn–Sham DFT computations, σ depends on the particular XC functional and the basis set used for the expansions of the MOs through the self-consistent computation of these MOs and their energies.

As the nuclei of interest become heavier, special consideration has to be paid to relativistic effects. Fully relativistic computations employing a four-component wavefunction are very involved for molecules, even when these are small. Four-component post-HF shielding calculations for the hydrogen halides have been reported recently,[24] but these approaches are too expensive for routine application to large transition-metal complexes. Essentially all current methods that are practical for these targets are based on two-component formulations of the wavefunction, with a variety of further approximations. Variational and perturbational methods based on the Pauli scheme, as well as the ZORA approach,[25] are landmarks in the field of magnetic shielding computations and have been reviewed repeatedly.[13,26] Of these, the ZORA method is probably the one that is most routinely applied to NMR properties of transition-metal nuclei. The ZORA expressions for σ contain dynamical scaling factors, which are smaller than unity in regions close to the nuclei and approach 1 in more remote areas.

It should be noted that the popular way to include these so-called scalar relativistic effects (excluding SO-coupling, see below) into NMR computations by way of relativistically adjusted pseudopotentials or ECPs is problematic when magnetic shieldings are evaluated for a nucleus that bears an EPC. Due to the wrong nodal properties of the valence-MOs in the core region around that nucleus, only part of the magnetic response is captured, and even trends within series of compounds can be prone to significant errors.[27] This problem can be remedied by reconstruction of the all-electron currents in the core region from the ECP calculation (e.g., in the GIPAW method),[28] but this approach has not yet been widely applied to transition-metal nuclei.[29]

SO-coupling is an inherently relativistic effect, which, in the presence of a magnetic field, can induce spin polarization also in a closed-shell wavefunction. This spin polarization is 'sensed' by the NMR-active nucleus via a Fermi-contact interaction. When the NMR nucleus is in the vicinity of a heavy one, these SO effects can be transmitted between both in analogy with indirect spin–spin coupling constants.[30] When the SO contributions are neglected, so-called scalar relativistic computations are performed. In general SO effects are more important for the shieldings of lighter nuclei bonded to a heavy atom (HALA effect of the heavy atom on a light atom) than on that of the heavy nucleus itself (HAHA effect of the heavy atom on the heavy atom).[26] The parts of the HALA effect originating from scalar relativistic effects can be computed with an ECP on the heavy atom (and a suitable all-electron basis on the light atoms), e.g., for chemical shifts of lighter nuclei (^{13}C etc.) bonded to transition metals.[31,12,14]

2.2 Chemical shifts

Because it is a mixed second derivative (Equation (1)), σ is, in general, an unsymmetrical tensor with 3×3 different elements. The symmetric part, σ^{sym}, with tensor elements

$$\sigma_{\alpha\beta}^{\mathrm{sym}} = \frac{1}{2}(\sigma_{\alpha\beta} + \sigma_{\beta\alpha}) \tag{3}$$

(α,$\beta = x$, y or z) can be diagonalized, affording three orthogonal eigenvectors, which span the principal axis system of the shielding tensor, and three eigenvalues, which constitute the three principal values, usually denoted σ_{11}, σ_{22} and σ_{33}, and ordered such that $\sigma_{11} \leqslant \sigma_{22} \leqslant \sigma_{33}$ (for a recommended convention see[32]). The mean value of these is called the isotropic average, σ_{iso}. In homogeneous solution, only differences between σ_{iso} values can be measured, which are usually reported in terms of relative chemical shifts δ with respect to an accepted standard compound. To a good approximation, δ can be calculated as

$$\delta = \delta_{\mathrm{iso}} = \sigma_{\mathrm{iso}}(\mathrm{standard}) - \sigma_{\mathrm{iso}} \tag{4}$$

where σ_{iso}(standard) is the isotropic shielding of the nucleus under scrutiny in the reference compound, computed at the same level of theory. That chemical shifts are obtained as differences in magnetic shieldings is the reason for much favourable error cancellation in such computations. For instance, relativistic effects on σ values of 4d-transition-metal nuclei are significant, but since these effects are dominated by the core electrons (via the diamagnetic part[33]), they are highly transferable from one complex to the other, and cancel to a large extent in the calculated δ values.

This error cancellation can be further exploited by using a primary reference compound that is chemically more similar to the substrate under scrutiny than the accepted standard. The resulting intermediate δ values can easily be converted to the usual δ scale by adding the experimental chemical shift of this primary reference. Alternatively, σ_{iso} values computed for a larger set of compounds can be correlated with the experimental δ values in a linear regression, and the resulting σ-intercept at $\delta = 0$ can be used as σ_{iso}(standard). The disadvantage of this approach is that, in principle, the σ_{iso}(standard) value has to be re-evaluated each time a new molecule is investigated. The latter two 'indirect' methods of calculating chemical shifts are advisable when the actual standard compound is difficult or impossible to calculate (e.g., for ^{103}Rh, where there is no such accepted standard at all).

2.3 Solid-state parameters

In ordered media, anisotropies of the shielding tensor come to the fore. The most common technique in that area, solid-state NMR spectroscopy, is applicable to many transition-metal nuclei and is expected to further benefit from developments in the instrumentation (see Section 1). From analysis of the NMR lineshapes, information on two tensorial properties can be inferred, namely the chemical-shift (or CSA) and NQR tensors. Details of the effects of

quadrupolar interaction on the solid-state NMR spectra can be found in excellent monographs and reviews.[34,35] Here it will be only briefly outlined how the salient parameters can be extracted from quantum-chemical computations.

Chemical-shift tensor elements δ_{ii}, the span Ω and the skew κ, are obtained as follows:

$$\delta_{ii} = \sigma_{\mathrm{iso}}(\mathrm{standard}) - \sigma_{ii}\,(i = 1, 2, 3) \tag{5}$$

$$\Omega = \delta_{11} - \delta_{33} = \sigma_{33} - \sigma_{11} \tag{6}$$

$$\kappa = \frac{3(\delta_{22} - \delta_{\mathrm{iso}})}{\Omega} = \frac{3(\sigma_{\mathrm{iso}} - \sigma_{22})}{\sigma_{33} - \sigma_{11}} \tag{7}$$

An alternative representation of the tensor quantities can be obtained in the CSA convention according to Haeberlen, Mehring and Spiess,[36] where the principal components are ordered according to $|\delta_{yy}-\delta_{\mathrm{iso}}| \leqslant |\delta_{xx}-\delta_{\mathrm{iso}}| \leqslant |\delta_{zz}-\delta_{\mathrm{iso}}|$ (x, y, z corresponding to 1, 2 or 3, depending on the pattern) and the reduced anisotropy δ_σ and the asymmetry parameter η_σ are defined as follows:

$$\delta_\sigma = \delta_{zz} - \delta_{\mathrm{iso}} \tag{8}$$

$$\eta_\sigma = \frac{\delta_{yy} - \delta_{xx}}{\delta_\sigma} \tag{9}$$

The quadrupolar interaction is parametrized by the NQC constant C_Q and the asymmetry parameter η_Q of the EFG tensor:

$$C_Q = \frac{e^2 Q V_{zz}}{h} \tag{10}$$

$$\eta_Q = \frac{V_{yy} - V_{xx}}{V_{zz}} \tag{11}$$

where V_{xx}, V_{yy} and V_{zz} are the principal components of the EFG tensor, ordered according to $|V_{xx}| \leqslant |V_{yy}| \leqslant |V_{zz}|$, and Q is the quadrupole moment of the metal nucleus. Chemical shifts, shieldings and spans are dimensionless and are given in ppm, skews and asymmetry parameters are likewise dimensionless and adopt values between 0 and 1, while NQC constants are usually given in MHz. For conversion of computed EFG-tensor elements (which are generally printed in atomic units) into eV values, $1\ \mathrm{au} = 9.717365 \times 10^{21}\,\mathrm{V\,m^{-2}}$. For quadrupolar nuclei, the magnitude of C_Q and η_Q also govern the line widths of the isotropic NMR signals in solution when quadrupolar relaxation is dominant. In this case, the line width $\Delta\nu_{1/2}$ should be proportional to:[37]

$$\Delta\nu_{1/2} \propto V_{zz}^2 \left(1 + \frac{\eta_Q^2}{3}\right) \tau_{\mathrm{c}} \tag{12}$$

where τ_{c} is the molecular correlation time, which measures the orientational mobility of a molecule and usually increases with molecular size.

Even though the EFG is a simple expectation value and a typical ground-state property, accurate calculations require the use of large basis sets and inclusion of

electron correlation at fairly sophisticated levels.[38] Computed NQC (or EFG) parameters will not be discussed in detail, but will just be touched briefly or reported for completeness.

2.4 Isotope and temperature effects

In most routine DFT applications, shielding constants are computed for the reference and for a single static structure of the substrate, typically derived from geometry optimizations at an appropriate level of DFT or from experiment. In the former case, the computations try to model the equilibrium value δ_e, which, like the equilibrium geometry itself, is rather elusive from an experimental point of view. In practice, molecules are rotating and vibrating (even at zero K), giving rise to changes in internuclear bonding parameters from their equilibrium values. Distances in particular may be related in a rovibrational frame to temperature-dependent variations in internal displacement coordinates Δr.[39,40] Because these displacements depend also on the atomic masses, the shielding tensor is also a function of isotopic substitution in the first or more distant coordination spheres.

Thermal averaging can be modelled computationally by performing classical MD simulations (either with an empirical force field or with QM-based energy and gradient evaluations, e.g., in the CPMD approach) and averaging the computed shielding constants over a sufficient number of snapshots from the trajectories.[41] For transition-metal NMR, the CPMD-based approach has first been applied to ^{51}V chemical shifts in vanadates.[42] Quantum-mechanical zero-point corrections can be approximated by expanding the magnetic shielding function around a reference geometry (either the equilibrium structure, r_e, or the one averaged over the zero-point motion, denoted effective, r_{eff}) along suitable displacement coordinates (e.g., normal modes).[43] For the magnetic shieldings of transition-metal nuclei, the shift from the equilibrium value σ_e to the value at this effective geometry σ_{eff} (which takes the anharmonicity of the potential energy surface into account) is usually the leading correction, and effects due to the curvature of the property surface at that effective geometry tend to be much smaller.[44] Computation of effective, vibrationally averaged geometries can be effected perturbationally, and can be automated to a large extent, using information from the cubic force field of the potential energy surface $V^{(3)}$ (usually computed numerically from harmonic second derivatives) and the harmonic vibrational frequencies ω_e:[43]

$$r_{\mathrm{eff},j} = r_{\mathrm{e},j} - \frac{1}{4\omega_{\mathrm{e},j}^2} \sum_m \frac{V_{\mathrm{e,jmm}}^{(3)}}{\omega_{\mathrm{e},m}} \tag{13}$$

Because vibrational frequencies are mass-dependent, different effective geometries and shieldings are obtained for different isotopomers. Numerical computation of third derivatives is rather involved, but can now be routinely done even for medium-sized transition-metal complexes.[45]

2.5 Scalar coupling

Computation of indirect (scalar) nuclear spin–spin coupling constants[46] J_{ML} between a spin M on the metal and L on a coordinated ligand atom has blossomed recently, due to the development and validation of suitable DFT-based approaches that can evaluate the different contributions to J (Fermi-contact, diamagnetic and paramagnetic spin–orbit and spin–dipolar term) at relativistic levels.[47,13] The observability of spin–spin coupling in transition-metal NMR is often hampered by unresolved coupling patterns due to line broadening. Even though not the main focus of this review, spin–spin coupling will be touched and discussed at the appropriate places, when available. Comparisons of couplings involving different nuclei are best made using the reduced coupling constants K_{ML} (normalized via the magnetogyric ratios g of nuclei M and L):

$$K_{ML} = \frac{4\pi^2}{h} \times \frac{J_{ML}}{\gamma_M \gamma_L} \tag{14}$$

3. 3d-METALS

3.1 Scandium

A joint solid-state ^{45}Sc NMR and DFT study of a number of scandium complexes has been reported recently, comprising $Sc(acac)_3$, $Sc(THMD)_3$, $Sc(NO_3)_3 \cdot 5H_2O$ (presumably modelled as *cis*-$[Sc(\eta^2\text{-}NO_3)_2(H_2O)_2]^+$ in the DFT computation), $Sc(OAc)_3$ (probably modelled as $[Sc(\eta^1\text{-}OAc)_6]^{3-}$), $ScCl_6 \cdot 6H_2O$ (probably modelled as *trans*-$[ScCl_2(H_2O)_4]^+$), *mer*-$ScCl_3(THF)_3$ and $ScCp_3$ (modelled as $[Sc(\eta^5\text{-}Cp)_3(\eta^1\text{-}Cp)]^-$).[48] The computations have been performed employing X-ray-derived geometries (with optimized H-positions), and δ_{iso} values have been referenced to a fully optimized $[Sc(H_2O)_6]^{3+}$. Tensor parameters obtained at the HF/6-311G** level appear to fit better to experiment than those computed at B3LYP/6-311+G**. However, the results have not been corrected for long-range electrostatic effects, which are known to be important already for lighter nuclei.[49] Selected results for monomeric neutral complexes (where such electrostatic effects should be minimal) are given in Table 1. In general, the orientations of the chemical-shift tensors are comparable between HF and DFT levels and are consistent with experiment.[48]

3.2 Titanium

A systematic performance study DFT methods for $\delta(^{49}Ti)$ has been reported, encompassing TiX_4 (X = Cl, Br, F), $TiCl_nMe_{(4-n)}$ (n = 0–3), $TiCp_2X_2$ (X = F, Cl, Br) and $[Ti(CO)_6]^{2-}$.[50] In this study, the first computed zero-point corrections to relative chemical shifts of a transition metal have been reported (after this methodology had been tested on absolute magnetic shielding constants of some 3d metals).[44] Very small zero-point corrections to $\delta(^{45}Ti)$ have been found, on the

Table 1 DFT-computed and experimental chemical-shift and NQC tensor elements for the metal nuclei (in boldface) in selected 3d-transition metal complexes[a]

Molecule	Method	δ_{iso}	Ω	κ	C_Q	η_Q	Ref.
^{45}**Sc**(acac)$_3$	B3LYP/6-311G**	102	95	−0.67	−12.3	0.40	48
	Experiment	82(1)	70(10)	−0.7(2)	13.0(3)	0.22(3)	48
^{45}**Sc**Cl$_3$(THF)$_3$	B3LYP/6-311G**	303	317	−0.26	10.0	0.35	48
	Experiment	202(1)	200(20)	−0.1(3)	8.4(2)	0.30(5)	48
^{51}**V**(VCPO)[b]	B3LYP/6-31+G*	−607	−551[c]	0.3[d]	9.5	0.51	56
	Experiment	−508	−520(13)[c]	0.4(5)[d]	10.5(15)	0.55(15)	10
^{51}**V**O$_2$(acpy-inh)	B3LYP/6-311+G	−746	546[c]	0.07[d]	−9.5	0.35	58
	Experiment	−504(2)	485(29)[c]	0.25(5)[d]	7.00(5)	0.25(5)	58
(^{51}**V**Oquin$_2$)$_2$O	B3LYP/6-311+G	−792	486[c]	0.12[d]	8.0	0.34	58
	Experiment	−510(2)	433(28)[c]	0.30(15)[d]	5.67(25)	0.45(5)	58
Al^{51}**V**O$_4$ *V*(1)[e]	GIPAW-PW91	−738	−96[c]	0.55[d]	2.17	0.94	62
	Experiment	−744(1)	−120(6)[c]	0.72(10)[d]	2.35(3)	0.93(3)	60
^{55}**Mn**Cp(CO)$_3$	B3LYP/II′	−2,009[f]	1,011	0.89	73.5	0.02	g
	ZORA-BP86/TZ2P	−2,155	567	0.80	66.3	0.01	69
	Experiment	−2,200(10)	920(10)	0.95(5)	64.3(5)	0.02(2)	69
^{55}**Mn**$_2$(CO)$_{10}$	B3LYP/II′	−2,282[f]	381	1.00	5.9	0.00	g
	Experiment	−2,288(2)	105(10)	0.95(5)	3.28(5)	0.35(2)	69

^{59}**Co**(acac)$_3$	B3LYP/II′	11,670	679	−0.97	2.17	n.a.	89
	B3LYP/6-31G*	11,158[h]	915	−0.39	n.a.	n.a.	88
	Experiment	12,498(5)	1,174(13)	−0.57(5)	5.53(7)	0.22(6)	86
[^{59}**Co**(CB)$_2$]$^{-i}$	B3LYP/II′ (*trans*)	−1,843[j]	6,086	0.78	241.8	0.00	g
	B3LYP/II′ (*cis*)	−2,042[j]	5,697	0.76	223.2	0.04	g
	Experiment	−2,000(75)	4,700(100)	1.0	163(2)	0.12(5)	11
^{67}**Zn**(OAc)$_2$	B3LYP/6-311G*	104[k]	n.a.	n.a.	8.36	n.a.	98
	Experiment	67	n.a.	n.a.	8.25	n.a.	98

[a]For definition of the tensorial quantities see Section 2.3; δ and Ω in ppm, C_Q in MHz.
[b]V-containing enzyme; computed data for model protonated at O^3 and O^4 (see Figure 1) and the largest QM-region.
[c]CSA tensor element δ_σ.
[d]CSA tensor element η_σ.
[e]V(1) site, using experimental cell parameters and optimized atomic positions.
[f]From ref. 66.
[g]M. Bühl, unpublished; $Q(^{55}\text{Mn})$ and $Q(^{59}\text{Co})$ taken as 33.0 and 42.0 fm^2, respectively.
[h]Calculated from the reported σ value relative to that of site 1 in $[Co(CN)_6]^{3-}$.
[i]CB = 1,2-$C_2B_9H_{11}$.
[j]From ref. 91.
[k]Scaled value.

order of 10 ppm. After some early success of the HF method for ^{45}Ti chemical shifts in the $TiCl_nMe_{(4-n)}$[51] and TiX_4 (X = F, Cl, Br, I) series,[52] DFT methods have been shown to be somewhat more accurate when Cp and carbonyl complexes are considered as well. A comparable performance of GGA and hybrid functionals has been noted,[50] and the $\delta(^{45}Ti)$ values for Cp and CO complexes are marginally improved upon inclusion of classical thermal effects via CPMD.[53] A slightly improved performance has been noted when geometries are optimized with B3LYP rather than with a GGA, when chemical shifts are computed using smaller basis sets and when unspecific solvent effects are included in a PCM approach.[54] Apparently, a somewhat better, fortuitous error cancellation is possible with this approach, affording mean absolute deviations between theory and experiment on the order of 70 ppm over a shift range of *ca*. 2,700 ppm. No clear-cut trend has been found between computed EFG and line widths (*cf*. Equation (12)), suggesting that other factor such as correlation times (possibly also adduct formation with a nucleophilic solvent) are decisive for the line widths.[50]

3.3 Vanadium

In a current review on ^{51}V NMR spectroscopy, DFT computations of salient parameters have been covered in detail for this nucleus.[55] Thus only recent applications are highlighted here. For a large set of small oxovanadium(V) complexes modeling the active site of a vanadium-containing enzyme, VCPO, the computed CSA and NQC tensor components have been compared to the corresponding quantities derived experimentally for the actual enzyme.[10] This comparison can provide insights into details of protonation state of the central vanadate moiety and the hydrogen-bond network around this active site, information that is not available from the positions of the heavy atoms, as previously obtained by X-ray crystallography in a VCPO single crystal. Of the 86 optimized model complexes, just 16 were found to match the experimental tensorial ^{51}V NMR data reasonably well (within 15–20% of the respective values). Recently, these data have been refined in a QM/MM framework for realistic models, taking the full protein environment into account.[56] Starting from the heavy-atom coordinates in the solid and after careful equilibration in constrained classical MD simulations, several models have been optimized, in which with the protein and solvent environment, described by a suitable classical force field, is coupled to a central region treated at the DFT level (BP86 functional). The NMR properties have been computed for the latter quantum-mechanical region, including the long-range electrostatic interactions of the surrounding protein in the form of point charges. It has turned out that, for large enough QM regions, the protein environment affects the ^{51}V NMR properties not so much via such direct electrostatic effects, but rather by providing a scaffold that determines the local coordination geometry about vanadium. Effects of specific geometrical parameters (bond distances, bond angles) on computed isotropic $\delta(^{51}V)$ values of simple vanadates had been found to be noticeable in some cases,[42,57] but rather small for vanadium(V) complexes in general (as evidenced, e.g., by relatively small shielding/bond-length derivatives).[53] Likewise, the isotropic ^{51}V chemical

shifts computed for the various QM/MM models of VCPO have shown little variation.[56]

The tensor elements, however, have proven to be more variable between models and are, thus, of considerable diagnostic value. Of the 12 models tested, three have afforded good accord with experiment (see Figure 1 and Table 1 for the actual numbers for one of these; the latter table also includes some selected examples of tensor elements for smaller vanadium complexes[58]). The same VCPO models had been identified previously as promising candidates on the basis of computed energies.[59] That these models can also reproduce the experimental NMR parameters provides compelling evidence that it is indeed one of them (or an equilibrium mixture) that is the actual resting state of the enzyme. This is a very nice example of how protein X-ray crystallography, solid-state NMR spectroscopy and QM/MM-computations of energies and NMR parameters can team up to unravel structural details of the active site of an enzyme.

For a seemingly simple aluminium vanadate, $AlVO_4$, the solid-state ^{51}V NMR signals[60] have been assigned to the three specific crystallographic vanadium sites in the solid, according to the best fit of observed and theoretical EFG parameters.[61] Recently, this assignment has been corroborated by calculations of the ^{51}V chemical shifts and CSA tensor parameters.[62] Both EFG and NMR parameters have been computed for the full, periodic crystal, including partial or fully optimized ionic positions in the crystal. As far as the NMR properties are concerned, this is the first application of periodic NMR computations to a transition-metal nucleus. For one of the vanadium sites, theoretical and experimental data are included in Table 1.

3.4 Chromium

A systematic study of isotropic ^{53}Cr chemical shifts has been presented for $[CrO_4]^{2-}$, $[Cr_2O_7]^{2-}$, $[CrO_3X]^-$, CrO_2X_2 (X = F, Cl) and $Cr(CO)_5L$ (L = CO, PF_3, $CHNH_2$, $CMeNMe_2$).[63] The $\sigma_{standard}$ values have been evaluated from $\sigma_{calc}-\delta_{exp}$ correlations. A GGA has proven superior to B3LYP in the NMR calculations, with

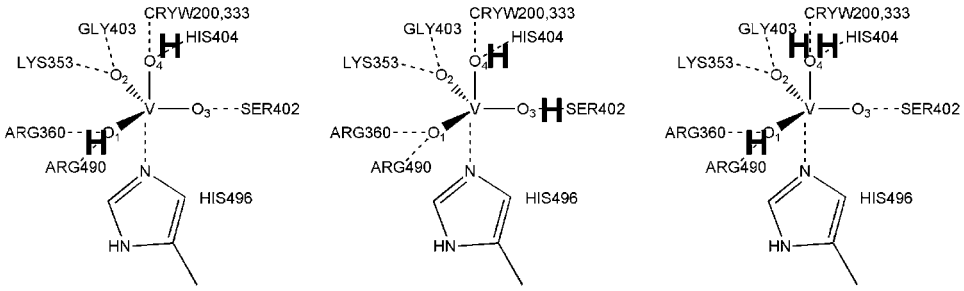

Figure 1 Schematic representation of the three models identified in ref. 56 that show good accord between QM/MM-computed and observed ^{51}V NMR chemical-shift and NQC tensors; protons attached to the central VO_4^{3-} moiety are highlighted in boldface.

mean absolute deviations for the former of *ca*. 50 ppm over a total shift range of *ca*. 2,100 ppm. Computed EFGs can be useful for the interpretation of linewidths in selected cases and for predicting if ^{53}Cr resonance of a given compound could be detectable. Thus, the ^{53}Cr NMR signal of $Cr(C_6H_6)_2$ should be observable at $\delta = -178$, those of quadruply bonded dichromium species should appear in a strongly deshielded region between $\delta \approx 3{,}300$–$4{,}600$, but are likely to be undetectably broad.

It is known for 3d metals that relativistic effects, while noticeable for the magnetic shieldings σ, cancel to a large extent for relative δ values.[13] Specifically, it has been shown that the $\delta(^{53}Cr)$ value of $Cr(CO)_6$ (relative to $[CrO_4]^{2-}$) changes only by *ca*. 20 ppm on going from a non-relativistic calculation to a scalar relativistic treatment (both for a more approximate two-component Pauli Hamiltonian and the more reliable ZORA method).[64,65]

3.5 Manganese

A systematic performance test has been reported for isotropic ^{55}Mn chemical shifts of $[MnO_4]^-$, $[Mn(CO)_6]^+$, $Mn_2(CO)_{10}$, $Mn(CO)_5X$ {X = H, Cl, C(O)Me}, $[Mn(CO)_5]^-$, $Mn(NO)_3(CO)$ and $MnCpL_x$ {L_x = $(CO)_3$, C_6H_6, C_7H_8}.[66] Hybrid functionals have been found to perform best, with a mean absolute deviation of *ca*. 200 ppm over a total shift range of nearly 4,000 ppm. The $\sigma_{standard}$ values were again evaluated from σ_{calc}–δ_{exp} correlations. Systematic deviations from experiment were encountered when the δ values were directly referenced to $[MnO_4]^-$ as model for the actual standard, 1 M aqueous $KMnO_4$. These deviations were first interpreted as evidence for the importance of solvation effects in the latter, polar solvent, because all other organometallic species had been recorded in inert organic solvents, for which much smaller solvent effects would be expected. Subsequent CPMD-based simulations of aqueous $[MnO_4]^-$, however, have afforded only a small effect of thermal averaging and solvation on the σ(Mn) value, namely a deshielding of 36 ppm.[67] The actual solvation effect has turned out to be very small, as essentially the same deshielding is found upon thermal averaging in the gas phase. Comparable numbers have been obtained for the gas phase when hybrid-DFT-based molecular dynamics simulations with classical propagation of the nuclei are performed,[68] or when the shielding constant is averaged over the quantum-mechanical zero-point motion.[44]

The corresponding thermal effects have turned out to be much larger for typical organomanganese complexes than for permanganate ion. For instance, upon going from the equilibrium to the CPMD-based average values, $\delta(^{55}Mn)$ tends to increase relative to $[MnO_4]^-$ by *ca*. 200–300 ppm in carbonyl complexes, which improves the accord with experiment in most cases.[53] The corresponding thermal deshielding for $MnCp(C_7H_8)$ amounts to more than 600 ppm, a value which is probably too large, as it results in a significant overestimation of this $\delta(^{55}Mn)$ value at the deshielded end, and leads to a deterioration of the whole $\delta_{calc}/\delta_{exp}$ correlation. Typical mean absolute errors for equilibrium (fitted standard) or thermally averaged ^{55}Mn chemical shifts (relative to $[MnO_4]^-$) are on the order of 200 ppm, over a total shift range covered of *ca*. 4,000 ppm.

The remarkable deshielding of the ^{55}Mn resonance in MnCp(C_7H_8) ($\delta = 1{,}077$) vs. that in MnCp(C_6H_6) ($\delta = -180$) is ascribed to a marked energetic lowering of the unoccupied MOs on going from the latter to the former.[66] The reduced energy gap between the magnetically coupled MOs results in enhanced paramagnetic contributions (*cf*. Equation (2)), consistent with the observed deshielding. Due to the symmetry properties of the involved MOs, these paramagnetic contributions are not isotropic, but are largest perpendicular to the axis passing through the metal and the Cp midpoint (*z*-axis in Figure 2).

As a consequence, huge anisotropies have been predicted for these two Cp complexes, with Ω exceeding 7,000 ppm (difference $\delta_{11}-\delta_{33}$ in Figure 2). Very recently, tensor elements in manganese carbonyl complexes have been obtained from solid-state ^{55}Mn NMR spectroscopy.[69,70] Small anisotropies have been found for octahedral pentacarbonyl complexes,[70] but a sizeable span of 920 ppm is obtained for the piano-stool complex MnCp$(CO)_3$.[69] The latter number is reasonably well reproduced with popular DFT methods (Table 1). Due to the strong backbonding from the carbonyl ligands, the metal d-character is smaller and the occupied–virtual MO separation is larger than in the sandwich complexes in Figure 2, consistent with the higher shielding and reduced anisotropy in the carbonyl complex. The same characteristics, MO energies and metal d-character, have also been found to be important for the paramagnetic contributions that determine the trends in the individual principal components, for instance on going from $Mn(CO)_5Cl$ to $Mn(CO)_5Me$.[70]

3.6 Iron

^{57}Fe is one of the first transition-metal nuclei, for which DFT-based chemical shifts have been validated systematically,[71] and it is the one for which the

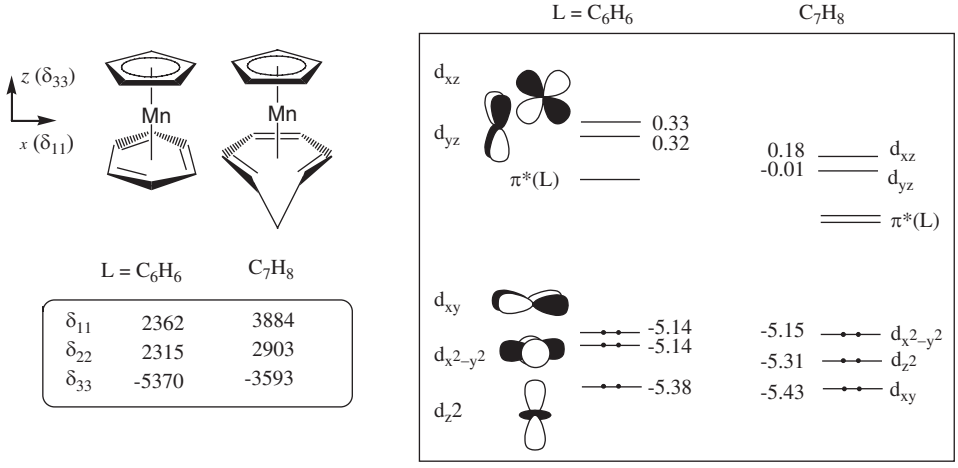

Figure 2 Left: principal components of the chemical shift tensor and the orientation of the principal axis system of manganese Cp complexes. Right (in box): sketch of MO scheme including B3LYP/II' eigenvalues (in eV) of d(Mn)-based MOs. (adapted from ref. 66.)

influence of a particular exchange-correlation functional appears to be most pronounced.[72] Inclusion of HF exchange, i.e., the use of a hybrid functional, is particularly beneficial in this case, an effect which has been analyzed in detail in a case study on ferrocene.[73] Performance tests have been conducted for a test set comprising $Fe(CO)_4L$ (L = CO, CH_2=CH–OMe, CH_2=CH–CN), $Fe(CO)_3L'$ (L′ = cyclobutadiene, butadiene, CH_2=CH–CH=O), $FeCp(CO)_2R$ (R = Me, *i*Pr) and ferrocene. Employing the B3LYP functional and GGA-optimized geometries, mean absolute deviations from observed $\delta(^{57}Fe)$ values are on the order of 100 ppm for this test set, over a shift range of *ca*. 2,100 ppm.[72,53]

A somewhat larger mean error (*ca*. 140 ppm) has been found for a different test set of neutral and cationic iron Cp complexes (spanning *ca*. 2,400 ppm), when both geometries and chemical shifts are computed at the B3LYP level.[74] A problem in this case may be the fact that B3LYP tends to overestimate metal–ligand bond distances for 3d-transition-metal complexes in general,[75] and for ferrocene in particular.[76] Nevertheless, ^{57}Fe chemical shifts can be computed routinely and reliably at the B3LYP level, and such computations are being used to complement experimental ^{57}Fe NMR studies, for instance for isocyanoferrocene or the tetrahedrane-type cluster $[Fe_2(CO)_6(\mu\text{-SNH})]$ (Scheme 1).[77] In the latter study, additional confidence in the structural assignment has been provided by the good agreement between computed and observed $^1J(^{57}Fe,^{13}C)$ coupling constants (better than 3 Hz or *ca*. 12%). Equilibrium $\delta(^{57}Fe)$ values have also been used as evidence that the intramolecular Fe···H interaction in ferrocenylmethanol (Scheme 1) is very weak.[78]

^{57}Fe chemical shifts, tensor components and electric field gradients have been reported for iron porphyrins and cytochrome-*c* and CO–myoglobin model systems, validating hybrid-DFT methods on a chemical-shift range of this nucleus that exceeds 10,000 ppm.[79] $\delta(^{57}Fe)$ values have further been used in a theoretical refinements of geometrical parameters (ligand tilt and bending angles) in a CO myoglobin and in other Fe-porphyrins.[80]

In context with empirical correlations between transition-metal chemical shifts and reactivities,[7] one such correlation, namely between $\delta(^{57}Fe)$ and carbonyl insertion barriers in $FeCp(CO)_2R$ (R = alkyl), has been rationalized in terms of larger paramagnetic contributions from the Fe–C sigma bond as the bulkiness of R increases, and concomitant decrease in the strength of that bond.[71] A general common trend has been noted between computed ^{57}Fe chemical shifts in Cp-substituted $FeCp(CO)(PH_3)Me$ model complexes and rate-limiting barriers for silane alcoholysis at catalytic centers derived from these precursors.[81] If such a trend or a correlation would also hold for the real systems with bulkier

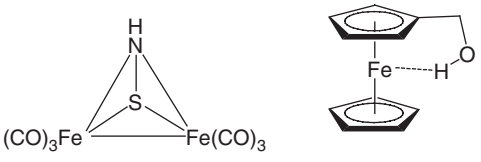

Scheme 1.

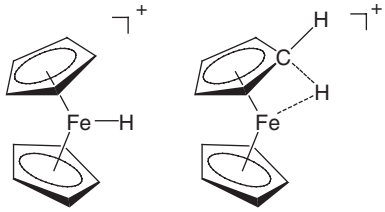

Scheme 2.

phosphine ligands, a screening of potential catalysts could be affected by ^{57}Fe NMR spectroscopy.

An interesting application of ^{57}Fe chemical-shift computations is protonated ferrocene, which has defied precise structural characterization so far. From ^{1}H NMR spectroscopy it is evident that the system is highly fluxional, and two distinct species are believed to be involved in rapid rearrangements, namely a metal-protonated and a ring-protonated (or agostic) form (Scheme 2). DFT-computed $\delta(^{1}H)$[82] and $\delta(^{57}Fe)$ values[74] of these isomers have been found to bracket the respective experimental numbers by a wide margin, suggesting that a roughly equimolar mixture of both forms could actually be present in rapid equilibrium. This possibility has been explored by explicit MD simulations on several DFT-derived potential energy surfaces.[76] Details of these surfaces and, thus, the course of the respective MD on them can depend noticeably on intricacies such as the particular choice of exchange-correlation functional or basis set. In general, rearrangements via proton migrations and Cp ring rotations are observed within few picoseconds, consistent with the fluxional character on the NMR time scale. When the magnetic shieldings (computed at the B3LYP level) are averaged along the trajectories, good accord with the experimental ^{57}Fe chemical shift is indeed found for MD trajectories that sample both isomers with comparable frequency. At the same time, the corresponding, averaged $\delta(^{1}H)$ values appear to be in favour of an agostic form as the predominant component of such a mixture.[76] Assessing chemical shifts as thermal averages over reactive MD trajectories is a stringent test for the underlying theoretical models, a test that DFT methods have yet to pass for protonated ferrocene.

Highly charged iron cyanide complexes have turned out to be excellent model systems for the computational study of solvent effects. The observed shielding of the ^{57}Fe nucleus by *ca*. 450 ppm upon going from $[Fe(CN)_6]^{4-}$ to $[Fe(CN)_5(NO)]^{2-}$ in aqueous solution[83] has been modelled with two MD-based approaches, one using CPMD simulations in a small periodic box,[84] and one involving single complexes coupled to a large surrounding water cluster in a QM/MM scheme.[85] The different setup of the two computational procedures is illustrated in Figure 3.

For the dianionic nitrosyl complex, both procedures give similar results close to the experiment.[84] For the parent tetraanion, the CPMD-based approach appears to be plagued by artefacts due to the small box size that could be employed, and the non-periodic QM/MM-based protocol is preferable in this case.[85] Large solvation effects on $\delta(^{57}Fe)$ of $[Fe(CN)_6]^{4-}$, on the order of

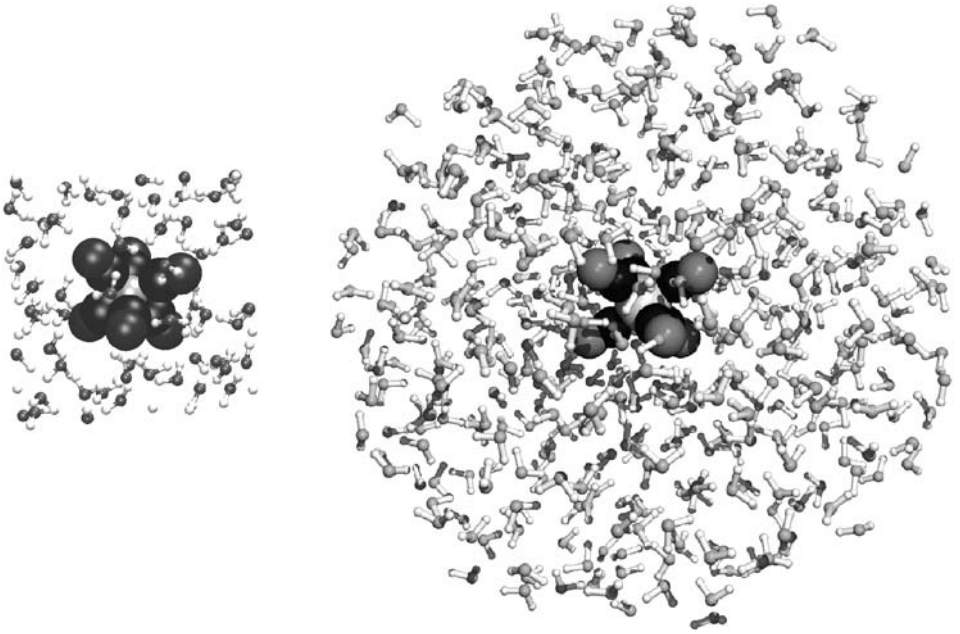

Figure 3 Snapshots from MD-simulations of $[Fe(CN)_6]^{4-}$ in water (using space-filling and ball-and-stick representation for solute and solvent, respectively). Left: unit cell of a CPMD-simulation with periodic boundary conditions; right: QM/MM-based MD with a large water cluster. (taken from the trajectories analyzed in ref. 84.)

2,000 ppm, have been obtained, and have been traced back to substantial solvation effects on the Fe–C bond distance (which shrinks by more than 6 pm upon hydration), together with an exceptional sensitivity of the metal shielding constant on this parameter (with a computed shielding/bond-length derivative exceeding $-350\,\mathrm{ppm\,pm^{-1}}$).[85] It is noteworthy that for this complex, the major part of the solvation effect is geometric in nature, as the change in shielding constants as direct response of the electronic wavefunction to the presence of the surrounding water molecules is indicated to be rather small.

3.7 Cobalt

Early computations of ^{59}Co NMR parameters have been reviewed in the year 2000.[86] As with ^{57}Fe, it had been noted almost from the onset that hybrid functionals such as B3LYP outperform pure GGAs for ^{59}Co chemical shifts.[87,88] A typical test set (employed in a recent study)[89] comprises complexes of the type $[Co(CN)_6]^{3-}$ (model for the standard), $CoH(CO)_4$, $[Co(CO)_4]^-$, $CoCp(C_2H_4)_2$, $Co(NH_3)_3(CO)_3$, $Co(acac)_3$, $[CoL_6]^{3+}$ ($L = H_2O$, NH_3) and $[Co(NH_3)_4CO_3]^+$, covering *ca*. 19,000 ppm of isotropic chemical shifts, all but the total range for ^{59}Co. Employing GGA-optimized geometries and the B3LYP functional in the NMR part, mean absolute deviations from the experimental isotropic $\delta(^{59}Co)$

values are on the order of *ca*. 500–700 ppm for this test set,[89] or *ca*. 3–4% of the total shielding range.

Owing to the rather favourable NMR properties of the ^{59}Co nucleus (at least compared to other transition metals), not only a huge body of solution NMR spectra is available, but also a sizeable amount of chemical-shift tensors is known from solid-state NMR studies.[86] Errors in computed tensor element appear to be somewhat larger than those in the isotropic shifts, presumably due to the neglect of intermolecular interactions in the gas-phase calculations. Nevertheless, trends are usually captured very well in such calculations, which can be useful for interpretative purposes, for instance in a study of electronic effects of remote substituents on the ^{59}Co shielding tensor in porphyrine derivatives (Scheme 3).[90]

With modern high-field NMR spectrometers, solid-state spectra can even be refined in cases where no signal can be recorded in solution because of excessive quadrupolar line broadening. A nice example is the cobaltacarborane $[Co(C_2B_9H_{11})_2]^-$,[10] the isotropic $\delta(^{59}Co)$ value of which has been predicted only recently.[91] In this case, the computed ^{59}Co chemical shift can depend noticeably on the mutual orientation of the two dicarbollide ligands (Scheme 3). Some selected tensor properties are included in Table 1.

For the Co complexes in Table 1, the computed NQC constants appear to be somewhat less accurate than for other metal nuclei. EFG computations may thus be less reliable for this metal. In this context it may be noted that also no general relationship between computed EFGs and ^{59}Co line widths has been found,[89] although such correlations may be apparent in closely related families of compounds, for instance Co porphyrine derivatives.[92]

An attempted structural application for fluxional dicobaltoctacarbonyl, $Co_2(CO)_8$, has met with little success: Despite significant structural differences between the three minima on the potential energy surface (Scheme 4), little discrimination is apparent in terms of the computed isotropic $\delta(^{59}Co)$ values.

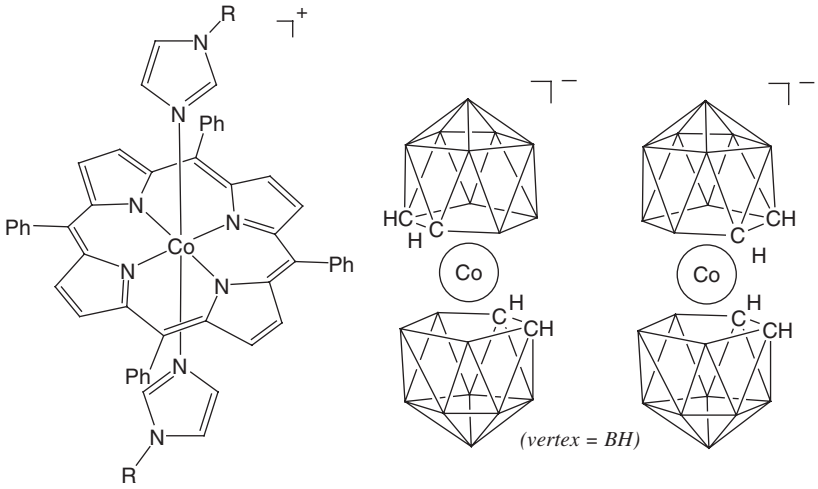

Scheme 3.

As these values are all within 200 ppm of experiment,[89] they cannot provide information concerning the presence or absence of any of these isomers in the equilibrium mixture.

The aforementioned test sets for ^{59}Co chemical-shift computations contain highly charged ions (triply negative or positive), which — in the experiments — are commonly investigated in aqueous solution. Even though large solvation effects are to be expected in these cases, static calculations in the gas phase already seem to reproduce the experimental data reasonably well.[87,88,89] Thermal and solvent effects on ^{59}Co chemical shifts have recently been studied in detail.[93] The CPMD- and QM/MM-based protocols that had been previously applied to ^{57}Fe chemical shifts[84] (see preceding chapter) have been validated for a small set of ionic Co complexes (Scheme 5), together with quantum-mechanical zero-point corrections in the gas phase and in a simple polarizable continuum.

$[Co(CN)_6]^{3-}$ is a model for the actual standard, aqueous $K_3[Co(CN)_6]$. As with the isoelectronic hexacyanoferrate complex, thermal averaging and solvation strongly affects the metal–ligand bond distance in this model and, concomitantly, the ^{59}Co shielding constant. The close relation between both parameters is illustrated in Figure 4. The slope of the linear fit, that is, the shielding/bond-length derivative, is $-285\,\mathrm{ppm\,pm^{-1}}$, or $-48\,\mathrm{ppm\,pm^{-1}}$ per bond. These values are very close to those computed directly for the pristine ion,[88,89] but smaller than an empirical estimate ($-75\,\mathrm{ppm\,pm^{-1}}$ per bond).[94] Incidentally, the σ value averaged over the CPMD trajectory in water is $-5{,}475$ ppm, in excellent agreement with an experimental estimate for σ of the standard, $-5{,}400$ ppm.[95]

Thermal and solvent effects on relative δ values for the other ions in this smaller test set are also substantial, but are of opposite sign and tend to cancel to a large extent.[93] For instance, on going from the equilibrium value to the thermal average in the gas-phase, $\delta(^{59}\mathrm{Co})$ in the hexaquo relative to the hexacyano

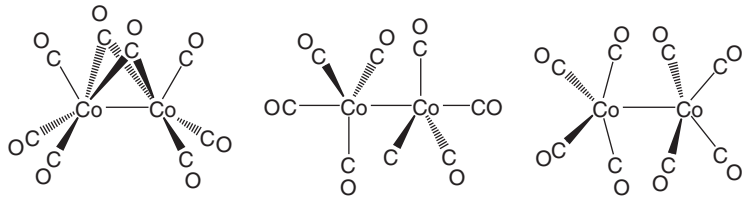

Scheme 4.

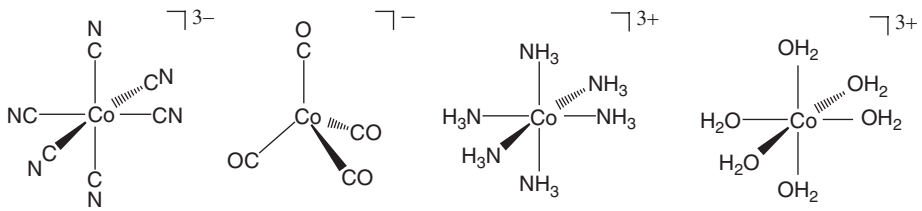

Scheme 5.

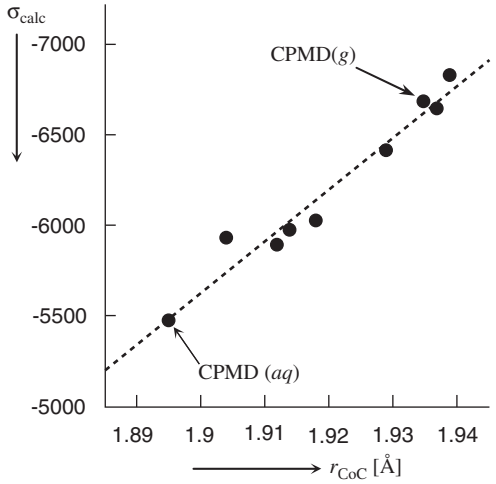

Figure 4 Plot of B3LYP computed ^{59}Co shielding constant in $[Co(CN)_6]^{3-}$ vs. the Co–C distance, as obtained in a number of static and dynamic calculations in the gas phase (g) and in aqueous solution (aq). CPMD-based results are labelled in order to highlight the solvent effect. (data taken from ref. 93.)

complex increases from *ca*. 16,200 to 17,700 ppm,[89] and decreases again to *ca*. 15,700 ppm upon thermal averaging in water[93] (experiment: 15,100 ppm).

Quantum-mechanical zero-point corrections to geometries and ^{59}Co chemical shifts are qualitatively similar to the classical thermal effects evaluated from MD simulations, but are usually smaller in magnitude.[89,93] Because these zero-point corrections depend on the atomic masses, they can be used to compute isotope effects, which are not accessible from simple geometry optimizations. Fairly subtle isotope effects on ^{59}Co chemical shifts can be reproduced with such an approach. Due to the high sensitivity of the ^{59}Co nucleus, only small geometric changes have to be induced in the immediate ligand environment about the metal upon remote isotopic substitution in order to account for the observed effects (e.g., on the order of 0.001 Å change in the metal–ligand distances, Table 2).

With the advent of ever stronger magnetic fields in NMR spectroscopy, the question arises as to what extent the values of the shielding constants (in ppm) are becoming dependent on the field strength. For $Co(acac)_3$ and $[Co(NH_3)_6]^{3+}$, this dependence has been computed specifically by implementing an analytical response formulation for the expressions for σ to the external field.[96] The resulting values are on the order of ppb T^{-2}, about one order of magnitude smaller than experimental estimates, corresponding to changes in $\sigma(^{59}Co)$ of a few ppm on a 900 MHz spectrometer.

3.8 Nickel

In keeping with the paucity of experimental ^{61}Ni NMR data and the limited use of this NMR nucleus for analytical purposes, corresponding chemical-shift

Table 2 Isotope effects on $\delta(^{59}Co)$ and r(Co–N) distance in two cobalt complexes, evaluated at B3LYP and BP86 levels, respectively

Complex/property	$(\delta,r)_e$[a]	$(\delta,r)_{eff}$[b] (X = H)	$(\delta,r)_{eff}$[b] (X = D)	$^n\Delta$
$[Co(NX_3)_6]^{3+}$ [c]				
δ_{calc}	8,491	9,010	8,905	−105
δ_{expt}		8,176	8,075	−101
$r(Co\text{-}N)_{calc}$	2.032	2.047	2.045	
$[Co(Xdmg)_2(py)Me]$[d]				
δ_{calc}	3,362	3,211	3,276	+65
δ_{expt}		3,645	3,700	+55
$r(Co–N)_{calc}$	1.910	1.911	1.912	

Note: In boldface: change in $\delta(^{59}Co)$ upon substitution of H with D.
[a]Equilibrium value.
[b]'Effective' value at 0 K, which contains the leading effect due to the vibrationally averaged geometry.
[c]From ref. 93.
[d]Computations for the glyoximato parent, from ref. 89.

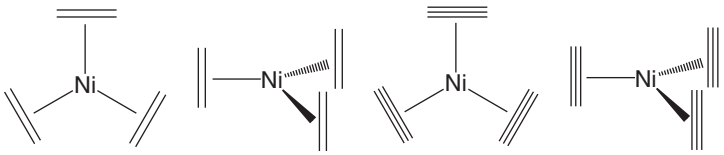

Scheme 6.

computations are scarce. DFT-derived ^{61}Ni chemical shifts have been reported for $Ni(C_2H_4)_3$ and $Ni(C_2H_2)_3$ in two different conformations (Scheme 6).[97] The strong upfield shift of the ^{61}Ni resonance of more than −1,800 ppm upon going from the all-perpendicular to the (more stable) all-in-plane arrangement has been taken as evidence for the presence of strong diatropic ring currents in the latter and, thus, as support for homoconjugation between non-bonded C atoms in the planar forms.[97] That such ring currents can give rise to effects this large, however, may be doubted. Ring-current induced shieldings or deshieldings affect all nuclei by the same amount (in ppm), which is usually a few to a few dozen ppm at most.

3.9 Copper and zinc

The first DFT-derived ^{63}Cu NMR parameters have been published only recently. Isotropic ^{67}Zn chemical shifts and NQC constants have been computed for biomimetic zinc complexes and fragments of extended solids, and have been compared to the corresponding solid-state NMR data (which for the most part have become available only recently).[98] In order to model polymeric solids, nearest-neighbour effects have been included via suitable point charges, the

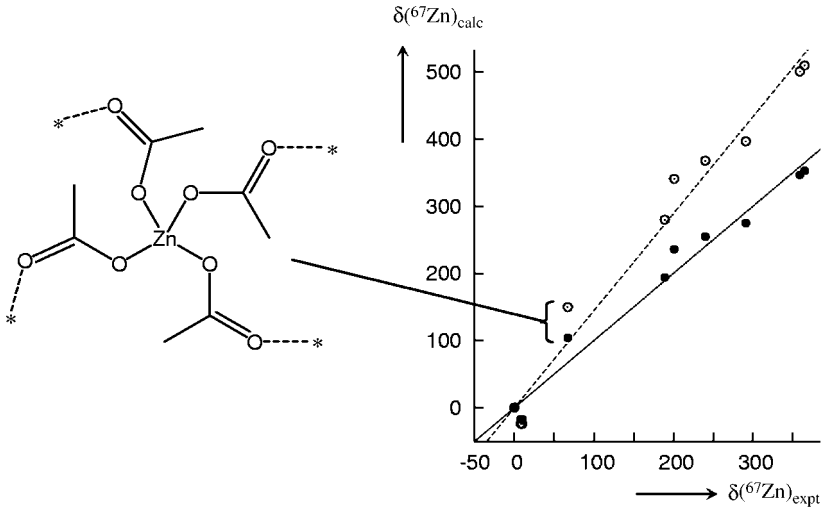

Figure 5 Left: Schematic model for solid $Zn(OAc)_2$, including point charges (denoted by asterisks) at positions of nearest-neighbour Zn atoms. Right: Plot of computed vs. experimental isotropic ^{67}Zn chemical shifts of various solids; open circles: unscaled values, filled circles: scaled by 1/1.445. (data taken from ref. 98.)

values of which have been determined in a self-consistent manner. For instance, solid $Zn(OAc)_2$ has been modelled as a $[Zn(OAc)_4]^{2-}$ complex surrounded by four point charges at the positions of the four nearest Zn ions in the lattice (see left-hand side of Figure 5).

With this approach, the observed NQC constants are very well reproduced over a wide range of coordination environments comprising various combinations of O-, N- and S-donors (see Table 1 for a representative example). The qualitative trends in the isotropic $\delta(^{67}Zn)$ values are well captured in the calculations, but the substituent effects are significantly overestimated at the chosen level (B3LYP), and scaling by a factor of *ca*. 0.7 is necessary to obtain good accord with experiment[98] (right-hand side of Figure 5b). NQC constants have also been computed for three models of human carbonic anhydrase (at an undisclosed level, however — presumably Hartree–Fock). In conjunction with the experimental value determined by solid-state ^{67}Zn NMR spectroscopy on the enzyme, these results have been used to propose that the O-donor at the metal is a hydroxy group rather than a water molecule.[99]

4. 4d-METALS

4.1 Yttrium

The ground for computational ^{89}Y NMR spectroscopy has been broken in a recent performance study on a set of 16 organometallic yttrium complexes

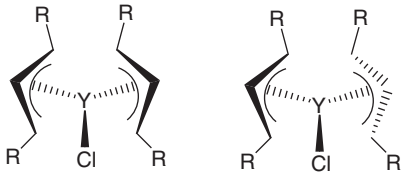

Scheme 7.

with Cp, alkyl, allyl, Cl, THF, phenoxy and H ligands.[100] Hybrid functionals (in non-relativistic calculations using X-ray-based or optimized geometries) are found very slightly superior to GGAs, but tend to overestimate substituent effects on $\delta(^{89}Y)$ notably. After scaling by a factor of *ca*. 0.8, the theoretical ^{89}Y chemical shifts agree with the experimental numbers within *ca*. ± 70 ppm over a range of *ca*. 1,250 ppm. The computations have furnished support for the formation of complexes with bulky allyl ligands in solution, but the $\delta(^{89}Y)$ values appear not to be sensitive enough to distinguish between structural details such as the relative orientation of the two allyl moieties in $Y\{1,3\text{-}(SiMe_3)_2C_3H_3\}_2Cl$ (Scheme 7).[100]

4.2 Zirconium

In early non-relativistic DFT calculations of ^{91}Zr chemical shifts (employing HF-geometries optimized with a relativistic ECP on Zr), the observed δ values in the zirconocenes $ZrCp_2X_2$ (X = Cl, Br, Me) have been reasonably well reproduced [101] (as had been shown earlier at the HF level for a larger set of compounds[102]). In the same study, a very strong shielding has been predicted for the metal in $Zr@C_{28}$,[101] an endohedral fullerene compound that had been characterized mass-spectroscopically in the gas phase.

Interest in ^{91}Zr NMR spectroscopy has recently been renewed, as the demonstrated possibility to record the solid-state NMR spectrum for an organometallic species, $ZrCp_2Cl_2$,[103] may open applications to larger species that cannot be observed in solution. The tensor components of $ZrCp_2Cl_2$, too strongly shielded by up to *ca*. -150 ppm at the HF level for DFT-optimized geometries,[102] are fairly well reproduced using B3LYP and experimental geometries.[103] The computed ^{91}Zr NQC constant is very sensitive to the basis set on all atoms, and is significantly overestimated at most of the (non-relativistic) HF and DFT levels employed (see Table 3). Presumably, more extended basis sets are necessary for convergence in this case. On the other hand, *relative* trends in the NQC constants of $ZrCp_2X_2$ (X = Cl, Br, Me) are very consistent between levels, and can be used to rationalize trends in observed linewidths of isotropic ^{91}Zr resonances in solution, in particular concerning the unusually broad line for the methyl derivative.[102]

Table 3 DFT-computed and experimental chemical-shift and NQC tensor elements for the metal nuclei (in boldface) in selected 4d- and 5d-transition metal complexes[a]

Molecule	Method	δ_{iso}	Ω	κ	C_Q	η_Q	Ref.
^{91}**Zr**Cp_2Cl_2	HF/II[b]	−91[c]	396	−0.69	8.5[d]	0.74[d]	102
	B3LYP/6-311G**[b]	0[e]	423	−0.50	14.81	0.19	103
	Experiment	40[f]	430	−0.50	6.35(10)	0.3(1)	103
^{93}**Nb**$Cp(CO)_4$	HF/6-311G**[b]	−1,720	252	−0.95	22.4	0.27	105
	B3LYP/6-311G**[b]	−2,166	479	0.29	20	0.29	105
	Experiment	−2,027(4)	35.0(5)	−0.90(5)	1.0(2)	0.80(10)	105
^{93}**Nb**$CpCl_4$	HF/6-311G**[b]	−487	484	0.11	47.8	0.39	105
	B3LYP/6-311G**[b]	−388	468	−0.71	58.1	0.22	105
	Experiment	−600(30)	150(30)	−0.60(4)	54.5(5)	0.83(3)	105
^{95}**Mo**$(Mes)(CO)_3$	B3LYP/II′[b]	−1,803[g]	878	0.99	−1.58	0.04	[h]
	BPW91/II′[b]	−1,851[g]	774	0.98	−1.44	0.05	[h]
	ZORA-BP86/TZP[i]	−1,873[g]	740	0.58	−1.55	0.34	108
	Experiment	−1,885(2)	775(30)	0.87(13)	−0.96(15)	0.30(15)	108
$[^{95}$**Mo**$(CN)_8]^{4-}$	ZORA-SO-BP86/QZ4P	−1,223	971	−1.00	−7.08	0.03	109
$(\approx D_{2d})$[j]	Experiment	−1,322(5)	1,160(30)	−0.99(1)	−7.08(5)	0.07(3)	109
$[^{95}$**Mo**$(CN)_8]^{4-}$	ZORA-SO-BP86/QZ4P	−1,308	989	0.50	6.34	0.86	109
$(\approx D_{4d})$[k]	Experiment	−1,350(10)	1,350(30)	−0.50(5)	6.35(15)	0.50(8)	109

Table 3 *(Continued)*

Molecule	Method	δ_{iso}	Ω	κ	C_Q	η_Q	Ref.
$^{99}Ru_3(CO)_{12}$[l]	ZORA-BP86/TZ2P[i]	−1,186	1,445	0.34	−3.0	0.50	117
	B3LYP/DZVP[b,i]	−1,411	1,349	0.58	−4.1	0.64	117
	B3LYP/II[b]	−1,227	1,512[m]	0.50[m]	2.4[n]	0.66	112
	Experiment	−1,302(5)	1,363(30)	0.33(8)	1.60(1)	0.7(1)	117
$^{195}Pt[S_2C_2(CF_3)_2]_2$	ZORA-BP86/QZ4P	−3,421	6,847	0.45	n.a.	n.a.	153
	Experiment	−3,986(7)	5,913(150)	0.35(3)	n.a.	n.a.	153

[a]For definition of the tensorial quantities see Section 2.3; δ and Ω in ppm, C_Q in MHz.
[b]Non-relativistic level.
[c]Relative to $ZrCp_2Br_2$.
[d]HF/6-31G* level (8.5 MHz and 0.53 for C_Q and η_Q, respectively, at the BP86/6-31G* level), employing $Q(^{91}Zr) = -17.6\,fm^2$.
[e]Fixed.
[f]Relative to concentrated $ZrCp_2Cl_2$ solution.
[g]Calculated using $Mo(CO)_6$ as primary reference and converted to the usual $[MoO_4]^{2-}$ scale.
[h]M. Bühl, unpublished; C_{3v} symmetry employed and $Q(^{95}Mo)$ taken as $-2.2\,fm^2$.
[i]X-ray geometry employed.
[j]In $K_4[Mo(CN)_8] \cdot 2H_2O$.
[k]In $Tl_4[Mo(CN)_8]$.
[l]Mean values of the three distinct sites are given.
[m]M. Bühl, unpublished.
[n]$Q(^{99}Ru)$ taken as $7.9\,fm^2$.

4.3 Niobium

Early HF data had reproduced the observed isotropic ^{93}Nb chemical shifts of anionic hexahaloniobates $[NbX_nY_{6-n}]^-$ (X, Y = F, Cl, Br, I) over a shift range exceeding 2,000 ppm fairly well.[104,52b] It had been noted in that study that the observed trends are dominated by the paramagnetic contributions involving orbitals with d-contributions from the metal, and that relativistic (notably spin-orbit) effects from heavy atoms bonded to Nb are very small. More recently, chemical-shift and NQC tensor elements have been computed at (non-relativistic) HF and B3LYP levels using X-ray-based geometries for $Nb(C_5H_4R)(CO)_4$ (R = H, OMe, CO_2Me, CO_2Et, $COCH_2Ph$), $NbCpCl_4$ and $NbCpCl_4(THF)$.[105] The observed shielding of δ_{iso} by $\Delta\delta \approx -1{,}300$ ppm on going from the Nb(I) to the Nb(V) complexes is underestimated at the HF level ($\Delta\delta$ around $-1{,}000$ ppm), and overestimated with B3LYP ($\Delta\delta$ around $-1{,}600$ ppm).

Very large discrepancies between observed and computed chemical-shift anisotropies have been noted in this set. For instance, for $NbCp(CO)_4$ the span Ω, as well as Q_C, are computed roughly one order of magnitude larger than the observed quantities (Table 3). In this case, the NMR spectra have been found to be temperature-dependent, affording larger Q_C values and larger deviations from apparent axial symmetry at lower temperatures. This observation has been interpreted in terms of motional averaging of the chemical-shift and NQR tensors, brought about by intramolecular rotations of the Cp ligand relative to the $Nb(CO)_4$ moiety.[105] Thus, even in a seemingly static structure of a solid that can be characterized by X-ray crystallography, dynamic effects can occur on the NMR time scale. The concomitant uncertainties in the assessment of individual tensor elements notwithstanding, the orientation of computed and observed tensors has in general been found to be mutually compatible.[105]

4.4 Molybdenum

The first DFT-based computations of ^{95}Mo chemical shifts and shielding tensor elements have been reported for a small set of phosphine complexes, $Mo(CO)_5(PR_3)$ (R = Ph, F, Cl).[22b] The isotropic shifts between $-1{,}523$ and $-1{,}743$ ppm (and their sequence) have been reproduced reasonably well at a non-relativistic level (BP86 functional), and have been shown to be governed by the paramagnetic part, which in turn increases (in absolute value) with decreasing HOMO–LUMO gap. Subsequently, isotropic $\delta(^{59}Mo)$ values were validated for a larger set of complexes comprising six $[MoX_nY_m]^{2-}$ ions (X, Y = O, S, Se; $m+n = 4$), $Mo(CO)_6$, $Mo(Cp)(CO)_3H$, $Mo(C_6H_6)_2$, $Mo_2(OMe)_6$ and $Mo_2(O_2CH)_4$,[106] the latter two species modeling somewhat higher substituted derivatives with Me groups instead of H atoms. 'Pure' GGAs, whether in an IGLO or GIAO framework, capture the observed trends in ^{95}Mo chemical shifts very well (with near-ideal slopes for δ_{calc} vs. δ_{expt} correlations and mean absolute deviations around *ca.* 250 ppm on a range of more than 5,700 ppm). In contrast, the B3LYP hybrid functional performs less satisfactory in this case, displaying a notable overestimation of substituent effects and a particularly large error

(more than 1,800 ppm) for $Mo_2(O_2CH)_4$ with its formal Mo–Mo quadrupole bond. Together with its congener ^{53}Cr (see above), ^{95}Mo is the only transition-metal nucleus so far, where the B3LYP hybrid functional appears to be clearly inferior to pure GGAs.

For a smaller set ($[MoX_4]^{2-}$, $Mo(CO)_6$, $Mo_2(O_2CH)_4$ and $Mo_2(OMe)_6$), the combined use of an empirically corrected IGLO scheme, a B3LYP variant with a slightly reduced amount of Hartree–Fock exchange (denoted B3LYP*) and a scalar relativistic method (denoted NESC-EP), has afforded excellent results (mean absolute deviations of better than 200 ppm over a shift range of more than 5,500 ppm.[107]

As in the case of 3d metals (see above) it is known for 4d metals that relativistic effects can be quite sizeable for the magnetic shieldings σ, but still tend to cancel to a large extent for relative δ values. For example, although absolute shielding constants change by almost 300 ppm, the $\delta(^{95}Mo)$ value of $Mo(CO)_6$ (relative to $[MoO_4]^{2-}$) changes only by *ca.* 10 ppm on going from a non-relativistic calculation to an approximate scalar relativistic treatment (two-component Pauli).[64]

Solid-state NMR of quadrupolar nuclei is a blossoming field, and ^{95}Mo is no exception. Two studies are highlighted here, where experiments have been augmented with DFT computations: The first concerns the piano-stool complex $Mo(Mes)(CO)_3$ (Scheme 8), where the scalar relativistic ZORA-BP86 method was reported to reproduce the observed CS and EFG tensors much better than the non-relativistic B3LYP level.[108] In the latter computations, however, an ECP has been (inadvertently) used on the metal, rendering the obtained nuclear properties meaningless. When the computations are repeated with a suitable all-electron basis (using the same methodologies as in ref. 106), much better mutual accord between the various computational levels is obtained (Table 3). The main differences in the skew and asymmetry parameters within the theoretical methods stems from the fact that the B3LYP and BPW91 data were computed for an optimized C_{3v}-symmetric structure (with axially symmetric chemical-shift and EFG tensors), whereas the ZORA value is based on the geometry in the crystal with lower symmetry.

A recent solid-state ^{95}Mo NMR study for two salts containing the $[Mo(CN)_8]^{4-}$ ion (a formal d^2 complex containing Mo^{IV}) furnished insights into the way how the tensorial quantities and, hence, the appearance of the NMR spectra can depend on intricate details of the structure of this ion.[109] With K^+ and

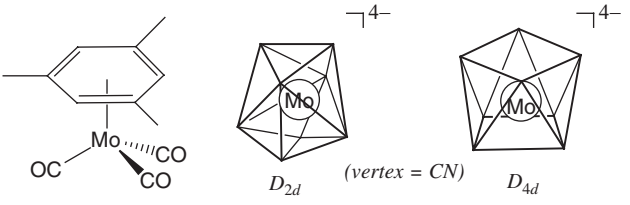

Scheme 8.

Tl^+ counterions, this ion adopts configurations with idealized D_{2d} (dodecahedral) and D_{4d} symmetry (square antiprismatic), respectively (Scheme 8). Interestingly, the skew parameters have different signs in both cases (see the corresponding κ values in Table 3), which has been rationalized in terms of variable paramagnetic contributions to the individual CS tensor components σ_{ii}. The sizeable NQC constant C_Q in the D_{4d} isomer is noteworthy, as a simple point-charge model would predict a zero EFG for that configuration. When the computation is performed for a symmetrized model with exact D_{4d} symmetry (rather than for the slightly distorted X-ray coordinates, for which the numbers in Table 3 were evaluated), a very similar C_Q value is obtained.[109]

In the latter two solid-state NMR studies,[108,109] the signs of the C_Q values, which cannot be determined experimentally, were taken from the DFT computations.

A possible chemical application for ^{95}Mo chemical shifts has been suggested in the area of catalytic imine metathesis, based on the finding that for model catalysts of the type $Mo(NH)_2X_2$ (X = F, Cl, Br, OMe, OCF_3) a key activation barrier in the catalytic cycle can be roughly correlated with the computed $\delta(^{95}Mo)$ value.[106] In this case, ligands that produce a higher shielding at the metal are predicted to have some potential for increasing the catalytic activity.

4.5 Technetium

Published DFT-computations of ^{99}Tc NMR parameters are sparse. Besides a singular $\delta(^{99}Tc)$ value for $TcOF_5$, computed at the rather low LDA level of DFT,[110] the most involved study so far concerns thermal (vibrational) effects on the ^{99}Tc magnetic shielding and indirect spin–spin coupling constants of aqueous $[TcO_4]^-$,[111] the commonly used standard in ^{99}Tc NMR spectroscopy. This latter study employed the ZORA-SO/LDA level (here effects from gradient corrections have been shown to be relatively small and constant), TZ2P basis and the COSMO variant of PCMs to account for bulk solvation effects. Rovibrational and isotope effects on the NMR properties were computed from anharmonic force fields and property surfaces, which were evaluated on a symmetry-adapted, numerical grid. Very good accord was found between observed and computed temperature (238–318 K) and isotope effects ($^{16}O \rightarrow {}^{17}O/{}^{18}O$) on the ^{99}Tc magnetic shielding constant (see Figure 6 for an illustrative example), as well as for the temperature effect on the $^1J(^{99}Tc,^{17}O)$ SSCC. The observed changes in the NMR properties were found to be about one order of magnitude larger than for the $[MnO_4]^-$ congener, and could be related to changes in Tc–O bond distances (due to vibrational averaging) of as little as 10^{-4} Å.

4.6 Ruthenium

A number of validation studies have been published for DFT-computed ^{99}Ru chemical shifts, using different test sets out of the combined set of molecules comprising RuO_4, $RuCp_2$, $K_4[Ru(CN)_6]$, $[Ru(CN)_6]^{4-}$, $Ru_3(CO)_{12}$, $[Ru(CO)_3X_3]^-$ (X = Cl, I), $[Ru(CO)_2Cl_4]^{2-}$, $RuCl_2(DMSO)_4$, $[Ru(bipy)_3]^{2+}$, $Ru(CO)_2$(*i*Pr-DAB)(X)(Y) [X,Y = Cl_2, I_2, $(SnMe_3)_2$ and Me,Cl] and $[RuL_6]^{2+}$ (L = NH_3, H_2O).

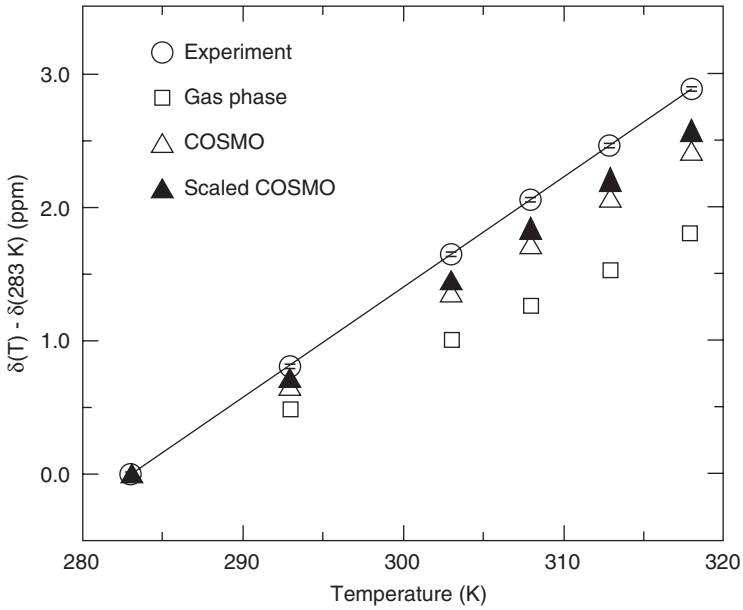

Figure 6 Measured and computed temperature effect on the ^{99}Tc chemical shift of aqueous $[Tc(^{16}O)_4]^-$ (relative to the value at 283 K, for which δ is set to zero). Squares: computations in the gas phase; triangles: computations in a continuum (raw and scaled so as to reproduce vibrational frequencies). (Reprinted with permission from ref. 111, copyright 2004 by the American Chemical Society.)

Using geometries optimized with the BP86 functional and a scalar relativistic ECP on the metal, and the non-relativistic GIAO variant with a fairly large basis set in the NMR part, the B3LYP hybrid functional was found to be somewhat superior to a pure GGA, affording a good description of trends in $\delta(^{99}Ru)$ (mean absolute deviation *ca*. 130 ppm over a shift range of *ca*. 6,000 ppm).[112] A similar degree of agreement has been found with similar functionals and somewhat smaller basis sets.[113] Using smaller all-electron basis sets and non-relativistic B3LYP geometries, somewhat larger errors are found (even larger ones when an ECP is used on the metal in the NMR computation[27b]). A very good performance has also been found employing the ZORA and ZORA-SO methods with TZ2P basis, with mean absolute deviation of *ca*. 600 ppm over a range of more than 17,000 ppm (excluding an obvious outlier, $[Ru(SnCl_3)_5Cl]^{4-}$).[114] At that level (with somewhat smaller basis sets), complexes as large as α-$[PW_{11}RuO_{39}(DMSO)]^{5-}$ can be treated. In a recent systematic ZORA and ZORA-SO study, effects of the XC functional, the source of the geometries and the way of referencing have been addressed in some detail.[115]

The latter issue, referencing, is a major concern for this nucleus, as the actual standard, an aqueous solution of $K_4[Ru(CN)_6]$, may be difficult to model computationally (*cf*. the abovementioned related $[Fe(CN)_6]^{4-}$ system). The use of an isolated $[Ru(CN)_6]^{4-}$ ion as theoretical reference may be problematic, and indeed some systematic deviations of $\delta(^{99}Ru)$ values can be found when this

standard is used.[115] It is beneficial to adopt a neutral $K_4[Ru(CN)_6]$ cluster as theoretical standard, or another primary reference altogether, or even to correlate computed σ and experimental δ values directly.[112]

Complexes with heavy elements bonded to Ru, such as $[Ru(CO)_3I_3]^-$, are surprisingly well described even in non-relativistic NMR computations, even though such heavy elements can in some cases induce significant shielding due to SO-coupling.[116] That such SO-effects should indeed be small for the Ru complexes has been suggested from the beginning (because of small s-character at the metal in the highly polarized Ru–I bonds),[112] and indeed, relatively minor effects have been noted in subsequent explicit ZORA-SO computations[114,115] (e.g., between *ca*. 300–600 ppm on the isotropic shieldings[115] and correspondingly less on the relative shifts).

Solvent effects on ^{99}Ru chemical shifts in *fac*-$[Ru(CO)_3I_3]^-$ have been studied in detail.[115] In solvents ranging in polarity from chloroform to water, $\delta(^{99}Ru)$ of this complex has been shown to vary by *ca*. 100 ppm, a small but noticeable effect. When only bulk solvation effects are taken into account via PCM-based approaches, the observed solvent-induced shifts are grossly underestimated. When only a small number of explicit solvent molecules are included in geometry optimization and NMR computation, the observed trends are likewise not well reproduced. If both explicit solvation and bulk medium effects are included simultaneously, the observed solvent-induced shifts are well captured theoretically.[115] This result is encouraging, because the applied methodology, static optimization of microsolvated clusters in a continuum, can be viewed as simple approximation to proper averaging of NMR properties computed over many snapshots from MD trajectories. The latter simulations of the full solution tend to be much more involved at QM-based levels.

Environment effects can also be present in the solid state. Recently, the first high-field MAS ^{99}Ru NMR spectra have been reported for a number of salts containing the $[Ru(CN)_6]^{4-}$ ion, $[Ru(NH_3)_6]Cl_2$ and $Ru_3(CO)_{12}$.[117] For the latter complex, three distinct resonances are resolved because, due to packing forces, the symmetry in the crystal is slightly lower than that for the pristine complex (D_{3h}). The NMR parameters are well reproduced at the relativistic ZORA/BP86 level and, even slightly better, with the non-relativistic B3LYP method (see Table 3).

EFG computations, relevant for the NQC interactions affecting the appearance of the solid-state NMR spectra, have also been computed in the context of ^{99}Ru NMR line widths in solution NMR. In selected cases, e.g., in the $Ru(CO)_2$(*i*Pr-DAB)(X)(Y) family of complexes, trends in observed $\Delta\nu_{1/2}$ values could be traced back to variations in the EFG (viz. q_{zz}).[112] Even though the theoretical EFG at the metal in $RuCp_2$ was found comparable to that evaluated from ^{99}Ru Mössbauer spectroscopy, a much narrower line is found for this complex as expected from the overall correlation for the remaining compounds.

Due to symmetry, rather narrow lines are to be expected for pseudo-octahedral $[Ru(L)_6]^{2+}$ complexes, and predictions have been made for L = imidazole and a nitro derivative (dimetro, a potent radiosensitizer), for which $\delta(^{99}Ru) = 6{,}531$ and 10,191, respectively, have been obtained at the B3LYP level.[118]

For RuO_4, $[Ru(CN)_6]^{4-}$ and $[Ru(SnCl_3)_5Cl]^{4-}$ the observed ^1J couplings between ^{99}Ru and, respectively, ^{17}O, ^{13}C and ^{119}Sn are qualitatively well reproduced at the ZORA-SO/BP86 level, even though no medium effects were included for the highly charged ions.[114]

4.7 Rhodium

Owing to the rather favourable NMR properties (for a transition metal, that is) of the spin-1/2 nucleus ^{103}Rh and the unabated importance of Rh complexes in homogeneous catalysis, a bountiful amount of ^{103}Rh NMR data is known.[119] Experimental studies are also being augmented by DFT computations,[120–122] in order to unravel steric and electronic effects on the observed chemical shifts.

The first validation studies on a small test set comprising $[RhCp_2]^+$, $Rh(Cp)(CO)_2$, $Rh(C_5H_4NO_2)(CO)_2$, $[Rh(CO)_4]^-$, *cis*-$[RhCl_2(CO)_2]^-$, $Rh(acac)(C_2H_4)_2$, Rh(acac)(COT), and $Rh(acac)_3$, which covers a shift range of *ca.* 10,000 ppm, have shown the superiority of the B3LYP level over pure GGAs when relativity is neglected.[123,72] The ZORA-BP86 method later has been shown to perform very well for a larger set of mono- and binuclear Rh(I) complexes. Subtle trends in $\delta(^{103}Rh)$ of a family of annelated Cp-complexes (see Scheme 9) could only be reproduced when the position of the Rh atoms over the Cp moieties were constrained during the geometry optimizations in order to prevent spurious 'ring slippage'.[121]

For this nucleus, referencing is always a concern for theory, due to the compete lack of an experimental reference compound (signals are reported relative to a standard frequency). As discussed in the preceding chapter, correlations of computed σ vs. experimental δ values can be used to derive a shielding constant for the standard (which is the practice adopted so far); alternatively, a suitable primary reference compound could also be picked.

Early applications of ^{103}Rh chemical-shift computations ion context with NMR/reactivity correlations have been reviewed,[7,124] as have detailed analyses of the geometry dependence in chelating bidentate phosphine and amine complexes,[124] according to which it is the variation in the Rh–X bond length, rather than the X–Rh–X bite angle (X = P, N) that is decisive for the observed trends.[120,125]

An empirical NMR/stability correlation has been assessed computationally for a set of $Rh(acac)(L)_2$ complexes (L = η^2-olefin).[126] For simple olefins, this relationship is corroborated theoretically because $\delta(^{103}Rh)$ correlates with the computed relative binding energies of the olefins. The correlation reaches its

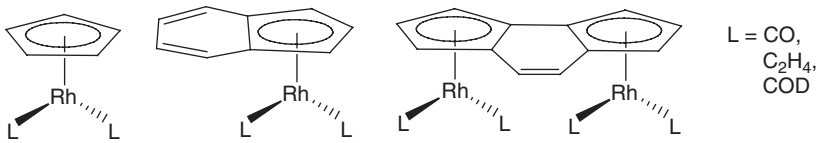

Scheme 9.

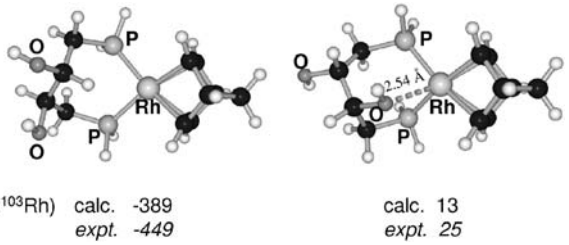

Figure 7 DFT-optimized isomers of a model Rh(I) complex with OH substituents in the phosphine backbone showing the usual four-coordination (left) and five-coordination (right), together with GIAO-B3LYP computed ^{103}Rh chemical shifts; the experimental numbers (in italics) refer to a larger complex with phenyl instead of hydrogen substituents at P and COD as diene. (data taken from ref. 127.)

limits, however, for fluorinated ethylene or chelating diolefins, because in these cases additional steric and electronic factors come into play.[126]

In an early structural application, GIAO-B3LYP model computations have corroborated the assignment of an unusually deshielded ^{103}Rh NMR signal in a chelating diphosphine/diolefin complex to an isomer with increased coordination number due to bonding of a (so-called hemilabile) OH group at one of the chelate backbones (see Figure 7).[127]

Relatively small relativistic effects on the ^{103}Rh shielding are computed for $Rh_2(O_2CH)_4(NCH)_2$, a model complex with a Rh–Rh bond. Scalar and SO relativistic effects are less than 200 ppm in magnitude and cancel each other to a large extent.[118] Thus, non-relativistic computation of NMR shifts should be reasonable even for this type of compounds, and indeed, the experimental ^{103}Rh shift for $Rh_2(OAc)_4\{P(OMe)_3\}_2$ is reasonably well reproduced at the non-relativistic GIAO-B3LYP level.[118]

4.8 Palladium and silver

Because of the utter lack of experimental data, ^{105}Pd NMR parameters have so far failed to attract the attention of computational chemists. ^{107}Ag and ^{109}Ag have slightly less unfavourable NMR characteristics, but solution spectra of these nuclei are not always easy to acquire and can be difficult to interpret when the solvent can coordinate to the metal, which frequently gives rise to dynamic equilibria between complexes of varying composition. Solid-state $^{107/109}$Ag NMR is flourishing, however, and DFT computations are beginning to be used in the interpretation of experimental data.[128,129] Care should be taken to employ sensible levels of theory, however. For instance, for a monomeric imidazol-2-ylidene silver(I) chloride complex, the orientations of the ^{109}Ag chemical-shift tensor elements have been assigned based on GIAO-B3LYP computations.[128] Because in the latter an ECP was employed on the metal, and because of the aforementioned conceptual and practical problems with this approach, the reliability of these results may be doubted. A recent study on diammine silver(I) nitrate and sulphate salts encompassed NMR computations at the more

appropriate all-electron ZORA-BP86/TZ2P level.[129] It has been shown that the elements of the ^{109}Ag shielding tensor in the $[Ag(NH_3)_2]^+$ cation do not depend strongly on the N–Ag–N bond angle. These tensor elements, and in particular the asymmetry parameter η_σ, are more sensitive to the presence of neighbouring anions and cations, and a larger array of these from the solid has to be included in the computations in order to obtain converged results.[129]

ZORA-BP86 $^1J(^{109}Ag,^{13}C)$ SSCCs have been used to assign ^{13}C NMR signals observed in solid silver cyanide to [· · ·NC–Ag–CN· · ·] and [· · ·CN–Ag–CN· · ·] sites in the polymeric chains.[130]

4.9 Cadmium

Following pioneering studies of ^{113}Cd chemical shifts at the HF level,[131] the first DFT validation study appeared in 2002.[132] For a small set of molecular compounds comprising $CdMe_2$, $CdEt_2$, CdEtMe and sections from solid $Cd(NO_3)_2 \cdot 4H_2O$ and $Cd(OAc)_2 \cdot 2H_2O$, DFT-derived isotropic $\delta(^{113}Cd)$ values and chemical-shift tensor components were found to agree somewhat better with experiment than those obtained at the HF level. Subsequently, a larger number of Cd complexes with biogenic ligands (mostly N and O donors) and discrete or polymeric structures was studied.[133] The good performance of the non-relativistic GIAO-B3PW91 hybrid functional together with a large all-electron basis set and experimental geometries is shown graphically in Figure 8. Not only isotropic δ values are reproduced quite well, but also the principal values of the CS tensors in the solids.

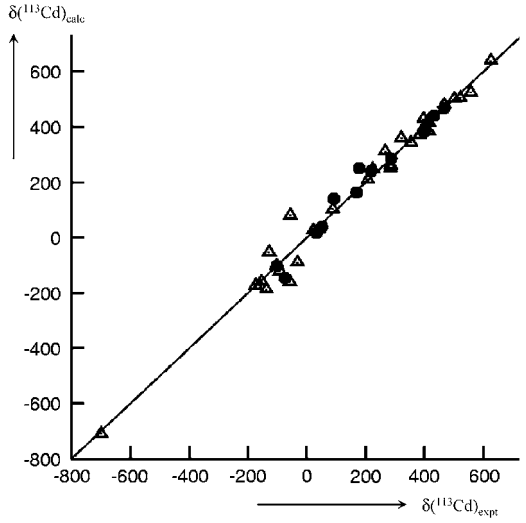

Figure 8 Plot of computed vs. experimental ^{113}Cd chemical shifts of various solids; open triangles: tensor elements δ_{ii}, filled circles: isotropic averages. (data taken from ref. 133a.)

Similar findings were reported for a different set of Cd complexes that were designed to model specific Cadmium binding sites in metalloproteins (including S donors).[134] Again, the good overall performance of DFT (the B3LYP functional in this case) was noted, and a basis for a detailed interpretation of substituent effects was provided by studying explicitly the variation of the ^{113}Cd chemical shifts with selected geometrical parameters in one of the models (for carbonic anhydrase C). There is also evidence that the simple picture of σ_p being dominated by charge transfer involving the 5p orbitals on Cd, as it had been advocated earlier,[131a] is too simple to explain all the data.[134]

5. 5d-METALS

5.1 Lanthanum and lanthanides

In a validation study on solid-state ^{139}La NMR parameters of 10 La(III) complexes with O- and N-donor atoms about the metal, trends in isotropic chemical shifts covering nearly 350 ppm were reasonably well reproduced at the scalar ZORA level and, slightly better, using ZORA-SO.[135] The computations corroborate the observed trend toward an increase of the metal shielding with the coordination number (between 8 and 12). The good performance for the isotropic shifts may be to some extent fortuitous, because somewhat larger discrepancies were noted for the chemical-shift tensor components. Spans Ω appear to be significantly overestimated, albeit overall trends were captured qualitatively, and skews κ turned out to be very sensitive to inclusion of SO coupling.[135]

Larger deviations from experiment were also noted for the trends in ^{139}La isotropic and anisotropic chemical shifts in solid LaX_3 (X = Cl, Br, I).[136] In part, these discrepancies may be rooted in the small clusters used to model the periodic solid, $[LaX_9]^{6-}$ for X = Cl, Br and $[LaI_8]^{5-}$. More extended clusters, a suitable QM/MM embedding scheme or a fully periodic method should be employed for these highly ionic species.

Apparently no DFT data have been reported yet for ^{171}Yb, the only other nucleus with some practical importance among the lanthanides. For the majority of lanthanide complexes, their paramagnetic nature makes acquisition of the metal NMR signals virtually impossible.

5.2 Hafnium and tantalum

The NMR-active nuclei of both elements have high quadrupole moments, severely limiting the experimental accessibility of their NMR spectra. Very recently, ZORA-SO computations have been reported for a small set of compounds with available $\delta(^{181}\text{Ta})$ data, namely $[TaX_4]^{3-}$ (X = S, Se, Te) and $[TaX_6]^{-}$ (X = F, Cl, CO), which span roughly 7,000 ppm.[137] According to these rather preliminary results, the observed trends are reproduced qualitatively, but

are notably overestimated quantitatively (as reflected in a slope of 1.3 of the linear regression between computed and experimental δ values). Effects of counterions, solvent or crystal matrix (measurements for $[TaX_4]^{3-}$ refer to solid copper salts) have not been taken into account in the computations. An attempt to assign the ^{181}Ta NMR signal in a solution of tantalum in HF/HNO_3 to $[TaF_6]^-$, as surmised initially, or to $[TaF_7]^{2-}$, as proposed later,[6] was thwarted by the close similarity of the ^{181}Ta chemical shifts computed for both ions, which differed by less than 100 ppm.[137]

5.3 Tungsten

The availability of a large body of ^{183}W NMR data, including those for some small and symmetric inorganic and organometallic tungsten complexes, makes this nucleus an ideal testing ground for relativistic methods for NMR computations. That relativity is very important not only for absolute shieldings, but also for relative shifts of this 5d nucleus had been noted early on in the first DFT-based validation studies: it has been shown that the $\delta(^{183}W)$ value of $W(CO)_6$ (relative to $[WO_4]^{2-}$) changes by up to 400 ppm on going from a non-relativistic calculation to an approximate scalar relativistic treatment (two-component Pauli), with changes in absolute shielding exceeding 1,300 ppm in the case of the tungstate.[64] Comparable effects have later been noted with the scalar relativistic NESC-EP method,[107] where for a set of five molecules {$[WO_4]^{2-}$, $[WS_4]^{2-}$, WF_6, WCl_6, $W(CO)_6$} mean absolute deviations between theory and experiment around *ca*. 140–200 ppm have been obtained (depending on computational details), over a shift range of more than 7,000 ppm. At least for this set, small discriminations between a GGA and hybrid functionals have been noted. Spin-orbit contributions to $\delta(^{183}W)$, evaluated in the ZORA scheme, are indicated to be deshielding for the tetrahedral dianions (up to *ca*. 100 ppm for $[WS_4]^{2-}$), and shielding for the octahedral complexes (up to *ca*. −200 ppm for $W(CO)_6$).[138]

An important analytical use of ^{183}W NMR spectroscopy is the characterization of polyoxytungstates. Attempts to apply DFT methods to the salient NMR parameters of these targets face the challenge that quite large complexes, often with dozens of heavy atoms, have to be treated, and that the metal nuclei in these systems vary only by up to *ca*. 300–500 ppm, i.e., a tiny fraction of the total ^{138}W chemical-shift range. After an initial, rather unsatisfactory attempt using ECPs on the metal atoms,[27a] better results were obtained at the ZORA-BP86 level.[139] For Lindqvist-type complexes $[W_6O_{19}]^{2-}$, $[VW_5O_{19}]^{3-}$, $[V_2W_4O_{19}]^{4-}$ and $[W_{10}O_{32}]^{4-}$, observed trends were captured qualitatively, albeit somewhat overestimated, and after appropriate scaling, the mean errors between experiment and computations are *ca*. 12 ppm (over a range of 270 ppm). While this would appear to be a respectably small error, even higher accuracy may be needed for many applications (i.e., assignments of close-lying signals). Furthermore, larger errors (requiring different scaling constants) were noted for other types of complexes, specifically for the Keggin anion α-$[Ru(DMSO)PW_{11}O_{39}]^{5-}$.[139]

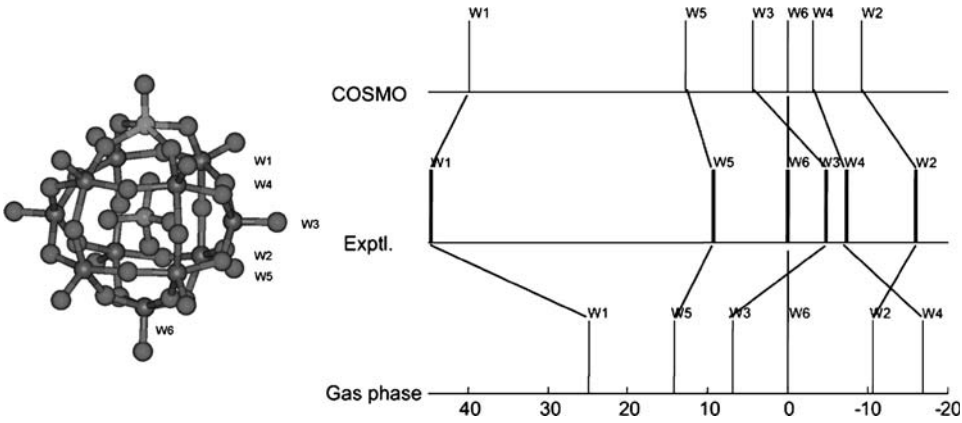

Figure 9 Schematic stick spectrum of α-$[PW_{11}TiO_{40}]^{5-}$ (see left for 3D plot; O, black; W, dark grey; Ti, light grey; central atom P), $\delta(^{183}W)$ relative to the resonance of W6. 'COSMO' and 'Gas phase' denote ZORA-SO results obtained in a solvent model and *in vacuo*, respectively. (Reprinted with permission from ref. 140, copyright 2006 by Wiley-VCH Publishers.)

It was later demonstrated that solvation effects can affect ^{183}W chemical shifts in polyoxytungstates noticeably, and a PCM-based protocol was proposed involving both geometry optimizations and ZORA-SO computations in a continuum (COSMO variant using the parameters of water), for which a relatively uniform mean error around *ca*. 35 ppm was obtained across a diverse set of 11 ions (17 resonances in total over a range of *ca*. 500 ppm).[140] The promise of this approach was illustrated for a typical tungstate, α-$[PW_{11}TiO_{40}]^{5-}$ (see Figure 9), where the observed pattern of the six resonances is well reproduced, save for the reversal of two closely spaced peaks (W3 and W6).[140]

Deeper analysis of the origin of the paramagnetic contributions to the ^{183}W shielding in polyoxymetalates is complicated by the fact that there are a large number of these contributions, with little transferability between clusters. Interestingly, so-called 'occupied–occupied' contributions are indicated to be unusually strong, and the 'occupied–virtual' contributions (see Equation (2)) are not dominated by the frontier MOs with small energy gap, but by low- and high-lying occupied and unoccupied MOs, respectively.[141a] Apparently, these results are difficult to reconcile with simple arguments based on charges and LUMO characteristics that have been put forward to rationalize ^{183}W chemical shifts.[142]

Changes of $\delta(^{183}W)$ values in γ-$[SiW_{12}O_{40}]^{4-}$, $[P_2W_{18}O_{62}]^{6-}$ and $[W_{10}O_{32}]^{4-}$ upon two-electron reduction have been analyzed in detail.[141b] Both direction and magnitude of these changes are qualitatively well reproduced at the ZORA-BP86/TZP level (Figure 10), and the site-specific shifts are rationalized in terms of the coefficients of the MO that is being filled upon reduction. According to the computations, a considerable fraction of the observed deshielding that is observed for most of the ^{183}W resonances is geometric in nature, arising from the local expansion of the clusters upon reduction.[141b]

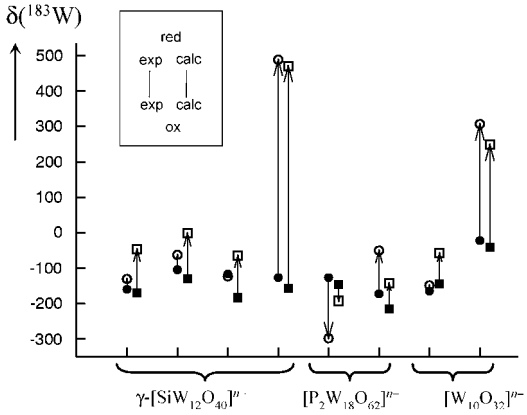

Figure 10 Changes in ^{183}W chemical shifts in selected polyoxytungstates upon two-electron reduction; filled symbols, oxidized form; open symbols, reduced form; circles, experiment; squares, ZORA-BP86. (data taken from ref. 141b.)

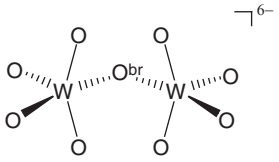

Scheme 10.

The intriguing icosahedral WAu_{12} cluster, predicted theoretically and detected mass-spectroscopically, is indicated to have a highly shielded ^{183}W nucleus in its center, at $\delta \approx -13{,}000$ at the ZORA-SO level.[143] Unusual, strongly shielding paramagnetic and SO contributions are responsible for this result.

Assessment of relativistic SSCC computations have included couplings between ^{183}W with ^{1}H, ^{13}C and ^{31}P, and reduced coupling constants ^{1}K covering three orders of magnitude have been very well reproduced at the ZORA/BP86 level, much better than at the corresponding non-relativistic level or using ZORA/LDA.[47b] Model computations for a $[W_2O_9]^{6-}$ cluster (Scheme 10) have furnished evidence that the $^{2}J(^{183}W,^{183}W)$ SSCC, empirically taken as a probe for the W–O^{br}–W angle, can also depend critically on the W–O^{br} bond distance,[144] i.e., a parameter usually not taken into account.

5.4 Rhenium and osmium

Due to rather unfavourable nuclear properties, ^{185,187}Re NMR spectroscopy has attracted only cursory interest from experimental, and none from computational chemists so far. ^{187}Os is better behaved in terms of NMR, but despite a number of interesting applications,[7] no corresponding DFT studies have appeared yet.

5.5 Platinum

The importance of Pt complexes in homogeneous catalysis and in pharmacological applications, combined with rather attractive NMR characteristics of this spin-1/2 nucleus, make ^{195}Pt NMR spectroscopy an invaluable analytical tool.[145] Spurred by this experimental interest, a sizeable number of computational papers on ^{195}Pt NMR parameters have appeared and have been covered, to a variable extent, in some recent reviews.[13c,145]

In the first ZORA-SO study, 20 square planar *cis*- and *trans*-PtX_2L_2 complexes (X = Cl, Br, I; L = SMe_2, NH_3, PMe_3, $AsMe_3$) were investigated.[146] Employing idealized geometries, a mean absolute deviation from experiment of roughly 250 ppm was achieved, on a ^{195}Pt shift range of *ca*. 3,500 ppm. An even better agreement was obtained at the ZORA-SO-PW91/TZP level for a less diverse set of 10 $[PtCl_nBr_{6-n}]^{2-}$ complexes ($n = 0,1,..,6$).[147] Using LDA-optimized geometries, the mean absolute error is only 13 ppm over a shift range of *ca*. 1,900 ppm. Very similar results were obtained independently using ZORA-BPW91 optimized geometries, and were extended to $[PtCl_n(OH)_{6-n}]^{2-}$ complexes ($n = 0,1,3,5$), for which somewhat larger errors were encountered.[148] For $[PtBr_6]^{2-}$ a shielding/bond-length derivative of *ca*. $-150\,\text{ppm}\,\text{pm}^{-1}$ has been computed, or $-25\,\text{ppm}\,\text{pm}^{-1}$ per Pt–Br bond,[147] corroborating the general experience that shieldings can be quite sensitive to structural parameters and that, hence, accurate geometries are needed in NMR computations. Experimental $\delta(^{195}\text{Pt})$ values of *cis*- and *trans*-$PtCl_2$(dimetro)$_2$ complexes containing a nitroimidazole-based radiosensitizer were also well reproduced computationally.[118] Representative ^{195}Pt chemical shifts for these systems are collected in Table 4.

In all these cases, favourable error cancellation can be achieved by choosing appropriate primary reference complexes, e.g., *cis*-$PtCl_2(SMe_2)_2$ or cisplatin for square-planar Pt(II) complexes, and $[PtCl_6]^{2-}$ (the actual standard used experimentally) for octahedral Pt(IV) species. The question of referencing has been addressed for a series of dinuclear Pt–Tl complexes, namely $[Pt(CN)_5–Tl(CN)_n]^{n-}$ ($n = 0,1,..,3$), $[Pt(CN)_5–Tl–Pt(CN)_5]^-$ and two bridged species (Scheme 11),[149] and, in a recent study, for $[PtCl_4]^{2-}$, $[PtCl_6]^{2-}$ and a bridged dinuclear Pt(III) complex (Scheme 11).[150] Bulk solvation effects were included via the COSMO model, and for $[PtCl_4]^{2-}$ and $[PtCl_6]^{2-}$, thermal and solvation effects were explicitly studied by way of BOMD simulations of microsolvated clusters with 12 water molecules and averaging of the shielding constants along the trajectories[150] (similar to approaches discussed above for some 3d-metal complexes). Notable variations of the Pt–Cl bond lengths were encountered upon increase of the basis set or inclusion of solvation and dynamics, and while the effects tend to be similar for the magnetic shieldings of both complexes, they do not fully cancel for the relative difference.

The experience with theoretical ^{195}Pt chemical shifts accumulated so far suggests that qualitative trends can usually be well described already in static gas-phase computations at a suitable relativistic level (such as ZORA), but that it can be very difficult to achieve more quantitative accuracy. For that purpose,

Table 4 Selected computed and experimental isotropic ^{195}Pt chemical shifts

Entry	Complex	Level	δ_{calc}	δ_{expt}	Ref.
1	*cis*-$PtCl_2(NH_3)_2$	ZORA-SO-BPW91/TZP′	−2,176	−2,104	146
2	*trans*-$PtCl_2(SMe_2)_2$	ZORA-SO-BPW91/TZP′	−3,545	−3,424	146
3	*cis*-$PtCl_2(SMe_2)_2$[a]	ZORA-SO-BPW91/TZP′	−3,551	−3,551	146
4	*cis*-$PtBr_2(SMe_2)_2$	ZORA-SO-BPW91/TZP′	−3,908	−3,879	146
5	*cis*-$PtI_2(PMe_3)_2$	ZORA-SO-BPW91/TZP′	−4,412	−4,588	146
6	*trans*-$PtI_2(SMe_2)_2$	ZORA-SO-BPW91/TZP′	−5,276	−5,152	146
7	*trans*-$PtI_2(PMe_3)_2$	ZORA-SO-BPW91/TZP′	−5,226	−5,539	146
8	$[PtCl_6]^{2-}$	ZORA-SO-BPW91/TZP	0	0	147
9	*fac*-$[PtCl_3Br_3]^{2-}$	ZORA-SO-BPW91/TZP	−867	−889	147
10	$[PtBr_6]^{2-}$	ZORA-SO-BPW91/TZP	−1,915	−1,870	147
11	*fac*-$[PtCl_3(OH)_3]^{2-}$	ZORA-SO-BPW91/TZP	1,638	1,843	148
12	$[Pt(OH)_6]^{2-}$	ZORA-SO-BPW91/TZP	2,273	3,291	148
13	*cis*-$PtCl_2(dimetro)_2$[b]	ZORA-SO-BP86/TZP′	−2,104	−2,069	118
14	$[PtCl_4]^{2-}$	ZORA-SO-revPBE/QZ4P	−1,389	−1,630	150
15	$Pt_2(NH_3)_2Cl_4L_2$, Pt(2)[c]	ZORA-SO-revPBE/QZ4P	−1,594	−1,023	150
	$Pt_2(NH_3)_2Cl_4L_2$, Pt(1)	ZORA-SO-revPBE/QZ4P	409	535	150

[a]Used in ref. 146 as primary standard for entries 1–7 and converted to the $[PtCl_6]^{2-}$ scale for this review using the $\delta(^{195}Pt)$ value given in ref. 6.
[b]Referenced against cisplatin and converted to the $[PtCl_6]^{2-}$ scale via the experimental value of entry 1.
[c]L = bridging amidate ligand, NH–C(=O)–*t*Bu$^-$, *cf*. Scheme 11; Pt(1) and Pt(2) denote the two different Pt sites.

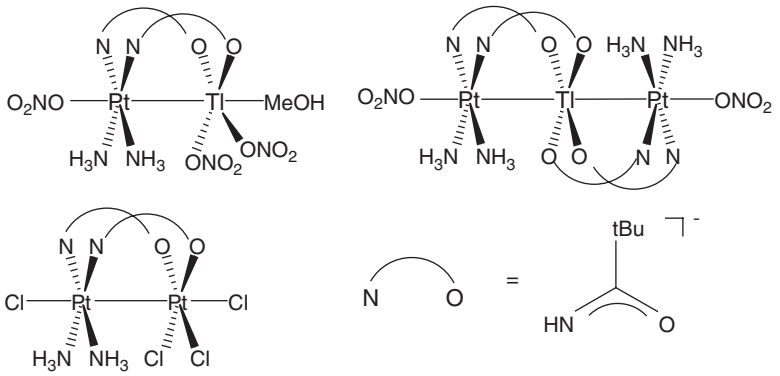

Scheme 11.

large basis sets, SO contributions and effects of dynamics and solvation have to be taken into account.

For $PtCl_2$(His) meaningless non-relativistic $\delta(^{195}Pt)$ values have been reported using an ECP on the metal;[151] reasonable agreement was obtained in the same study with the relativistic ZORA/DZ method, despite the small basis set and neglect of SO contributions.

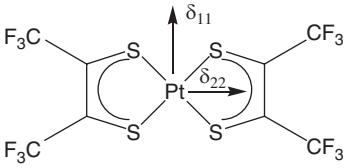

Scheme 12.

Dynamic averaging of ^{195}Pt chemical shifts was pioneered in a QM/MM-CPMD study of the binding of a $[Pt(NH_3)]^{2+}$ fragment to DNA oligomers.[152] Three models were investigated with that fragment attached to pairs of guanine residues in different DNA domains. $\delta(^{195}Pt)$ values were computed at the scalar ZORA-BP86/TZP′ level and were averaged over *ca*. 50 snapshots taken during 2 ps of simulation. Unfortunately, little discrimination was found for the three models, with simulated δ values between *ca*. 500–600 ppm (experiment: *ca*. 310 ppm), precluding structural assignments based on these results.

The ^{195}Pt tensor components in a Pt–dithiolene complex (Scheme 12) are qualitatively reproduced at the ZORA level (see Table 3),[153] and the orientation of the principal axes system has been taken from the computations.

SSCCs involving ^{195}Pt have been studied in quite some detail with ZORA-based approaches.[47b,149,154] Solvent effects, included either by including discrete solvent molecules, by employing a continuum model, or a combination of both, can be very important, in particular for $^1J(^{195}Pt,^{205}Tl)$ in those $[Pt(CN)_5–Tl(CN)_n]^{n-}$ complexes ($n = 0,1,..,3$), that are coordinatively unsaturated. Because these results have been thoroughly reviewed,[13c,145] they will not be discussed further. In two recent structural applications, scalar ZORA-BP86 computations of $^1J(^{195}Pt,^{13}C)$ SSCCs have been used to support the assignments of the *cis* and *trans* stereoisomers in $Pt(L)_2(aryl)_2$ complexes (L = DMSO, PEt_3).[155]

5.6 Gold and mercury

Due to the lack of any experimental ^{197}Au NMR data of diamagnetic gold complexes there have been no computational studies for this nucleus to date. In contrast, ^{199}Hg NMR is well developed, and has been a target of computations since the advent of relativistic methods for NMR computations.[156] The first DFT results were reported for a set of nine HgX_2 and Hg(Me)X complexes (X = Me, CN, Cl, Br and I) at the ZORA-SO-PW91/TZ2P level.[25] Isotropic shifts were well reproduced when experimental geometries were employed, with a mean absolute deviation of 145 ppm over a shift range of *ca*. 3,500 ppm. Effects of a strongly donating solvent, pyridine, were modelled by computing adducts of the type $HgX_2(NH_3)_2$ (X = Cl, Br, I).[25] The results are quite sensitive to structural parameters and again, accurate geometries are needed.

The good performance of the particular ZORA level may be in part fortuitous, as it has later been shown that the results get somewhat worse with a larger (QZ4P-type) basis set.[157] This observation was made for methylmercury halides, both for their isotropic ^{199}Hg chemical shifts and chemical-shift anisotropies

(defined as $\sigma_{||}-\sigma_{\perp}$ for axially symmetric molecules). These quantities were determined experimentally in the same study in a liquid crystalline medium, and the corresponding effect of the environment, which was not included in the computations, was suggested to be one reason for the quantitative discrepancies between theory and experiment.[157]

Trends in $\delta(^{199}\mathrm{Hg})$ values are governed by the paramagnetic contributions to the shielding tensor and, especially when heavier halogens are attached to Hg, by SO coupling.[25,158] The latter contributions are also important for chemical shifts of lighter nuclei bonded to Hg, e.g., ^{13}C in methylmercury halides.[159,157]

For computations of SSCCs involving ^{199}Hg,[47b] the need to include solvent effects is even more pronounced than for the chemical shifts.[154] This is also the case for $^{1}J(^{199}\mathrm{Hg},^{199}\mathrm{Hg})$ in Hg_2^{2+}, where a huge value exceeding 800 kHz has been predicted for the bare ion, which approaches the experimental value of 284 kHz only when the full ligand environment (crown ethers and axial water molecules) is included in the computation.[160] For the bare Hg_3^{2+} and Hg_4^{2+} ions, the ^{2}J and ^{3}J SSCCs are indicated to be larger than the respective ^{1}J values,[160,137] interesting predictions that await experimental confirmation. The effect of specific and unspecific solvent effects, and of thermal fluctuations on the SSCCs of Hg_3^{2+} in SO_2 solution have very recently been studied with BOMD simulations.[161] Not unexpectedly, solvent effects are also important for the ^{199}Hg–^{13}C spin–spin coupling tensors in methyl mercury halides.[162]

6. ACTINIDES

Experimental NMR observation of actinide nuclei in diamagnetic compounds so far is limited to the single ^{235}U resonance in liquid, ^{235}U-enriched UF_6.[163] The lack of any observed relative chemical shift makes a critical assessment of computed $\delta(^{235}\mathrm{U})$ values difficult. However, in light of the good performance of the ZORA-SO approach for the heaviest 5d nuclei (and beyond, for ^{207}Pb),[138] it is to be expected that predictions at that level should be rather reliable, at least qualitatively. Such predictions have been reported for UCl_nX_{6-n} (X = F, OMe, $n = 0,1,\ldots,6$), $[UO_2X_4]^{2-}$ (X = F, Cl), $[UO_2(CO_3)_3]^{4-}$ and $[UO_2(H_2O)_5]^{2+}$.[164] UCl_6 marks the deshielded end in this series, with $\delta(^{235}\mathrm{U}) \approx 12{,}700$, whereas a strong shielding, up to $\delta(^{235}\mathrm{U}) \approx -8{,}300$, is obtained for uranyl hydrate.

The credibility of these predictions is further supported by the finding that, minor inconsistencies in some cases notwithstanding,[17]O, ^{19}F and ^{1}H chemical shifts of uranium compounds are well reproduced at this and similar levels.[5,165]

7. CONCLUDING REMARKS

Owing to rapid methodological advancements in the past decade, computational transition-metal NMR spectroscopy is coming of age. With DFT as practicable means to treat large parts of the electron correlation in an economical way, and with suitable approximations to take the leading relativistic effects into account,

tools are now at hand that allow computation of NMR properties for nuclei from essentially the whole Periodic Table.

Many of the studies covered in this review were geared toward validation of the computational NMR toolkit, in order to identify the best method for calculating a given property. Isotropic chemical shifts for 3d- and 4d-metal nuclei can often be described reasonably well at routine non-relativistic DFT levels, provided accurate geometries and suitably large all-electron basis sets are employed. From the third transition row onward, additional inclusion of relativistic effects is mandatory, and there are well-tested, robust methods available for this purpose (e.g., ZORA). Strong interactions with the environment, for instance with a polar crystal matrix or a protic solvent, must be taken into account specifically. Experience accumulated so far suggests that such medium effects can be particularly important for the chemical-shift tensor components and spin–spin coupling constants involving the metal.

Such validation work is bound to continue, and besides ever better modeling of the actual conditions of the NMR experiment, the most promising prospect for increasing the accuracy of DFT-computed NMR parameters is the identification of better exchange-correlation functionals. In fact, the pronounced sensitivity of many transition-metal chemical shifts makes them ideal probes for assessing new functionals at the development stage.

NMR computations are most favourably applied to interpretation and structural assignment. The modern quantum-chemical techniques offer unprecedented insights into the way how the magnetic response functions depend on details of the electronic structure of a given metal complex. When the structures of the species that give rise to NMR signals are not or not fully known, the combination of computed and observed NMR properties can be a powerful structural tool, because significant discrepancies between theory and experiment can be disproof of the structural candidates underlying the computations. In addition, the calculations can complement experiments by furnishing information that may not be easy to gather otherwise, e.g., the tensor orientations in ordered samples.

All these points hold for the lighter, more common NMR-nuclei as well, and the possibility to treat heavy metals with sufficient accuracy has widened the scope of NMR computations considerably. Future applications of such computations for transition-metal nuclei will be closely linked to experimental progress in recording spectra of quadrupolar nuclei. Recent advances in solid-state NMR spectroscopy at ultra-high fields are very encouraging in that respect. It can be anticipated that experiment and theory can team up very fruitfully in this area, for instances in cases of insufficiently characterized materials (e.g., metalloenzymes or active heterogeneous catalysts).

ABBREVIATIONS

6-31+G* etc.	polarized split-valence basis sets according to Pople
acac	acetylacetonate
acpy-inh	hydrazone of acetylpyridine and isonicotinic acid hydrazide

bipy	2,2′-bipyridine
B3LYP	popular 3-parameter hybrid density functional according to Becke, Lee, Yang and Parr
BOMD	Born–Oppenheimer molecular dynamics
BP86	common density functional of GGA type according to Becke and Perdew
CB	1,2-$C_2B_9H_{11}^{2-}$ (dicarbollide)
COD	1,5-cyclooctadiene
COSMO	conductor-like screening model
COT	1,3,5,7-cyclooctatetraene
Cp	cyclopentadienyl
CSA	chemical-shift anisotropy
CPMD	Car–Parrinello molecular dynamics
DAB	1,4-diazabutadiene
DFT	density functional theory
dimetro	dimetridazol (=1,2-dimethyl-5-nitro-1*H*-imidazole)
dmg	dimethylglyoximate
DMSO	dimethylsulphoxide
DZ	double-zeta
ECP	effective core potential
EFG	electric field gradient
GIAO	gauge-including atomic orbitals
GIPAW	gauge-including projected augmented wave
GGA	generalized gradient approximation (i.e., gradient-corrected exchange-correlation functionals in DFT)
HF	Hartree–Fock
His	histidine
IGLO	individual gauge for localized orbitals
II	triple-zeta basis designed for chemical-shift computations
LDA	local density approximation (the simplest exchange-correlation functional in DFT)
LORG	localized orbitals/local origin
MD	molecular dynamics
Mes	mesitylene (1,3,5-trimethylbenzene)
MO	molecular orbital
NQC	nuclear quadrupole coupling
NESC-EP	normalized elimination of the small component using an effective potential
PCM	polarizable continuum model
py	pyridine
PW91	common density functional of GGA type according to Perdew and Wang
QM/MM	hybrid quantum-mechanical/molecular-mechanical method
QZ4P	quadrupole-zeta with four polarization functions
quin	8-quinolinate
SO	spin-orbit

SSCC	(indirect) spin–spin coupling constant
THF	tetrahydrofuran
TMHD	2,2,6,6-tetramethyl-3,5-heptanedionato
TZP	triple-zeta plus polarization (prime denotes mixed basis, usually smaller basis on the ligands)
VCPO	vanadium-containing chloroperoxidase
XC	exchange and correlation
ZORA	zero-order regular approximation

ACKNOWLEDGEMENTS

The author thanks Prof. W. Thiel and the MPI in Mülheim for continuous support, and his coworkers, F. T. Mauschick, R. Schurhammer, T. de C. Ramalho, P. Imhof, S. Grigoleit, H. Kabrede, K. R. Geethalakshmi, M. Waller and V. Golubnychiy, for their contributions and their enthusiasm. Fruitful collaborations with C. J. Elsevier, L. Öhrström, M. Parrinello, B. Wrackmeyer, D. Hnyk, V. Vrček, I. Vinkovic Vrček, M. Biruš, D. Rehder and T. Polenova are also gratefully acknowledged. Thanks are also due to J. Autschbach for a preprint of an unpublished paper. After submission of the manuscript, a number of DFT studies on transition-metal containing systems have appeared, as well as some general reviews on the calculation of NMR parameters.[166–168] An exciting new development is the possibility to compute chemical shifts of periodic metallic compounds (including Knight shifts) from first principles.[169] Periodic GIAPW computations have been validated for large set of 3d-metal complexes and applied to 51V shift tensors in several vanadium oxide materials.[170] Solid-state 51V NMR parameters of a number of vanadium dipicolinate complexes have been reproduced and interpreted in terms of DFT results.[171, 172] GIAO-B3LYP computed 51V chemical shifts have been used to assess the degree of non-innocence of vanadium(V)-catecholate complexes and have furnished no evidence for such non-innocence of the ligand in oxidized amavadin.[173] The first DFT (B3LYP)-based $^{63/65}$Cu chimacl shift and NQC tensors have been reported for several dimeric Cu(I) chloride-phosphine and monomeric Cu(I) cyclopentaienly complexex.[174] In a recent multinuclear NMR study of group-12 metal diselenoimidophosphinato complexes in the solid state, the orientation of the ^{113}Cd and ^{199}Hg chemical shift tensors has been taken from ZORA-BP86 computations.[175] The same level has been used to compute and interpret ^{113}Cd and ^{199}Hg chemical shift anisotropies in bis(thymine) adducts of these metals, as well as the SSCCs involiving or across them.[176] These studies are testimony that DFT computation of transition metal NMR parameters continues to be a vibrant field.

REFERENCES

1. H. Chermette, *Coord. Chem. Rev.*, 1998, **178**, 699.
2. E. R. Davidson, *Chem. Rev.*, 2000, **100**, 351. and other articles in this special issue.
3. W. Koch and M. C. Holthausen, *A Chemist's Guide to Density Functional Theory*, Wiley-VCH, Weinheim, 2000.
4. (a) P. J. Wilson, R. D. Amos and N. C. Handy, *Phys. Chem. Chem. Phys.*, 2000, **2**, 187; (b) A. M. Teale, A. J. Cohen and D. J. Tozer, *J. Chem. Phys.*, 2007, **126**, 074101.
5. G. Schreckenbach, S. K. Wolff and T. Ziegler, *J. Phys. Chem. A*, 2000, **104**, 8244.
6. P. S. Pregosin, ed., *Transition Metal Nuclear Magnetic Resonance*, Elsevier, Amsterdam, 1991.
7. W. von Philipsborn, *Chem. Soc. Rev.*, 1999, 95.
8. (a) For some selected examples see: A. S. Lipton, J. A. Sears and P. D. Ellis, *J. Magn. Reson.*, 2001, **151**, 48; (b) S. E. Ashbrook and S. Wimperis, *J. Magn. Reson.*, 2002, **156**, 269; (c) D. D. Law, H. M. L. Bitter and A. Jerschow, *Angew. Chem. Int. Ed.*, 2002, **41**, 3096.
9. (a) S. Gaemers and C. J. Elsevier, *Chem. Soc. Rev.*, 1999, **28**, 135; (b) S. Gaemers, J. Groenevelt and C. J. Elsevier, *Eur. J. Inorg. Chem.*, 2001, 829.

10. N. Pooransingh-Margolis, R. Renirie, Z. Hasan, R. Wever, A. J. Vega and T. Polenova, *J. Am. Chem. Soc.*, 2006, **128**, 5190.
11. K. J. Ooms, V. V. Terskikh and R. E. Wasylishen, *J. Am. Chem. Soc.*, 2007, **129**, 6407.
12. M. Bühl, M. Kaupp, V. G. Malkin and O. L. Malkina, *J. Comput. Chem.*, 1999, **20**, 91.
13. (a) J. Autschbach, *Struct. Bonding*, 2004, **112**, 1; (b) J. Autschbach and T. Ziegler, *Coord. Chem. Rev.*, 2003, **238**, 83; (c) J. Autschbach, *Coord. Chem. Rev.*, 2007, **251**, 1796.
14. M. Bühl, in: *Calculation of NMR and EPR Parameters. Theory and Applications*, M. Kaupp, M. Bühl and V. G. Malkin, eds., Wiley-VCH, Weinheim, 2004, p. 421.
15. T. Helgaker, M. Jaszunski and K. Ruud, *Chem. Rev.*, 1999, **99**, 293.
16. M. Kaupp, M. Bühl and V. G. Malkin, eds., *Calculation of NMR and EPR Parameters. Theory and Applications*, Wiley-VCH, Weinheim, 2004.
17. V. G. Malkin, O. L. Malkina, M. E. Casida and D. R. Salahub, *J. Am. Chem. Soc.*, 1994, **116**, 5898.
18. G. Schreckenbach and T. Ziegler, *J. Phys. Chem.*, 1995, **99**, 606.
19. J. R. Cheeseman, G. W. Trucks, T. A. Keith and M. J. Frisch, *J. Chem. Phys.*, 1996, **104**, 5497.
20. T. Helgaker, P. J. Wilson, R. D. Amos and N. C. Handy, *J. Chem. Phys.*, 2000, **113**, 2983.
21. J. Gauss, in: *Modern Methods and Algorithms of Quantum Chemistry*, J. Grotendorst, ed., NIC Series, Vol. 1, Jülich (Germany), 2000, p. 509.
22. (a) S. Berger, U. Fleischer, C. Geletneky and J. C. W. Lohrenz, *Chem. Ber.*, 1995, **128**, 1183; (b) Y. Ruiz-Morales and T. Ziegler, *J. Phys. Chem. A*, 1998, **102**, 3970.
23. (a) N. F. Ramsay, *Phys. Rev.*, 1950, **78**, 699; (b) N. F. Ramsay, *Phys. Rev.*, 1952, **86**, 243; (c) J. S. Griffith and L. E. Orgel, *Trans. Farad. Soc.*, 1957, **53**, 601.
24. (a) M. Kato, M. Hada, R. Fukuda and H. Nakatsuji, *Chem. Phys. Lett.*, 2005, **408**, 150; (b) Y. Xiao, D. Peng and W. Liu, *J. Chem. Phys.*, 2007, **126**, 081101; (c) S. Komorowsky, M. Repisky, O. L. Malkina, V. G. Malkin, I. M. Ondik and M. Kaupp, *J. Chem. Phys.*, 2008, **128**, 104101.
25. S. K. Wolff, T. Ziegler, E. van Lenthe and E. J. Baerends, *J. Chem. Phys.*, 1999, **110**, 7689.
26. (a) J. Vaara, P. Manninen and P. Lantto, in: *Calculation of NMR and EPR Parameters. Theory and Applications*, M. Kaupp, M. Bühl and V. G. Malkin, eds., Wiley-VCH, Weinheim, 2004, p. 209.; (b) J. Autschbach, in: *Calculation of NMR and EPR Parameters. Theory and Applications*, M. Kaupp, M. Bühl and V. G. Malkin, eds., Wiley-VCH, Weinheim, 2004, p. 227.
27. (a) A. Bagno and M. Bonchio, *Chem. Phys. Lett.*, 2000, **317**, 123; (b) A. Bagno and M. Bonchio, *Eur. J. Inorg. Chem.*, 2002, 1475.
28. (a) C. J. Pickard and F. Mauri, *Phys. Rev. B*, 2001, **63**, 245101; (b) C. J. Pickard and F. Mauri, in: *Calculation of NMR and EPR Parameters. Theory and Applications*, M. Kaupp, M. Bühl and V. G. Malkin, eds., Wiley-VCH, Weinheim, 2004, p. 265.
29. For a recent application to ^{23}Na NMR properties in some perovskites see: S. E. Ashbrook, L. Le Polles, R. Gautier, C. J. Pickard and R. I. Walton, *Phys. Chem. Chem. Phys.*, 2006, **8**, 3423.
30. M. Kaupp, O. L. Malkina, V. G. Malkin and P. Pyykkö, *Eur. J. Chem.*, 1998, **4**, 118.
31. (a) M. Kaupp, V. G. Malkin, O. L. Malkina and D. R. Salahub, *Chem. Phys. Lett.*, 1995, **235**, 382; (b) J. Vaara, in: *Calculation of NMR and EPR Parameters. Theory and Applications*, M. Kaupp, M. Bühl and V. G. Malkin, eds., Wiley-VCH, Weinheim, 2004, p. 209.
32. J. Mason, *Solid State NMR*, 1993, **2**, 285.
33. S. G. Gomez, J. I. Melo, R. H. Romero, G. A. Aucar and M. R. de Azua, *J. Chem. Phys.*, 2005, **122**, 064103.
34. (a) M. E. Smith and E. R. H. van Eck, *Prog. Nucl. Magn. Reson. Spectrosc.*, 1999, **34**, 159–201; (b) S. E. Ashbrook and S. Winperis, *Prog. NMR. Spectrosc.*, 2004, **45**, 53.
35. (a) M. H. Cohen and F. Reif, *Solid State Phys.*, 1957, **5**, 321; (b) L. Frydman, *Annu. Rev. Phys. Chem.*, 2001, **52**, 463; (c) A. P. M. Kentgens, *Geoderma*, 1997, **80**, 271.
36. (a) U. Haeberlen, in: *Advances in Magnetic Resonance; Suppl. 1*, J. S. Waugh, ed., Academic Press, New York, 1976. (b) M. Mehring, *Principles of High Resolution NMR in Solids*, 2nd Ed., Springer Verlag, Berlin, 1983. (c) H. W. Spiess, in: *NMR Basic Principles and Progress*, P. Diehl, E. Fluck and R. Kosfeld, eds., Vol. 15, Springer Verlag, Berlin, 1978.
37. A. Abragam, ed., *The Principles of Nuclear Magnetism*, Oxford University Press, Oxford, 1961, p. 314, Chapter 9.

38. See for example: (a) V. Kellö, A. Sadlej, P. Pyykkö, D. Sundholm and M. Tokman, *Chem. Phys. Lett.*, 1999, **304**, 414; (b) M. Gee and R. E. Wasylishen, in: *Modeling NMR Chemical Shifts, ACS Symposium Series*, Vol. 732, J. C. Facelli and A. D. deDios, eds., American Chemical Society, Washington DC, 1999, p. 259; (c) P. Schwerdtfeger, M. Pernpointer and W. Nazarewicz, in: *Calculation of NMR and EPR Parameters. Theory and Applications*, M. Kaupp, M. Bühl and V. G. Malkin, eds., Wiley-VCH, Weinheim, 2004, p. 279.
39. (a) C. J. Jameson, D. Rehder and M. Hoch, *J. Am. Chem. Soc.*, 1987, **109**, 2589; (b) C. J. Jameson, D. Rehder and M. Hoch, *Inorg. Chem.*, 1988, **27**, 3490.
40. D. Rehder, M. Hoch and C. J. Jameson, *Magn. Reson. Chem.*, 1990, **28**, 138.
41. (a) V. G. Malkin, O. L. Malkina, G. Steinebrunner and H. Huber, *Chem. Eur. J.*, 1996, **2**, 452; (b) D. J. Searles and H. Huber, in: *Calculation of NMR and EPR Parameters. Theory and Applications*, M. Kaupp, M. Bühl and V. G. Malkin, eds., Wiley-VCH, Weinheim, 2004, p. 175.
42. M. Bühl and M. Parrinello, *Chem. Eur. J.*, 2001, **7**, 4487.
43. For instance: (a) P.-O. Åstrand, K. Ruud and P. R. Taylor, *J. Chem. Phys.*, 2000, **112**, 2655; (b) K. Ruud, P.-O. Åstrand and P. R. Taylor, *J. Chem. Phys.*, 2000, **112**, 2668; (c) T. A. Ruden and K. Ruud, in: *Calculation of NMR and EPR Parameters. Theory and Applications*, M. Kaupp, M. Bühl and V. G. Malkin, eds., Wiley-VCH, Weinheim, 2004, p. 153.
44. M. Bühl, P. Imhof and M. Repisky, *Chem. Phys. Chem.*, 2004, **5**, 414.
45. M. P. Waller and M. Bühl, *J. Comput. Chem.*, 2007, **28**, 1531.
46. For a recent review see: L. B. Krivdin and R. H. Contreras, *Ann. Rep. NMR Spectrosc.*, 2007, **61**, 133.
47. (a) J. Khandogin and T. Ziegler, *J. Phys. Chem. A*, 2000, **104**, 113; (b) J. Autschbach and T. Ziegler, *J. Chem. Phys.*, 2000, **113**, 936; (c) J. Autschbach and T. Ziegler, *J. Chem. Phys.*, 2000, **113**, 9410; (d) J. Autschbach and T. Ziegler, in: *Calculation of NMR and EPR Parameters. Theory and Applications*, M. Kaupp, M. Bühl and V. G. Malkin, eds., Wiley-VCH, Weinheim, 2004, p. 249.
48. A. J. Rossini and R. W. Schurko, *J. Am. Chem. Soc.*, 2006, **128**, 10391.
49. N. Di Fiori, A. M. Orendt, M. C. Caputo, M. B. Ferraro and J. C. Facelli, *Magn. Reson. Chem.*, 2004, **42**, S41.
50. M. Bühl and F. T. Mauschick, *Magn. Reson. Chem.*, 2004, **42**, 737.
51. S. Berger, W. Bock, G. Frenking, V. Jonas and V. Müller, *J. Am. Chem. Soc.*, 1995, **117**, 3820.
52. (a) Nakatsuji, T. Nakao and H. Nakatsuji, *Chem. Phys. Lett.*, 1990, **167**, 571; (b) Z.-M. Hu and T. Nakajima, *Chem. Phys. Lett.*, 1997, **275**, 429.
53. S. Grigoleit and M. Bühl, *Chem. Eur. J.*, 2004, **10**, 5541.
54. R. Koch and T. Bruhn, *J. Mol. Model.*, 2006, **12**, 723.
55. D. Rehder, T. Polenova and M. Bühl, *Ann. Rep. NMR Spectrosc.*, 2007, **62**, 49.
56. M. P. Waller, M. Bühl, K. R. Geethalakshmi, D. Wang and W. Thiel, *Chem. Eur. J.*, 2007, **13**, 4723.
57. M. Bühl, R. Schurhammer and P. Imhof, *J. Am. Chem. Soc.*, 2004, **126**, 3310.
58. N. Pooransingh, E. Pomerantseva, M. Ebel, S. Jantzen, D. Rehder and T. Polenova, *Inorg. Chem.*, 2003, **42**, 1256.
59. (a) J. Y. Kravitz, V. L. Pecoraro and H. A. Carlson, *J. Chem. Theory Comput.*, 2005, **1**, 1265; (b) S. Raugei and P. Carloni, *J. Phys. Chem. B*, 2006, **110**, 3747.
60. U. G. Nielsen, A. Boisen, M. Brorson, C. J. H. Jacobsen, H. J. Jakobsen and J. Skibsted, *Inorg. Chem.*, 2002, **41**, 6432.
61. M. R. Hansen, G. K. H. Madsen, H. J. Jakobsen and J. Skibsted, *J. Phys. Chem. B*, 2006, **110**, 5975.
62. L. Truflandier, M. Paris, C. Payen and F. Boucher, *J. Phys. Chem. B*, 2006, **110**, 21403.
63. M. Bühl, *Magn. Reson. Chem.*, 2006, **44**, 661.
64. G. Schreckenbach and T. Ziegler, *Int. J. Quant. Chem.*, 1997, **61**, 899.
65. R. Bouten, E. J. Baerends, E. vam Lenthe, L. Visscher, G. Schreckenbach and T. Ziegler, *J. Phys. Chem. A*, 2000, **104**, 5600.
66. M. Bühl, *Theor. Chem. Acct.*, 2002, **107**, 336.
67. M. Bühl, *J. Phys. Chem. A*, 2002, **106**, 10505.
68. I. Ciofini and C. Adamo, *J. Mol. Struct. (Theochem.)*, 2006, **762**, 133.
69. K. J. Ooms, K. W. Feindel, V. V. Terskikh and R. E. Wasylishen, *Inorg. Chem.*, 2006, **45**, 8492.
70. K. W. Feindel, K. J. Ooms and R. E. Wasylishen, *Phys. Chem. Chem. Phys.*, 2007, **9**, 1226.
71. M. Bühl, O. L. Malkina and V. G. Malkin, *Helv. Chim. Acta*, 1996, **79**, 742.

72. M. Bühl, *Chem. Phys. Lett.*, 1997, **267**, 25.
73. G. Schreckenbach, *J. Chem. Phys.*, 1999, **110**, 11936.
74. B. Wrackmeyer, O. L. Tok and A. A. Koridze, *Magn. Reson. Chem.*, 2004, **42**, 750.
75. M. Bühl and H. Kabrede, *J. Chem. Theory Comput.*, 2006, **2**, 1282.
76. M. Bühl and S. Grigoleit, *Organometallics*, 2005, **24**, 1516.
77. (a) B. Wrackmeyer, H. E. Maisel, O. L. Tok, W. Milius and M. Herberhold, *Z. Anorg. Allg. Chem.*, 2004, **630**, 2106. (b) No data are tabulated in that paper; for isocyanoferrocene, observed and computed $\delta(^{57}\mathrm{Fe})$ are 1613.7 and 1648.1 ppm, respectively: B. Wrackmeyer, private communication.
78. V. Vrček and M. Bühl, *Organometallics*, 2006, **25**, 358.
79. N. Godbout, R. Havlin, R. Salzmann, P. G. Debrunner and E. Oldfield, *J. Phys. Chem. A*, 1998, **102**, 2342.
80. (a) M. T. McMahon, A. C. deDios, N. Godbout, R. Salzmann, D. D. Laws, H. Le, R. H. Havlin and E. Oldfield, *J. Am. Chem. Soc.*, 1998, **120**, 4784; (b) Review: L. K. Sanders, W. D. Arnold and E. Oldfield, *J. Porphyrins Phthalocyanines*, 2001, **5**, 323.
81. M. Bühl and F. T. Mauschick, *Organometallics*, 2003, **22**, 1422.
82. A. Karlsson, A. Broo and P. Ahlberg, *Can. J. Chem.*, 1999, **77**, 628.
83. C. Janak, T. Dorn, H. Paulsen and B. Wrackmeyer, *Z. Anorg. Allg. Chem.*, 2001, **627**, 1663.
84. M. Bühl and F. T. Mauschick, *Phys. Chem. Chem. Phys.*, 2002, **4**, 5508.
85. M. Bühl, F. T. Mauschick, F. Terstegen and B. Wrackmeyer, *Angew. Chem. Int. Ed.*, 2002, **41**, 2312.
86. J. C. C. Chan and S. C. F. Au-Yeung, *Ann. Rep. NMR Spectrosc.*, 2000, **41**, 1.
87. (a) J. C. C. Chan, S. C. F. Au-Yeung, P. J. Wilson and G. A. Webb, *J. Mol. Struct. (Theochem.)*, 1996, **365**, 125; (b) J. C. C. Chan and S. C. F. Au-Yeung, *J. Mol. Struct. (Theochem.)*, 1997, **393**, 93; (c) J. C. C. Chan and S. C. F. Au-Yeung, *J. Phys. Chem.*, 1997, **101**, 3637.
88. N. Godbout and E. Oldfield, *J. Am. Chem. Soc.*, 1997, **119**, 8065.
89. S. Grigoleit and M. Bühl, *J. Chem. Theory Comput.*, 2005, **1**, 181.
90. X.-P. Xu and S. C. F. Au-Yeung, *J. Am. Chem. Soc.*, 2000, **122**, 6468.
91. M. Bühl, D. Hnyk and J. Macháček, *Chem. Eur. J.*, 2005, **11**, 4109.
92. O. Q. Munro, S. C. Shabalala and N. J. Brown, *Inorg. Chem.*, 2001, **40**, 3303.
93. M. Bühl, S. Grigoleit, H. Kabrede and F. T. Mauschick, *Chem. Eur. J.*, 2006, **12**, 477.
94. C. J. Jameson and D. Rehder, *J. Am. Chem. Soc.*, 1987, **109**, 2589.
95. R. Bramley, M. Brorson, A. M. Sargeson and C. E. Schäffer, *J. Am. Chem. Soc.*, 1985, **107**, 2780.
96. P. Manninen and J. Vaara, *Phys. Rev. A*, 2004, **69**, 022503.
97. R. Herges and A. Papafilippopoulos, *Angew. Chem. Int. Ed.*, 2001, **40**, 4671.
98. Y. Zhang, S. Mukherjee and E. Oldfield, *J. Am. Chem. Soc.*, 2005, **127**, 2370.
99. A. S. Lipton, R. W. Heck and P. D. Ellis, *J. Am. Chem. Soc.*, 2004, **126**, 4735.
100. R. E. White and T. P. Hanusa, *Organometallics*, 2006, **25**, 5621.
101. M. Bühl, *J. Phys. Chem. A*, 1997, **101**, 2514.
102. M. Bühl, G. Hopp, W. v. Philipsborn, S. Beck, M. Prosenc, U. Rief and H.-H. Brintzinger, *Organometallics*, 1996, **15**, 778.
103. I. Hung and R. W. Schurko, *J. Phys. Chem. B*, 2004, **108**, 9060.
104. M. Sugimoto, M. Kanayama and H. Nakatsuji, *J. Phys. Chem.*, 1992, **96**, 4375.
105. A. Y. H. Lo, T. E. Bitterwolf, C. L. B. Macdonald and R. W. Schurko, *J. Phys. Chem. A*, 2005, **109**, 7073.
106. M. Bühl, *Chem. Eur. J*, 1999, **5**, 3514.
107. M. Filatov and D. Cremer, *J. Chem. Phys.*, 2003, **119**, 701.
108. D. L. Bryce and R. E. Wasylishen, *Phys. Chem. Chem. Phys.*, 2002, **4**, 3591.
109. M. A. M. Forgeron and R. E. Wasylishen, *J. Am. Chem. Soc.*, 2006, **128**, 7817.
110. N. LeBlond, H. P. A. Mercier, D. A. Dixon and G. J. Schrobilgen, *Inorg. Chem.*, 2000, **39**, 449.
111. H. Cho, W. A. de Jong, B. K. McNamara, B. M. Rapko and I. E. Burgeson, *J. Am. Chem. Soc.*, 2004, **126**, 11583.
112. M. Bühl, S. Gaemers and C. J. Elsevier, *Chem. Eur. J.*, 2000, **6**, 3272.
113. H. P. Hratchian and M. C. Milletti, *J. Mol. Struct. (Theochem.)*, 2005, **724**, 45.
114. A. Bagno and M. Bonchio, *Magn. Reson. Chem.*, 2004, **42**, S79.

115. J. Autschbach and S. Zheng, *Magn. Reson. Chem.*, 2006, **44**, 989.
116. See for instance: V. G. Malkin, O. L. Malkina and D. R. Salahub, *Chem. Phys. Lett.*, 1996, **261**, 335.
117. K. J. Ooms and R. E. Wasylishen, *J. Am. Chem. Soc.*, 2004, **126**, 10972.
118. T. C. Ramalho, M. Bühl, J. D. Figueroa-Villa and R. B. de Alencastro, *Helv. Chim. Acta*, 2005, **88**, 2705.
119. J. M. Ernsting, S. Gaemers and C. J. Elsevier, *Magn. Reson. Chem.*, 2004, **42**, 721.
120. W. Leitner, M. Bühl, R. Fornika, C. Six, W. Baumann, E. Dinjus, M. Kessler, C. Krüger and A. Rufinska, *Organometallics*, 1999, **18**, 1196.
121. L. Orian, A. Bisello, S. Santi, A. Ceccon and G. Saielli, *Chem. Eur. J.*, 2004, **10**, 4029.
122. J. Holz, O. Zayas, H. Jiao, W. Baumann, A. Spannenberg, A. Monsees, T. H. Riermeier, J. Almena, R. Kadyrov and A. Börner, *Chem. Eur. J.*, 2006, **12**, 5001.
123. M. Bühl, *Organometallics*, 1997, **16**, 261.
124. M. Bühl, in: *Modeling NMR Chemical Shifts: Gaining Insights into Structure and Environment*, J. C. Facelli and A. DeDios, eds., ACS Symposium Series, Vol. 732, Washington DC, 1999, p. 240.
125. J. G. Donkervoort, M. Bühl, J. M. Ernsting and C. J. Elsevier, *Eur. J. Inorg. Chem.*, 1999, 27.
126. M. Bühl, M. Håkansson, A. H. Mahmoudkhani and L. Öhrström, *Organometallics*, 2000, **19**, 5589.
127. M. Bühl, W. Baumann, R. Kadyrov and A. Börner, *Helv. Chim. Acta*, 1999, **82**, 811.
128. T. Ramnial, C. D. Abernethy, M. D. Spicer, I. D. McKenzie, I. D. Gay and J. A. C. Clyburne, *Inorg. Chem.*, 2003, **42**, 1391.
129. G. A. Bowmaker, R. K. Harris, B. Assadollahzadeh, D. C. Apperley, P. Hodgkinson and P. Amornsakchai, *Magn. Reson. Chem.*, 2004, **42**, 819.
130. D. L. Bryce and R. E. Wasylishen, *Inorg. Chem.*, 2002, **41**, 4131.
131. (a) H. Nakatsuji, K. Kanda, K. Endo and T. Yonezawa, *J. Am. Chem. Soc.*, 1984, **106**, 4653; (b) H. Nakatsuji, T. Nakao and K. Kanda, *Chem. Phys.*, 1987, **118**, 25; (c) P. D. Ellis, J. D. Odom, A. S. Lipton and J. M. Gulick, *J. Am. Chem. Soc.*, 1993, **115**, 755; (d) T. Higashioji, M. Hada, M. Sugimoto and H. Nakatsuji, *Chem. Phys.*, 1996, **202**, 159.
132. S. Kidamby and A. Ramamoorthy, *J. Phys. Chem. A*, 2002, **106**, 10363.
133. (a) S. S. Kidamby and A. Ramamoorthy, *Inorg. Chem.*, 2003, **42**, 2200; (b) S. S. Kidamby, D.-K. Lee and A. Ramamoorthy, *Inorg. Chem.*, 2003, **42**, 3142.
134. L. Hemmingsen, L. Olsen, J. Antony and S. P. A. Sauer, *J. Biol. Inorg. Chem.*, 2004, **9**, 591.
135. M. J. Willians, K. W. Feindel, K. J. Ooms and R. E. Wasylishen, *Chem. Eur. J.*, 2006, **12**, 159.
136. K. J. Ooms, K. W. Feindel, M. J. Willans, R. E. Wasylishen, J. V. Hanna, K. J. Pike and M. E. Smith, *Solid State Nucl. Magn. Reson.*, 2005, **28**, 125.
137. A. Bagno and G. Saielli, *Theor. Chem. Acct.*, 2007, **117**, 603.
138. A. Rodriguez-Forta, P. Alemany and T. Ziegler, *J. Phys. Chem. A*, 1999, **103**, 8288.
139. A. Bagno, M. Bonchio, A. Sartorel and G. Scorrano, *Chem. Phys. Chem.*, 2003, **4**, 517.
140. A. Bagno, M. Bonchio and J. Autschbach, *Chem. Eur. J.*, 2006, **12**, 8460.
141. (a) J. Gracia, J. M. Poblet, J. Autschbach and L. P. Kazanski, *Eur. J. Inorg. Chem.*, 2006, 1139; (b) J. Gracia, J. M. Poblet, J. A. Fernandez, J. Autschbach and L. P. Kazanski, *Eur. J. Inorg. Chem.*, 2006, 1149.
142. L. P. Kazansky and T. Yamase, *J. Phys. Chem. A*, 2004, **108**, 6437.
143. J. Autschbach, B. A. Hess, M. P. Johansson, J. Neugebauer, M. Patzchke, P. Pyykkö, M. Reiher and D. Sundholm, *Phys. Chem. Chem. Phys.*, 2004, **6**, 11.
144. A. Bagno and M. Bonchio, *Angew. Chem. Int. Ed.*, 2005, **44**, 2023.
145. B. M. Still, P. G. A. Kumar, J. R. Aldrich-Wright and W. S. Price, *Chem. Soc. Rev.*, 2007, **36**, 665.
146. T. M. Gilbert and T. Ziegler, *J. Phys. Chem. A*, 1999, **103**, 7535.
147. E. P. Fowe, P. Belser, C. Daul and H. Chermette, *Phys. Chem. Chem. Phys.*, 2005, **7**, 1732.
148. K. R. Koch, M. R. Burger, J. Kramer and A. N. Westra, *Dalton Trans.*, 2006, 3277.
149. (a) J. Autschbach and B. LeGuennic, *Chem. Eur. J.*, 2004, **10**, 2581; (b) B. LeGuennic, K. Matsumoto and J. Autschbach, *Magn. Reson. Chem.*, 2004, **42**, S99; (c) W. Chen, F. Liu, K. Matsumoto, J. Autschbach, B. LeGuennic, T. Ziegler, M. Maliarik and J. Glaser, *Inorg. Chem.*, 2006, **45**, 4526–4536.
150. M. Sterzel and J. Autschbach, *Inorg. Chem.*, 2006, **45**, 3316.

151. W. P. Oziminski, P. Garnuszek, E. Bednarek and J. C. Dobrowolski, *Inorg. Chim. Acta*, 2007, **360**, 1902.
152. K. Spiegel, U. Rothlisberger and P. Carloni, *J. Phys. Chem. B*, 2004, **108**, 2699.
153. E. Kogut, J. A. Tang, A. J. Lough, C. M. Widdifield, R. W. Schurko and U. Fekl, *Inorg. Chem.*, 2006, **45**, 8850.
154. (a) J. Autschbach and T. Ziegler, *J. Am. Chem. Soc.*, 2001, **123**, 3341; (b) J. Autschbach, *J. Chem. Phys.*, 2007, **127**, 124106.
155. (a) A. Klein, T. Schurr, A. Knödler, D. Gudat, K.-W. Klinkhammer, V. K. Jain, S. Zalis and W. Kaim, *Organometallics*, 2005, **24**, 4125; (b) D. Gudat, V. K. Jain, A. Klein, T. Schurr and S. Zalis, *Eur. J. Inorg. Chem.*, 2005, 4056.
156. H. Nakatsuji, M. Hada, H. Kaneko and C. C. Ballard, *Chem. Phys. Lett.*, 1996, **255**, 195.
157. J. Jokisaari, S. Jarvinen, J. Autschbach and T. Ziegler, *J. Phys. Chem. A*, 2002, **106**, 9313.
158. R. Fukuda, M. Hada and H. Nakatsuji, *J. Chem. Phys.*, 2003, **118**, 1027.
159. J. Vaara, O. L. Malkina, H. Stoll, V. G. Malkin and M. Kaupp, *J. Chem. Phys.*, 2001, **114**, 61.
160. J. Autschbach, C. D. Igna and T. Ziegler, *J. Am. Chem. Soc.*, 2003, **125**, 4937.
161. J. Autschbach and M. Sterzel, *J. Am. Chem. Soc.*, in press.
162. J. Autschbach, A. M. Kantola and J. Jokisaari, *J. Phys. Chem. A*, 2007, **111**, 5343.
163. H. Le Bail, C. Chachaty, P. Rigny and R. Bougon, *J. Phys. Lett.*, 1983, **44**, 1017.
164. (a) G. Schreckenbach, *Inorg. Chem.*, 2002, **41**, 6560; (b) G. Schreckenbach, *Int. J. Quant. Chem.*, 2005, **101**, 372.
165. M. Straka and M. Kaupp, *Chem. Phys.*, 2005, **311**, 45.
166. J. Vaara, *Phys. Chem. Chem. Phys.*, 2007, **40**, 5399.
167. R. K. Harris, P. Hodgkinson, C. J. Pickard, J. R. Yates and V. Zorim, *Magn. Reson. Chem.*, 2007, **45**, S174.
168. L. B. Casablanca and A. C. di Dios, *J. Chem. Phys.*, 2008, **128**, 052201.
169. M. d'Avezac, N. Marzari and F. Mauri, *Phys. Rev. B*, 2007, **76**, 165122.
170. L. Truflandier, M. Paris and F. Boucher, *Phys. Rev. B*, 2007, **76**, 035102.
171. K. J. Ooms, S. E. Bolte, J. J. Smee, B. Baruah, D. C. Crans and T. Polenova, *Inorg. Chem.*, 2007, **46**, 9285.
172. S. E. Bolte, K. J. Ooms, T. Polenova, B. Baruah, D. C. Crans and J. J. Smee, *J. Chem. Phys.*, 2008, **128**, 052317.
173. K. R. Geethalakshmi, M. P. Waller and M. Bühl, *Inorg. Chem.*, 2007, **46**, 11297.
174. J. A. Tang, B. D. Ellis, T. H. Warren, J. V. Hanna, C. L. B. MacDonald and R. W. Schurko, *J. Am. Chem. Soc.*, 2007, **129**, 13049.
175. B. A. Demko and R. E. Wasylishen, *Dalton Trans.*, 2008, **481**.
176. A. Bango and G. Saielli, *J. Am. Chem. Soc.*, 2007, **129**, 11360.

CHAPTER 4

Solid-State NMR Studies of Collagen Structure and Dynamics in Isolated Fibrils and in Biological Tissues

Daniel Huster

Contents

Abstract

Collagen is the most abundant protein on earth. Having a unique amino acid sequence featuring a high content of glycine, proline and hydroxyproline residues, the collagen α-chains form a slightly twisted left-handed polyproline-II-type helix with three amino acids per turn. Three such α-chains form the collagen triple helix, which is the basic building block for collagen fibrils that are characterized by very high tensile strength. Collagen fibrils form basic structures of the extracellular matrix of many biological tissues such as bone, skin, cartilage, teeth, blood vessels tendon and many others. Since collagen is

Institute of Medical Physics and Biophysics, Härtelstr. 16–18, D-04107 Leipzig, Germany

Annual Reports on NMR Spectroscopy, Volume 64
ISSN 0066-4103, DOI 10.1016/S0066-4103(08)00004-5

neither water soluble nor does it form highly ordered crystals, a significant amount of information about isolated and tissue collagen has been acquired by solid-state NMR techniques over the last 30 years. This review will provide an overview of solid-state NMR applications to study structural and dynamical features of collagen. The discussed examples include static and magic-angle spinning NMR studies on isolated collagen fibrils as well as solid-state NMR applications on the dynamics of collagen in biological tissues such as cartilage and bone. Finally, the interaction of water with collagen fibrils will be discussed as the molecular basis for magnetic resonance imaging techniques on the orientation of collagen fibrils in biological tissues.

Keywords: solid-state NMR; molecular dynamics; order parameter; hydration; extracellular matrix

1. INTRODUCTION

With a content of 25–30%, collagen is the most abundant protein in the vertebrate organism. Collagen is an essential scaffold protein, which represents the fibril forming component of connective tissue. Fibrillar collagen is for instance found in the corium, the connective tissue of the intestine and other organs, in cartilage, bone and teeth, in the blood vessels, in tendon, in the cornea and other tissues. Apart form fibrillar collagen a number of other collagen subfamilies are known, such as network, transmembrane, fibril associated collagens with interrupted triplehelices (FACIT) or multiple triple helix and interruptions (MULTIPLEXIN) collagens.[1] Today, as many as 27 different unique collagen types are known. This overwhelming variety is mirrored in the molecular assembly, the supermolecular structure, the distribution of collagen in different tissues, its function and finally the pathology of the different collagen types.[1]

With a tensile strength comparable to that of steel fibrillar collagen represents an ideal material to impart stability to tissues like tendons, ligaments, skin, cartilage, blood vessels and bone.[2] The remarkable tensile strength of collagen can be understood from its unique amino acid composition and secondary structure. Collagen is rich in glycine (Gly), proline (Pro), hydroxyproline (HyPro), alanine (Ala) and glutamic acid (Glu). A single collagen polypeptide chain (called α-chain) consisting of ~1,000 residues forms a slightly twisted left-handed polyproline-II-type helix with three amino acids per turn. There are 42 different polypeptide chains known that form the structural basis of the 27 collagen types.[1] In the α-chain, all peptide bonds of Pro are in *trans* conformation. Three collagen α-chains are coiled together in parallel to form the three stranded collagen triple helix. A requirement of the formation of the superhelix structure is the tightly controlled repeating sequence $(Gly–X–Y)_n$, with X being frequently Pro and Y is often HyPro. This means that in the α-chain every third residue is Gly. In the triple helix, the NH-group of the Gly and the backbone CO of a residue in X-position of a neighbouring chain form a hydrogen bond. These hydrogen bonds are the major stabilizing motifs in the collagen structure. A Gly residue faces a residue in position X of a neighbouring chain and this residue faces a residue in

position Y of the third chain. This structural arrangement is too dense to allow a large side chain explaining the high Gly (~33%) and Ala (~9%) content of collagen. Together with approximately 21% Pro and HyPro and 5% Glu, these five amino acids account for more than two thirds of all residues in collagen. Another structural feature that is important for collagen function is that the side chains of the residues in X- and Y-position point out of the triple helix and are free for binding interactions.[3] A sketch of the collagen architecture with the chemical structure of the most abundant amino acids in collagen is given in Figure 1.

A large variety in the size of the collagen triple helices is found in nature comprising lengths between 14 and 2,400 nm.[4] For collagen type I, the typical length of the collagen triple helix is approximately 300 nm and its diameter is

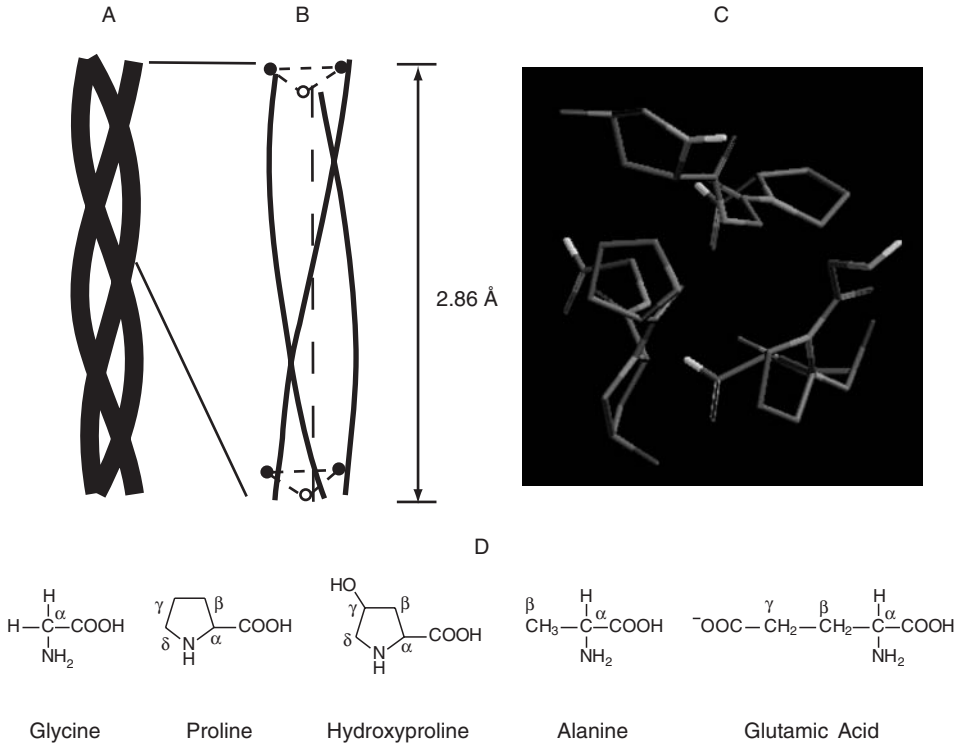

Figure 1 Schematic structure of the collagen triple helix and the most abundant amino acids in collagen. (A) Schematic side view of the collagen triple helix. Three left-handed polyproline-II-type helices are arranged in parallel. (B) The supercoiled helix is schematically shown in this model. On average, the rise per amino acid is 2.9 Å. In the amino acid sequence $(Gly–Pro–HyPro)_n$, Gly (white circle) is facing a Pro residue in X-position and a HyPro in Y-position (black circles). Hydrogen bonds link the three α-chains between the backbone NH of Gly and the backbone CO of Pro in X-position. (C) Atomistic model of a collagen-like peptide determined by X-ray crystallography indicating the dense packing between the three collagen α-chains (top view).[154] Only the sequences Gly–Pro–HyPro, Pro–HyPro–Gly and HyPro–Pro–Gly of each α-chain are shown for clarity. (D) Chemical structures of the five most abundant amino acids in collagen.

about 1.4 nm. A single collagen type I triple helix has an approximate molecular weight of 285 kDa. Collagen types I, II, III, V, XI, XXIV and XXVII form fibrils, which are superstructures of collagen triple helices.[1,3] In the fibril, the collagen molecules are staggered relative to one another by ~67 nm and covalently cross-linked by lysine–hydroxylysine bridges at their non-helical ends.[2,5] In this structure, the arrangement of the collagen triple helices determines the tensile strength of collagen. The fibrillar collagens share a common chain structure that is composed of large collagenous domains. These structures are flanked by N- and C-terminal non-helical extensions called N- and C-propeptides that are characteristic for each collagen type.[6] The typical diameter of the collagen fibrils is between 30 and 300 nm.

The intriguing relation between structure and properties of the different collagens are of interest for several fields of current research and medicine. First, many connective tissues are characterized by very unique properties. Tendons, ligaments or cartilage must respond quickly, robustly and reversibly to deformations caused by mechanical load or dynamic stresses.[7] The viscoelastic properties of many biological tissues are a consequence of the structural arrangement of fibrillar collagen and proteoglycans.[8–11] A schematic representation of the collagen architecture in articular cartilage is given in Figure 2. The versatile molecular dynamics of the different macromolecules, the osmotic pressure and the flow of aqueous tissue fluids represent the physical basis of the unique viscoelastic properties of these soft biological tissues. Therefore, to cope with the various compressive stresses, acting on the tissue under load, these molecules undergo dynamic reorientations of very different geometries within a broad time window.[7] Bone on the other hand represents a composite material of bioapatite and collagen type I, which comprises its stability from the inorganic

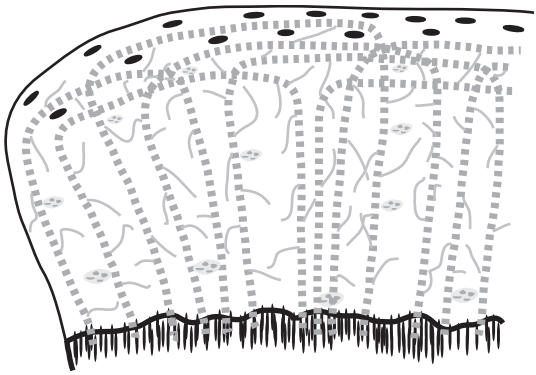

Figure 2 Schematic representation of the spatial organization of the macromolecules in articular cartilage. Collagen (dotted lines) orientation varies with the depth from the articular surface. In the surface zone, the collagen II fibrils run approximately parallel to the surface but reorient in the middle and deep zone to a perpendicular orientation with respect to the surface. The interface to the subchondral bone is formed by more calcified collagen. Proteoglycans (solid lines) form other components of the extracellular matrix in cartilage.

bioapatite and its elasticity from its organic collagen component. Understanding these basic properties of biological materials from a structural and dynamical point of view is an active field of current research in bioscience.

Second, a number of diseases are related to pathological alterations of the connective tissue and in particular of the collagen. For instance, diseases of the intervertebral discs, osteoarthrisis, various skin diseases, osteogenesis imperfecta and Ehlers–Danlos syndrome and others have alerted the public.[12–14] Osteoarthritis and diseases of the intervertebral discs affect a large portion of the population with high life expectancy.[15] Knowledge about collagen structure and biosynthesis is essential for the prevention and therapy of these diseases.

Third, tissue engineering of bone, cartilage, skin, intervertebral discs and other connective tissues is considered a promising therapeutical procedure to treat tissue losses caused by diseases, trauma or age-related wear.[16–19] The success of tissue engineering attempts is strongly related to the choice of the right scaffold materials, in which the artificial tissue is grown. Naturally, this material should closely resemble the natural extracellular matrix of the tissue. In this field, collagen gels have been successfully applied as scaffold materials for tissue engineering.[20–22]

Finally, a number of collagen-based biomaterials are applied in ophthalmology, wound healing, tumor treatment, drug delivery and burn dressing or are used as glue in various biomedical applications.[23]

In all these fields of biophysics, medicine and material science detailed knowledge about structure and dynamics of collagen on an atomic level is indispensable. However, the classical structure methods in chemistry fail to characterize collagen fibrils because they neither form highly ordered crystals for X-ray diffraction studies nor are collagen fibrils soluble to apply solution NMR techniques. Therefore, solid-state NMR spectroscopy has played a central role in the structural and dynamical characterization of collagen since the mid 70s.[24,25] Some of this work has already been reviewed before.[11,26–29] Since collagen is not water soluble, it is naturally amenable to solid-state NMR techniques, however, a few solution NMR studies on relatively short but water soluble collagen-like peptides have been published.[30–32] While first studies required specific labelling with NMR active isotopes, the routine application of magic-angle spinning (MAS) techniques allowed to investigate collagen at natural abundance.[33] The introduction of high-field NMR magnets in solid-state NMR has further prompted researchers to investigate collagen structure and dynamics in intact biological tissues such as cartilage and bone.[34,35]

In addition to determining structural features of biomolecules, solid-state NMR is a very versatile method to study the molecular dynamics of biological macromolecules.[36–41] Motions with correlation times from picoseconds to seconds can be investigated by relaxation time measurements, lineshape analysis or exchange methods. In the solid state, all molecular motions are studied in the absence of an overall tumbling of the molecules that is present in solution NMR and might interfere with the motional analysis.[39] Several parameters accessible from different solid-state NMR experiments contain dynamical information.

First and almost exclusively applied to collagen research are measurements of the amplitudes of the molecular motions. Such information can be easily obtained from motionally averaged anisotropic interactions manifested in motionally averaged solid-state NMR lineshapes. The second method to study molecular dynamics by NMR is based on relaxation time measurements. This is also the standard way of obtaining dynamical information in solution NMR typically involving Lipari–Szabo analysis of T_1, T_2 and NOE data,[42,43] which has been applied to soluble collagen-like peptides in aqueous solution[30] or reconstituted chick calvaria collagen dissolved in acetic acid.[25,44] Third, exchange NMR methods can probe slow motions with correlation times in the millisecond window of correlation times. Several new MAS methods based on the basic three pulse exchange sequence employed on static samples have been developed[45] and a first applications to collagen has already been demonstrated.[46] Fourth, pulsed field gradient (PFG) methods can be applied to investigate translational motions on length scales on the order of tens of nanometers. Such methods are particularly interesting with regard to the diffusion of metabolites and nutrients in biological tissue.[11,47,48]

This review will focus on the application of solid-state NMR methods to investigate collagen with particular emphasis on the dynamical properties of isolated and tissue collagen. We will discuss static and MAS solid-state NMR methods that have been applied to investigate the dynamic properties of fibrillar collagen both in the isolated form and in biological tissue.

2. EXPERIMENTAL METHODS TO STUDY THE MOLECULAR DYNAMICS IN COLLAGEN

For the most part, solid-state NMR studies on collagen helped understanding the dynamics of this molecule in the isolated, hydrated and mineralized form as well as in biological tissues. Here, we will briefly summarize the basics of the NMR methods that were most frequently used to study the molecular dynamics of collagen. For a more comprehensive review of the physical background of these methods, the reader is referred to literature.[41,45,49–53] Relaxation time measurements have not extensively been carried out for collagen and will be omitted from the discussion of methods. We will focus our attention on motional averaged anisotropic interactions and exchange NMR techniques.

2.1 Fast molecular motions: motionally averaged anisotropic interactions

All NMR interactions that are relevant in the solid state are anisotropic and can be described by second rank tensors. Static solid-state NMR lineshapes are typically characterized by a broad powder distribution because the NMR frequency depends on the orientation of a molecular site with respect to the external magnetic field. The orientation dependence of the anisotropic part of the NMR frequency is conveniently expressed in terms of the polar angles (θ, ϕ)

of the $\vec{\mathbf{B}}_0$ field in the principle axis system (PAS) of the respective interaction tensor:[54,55]

$$\omega(\phi,\theta) = \frac{\delta}{2}[3\cos^2\theta - 1 - \eta\sin^2\theta\cos(2\phi)] \tag{1}$$

Here, δ is the anisotropy parameter and η the asymmetry parameter of the respective tensor interaction. In solid samples usually all polar angles are equally populated (powder average) and the NMR spectra are expressed by broad powder lineshapes. Depending on the type of spin interaction, the anisotropy parameter contains the information from the respective tensor interaction. (i) For anisotropic chemical shifts, $\delta_{\mathrm{CSA}} = -\omega_0\sigma_{zz}^{\mathrm{PAS}}$, where ω_0 is the Larmor frequency and $\sigma_{zz}^{\mathrm{PAS}}$ the zz element of the chemical shift tensor in the PAS. The asymmetry parameter may vary between 0 and 1. (ii) In the case of dipolar coupling, the anisotropy parameter is given by $\delta_D^{\mathrm{IS}} = D_{zz}^{\mathrm{PAS}}/2$ for heteronuclear and $\delta_D^{\mathrm{II}} = 3D_{zz}^{\mathrm{PAS}}/2$ for homonuclear dipolar coupling in an isolated spin pair. Here, D_{zz}^{PAS} is the zz element of the dipolar coupling tensor. Since the dipolar interaction is axially symmetric, its asymmetry parameter vanishes. (iii) Finally, for quadrupolar nuclei (such as ^{2}H) the anisotropy parameter is given by the zz element of the electric field gradient tensor of the chemical bond in the PAS according to $\delta_Q = V_{zz}^{\mathrm{PAS}}$. The asymmetry parameter for the electric field gradient tensor in aliphatic C–^{2}H bonds is usually negligible, but molecular motions can yield non-vanishing η_Q values.[52,56]

Molecular motions have a strong effect on the powder lineshapes in solid-state NMR because of the dependence of the NMR frequency on the orientation of a molecule. In the fast motional limit, the correlation times of motions become much shorter than the inverse of the interaction strength ($\tau \ll 1/\delta$). Since many frequency changes occur during one period of signal modulation, the anisotropic NMR frequency is averaged according to

$$\bar{\omega} = \sum_{i=1}^{N} p_i\omega_i = \begin{cases} \gamma B_0 \sum_{i=1}^{N} p_i(\sigma_i^{\mathrm{LF}})_{zz} & \text{for chemical shift anisotropy} \\ \frac{1}{2}\sum_{i=1}^{N} p_i(D_i^{\mathrm{LF}})_{zz} & \text{for heteronuclear dipolar interaction} \\ \sum_{i=1}^{N} p_i(V_i^{\mathrm{LF}})_{zz} & \text{for quadrupolar interaction} \end{cases} \tag{2}$$

Here, a reorientation between N different sites with occupation probabilities p_i is assumed. The motionally averaged interaction tensor is given by the sum of each tensor expressed in the laboratory frame (LF) for a specific molecular orientation weighted by the occupation probability. The average tensor is typically calculated using rotation matrices.[54] For ^{2}H NMR applications, the interaction tensor is more conveniently expressed in its spherical irreducible tensor notation[57] and the time-dependent transformations from the PAS into the LF is expressed by Wigner rotation matrices applying the closure property of the rotation group.[58]

Fast motions lead to a reduction of the width of the anisotropic lineshapes, examples for phenylalanine ring flips and methyl group rotations are given in Figure 3. Therefore, from the shape of a respective anisotropic spectrum, the geometry of motion and an estimate for the upper limit of its correlation time ($\tau \ll 1/\delta$) can be obtained.

For anisotropic interactions with vanishing asymmetry parameter (e.g., dipolar couplings and quadrupolar interaction in aliphatic sites), it is convenient to

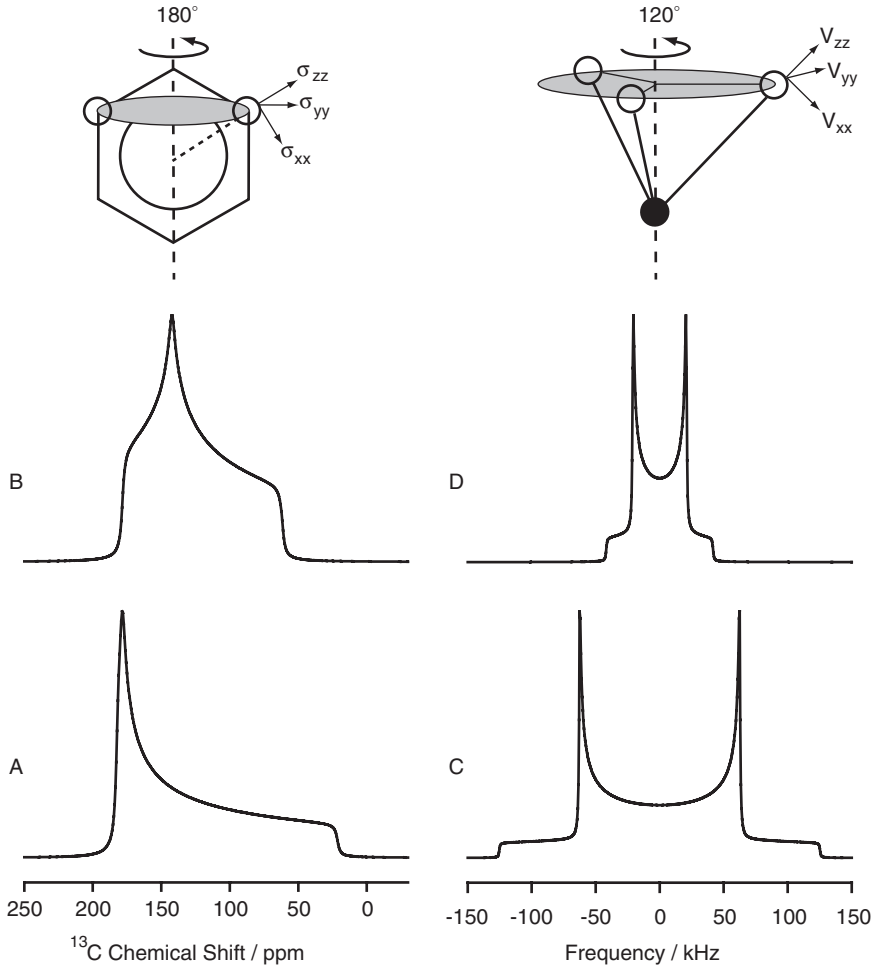

Figure 3 Influence of molecular motions on static solid-state NMR lineshapes. The left column shows simulated ^{13}C NMR spectra in the absence (A) or in the presence (B) of fast 180° ring flips of an aromatic compound. Both the width and the asymmetry parameter of the CSA tensor are influenced by the molecular motion. The right column shows simulated ^{2}H NMR spectra of a CH_3 group in the absence (C) and in the presence (D) of a three-site rotation. Due to the geometry of the methyl group, these motions lead to a reduction of the width of the ^{2}H NMR spectrum to 1/3.

define an order parameter for the amplitude of motion according to:

$$S = \frac{\bar{\delta}}{\delta} \tag{3}$$

where $\bar{\delta}$ and δ are the motionally averaged and full interaction strength, respectively. The order parameter is unity in a rigid molecular segment and zero for fast isotropic reorientations. From the order parameter, the amplitude of motion can be estimated assuming a wobbling in a cone model:[41,59,60]

$$S^2 = \left[\cos\theta_0 \frac{1+\cos\theta_0}{2}\right]^2 \tag{4}$$

In organic solids, most of the dynamical studies were conducted on static samples with selectively deuterated sites[61–71] but also static ^{13}C and ^{15}N measurements have been carried out.[29,39,41] Deuterium is perhaps the most suited nucleus to study molecular dynamics since it has very favourable properties both for lineshape and relaxation analysis.[29,49,50,52,72,73] Very importantly, in an NMR experiment ^{2}H is directly excited as opposed to ^{13}C and ^{15}N, which are usually cross-polarized to improve the sensitivity. Since cross polarization (CP) is sensitive to the strength of the dipolar couplings, large amplitude motions are likely to be overlooked by CP-based methods because little or no polarization transfer is achieved in highly mobile sites.

While anisotropic lineshapes contain a wealth of structural information, they also offer some serious disadvantages. All the spectral intensity is spread out over a relatively broad frequency range, which renders the experiments rather insensitive. Further, due to signal superposition only one or very few molecular sites of a molecule can be observed in one sample, which calls for (specific) isotopic labelling, which is expensive, biochemically highly demanding, or simply not possible for some biological samples. These drawbacks can be overcome by application of MAS.[74] In the MAS experiment, the sample is oriented at an angle of 54.74° with respect to the external $\vec{B}_0$ field and spun about the rotor axis with typical frequencies between ~2 and 15 kHz. By MAS, the spatial spherical tensor components of the CSA Hamiltonian are coherently averaged to yield reasonably narrow lines. With small rotor diameters, MAS frequencies of up to 60 kHz can be achieved. At such high MAS frequencies, dipolar couplings are also averaged. MAS collects the spectral intensity of the anisotropic NMR signal into a narrow centerband and a series of spinning sidebands that are placed at integer multiples of the rotational frequency. In combination with high-power dipolar decoupling, highly resolved NMR spectra are obtained, where the signal line width is of the order of a fraction of one ppm up to a few ppm. This allows the simultaneous detection of several sites of a given molecule. The disadvantage of the MAS technique is that all anisotropic interactions and their information content with regard to molecular structure and dynamics are averaged out. However, the anisotropic information of the solid-state NMR spectra can be reintroduced by slow spinning[75] or recoupling methods.[76–78] MAS lineshapes are also sensitive to molecular motions, which can

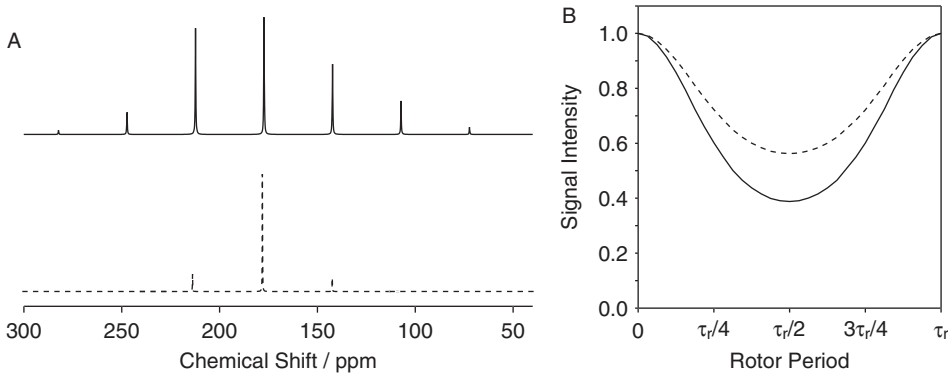

Figure 4 Influence of molecular dynamics on NMR data acquired under MAS conditions. Molecular motions reduce the intensity of the MAS sidebands in the NMR spectrum (A) or lead to less pronounced signal dephasing of the MAS time signal over one rotor period (B). NMR time domain signals and spectra of rigid and mobile sites are shown as solid and dashed lines, respectively.

be observed either in the frequency or in the time domain. Molecular motions lead to a decrease in the sideband intensity in the frequency domain or smaller dephasing of the MAS time domain signal as shown in Figure 4. If MAS measurements are carried out as two-dimensional separated local field experiments,[79] these techniques provide comprehensive dynamical information about all resolved signals in one experiment. This means that the information about the averaged interaction tensor, e.g., the motional amplitude, can be determined for each resolved signal of a single separated local field experiment. A number of recoupling pulse sequences have been developed to reintroduce CSAs, dipolar couplings or quadrupolar interactions.[76–78] In the indirect dimension of a separated local field experiment, either powder lineshapes or MAS sideband spectra are measured. The information about the anisotropic interaction tensor is then obtained by numerical simulations of the spectra or sideband analysis.[80] Numerous studies on molecular dynamics in solids determined by separated local field experiments under magic-angle spinning conditions are available in literature, including for instance crystalline proteins,[81–83] membrane proteins[84–91] and polymers.[92]

2.2 Intermediate timescale motions: dynamic lineshapes

For dynamic processes with correlation times comparable to the inverse of the strength of the NMR interaction ($\tau \sim 1/\delta$), very characteristic alterations of the NMR lineshapes and intensities are observed. Such effects are typically observed for dynamic processes with correlation times in the microsecond time window. This represents the classical exchange problem that is described in many NMR textbooks.[93–96] If a molecule exists in two (or more) different states with characteristic resonance frequencies, molecular dynamics that interconverts between these states will influence the resulting NMR spectrum. If the exchange

rate is slow compared to the difference in resonance frequencies, both NMR signals characteristic of each state are observed. For dynamic processes with an exchange rate of the order of the difference of the resonance frequencies a severe broadening of the NMR spectrum is obtained eventually yielding a single broad line of low intensity. Further increase in the exchange rate will result in a single narrow line again indicative of fast exchange.

Static solid-state NMR lineshapes that are influenced by intermediate timescale dynamics not only provide information about the geometry of motion but also about its exact correlation time. Unlike NMR spectra averaged by fast motional processes that only provide the upper limit of correlation time, in the intermediate timescale regime the lineshapes very sensitively depend on the correlation time of motion. Thus the exchange rate can be obtained by comparison of experimental with numerically simulated NMR spectra.

In this treatment, the time evolution of the complex transverse magnetization $\vec{\mathbf{M}}$ is given by:[53,97]

$$\frac{\mathrm{d}\vec{\mathbf{M}}(t)}{\mathrm{d}t} = (i\tilde{\boldsymbol{\omega}} + \tilde{\boldsymbol{\Pi}})\vec{\mathbf{M}}(t) \tag{5}$$

where $\vec{\mathbf{M}}$ represents a vector with a complex transverse magnetization for each site, $M_i(t)$. The diagonal matrix $\tilde{\boldsymbol{\omega}}$ is composed of the precession frequencies of the jth site and depends on the molecular orientation according to Equation (1). The matrix $\tilde{\boldsymbol{\Pi}}$ is the exchange matrix composed of off-diagonal elements Π_{jl} that represent the exchange rate k from a given state l to the state j, each representative of a specific orientation of the molecule. The exchange rates are directly related to the correlation time of motion, for instance for a two-site exchange $k = 1/(2\tau_c)$.

The solution of the differential Equation (5) is simply given by

$$\vec{\mathbf{M}}(t) = \vec{\mathbf{1}}\{\exp[(i\tilde{\boldsymbol{\omega}} + \tilde{\boldsymbol{\Pi}})t]\}\vec{\mathbf{M}}(0) \tag{6}$$

The resulting magnetization therefore depends on the frequencies of the different states and the exchange rate(s) between them. The NMR spectrum is obtained after diagonalizing the matrix $(i\tilde{\boldsymbol{\omega}} + \tilde{\boldsymbol{\Pi}})$, exponentiating it and rotating it back to the original frame of reference and subsequently Fourier transforming it.

Most often, intermediate timescale NMR spectra are acquired for ^{2}H. Due to the fast decay of the free induction decay of this quadrupolar nucleus, it is technically difficult to detect the first points of the NMR signal because of the ring down of the transmitter (dead-time problem). The application of a solid echo[98] circumvents this problem, but molecular motions that occur during the refocusing time of typically some tens of microseconds interfere with the refocusing of the signal resulting in lineshape distortions. These effects need to be taken into account when experimental lineshapes are simulated, which adds two extra time periods to the evolution of the magnetization during the echo time τ:

$$\vec{\mathbf{M}}(t) = \vec{\mathbf{1}}\{\exp[(\tilde{\boldsymbol{\Pi}} \pm i\tilde{\boldsymbol{\omega}})\tau]\exp[(\tilde{\boldsymbol{\Pi}} \mp i\tilde{\boldsymbol{\omega}})\tau]\exp[(i\tilde{\boldsymbol{\omega}} + \tilde{\boldsymbol{\Pi}})t]\}\vec{\mathbf{M}}(0) \tag{7}$$

Intermediate timescale motions can also influence MAS NMR spectra. Molecular motions with frequencies close to the characteristic frequencies of the MAS experiment, which are several tens of kHz for the dipolar decoupling[99] and several kHz for the MAS frequency,[100] will interfere with the line narrowing of MAS. Such 'dynamic MAS' spectra can be understood and simulated using Floquet[101] or extended exchange theory methods.[102]

2.3 Slow motions: exchange NMR

Slow dynamics of collagen has only been investigated in one study so far,[46] but it is of crucial importance for the viscoelastic properties of biological tissues and collagen-based materials. Therefore, we will briefly summarize the principle of the experiment and refer to literature for a comprehensive description of the various static and MAS exchange techniques.[45,54,92,103]

Slow molecular dynamic processes with correlation times longer than the inverse of the interaction strength ($\tau \gg 1/\delta$) do not influence the NMR lineshape. Information about the geometry and correlation time of motion can be obtained from exchange NMR methods that were first introduced by the two-dimensional exchange method.[104] The idea of that experiment is that the NMR frequency is detected before and after a mixing time period t_m during which the dynamic process takes place. A molecular reorientation is recorded by a change in the anisotropic chemical shifts, which are characteristic for each molecular orientation leading to off-diagonal intensity in two-dimensional exchange spectra.[45] The signal intensity in the one- or two-dimensional exchange experiment that probes slow exchange can be calculated from the sum of all spectral contributions from exchanges between sites i and j ($S^{i,j}$)weighted by the probability ($p_{ij}(\tau_m)$) for the exchange to take place during the mixing time t_m:

$$\begin{aligned} S(\omega, \tau_m) &= \sum_{i,j} p_{i,j}(\tau_m) S^{i,j}(\omega) \text{ for 1D} \\ S(\omega_1, \omega_2, \tau_m) &= \sum_{i,j} p_{i,j}(\tau_m) S^{i,j}(\omega_1, \omega_2) \text{ for 2D} \end{aligned} \tag{8}$$

Later, MAS exchange experiments were developed to increase spectral resolution and overall sensitivity of the experiment. The most recent innovations are one-dimensional MAS exchange experiments such as trODESSA[56] and CODEX.[105] In the CODEX experiment, the change in the anisotropic chemical shift that is usually observed in static exchange experiments,[104] is converted into an intensity change that can be observed under MAS conditions.[105] The anisotropic chemical shift information is obtained by recoupling using a train of π pulses for several rotor periods ($N\tau_r$). This not only increases the sensitivity of the experiment, it also allows the site-specific detection of exchange in larger molecules. The signal intensity of the CODEX exchange experiment is calculated according to:

$$S(\omega, N\tau_r, \tau_m) = \sum_{i,j} p_{i,j}(\tau_m) \langle \cos[N\tau_r(\phi^i - \phi^j)] \rangle S^{MAS}(\omega) \tag{9}$$

The cosine term contains the information about the amplitude of the dynamic process, since the change in NMR frequency that follows the reorientation of the molecule in the magnetic field is recorded as an NMR phase of the MAS signal. Accordingly, no alterations of the MAS signal intensity (S^{MAS}) are observed in the absence of slow dynamic processes. From the $p_{ij}(\tau_m)$ the correlation time of the molecular process is determined.

3. SELECTED EXAMPLES

In this chapter, we will review the experimental work that has been carried out over the last 30 years to study the structure and dynamics of collagen by solid-state NMR methods. These studies started out on samples of mostly isolated isotopically enriched collagen and developed with improving NMR technology such that collagen NMR spectra could be acquired at natural abundance. With ongoing technological development, it is now routinely possible to study collagen in biological tissues and extract information about the molecular dynamics of the collagen fibrils. The data will be presented in a somewhat chronological order, which also coincides with the development of the NMR methods. While this review focuses on NMR spectroscopic studies, some remarks about its impact on magnetic resonance imaging will conclude this chapter.

3.1 Static NMR studies on isolated collagen fibrils

More than 30 years ago, the group of Dennis A. Torchia started the first solid-state NMR studies on collagen.[25,26,29] First solid-state NMR studies were carried out on calf Achilles tendon and rat tail tendon collagen since collagen constitutes about 95% of the dry weight of these tissues.[25] A typical static ^{13}C NMR spectrum of calf tail tendon collagen recorded in 1976 is shown in Figure 5(A). The ^{13}C NMR spectrum is characterized by a well-defined carbonyl/aromatic signal and a prominent aliphatic peak. Since neither MAS nor separated local field experiments were routine in these days, this static solid-state NMR spectrum at natural abundance is characterized by a large amount of signal superposition that could not be resolved in one dimension. Therefore, selective isotopic labelling with ^{13}C was used to highlight the signals of single amino acids in collagen obtained from natural sources.[106] The effect of isotopic labelling can be seen in Figure 5, where reconstituted chick calvaria collagen was detected enriched in Gly ^{13}CO (B) or $^{13}C\alpha$ (C). In contrast to the 19,500 accumulations of spectrum (A), only 4,900 scans were acquired for spectrum (B). These relatively simple NMR spectra already revealed the power of the NMR technique to detect molecular motions: (i) the Cα linewidth of the Gly Cα signal at 20°C is motionally averaged because the same signal shows about twice the linewidth at –95°C, where molecular motions were frozen out (Figure 5(D)). (ii) First ^{13}C relaxation measurement indicated that the collagen backbone motions are anisotropic with an amplitude of $\sim 30^{\circ}$. The correlation time of that motion was estimated to be in the range 10^{-6} to 10^{-8} s.[25]

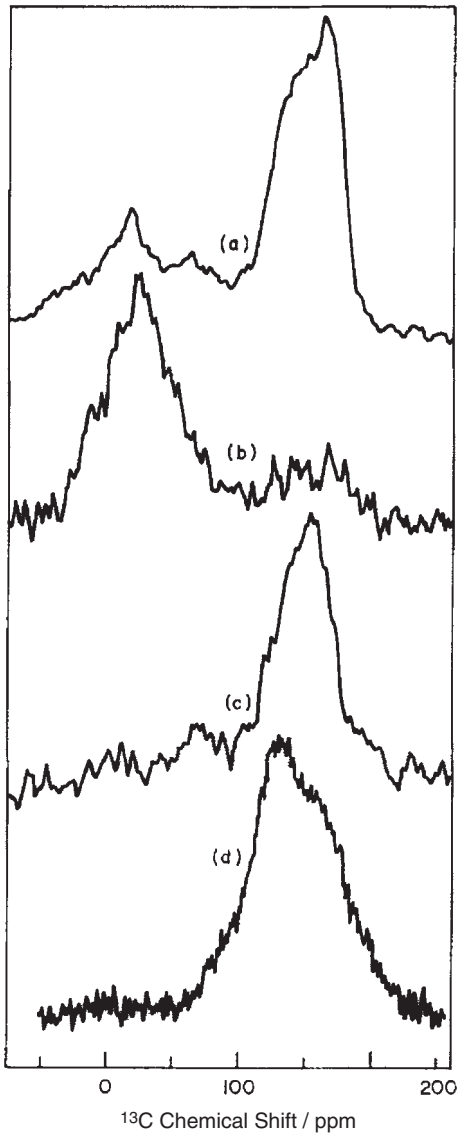

Figure 5 ^{1}H decoupled 15.09 MHz static ^{13}C NMR spectra of various collagen samples. (A) Calf tail tendon collagen at natural abundance, (B) ^{13}CO Gly and (C) $^{13}C\alpha$ Gly enriched reconstituted chick calvaria collagen. Spectra A–C were collected at 20°C. (D) Dehydrated $^{13}C\alpha$ Gly enriched reconstituted chick calvaria collagen recorded at −95°C. Chemical shifts were recorded relative to CS_2. Reprinted from ref. 25 (with permission).

More comprehensive ^{13}C NMR investigations on natural abundance and ^{13}C labelled collagen revealed that the molecular motions in collagen are not greatly influenced by cross-links present in native collagen.[44] Further, the principle values of the Gly ^{13}CO chemical shift tensor were determined. A significant

reduction of the span of the CSA tensor from $\Delta\sigma = 144$ ppm in rigid polyglycine to $\Delta\sigma = 103$ ppm in collagen was observed, which could be explained by molecular rotations about the long axis of collagen.

To conclude this series of ^{13}C NMR studies on collagen the side chain motions of the molecule were studied.[107] To this end, chick calvaria collagen with ^{13}C enriched $^{13}C\beta$ Ala, $^{13}C\varepsilon$ Met, $^{13}C\delta$ Lys or $^{13}C\delta$ Glu were prepared. Although most of the NMR work on these samples was carried out in acetic acid solution, the solid-state NMR spectra of these samples showed motionally averaged anisotropic ^{13}C NMR lines (with $\Delta\sigma$ values between 29 and 34 ppm for the aliphatics and 153 ppm for the Glu CO) for the respective sites indicating rapid reorientations of these molecular segments.

Next, a series of papers from the Torchia group reported the application of ^{2}H labelling as a probe for molecular mobility.[108–110] Deuterium is a very well-suited NMR nucleus because both amplitudes and correlation times of motions can be determined from ^{2}H NMR spectra. In particular in the intermediate timescale regime ^{2}H NMR spectra are very sensitive to molecular motions. The deuterium electric field gradient tensor is axially symmetric along the C–^{2}H bond, which further simplifies the analysis. Further, quadrupolar relaxation dominates all other relaxation mechanisms, which simplifies the analysis. Finally, the low natural abundance of ^{2}H of 0.016% virtually eliminates the unlabelled background if sufficient isotopic enrichment is achieved.

For the analysis, experimental ^{2}H NMR spectra are compared to simulated spectra, that are calculated applying a specific motional model. In particular, side chain motions have been studied by ^{2}H NMR spectroscopy. Using collagen molecules with ^{2}H labelled Ala,[108,109] and leucine (Leu)[109,110] these spectra showed typical features of motionally averaged lineshapes at ambient temperature. Only at low temperature, the characteristic Pake spectra with the full quadrupolar splitting were detected. Application of a two-site jump for the Ala side chains in chick calvaria collagen revealed fast reorientations of the Cα–Cβ bond vector over an angle of $\sim 30^{\circ}$ with a correlation time $\sim 10^{-7}$ s.[108,109] Fast two-site exchange with an amplitude of $\sim 55^{\circ}$ and a correlation time of 8×10^{-7} s were also found for Leu side chains at 30°C.[110] A typical example of static ^{2}H NMR lineshapes for [$^{2}H_{10}$] Leu-labelled collagen as a function of temperature is given in Figure 6.

In a series of papers from the second half of the 1980s Torchia and co-workers investigated the molecular dynamics of collagen in intact hard and soft connective tissues. To this end, animals were either fed with isotopically labelled amino acids or these compounds were directly injected into the animals. Thus, collagen labelled with ^{2}H, ^{13}C, ^{15}N or ^{19}F was produced and isolated from tendon, calvaria, tail or sternum of those animals.

The backbone motions of collagen were investigated by static ^{13}C solid-state NMR methods using ^{13}CO Gly labelled collagen.[111] The amplitude of the backbone motion was determined from an analysis of the motionally averaged CSA tensor of ^{13}CO Gly in collagen. The analysis assumed a reorientation about the long axis of the collagen molecule. Root mean square amplitudes of 41, 33 and 14° were calculated for the backbone motions in uncross-linked, cross-linked, and

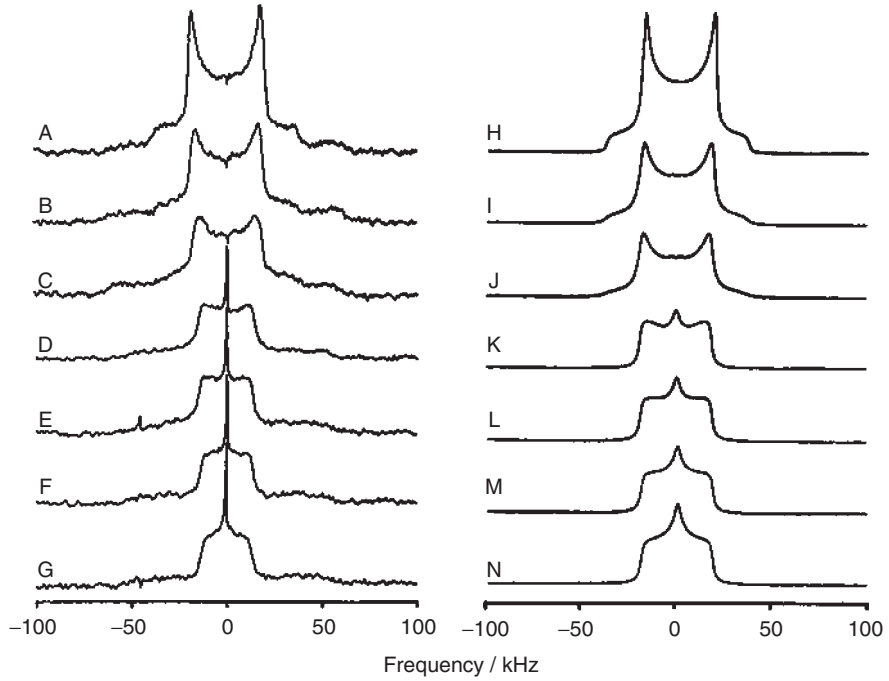

Figure 6 Static ^{2}H NMR lineshapes of collagen to determine side chain mobility in [$^2H_{10}$]-Leu labelled collagen. The left column shows the experimental 38.5 MHz ^{2}H NMR spectra of [$^2H_{10}$]-Leu labelled collagen at various temperatures (A, −85°C; B, −43°C; C, −18°C; D, −6°C; E, +1°C; F, +15°C; G, +30°C). In the right column, lineshape simulations of the experimental spectra are displayed. These simulations implemented a two-site hop model, in which the Cγ–Cδ bond axes were assumed to hop between two sites separated by 108–112° and κ defines the hopping rate (H, $\kappa \leqslant 6 \times 10^3$ rad/s; I, $\kappa = 1.9 \times 10^4$ rad/s; J, $\kappa = 3.1 \times 10^4$ rad/s; K, $\kappa = 3.7 \times 10^5$ rad/s; L, $\kappa = 6.3 \times 10^5$ rad/s; M, $\kappa = 8.7 \times 10^5$ rad/s; N, $\kappa = 1.2 \times 10^6$ rad/s). Figure reproduced from ref. 110 (with permission).

mineralized and cross-linked collagen, respectively. These measurements provided insight into the extent at which cross-linking and mineralization restricts the molecular dynamics in collagen.

These findings were derived from the anisotropic carbonyl chemical shift tensor measurements at a ^{13}C resonance frequency of 62.98 MHz indicating that the upper limit for the correlation times of these motions is 10^{-4} s. In addition to these somewhat slower motions, combined relaxation and nuclear Overhauser enhancement studies on collagen labelled with ^{13}Cα Gly revealed the presence of fast motions with correlation times in the 1–5 ns range exhibiting small amplitudes of 10, 9 and 5.5° uncross-linked, cross-linked and mineralized collagen, respectively.[112] Because of their very fast correlation times, these motions must be segmental. Overall, the fast backbone dynamics of collagen was not found to be greatly affected by cross-links.

To conclude this investigation on hard and soft tissue collagen, the side chain mobility of the molecule was studied.[113] To this end, [methyl-$^2H_3$]methionyl, [4,4-$^2H_2$]pyrrolidinyl, (4-fluorophenyl)alanyl and [6-^{15}N]lysyl labelled cross-linked and mineralized, cross-linked but not mineralized and not cross-linked and not mineralized collagens were prepared.[113] While there is an obvious dependence of the backbone motion on the degree of cross-linking and mineralization, surprisingly, the side chain motions are only slightly affected by mineralization of collagen.

[Methyl-$^2H_3$]methionyl labelled collagen showed lineshapes that differed substantially from Pake patterns indicative of intermediate timescale motions as shown in Figure 7. Only at very low temperature of -135°C all segmental motions are frozen out to yield a Pake spectrum with a quadrupolar splitting of $\sim$40 kHz as for rotating methyl groups.[114] These results showed that the motions of the Lys and Met side chains were shown to be slightly more hindered in the cross-linked collagen fibers but only slightly more restricted in mineralized collagen.

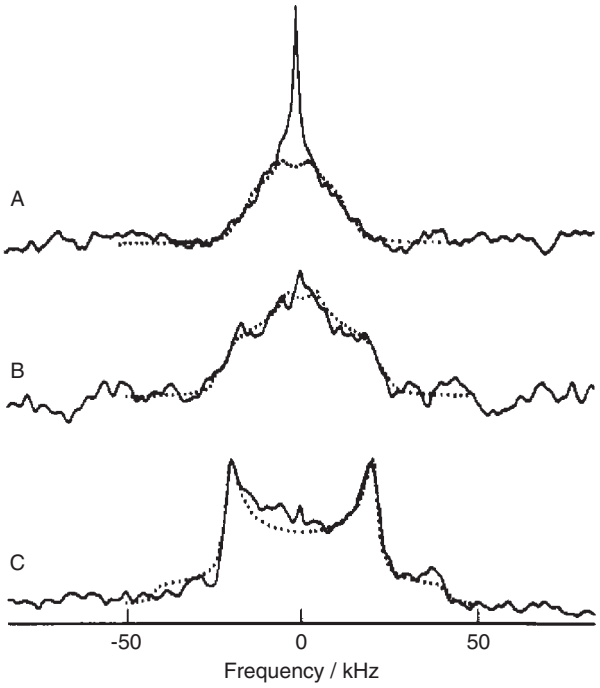

Figure 7 38.45 MHz solid-state ^{2}H NMR spectra of [*methyl*-$^2H_3$] methionine-labelled rat calvaria collagen at a temperature of 22°C (A), -35°C (B) and -135°C (C). Spectra represent the superposition of 250,000 (A), 60,000 (B) and 120,000 transients, respectively. Dotted lines represent the best-fit simulations of the experimental line shape. Reproduced from ref. 113 (with permission).

Next, molecular motions in Pro and HyPro residues were studied in $^{2}H^{\gamma}$ labelled pyrrolidinyl rings in collagen. Characteristic ^{2}H NMR spectra are shown in Figure 8. In contrast to the ^{2}H NMR spectra of Met, the lineshapes produced by the Pro and HyPro residues were broad, covering a frequency range of 125 kHz. These spectra could be simulated assuming the superposition of three distinct motionally averaged lineshapes corresponding to the β-, γ- and δ-deuterons of the Pro ring.[115] As each ring position experiences a different root mean square amplitude, the deuterons in the different ring sites have different quadrupole splittings and lineshapes, which yield a plateau peak in the sum. This analysis showed that the Pro and HyPro residues in collagen undergo puckering motions with root mean square amplitudes in the 11–30° range in all samples. With respect to the hydrogen-bonding capacity of HyPro, it was suggested that the more flexible rings should be assigned to Pro.

The ^{19}F and ^{15}N solid-state NMR lineshapes of (4-fluorophenyl)alanyl and [6-^{15}N]lysyl labelled collagen showed mostly narrow components indicative of large amplitude motions of these side chain sites.[113] In contrast to the backbone, the side chain motions of collagen did not show a clear correlation with the formation of cross-links and/or the mineralization of collagen.

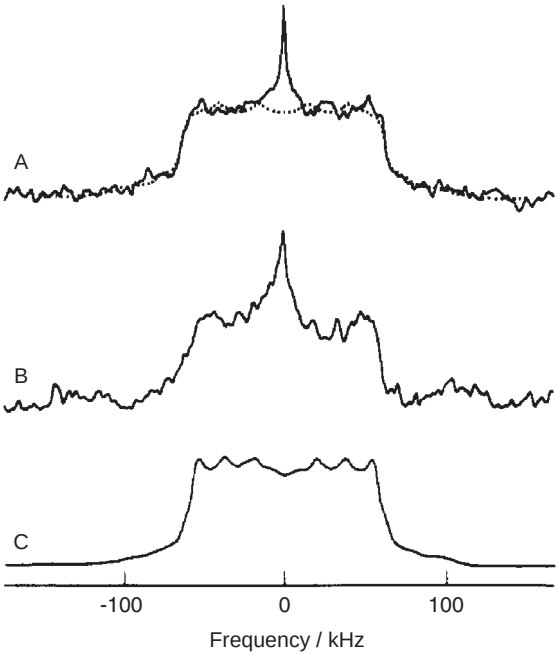

Figure 8 38.45 MHz solid-state NMR spectra of [$^{2}H\gamma$] proline and hydroxypoline labelled rat calvaria collagen (A), rat tail collagen (B) and polycrystalline DL-[3,3,4,4,5,5-$^{2}H_6$] proline. The spectra were obtained at 22°C. Spectrum (A) was also simulated (dotted line). The spectra represent the sum of 89,000 (A), 90,000 (B) and 128 (C) accumulations. Reproduced from ref. 113 (with permission).

Recently, the static solid-state NMR data from the Torchia group have been reanalysed and interpreted in terms of a librational rod model.[116] This analysis revealed that the ^{2}H NMR data is also consistent with small-angle librations about internal bond directions.

3.2 Magic-angle spinning NMR experiments on collagen dynamics

While static solid-state NMR spectra are broad and typically signals of only one or very few sites can be resolved in one dimension, MAS methods allow resolving many relatively sharp signals at once. Typical ^{13}C MAS NMR line widths of organic solids are of the order of 1 ppm. Since about two thirds of all amino acids in collagen are due to Gly, Ala, Pro, HyPro and Glu, the ^{13}C MAS spectra of collagen are relatively simple to assign.[117] Application of ^{13}C CP MAS methods to collagen was first shown by Schaefer and Stejskal in 1976.[24] In their paper that had the purpose to first demonstrate the CP MAS technique on solid materials, the authors presented a ^{13}C CP MAS spectrum of ivory, which showed the typical signature of organic collagen (Figure 9). A dramatic improvement in the resolution of the CP MAS spectrum compared to the non-spinning

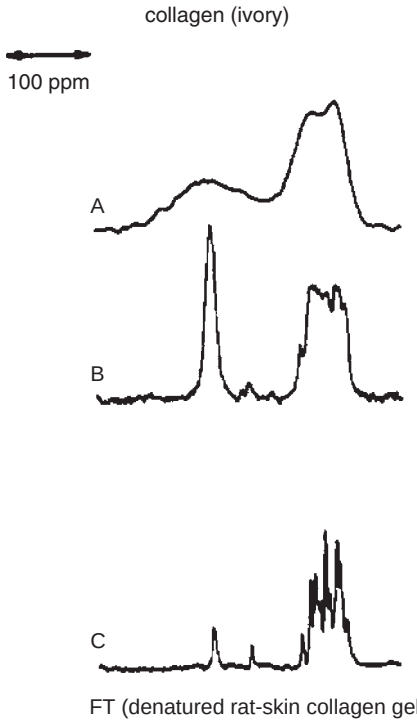

Figure 9 Dipolar decoupled natural abundance 22.6 MHz ^{13}C CP NMR spectra of collagen (ivory) without (A) and with magic-angle spinning (B). For comparison, the NMR spectrum of denatured rat skin collagen gel is shown (C). Reproduced from ref. 24 (with permission).

experiment. By application of MAS the spectral intensity of the broad anisotropic solid-state NMR spectra is collected into a sharp central band of a line width of the order of one or a few ppm and a series of spinning sidebands. The number and intensity of the spinning sidebands depends on the MAS frequency and the Larmor frequency of the NMR spectrometer. Thus, relatively well-resolved ^{13}C NMR spectra from isolated collagen samples have been obtained at natural abundance.

The ^{13}C MAS NMR work on collagen was systematically continued by Hazime Saitô and co-workers.[27] The group showed ^{13}C CP MAS spectra of dried collagen from bovine tendon, bovine skin and atelocollagen. The NMR signals of ^{13}C CP MAS spectra could be assigned to the most abundant amino acids in collagen (Gly, Ala, Pro, HyPro, Glu).[33] Conformation dependent ^{13}C chemical shifts were compared to a reference system revealing the typical chemical shifts for collagen.

Further, a comparison of ^{13}C CP MAS NMR spectra in the anhydrous and hydrated states were acquired.[118] Collagen hydration was achieved by exposure to a saturated vapour phase with a relative humidity of 96%. Representative spectra are shown in Figure 10. Two hydration-induced types of spectral changes were observed in the collagen spectra: First, some resonance lines were substantially narrowed by hydration as for instance seen for the Ala Cβ peak. Second, intensity changes in the ^{13}C Cγ signal of HyPro were recorded induced by hydration of the collagen. These changes were explained by the versatile molecular dynamics of collagen that was determined by static solid-state NMR methods such as rapid Pro puckering motions with correlation times comparable to those in aqueous solution.[113,115,119] It was further pointed out that increasing hydration levels only resulted in peak narrowing and not in reorganization of a local conformational disorder. Additionally, it was suggested that the intensity changes of the ^{13}C Cγ signal of HyPro might be due to *cis–trans* isomerization. Thus, in addition to cross-linking and the degree of mineralization as discussed above, the level of hydration seems to be a determining factor for the molecular mobility of collagen in tissue. This is also consistent with the static NMR spectra that indicated that the collagen dynamics is dependent on the state of the surrounding water.[117]

These observations prompted us to study collagen mobility systematically as a function of hydration using ^{13}C CP MAS techniques.[46] A series of ^{13}C CP MAS NMR spectra of collagen at varying degrees of hydration indicated the narrowing of the NMR signals with increasing hydration (Figure 11). To quantify these results, the ^{1}H–^{13}C dipolar couplings have been measured in a DIPSHIFT separated local field experiment.[120–122] Thus, the dipolar coupling of each resolved collagen signal could be determined. Fast molecular motions average out these dipolar couplings, which is described by an order parameter that represents the amplitude of these molecular motions. Generally, motional amplitudes were found to be larger in the side chains compared to the backbone of collagen underlying the importance of hydration for the molecular dynamics of collagen. Further, with increasing hydration level, a decrease in the order parameters has been observed. The upper limit for the correlation times of

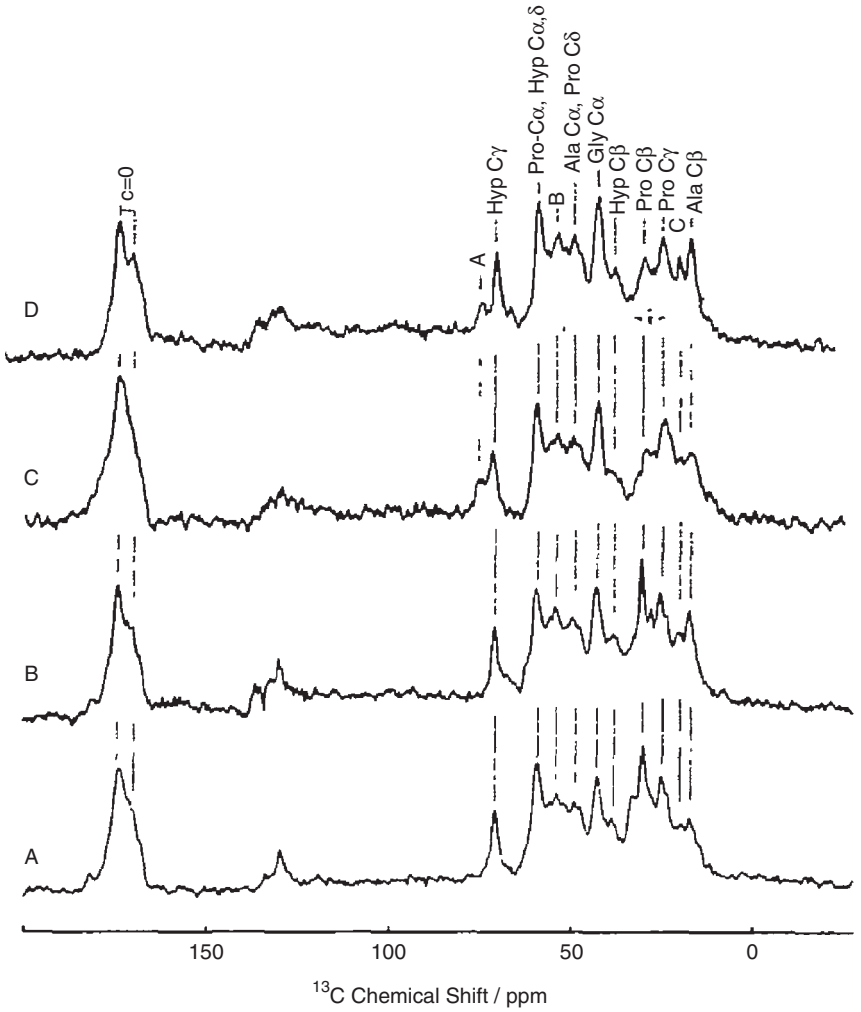

Figure 10 Dipolar decoupled natural abundance 75.46 MHz ^{13}C CP MAS spectra of insoluble bovine tendon collagen (A, B) and acid-soluble collagen from calf skin (C, D). Samples (A) and (C) are anhydrous, while spectra (B) and (D) were collected from collagen hydrated at a relative humidity of 96% for 12 h. Reproduced from ref. 118 (with permission).

motion calculated from motionally averaged ^{1}H–^{13}C dipolar couplings is of the order of 4×10^{-5} s.

The ^{1}H–^{13}C order parameters of collagen at varying hydration levels are shown in Figure 12. A moderate decrease in the order parameters is observed for all collagen sites upon increasing water content. Only for HyPro Cγ, the order parameter decrease is more pronounced. This is also consistent with the observation of Saitô and Yokoi[118] and indicates that the polar hydroxyl group of HyPro represents a primary hydration site in collagen. As also confirmed by

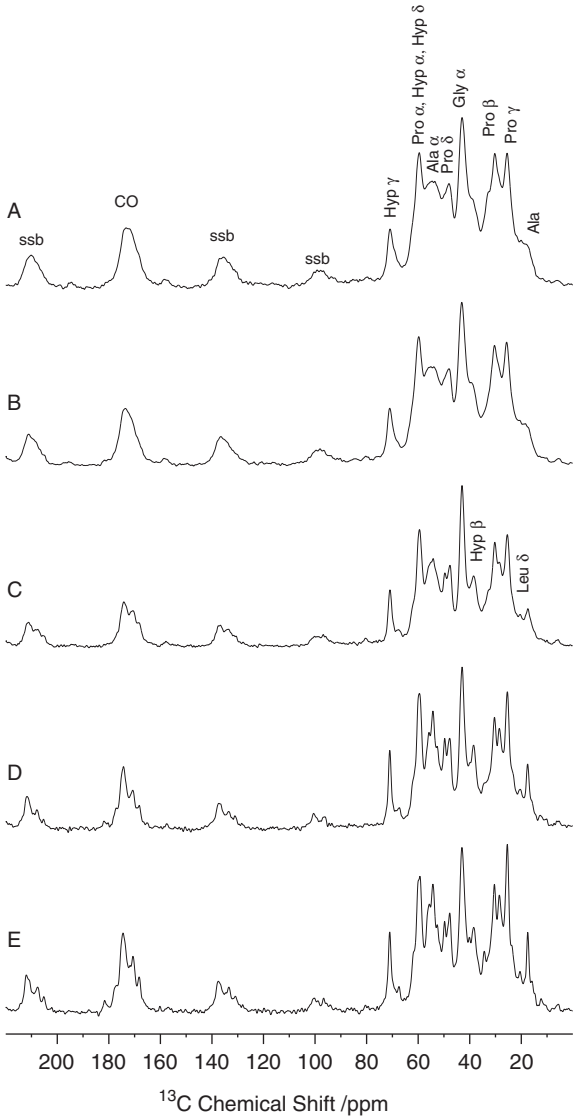

Figure 11 Dipolar decoupled natural abundance 188.6 MHz ^{13}C CP MAS spectra of dry collagen fibrils at a temperature of 25°C (A) and 50°C (B). Spectra (C–E) were acquired at 25°C and a hydration level of 10, 20 and 30 wt% D_2O, respectively. The MAS rotation frequency was 7 kHz. ssb, spinning sideband. Reproduced from ref. 46 (with permission).

X-ray studies on collagen-like peptides, the hydroxyl group of HyPro plays a central role in the hydration and stability of collagen as it offers hydrogen bond donor and acceptor properties.[123]

In addition to the fast segmental motions of both dry and hydrated collagen, Reichert et al., investigated also if slow motions with correlation times in the

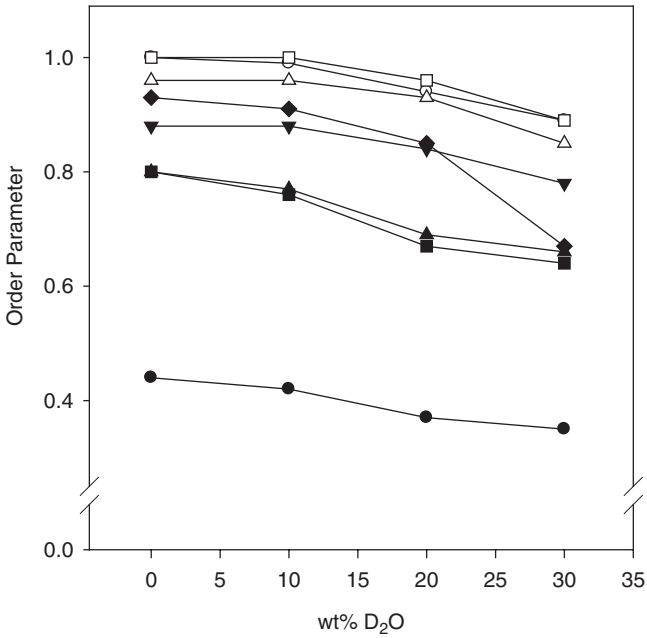

Figure 12 $^{1}H–^{13}C$ order parameters of collagen at varying hydration levels for the collagen backbone (open symbols) and side chain signals (filled symbols) determined at a temperature of 25°C. Gly Cα (open circles), Ala Cα (open spares), Pro Cα, Hyp Cα, Hyp Cδ (open triangles), Ala Cβ (filled circles), Pro Cγ (filled squares), Pro Cβ (filled triangles), Pro Cδ (filled up-side-down triangles), Hyp Cγ (filled diamonds). Experimental errors are of the size of the symbols. Reproduced from ref. 46 (with permission).

millisecond correlation time window were observable in collagen.[46] To this end, an exchange experiment under MAS conditions named CODEX[105] was carried out. In this experiment, the information about slow dynamical processes is observed for all spectroscopically resolved sites in the same set of experiments. This is important, since exchange due to molecular reorientation cannot be discriminated against undesired spin exchange that is present for all ^{13}C sites that are directly bound to a ^{14}N nucleus.[124,125] While the carbonyl signal of collagen is prone to these exchange processes, a clear effect could be observed for the HyPro Cγ signal, indicating that collagen is subject to dynamical processes with a correlation time of the order of 1–100 ms.

3.3 Magic-angle spinning NMR studies of collagen dynamics in biological tissues

The most obvious tissues to study collagen dynamics are bone[126–128] and dentin[129] that contain ~20–30% and ~20% collagen type I, respectively. With the recent introduction of high-field magnets, it is now also possible to study

collagen in biological tissues with relatively low collagen content such as cartilage. This is particularly remarkable since cartilage consists of ~82 wt% water, ~6 wt% proteoglycans and only ~12 wt% collagen.[7,130–132] Wet tissue samples are challenging for solid-state NMR at high magnetic field. Because of the high water and ion content of tissues, the sample volumes have to be restricted to avoid sample heating by the application of high-power decoupling fields.[133] The applied B_1 fields induce ion currents that may result in significant sample heating. Especially at high magnetic fields, which are more commonly used in solid-state NMR of biological samples, the radio frequency fields approach the microwave band, where water strongly absorbs the power. This means that only milligram quantities of collagen can be investigated, which calls for extremely sensitive instrumentation. Figure 13(A) shows a 188.6 MHz ^{13}C CP MAS spectrum of porcine articular cartilage obtained on approximately 15 mg cartilage tissue at natural abundance, which translates into less than ~2 mg of collagen. While still relatively noisy, the signals of the main amino acid of collagen could be identified and assigned. For comparison, the ^{13}C CP MAS spectra of dried porcine articular cartilage and isolated collagen type II are shown in Figure 13(B and C), respectively. This indicates that almost exclusively collagen signals are detected in ^{13}C CP MAS spectra of articular cartilage. In addition,

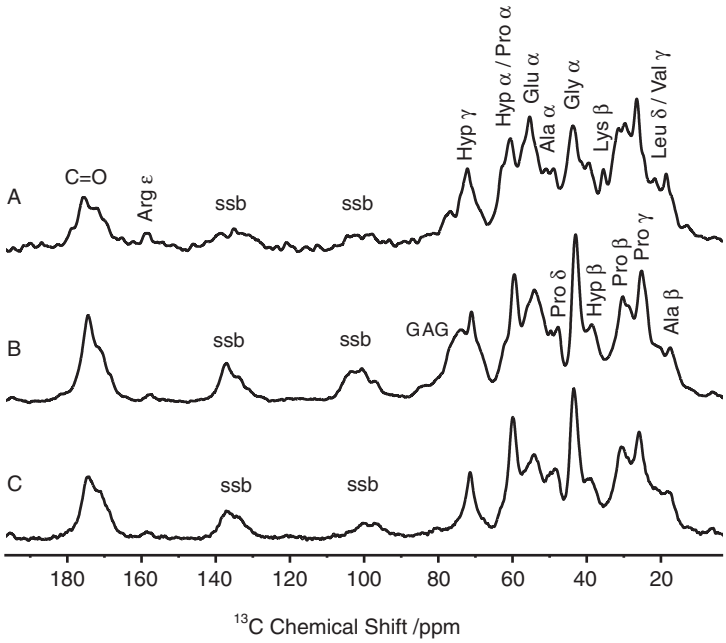

Figure 13 Proton decoupled 188.6 MHz ^{13}C CP MAS spectra of fully hydrated porcine articular cartilage (A), dried porcine articular cartilage (B) and dry collagen type II (C) at a MAS frequency of 7 kHz and a temperature of 37°C. The amino acid assignment is given. Spectra were externally calibrated with respect to TMS. ssb, spinning sideband; GAG, glycosaminoglycan.

signals from rigid proteoglycans of cartilage (mostly hyaluronan) can be detected in the ^{13}C CP MAS spectrum of cartilage. These signals are assigned to the ring carbons of the proteoglycans with typical chemical shifts between 65 and 80 ppm.[8,9,134,135] In fully hydrated cartilage, these signals are strongly attenuated in ^{13}C CP MAS spectra because of their high mobility, but contribute significantly to the NMR spectrum of dried cartilage.

Our group then investigated the motional amplitudes of the collagen segmental motions using different separated local field experiments. First wideline separation (WISE)[136] and Lee Goldburg-CP (LG-CP)[85,137] methods were applied on somewhat dried articular cartilage samples and compared to samples of isolated dry collagen.[34] Significantly narrower WISE spectra of cartilage indicated that the collagen in cartilage undergoes fast molecular reorientations. To further quantify these effects, motionally averaged ^{1}H–^{13}C dipolar coupling strengths were measured and used for order parameter calculations. Again, the comparison of cartilage collagen with dry isolated collagen indicated the fast mobility of the collagen segments in tissue.

These results made it obvious that the water content of cartilage was the determining factor for the molecular dynamics of the collagen in the tissue. In our next study, we systematically investigated the segmental mobility of cartilage collagen at varying hydration levels,[28] achieved by dialysis of cartilage against a polymer solution of high osmotic pressure.[138] The LG-CP experiment has the disadvantage of requiring the acquisition of a full time domain signal to pick up the modulation due to dipolar interaction. Since this signal is sampled in the indirect dimension, the experiment requires many t_1 increments leading to long acquisition times. Therefore, LG-CP techniques are not well suited for low concentrated samples of degradable biological tissue. An alternative represents the DIPSHIFT experiment,[120] that can be carried out in a constant time fashion[122] and all information about the strength of the dipolar coupling is sampled over one rotor period, which is split up into only 8–16 t_1 data points.[139]

Figure 14 shows order parameters of collagen at varying levels of hydration. Clearly, the amplitudes of the segmental mobility gradually increase with increasing water content of the tissue. In the dry sample, the backbone signals of collagen exhibit order parameters between 0.9 and 0.94 in agreement with a rigid molecular structure. For the side chains, order parameters vary between 0.64 and 0.87 indicating motions with root mean square amplitudes between 42.5 and 24.4°.

In contrast, much smaller order parameters have been observed in fully hydrated cartilage. For the backbone, order parameters between 0.73 and 0.78 are consistent with motions of amplitudes in the range of 36.1–32.3°. Even larger amplitudes of 48.6–41.1° are observed in the side chains of collagen in fully hydrated cartilage with order parameters of 0.55–0.66. For Ala Cβ, order parameters <0.33 are obtained, characteristic for the fast rotation of methyl groups about the Cα–Cβ bond and additional segmental mobility of the Cα–Cβ bond vector.

Our group has recently studied collagen dynamics in rabbit bone.[35] Compared to collagen in cartilage, mineralized collagen is more rigid than hydrated cartilage collagen undergoing only small amplitude motions with

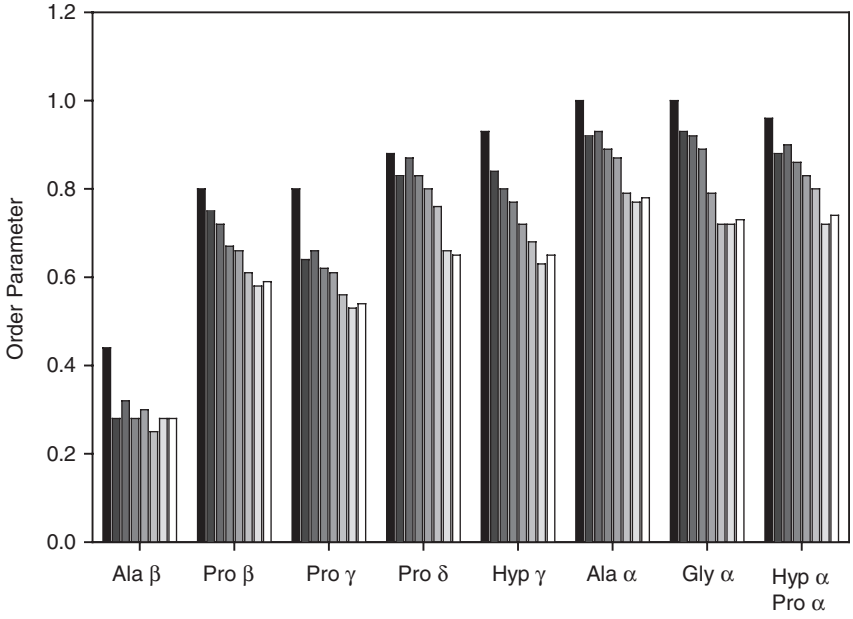

Figure 14 $^{1}H–^{13}C$ order parameters of collagen in articular cartilage at varying degrees of hydration. Each series of bars represents the following conditions from left to right: dry collagen type I (black bar), dried porcine articular cartilage, porcine articular cartilage at an osmotic pressure of 9.6, 4.3, 1.7, 0.6, 0.1 MPa and native porcine articular cartilage (white bar). The different grey tones indicate the measurements at the osmotic pressures given above (from dark to light grey). All measurements were carried out at 37°C.

amplitudes between 25 and 30° for the backbone and 30–40° for the side chains, which was also found by Torchia and co-workers.[111,113] Further, β-tricalciumphosphate implants that were loaded with mesenchymal stem cells and transplanted into the femoral condyle of rabbits were analyzed by solid-state NMR spectroscopy 3 months after implantation. Figure 15 shows a comparison of the ^{13}C MAS NMR spectrum of the rabbit implant with that of native rabbit bone and isolated collagen I. The good agreement indicates that in the implants new extracellular matrix composed of collagen I and bioapatite (which was also shown by ^{31}P solid-state NMR in this study) was synthesized by the osteoblasts. Although bone contains a number of other proteins that could also give rise to a similar solid-state NMR spectrum the HyPro Cγ signal at 71.1 ppm is highly indicative of collagen as no other aliphatic amino acids produces a signal at this chemical shift.[140]

Finally, the fast molecular dynamics of collagen in bone was investigated and compared with that of the newly synthesized collagen in the implant. The order parameters determined from the $^{13}C–^{1}H$ DIPSHIFT experiment are shown in Figure 16. On average, very similar order parameters were determined for the segmental motions of collagen in bone and in the implant. This provides a first

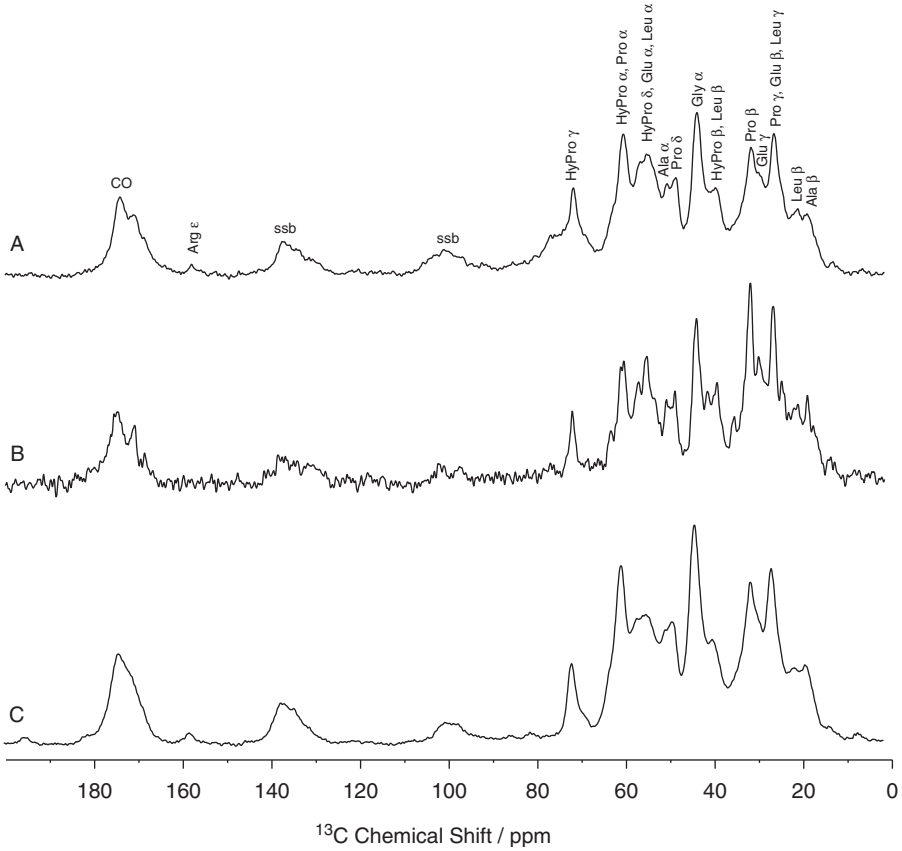

Figure 15 ^{1}H decoupled 188.5 MHz ^{13}C CP MAS spectra of native rabbit bone (A), a β-TCP implant removed from a rabbit's femoral condyle after 3 months (B), and isolated collagen type I (C). Spectra were recorded at a temperature of 37°C and a MAS frequency of 7 kHz. The spectra were Fourier transformed using an exponential line broadening of 50 Hz. ssb, spinning sideband.

indication that the newly synthesized collagen in the β-tricalciumphosphate implant is fully functional from the biophysical point of view and represents an adequate replacement material.

3.4 The orientation of collagen fibers in tissues measured through the interaction of water with collagen by solid-state NMR

Although not the focus of the current review, the orientation of collagen in a specific tissue has also been studied by solid-state NMR techniques probing the orientation of collagen bound water. The dipolar interaction of water with the anisotropic arrangement of the collagen network provides a very useful parameter to map the fiber orientation of collagen.[141,142] Since water is also the

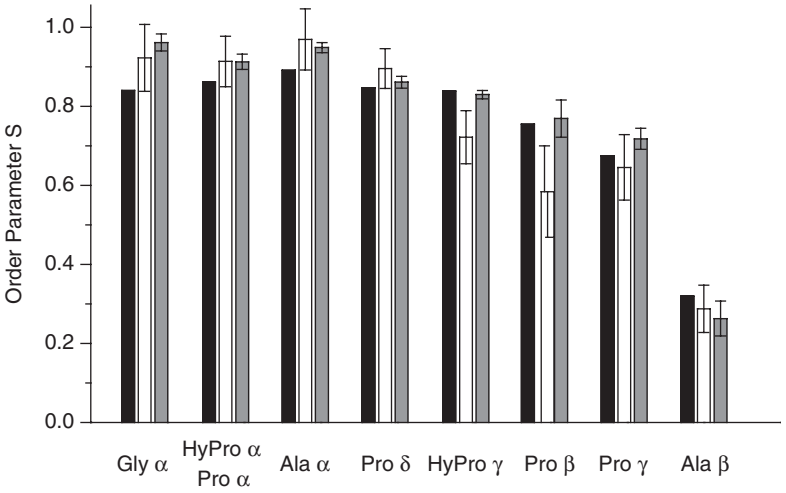

Figure 16 Order parameters of collagen I in native rabbit bone (black bar), average order parameter for collagen I in the β-TCP implants removed from rabbits after 3 months (white bar), and the order parameters obtained for isolated collagen I (grey bar). Measurements were carried out at 37°C. Reproduced from ref. 35 (with permission).

molecule that is most often detected in *in vivo* magnetic resonance imaging experiments, the collagen orientation and pressure induced changes of this orientation in tissue under mechanical load could be observed by this technique.[143–146] This field has recently been reviewed and will only be briefly mentioned here.[147,148]

One application involves multiple quantum filtered NMR[149,150] studies on the interaction of collagen and water in tendon. Fechete et al. used the double quantum filtered ^{1}H NMR signal of bound water to determine the anisotropy of the residual dipolar couplings in tendon.[151] Double quantum coherences can be exited as a result of the interaction of water with the collagen fibers in the tissue. Water that penetrates the interstitial volume of the triple helix structure of collagen is tightly bound and fixed by two hydrogen bonds. This provides a possibility to study the orientation of collagen fibers in tissue by the angular dependence of the residual dipolar couplings. The residual dipolar couplings were obtained from the double quantum build-up curves and double quantum filtered spectra of samples at varying macroscopic orientation with respect to the external magnetic field. At the magic angle, a non-vanishing residual dipolar coupling was measured, which is indicative of a distribution of the collagen directors around the macroscopic symmetry axis of the tendon. This distribution was modelled by a Gaussian function with a standard deviation of 19° and a centre of the distribution at 2°. This method can also be used for a quantitative investigation of the anisotropy in different ordered tissues and in response to mechanical load.[151]

4. CONCLUSIONS

Several static and MAS NMR solid-state NMR techniques have been applied over the last 30 years to study the structure and dynamics of fibril forming collagen with atomic resolution. These techniques have strongly contributed to our knowledge of the molecular dynamics in isolated and tissue collagen as a basis for understanding the material properties of biological tissues, such as their tensile strength, elasticity and viscoelasticity. The first interesting observation was that even dry collagen is not entirely rigid. The amplitude of collagen motions is not greatly influenced by cross-linking, however, mineralization as it occurs in bone collagen and other hard tissues reduces collagen flexibility. The amino acids in collagen undergo fast segmental reorientations that can be described by root mean square amplitude fluctuations. Very small amplitudes are observed for the collagen backbone, while the motional amplitudes increase into the side chains of the amino acids. For Pro and HyPro, puckering motions of the entire ring structure have been identified. The methyl groups of amino acid side chains undergo fast rotations about the C–C bond axis. Further, first hints for slow collagen motions in the millisecond time window were identified for dry collagen.

In hydrated collagen, a more versatile molecular dynamics with larger motional amplitudes was found. While the segmental motions of dry collagen occur on a fast timescale of the order of a few nanoseconds, in hydrated collagen also slower motions with correlation times of the order of 10^{-4} s have been observed. The motional amplitudes of hydrated collagen are significantly increased in comparison to dry collagen.

Tissue collagen of fully hydrated articular cartilage shows the largest motional amplitudes. This is caused by the high water content. Different types of collagen do not show any dynamical diversity as concluded from comparison of collagen types I and II. Although most amino acids in collagen are uncharged, there are several polar groups in the backbone and the side chains that represent water-binding sites. In particular, the hydroxyl groups of HyPro have been identified as hydration sites according to X-ray studies since they have both hydrogen-bond donor and acceptor properties.[152] It has been suggested that the collagen triple helices acquire extra hydrogen-bonding capacity by prolyl hydroxylation.[123]

The possible functional significance of the collagen mobility has already been suggested.[112] Due to their high tensile strength, collagen fibers provide mechanical stability to connective tissues. When tension is applied, collagen molecules are able to undergo rapid conformational changes. Thus, tensile stress is distributed uniformly and the mechanical energy can be dissipated and adsorbed by the segmentally flexible molecules. The motions that have been identified so far occur on a sub-microsecond time scale. However, the mechanical stress that is exerted on connective tissues by our daily tasks such as walking, climbing the stairs or exercising stresses the connective tissue on a slower time scale of tens to hundreds of milliseconds. Therefore, motions with these correlation times may also be relevant for collagen. At the moment, only

preliminary data for collagen motions in that time window is available.[46] However, several newly developed solid-state NMR methods will allow to investigate such motions in collagen as well.[45]

Besides understanding of the basic properties of collagen with regard to the viscoelasticity of biological tissue, recent tissue-engineering developments have led to an increasing interest in the quantitative characterization of artificial tissues. For various applications in regenerative medicine, (stem) cells are seeded into organic or inorganic scaffolds to produce extracellular matrix *in vitro*. The monitoring and quality control of the engineered tissues represents a major challenge to produce high-quality replacements. NMR spectroscopy is a well-suited experimental technique to contribute to this field. Artificially grown tissues need to exhibit very similar properties as the natural tissue in order to be built into cartilage, bone or other defects. First spectroscopic results have demonstrated the usefulness of the method for ongoing tissue engineering attempts.[35,153] The methods described in this review may be used to characterize artificial tissue and compare its properties with those of natural specimen. Clearly, there are much more solid-state NMR techniques available that allow to further and more comprehensively characterize the structure and dynamics of tissue collagen. Thus, the optimal procedures for tissue engineering may be determined aided by a comprehensive monitoring of the dynamical properties of the tissue macromolecules as a prerequisite for a successful implantation.

ACKNOWLEDGEMENTS

This research has been funded by the Deutsche Forschungsgemeinschaft (HU 720/7–1). The author acknowledges PD Dr. Detlef Reichert for helpful comments.

REFERENCES

1. J. Brinckmann, *Top. Curr. Chem.*, 2005, **247**, 1.
2. D. Nelson and M. Cox, *Lehninger Biochemie*, Springer-Verlag, Berlin, 2001.
3. J. Engel and H. P. Bächinger, *Top. Curr. Chem.*, 2005, **247**, 7.
4. J. Engel, *Science*, 1997, **277**, 1785.
5. T. E. Creighton, *Proteins. Structures and Molecular Properties*, W. H. Freeman and Company, New York, 1993.
6. S. Ricard-Blum, F. Ruggiero and M. van der Rest, *Top. Curr. Chem.*, 2005, **247**, 35.
7. J. E. Scott, *J. Physiol.*, 2003, **553**, 335.
8. D. A. Torchia, M. A. Hasson and V. C. Hascall, *J. Biol. Chem.*, 1977, **252**, 3617.
9. L. Naji, J. Kaufmann, D. Huster, J. Schiller and K. Arnold, *Carbohydr. Res.*, 2000, **327**, 439.
10. J. Schiller, L. Naji, D. Huster, J. Kaufmann and K. Arnold, *MAGMA*, 2001, **13**, 19.
11. D. Huster, J. Schiller, L. Naji, J. Kaufmann and K. Arnold, *Molecules in Interaction with Surfaces*, Springer-Verlag, Heidelberg, 2004, p. 455.
12. F. M. Pope, J. Dorling, A. C. Nicholls and J. Webb, *J. R. Soc. Med.*, 1983, **76**, 1050.
13. F. M. Pope, S. C. M. Daw, P. Narcisi, A. R. Richards and A. C. Nicholls, *J. Inherit. Metab. Dis.*, 1989, **12**, 135.
14. H. Kuivaniemi, G. Tromp and D. J. Prockop, *Hum. Mutat.*, 1997, **9**, 300.
15. L. A. Flugge, L. A. Miller-Deist and P. A. Petillo, *Chem. Biol.*, 1999, **6**, 57.
16. R. F. Service, *Science*, 2000, **289**, 1498.

17. J. Malda and C. G. Frondoza, *Trends Biotechnol*., 2006, **24**, 299.
18. C. K. Kuo, W. J. Li, R. L. Mauck and R. S. Tuan, *Curr. Opin. Rheumatol*., 2006, **18**, 64.
19. R. M. Schulz and A. Bader, *Eur. Biophys. J*., 2007, **36**, 539.
20. S. Roche, M. C. Ronziere, D. Herbage and A. M. Freyria, *Biomaterials*, 2001, **22**, 9.
21. M. Fuss, E. M. Ehlers, M. Russlies, J. Rohwedel and P. Behrens, *Ann. Anat*., 2000, **182**, 303.
22. D. A. Grande, C. Halberstadt, G. Naughton, R. Schwartz and R. Manji, *J. Biomed. Mater. Res*., 1997, **34**, 211.
23. K. P. Rao, *J. Biomater. Sci. Polym. Ed*., 1995, **7**, 623.
24. E. O. Stejskal and J. Schaefer, *J. Am. Chem. Soc*., 1976, **98**, 1031.
25. D. A. Torchia and D. L. VanderHart, *J. Mol. Biol*., 1976, **104**, 315.
26. D. A. Torchia, *Methods Enzymol*., 1982, **82**, 174.
27. H. Saitô, S. Tuzi and A. Naito, *Ann. Rep. NMR Spectrosc*., 1998, **38**, 79.
28. G. Zernia and D. Huster, *Handbook of Modern Magnetic Resonance*, Kluwer Academic Publisher, New York, 2006, p. 79.
29. D. A. Torchia, *Annu. Rev. Biophys. Bioeng*., 1984, **13**, 125.
30. P. Fan, M. H. Li, B. Brodsky and J. Baum, *Biochemistry*, 1993, **32**, 13299.
31. M. H. Li, P. Fan, B. Brodsky and J. Baum, *Biochemistry*, 1993, **32**, 7377.
32. G. Melacini, A. M. Bonvin, M. Goodman, R. Boelens and R. Kaptein, *J. Mol. Biol*., 2000, **300**, 1041.
33. H. Saitô, R. Tabeta, A. Shoji, T. Ozaki, I. Ando and T. Miyata, *Biopolymers*, 1984, **23**, 2279.
34. D. Huster, J. Schiller and K. Arnold, *Magn. Reson. Med*., 2002, **48**, 624.
35. J. Schulz, M. Pretzsch, I. Khalaf, A. Deiwick, H. A. Scheidt, G. von Salis-Soglio, A. Bader and D. Huster, *Calcif. Tissue Int*., 2007, **80**, 275.
36. D. Huster, *Prog. Nucl. Magn. Reson. Spectrosc*., 2005, **46**, 79.
37. H. Saitô, S. Tuzi, S. Yamaguchi, M. Tanio and A. Naito, *Biochim. Biophys. Acta*, 2000, **1460**, 39.
38. R. Tycko, *Nuclear Magnetic Resonance Probes of Molecular Dynamics*, Kluwer Academic Publishers, Dodrecht, 1994, p. 1.
39. S. J. Opella, *Methods Enzymol*., 1986, **131**, 327.
40. D. Reichert, *Ann. Rep. NMR Spectrosc*., 2005, **55**, 159.
41. A. G. Palmer III, J. Williams and A. McDermott, *J. Phys. Chem*., 1996, **100**, 13293.
42. G. Lipari and A. Szabo, *J. Am. Chem. Soc*., 1982, **104**, 4546.
43. G. Lipari and A. Szabo, *J. Am. Chem. Soc*., 1982, **104**, 4559.
44. L. W. Jelinski and D. A. Torchia, *J. Mol. Biol*., 1979, **133**, 45.
45. Z. Luz, P. Tekely and D. Reichert, *Prog. Nucl. Magn. Reson. Spectrosc*., 2002, **41**, 83.
46. D. Reichert, O. Pascui, E. R. deAzevedo, T. J. Bonagamba, K. Arnold and D. Huster, *Magn. Reson. Chem*., 2004, **42**, 276.
47. R. Trampel, J. Schiller, L. Naji, F. Stallmach, J. Karger and K. Arnold, *Biophys. Chem*., 2002, **97**, 251.
48. W. Ngwa, O. Geier, F. Stallmach, L. Naji, J. Schiller and K. Arnold, *Eur. Biophys. J*., 2002, **31**, 73.
49. R. R. Vold and R. L. Vold, *Advances in Magnetic and Optical Resonance*, Academic Press, San Diego, 1991, p. 85.
50. R. R. Vold, *Nuclear Magnetic Resonance Probes of Molecular Dynamics*, Kluwer Academic Publishers, Dodrecht, 1994, p. 27.
51. H. W. Spiess, *Adv. Polym. Sci*., 1985, **66**, 23.
52. M. F. Brown, *Biological Membranes. A Molecular Perspective from Computation and Experiment*, Birkhäuser, Boston, 1996, p. 175.
53. R. J. Wittebort, E. T. Olejniczak and R. G. Griffin, *J. Phys. Chem*., 1987, **86**, 5411.
54. K. Schmidt-Rohr and H. W. Spiess, *Multidimensional Solid-State NMR and Polymers*, Academic Press, San Diego, 1994.
55. M. Mehring, *Principles of High Resolution NMR in Solids*, Springer Verlag, Heidelberg, 1983.
56. D. Reichert, H. Zimmermann, P. Tekely, R. Poupko and Z. Luz, *J. Magn. Reson*., 1997, **125**, 245.
57. U. Haeberlen, *High Resolution NMR in Solids. Selective Averaging*, Academic Press, New York, 1976.
58. D. M. Brink and G. R. Satchler, *Angular Momentum*, Oxford University Press, Oxford, 1968.
59. R. Brüschweiler and P. E. Wright, *J. Am. Chem. Soc*., 1994, **116**, 8426.
60. V. Fedotov and H. Schneider, *Structure and Dynamics of Bulk Polymers by NMR Methods*, Springer-Verlag, Berlin, 1989.
61. K. Belohorcova, J. Qian and J. H. Davis, *Biophys. J*., 2000, **79**, 3201.
62. K. P. Pauls, A. L. MacKay, O. Soderman, M. Bloom, A. K. Tanjea and R. S. Hodges, *Eur. Biophys. J*., 1985, **12**, 1.
63. K. C. Lee and T. A. Cross, *Biophys. J*., 1994, **66**, 1380.

64. K. C. Lee, S. Huo and T. A. Cross, *Biochemistry*, 1995, **34**, 857.
65. K. C. Lee, W. Hu and T. A. Cross, *Biophys. J.*, 1993, **65**, 1162.
66. L. Mueller, M. H. Frey, A. L. Rockwell, L. M. Gierasch and S. J. Opella, *Biochemistry*, 1986, **25**, 557.
67. B. W. Koenig, J. A. Ferretti and K. Gawrisch, *Biochemistry*, 1999, **38**, 6327.
68. R. S. Prosser, J. H. Davis, F. W. Dahlquist and M. A. Lindorfer, *Biochemistry*, 1991, **30**, 4687.
69. R. S. Prosser and J. H. Davis, *Biophys. J.*, 1994, **66**, 1429.
70. R. S. Prosser, S. I. Daleman and J. H. Davis, *Biophys. J.*, 1994, **66**, 1415.
71. A. Vogel, C. P. Katzka, H. Waldmann, K. Arnold, M. F. Brown and D. Huster, *J. Am. Chem. Soc.*, 2005, **127**, 12263.
72. H. W. Spiess, *NMR Basic Principles and Progress*, Springer-Verlag, Berlin, 1978, p. 55.
73. J. C. Williams and A. E. McDermott, *Biochemistry*, 1995, **34**, 8309.
74. E. R. Andrew, A. Bradbury and R. G. Eades, *Nature*, 1958, **182**, 1659.
75. O. N. Antzutkin, *Prog. Nucl. Magn. Reson. Spectrosc.*, 1999, **35**, 203.
76. R. G. Griffin, *Nat. Struct. Biol.*, 1998, **5**, 508.
77. A. E. Bennett, R. G. Griffin and S. Vega, *NMR Basic Principles and Progress*, Springer Verlag, Berlin, 1994, p. 3.
78. S. Dusold and A. Sebald, *Ann. Rep. NMR Spectrosc.*, 2000, **41**, 185.
79. J. S. Waugh, *Proc. Natl. Acad. Sci. USA*, 1976, **73**, 1394.
80. J. Herzfeld and A. E. Berger, *J. Chem. Phys.*, 1980, **73**, 6021.
81. J. L. Lorieau and A. E. McDermott, *J. Am. Chem. Soc.*, 2006, **128**, 11505.
82. J. Lorieau and A. E. McDermott, *Magn. Reson. Chem.*, 2006, **44**, 334.
83. M. Hologne, K. Faelber, A. Diehl and B. Reif, *J. Am. Chem. Soc.*, 2005, **127**, 11208.
84. D. Huster, L. Xiao and M. Hong, *Biochemistry*, 2001, **40**, 7662.
85. M. Hong, X. Yao, K. S. Jakes and D. Huster, *J. Phys. Chem. B*, 2002, **106**, 7355.
86. K. Wagner, A. G. Beck-Sickinger and D. Huster, *Biochemistry*, 2004, **43**, 12459.
87. P. Barré, O. Zschörnig, K. Arnold and D. Huster, *Biochemistry*, 2003, **42**, 8377.
88. P. Barré, S. Yamaguchi, H. Saitô and D. Huster, *Eur. Biophys. J.*, 2003, **32**, 578.
89. G. Reuther, K.-T. Tan, A. Vogel, C. Nowak, J. Kuhlmann, H. Waldmann and D. Huster, *J. Am. Chem. Soc.*, 2006, **128**, 13840.
90. X. L. Yao and M. Hong, *Biochemistry*, 2006, **45**, 289.
91. S. Sharpe, W. M. Yau and R. Tycko, *Biochemistry*, 2006, **45**, 918.
92. E. R. deAzevedo, T. J. Bonagamba and D. Reichert, *Prog. Nucl. Magn. Reson. Spectrosc.*, 2005, **47**, 137.
93. R. R. Ernst, G. Bodenhausen and A. Wokaun, *Principles of Nuclear Magnetic Resonance in One and Two Dimensions*, Clarendon Press, Oxford, 1987.
94. C. P. Slichter, *Principles of Magnetic Resonance*, Springer-Verlag, Berlin, 1990.
95. J. Cavanagh, W. J. Fairbrother, A. G. Palmer III and N. J. Skelton, *Protein NMR Spectroscopy. Principles and Practice*, Academic Press, San Diego, 1996.
96. J. N. S. Evans, *Biomolecular NMR Spectroscopy*, Oxford University Press, Oxford, 1995.
97. M. S. Greenfield, A. D. Ronemus, R. L. Vold, R. R. Vold, P. D. Ellis and T. E. Raidy, *J. Magn. Reson.*, 1987, **72**, 89.
98. J. H. Davis, K. R. Jeffrey, M. Bloom, M. I. Valic and T. P. Higgs, *Chem. Phys. Lett.*, 1976, **42**, 390.
99. W. P. Rothwell and J. S. Waugh, *J. Chem. Phys.*, 1981, **74**, 2721.
100. D. Suwelack, W. P. Rothwell and J. S. Waugh, *J. Chem. Phys.*, 1980, **73**, 2559.
101. A. Schmidt, S. O. Smith, D. P. Raleigh, J. E. Roberts, R. G. Griffin and S. Vega, *J. Chem. Phys.*, 1986, **85**, 4248.
102. Z. Luz, R. Poupko and S. Alexander, *J. Chem. Phys.*, 1993, **99**, 7544.
103. H. W. Spiess, *Chem. Rev.*, 1991, **91**, 1321.
104. J. Jeener, B. H. Meier, P. Bachmann and R. R. Ernst, *J. Chem. Phys.*, 1979, **71**, 4546.
105. E. R. deAzevedo, W.-G. Hu, T. J. Bonagamba and K. Schmidt-Rohr, *J. Am. Chem. Soc.*, 1999, **121**, 8411.
106. G. Chandrakasan, D. A. Torchia and K. A. Piez, *J. Biol. Chem.*, 1976, **251**, 6062.
107. L. W. Jelinski and D. A. Torchia, *J. Mol. Biol.*, 1980, **138**, 255.
108. L. W. Jelinski, C. E. Sullivan and D. A. Torchia, *Nature*, 1980, **284**, 531.
109. L. W. Jelinski, C. E. Sullivan, L. S. Batchelder and D. A. Torchia, *Biophys. J.*, 1980, **32**, 515.

110. L. S. Batchelder, C. E. Sullivan, L. W. Jelinski and D. A. Torchia, *Proc. Natl. Acad. Sci. USA*, 1982, **79**, 386.
111. S. K. Sarkar, C. E. Sullivan and D. A. Torchia, *J. Biol. Chem*., 1983, **258**, 9762.
112. S. K. Sarkar, C. E. Sullivan and D. A. Torchia, *Biochemistry*, 1985, **24**, 2348.
113. S. K. Sarkar, Y. Hiyama, C. H. Niu, P. E. Young, J. T. Gerig and D. A. Torchia, *Biochemistry*, 1987, **26**, 6793.
114. K. Beshah, E. T. Olejniczak and R. G. Griffin, *J. Chem. Phys*., 1987, **86**, 4730.
115. S. K. Sarkar, P. E. Young and D. A. Torchia, *J. Am. Chem. Soc*., 1986, **108**, 6459.
116. A. E. Aliev, *Chem. Phys. Lett*., 2004, **398**, 522.
117. A. E. Aliev, *Biopolymers*, 2005, **77**, 230.
118. H. Saitô and M. Yokoi, *J. Biochem*., 1992, **111**, 376.
119. S. K. Sarkar, T. D. Kopple and D. L. VanderHart, *J. Am. Chem. Soc*., 1984, **106**, 3328.
120. M. G. Munowitz, R. G. Griffin, G. Bodenhausen and T. H. Huang, *J. Am. Chem. Soc*., 1981, **103**, 2529.
121. J. Schaefer, E. O. Stejskal, R. A. McKay and W. T. Dixon, *J. Magn. Reson*., 1983, **52**, 123.
122. M. Hong, J. D. Gross and R. G. Griffin, *J. Phys. Chem*., 1997, **101**, 5869.
123. J. Bella, B. Brodsky and H. M. Berman, *Structure*, 1995, **3**, 893.
124. D. P. Weliky and R. Tycko, *J. Am. Chem. Soc*., 1996, **118**, 8487.
125. K. Saalwächter and K. Schmidt-Rohr, *J. Magn. Reson*., 2000, **145**, 161.
126. W. Kolodziejski, *Top. Curr. Chem*., 2005, **246**, 235.
127. G. S. Johnson, M. R. Mucalo, M. A. Lorier, U. Gieland and H. Mucha, *J. Mater. Sci. Mater. Med*., 2000, **11**, 725.
128. G. S. Johnson, M. R. Mucalo and M. A. Lorier, *J. Mater. Sci. Mater. Med*., 2000, **11**, 427.
129. R. Fujisawa and Y. Kuboki, *Biochem. Biophys. Res. Commun*., 1990, **167**, 761.
130. A. Maroudas, *Methods in Cartilage Research*, Academic Press, London, 1990, p. 209.
131. A. Maroudas, *Adult Articular Cartilage*, Pitman Medical, Tunbridge Wells, 1973, p. 131.
132. A. Ratcliffe and V. C. Mow, *Extracellular Matrix, Volume 1, Tissue Function*, Harwood Academic Publishers GmbH, Amsterdam, 1996, p. 234.
133. S. V. Dvinskikh, V. Castro and D. Sandstöm, *Magn. Reson. Chem*., 2004, **42**, 875.
134. C. F. Brewer and H. Keiser, *Proc. Natl. Acad. Sci. USA*, 1975, **72**, 3421.
135. D. Huster, L. Naji, J. Schiller and K. Arnold, *Appl. Magn. Reson*., 2004, **27**, 471.
136. K. Schmidt-Rohr, J. Clauss and H. W. Spiess, *Macromolecules*, 1992, **25**, 3273.
137. B.-J. van Rossum, C. P. de Groot, V. Ladizhansky, S. Vega and H. J. M. de Groot, *J. Am. Chem. Soc*., 2000, **122**, 3465.
138. V. A. Parsegian, R. P. Rand and D. C. Rau, *Methods Enzymol*., 1995, **259**, 43.
139. D. Huster, J. Schiller and K. Arnold, *Osteoarthritis: Methods and Protocols*, Humana Press, Totowa, 2004, p. 307.
140. C. Ye, R. Fu, J. Hu, L. Hou and S. Ding, *Magn. Reson. Chem*., 1993, **31**, 699.
141. W. Gründer, M. Kanowski, M. Wagner and A. Werner, *Magn. Reson. Med*., 2000, **43**, 884.
142. H. Shinar, Y. Seo, K. Ikoma, Y. Kusaka, U. Eliav and G. Navon, *Magn. Reson. Med*., 2002, **48**, 322.
143. V. Mlynarik, P. Szomolanyi, R. Toffanin, F. Vittur and S. Trattnig, *J. Magn. Reson*., 2004, **169**, 300.
144. C. P. Neu and M. L. Hull, *J. Biomech. Eng*., 2003, **125**, 180.
145. M. Cova and R. Toffanin, *Eur. Radiol*., 2002, **12**, 814.
146. H. A. Alhadlaq and Y. Xia, *Osteoarthritis Cartilage*, 2004, **12**, 887.
147. H. Shinar and G. Navon, *NMR Biomed*., 2006, **19**, 877.
148. W. Gründer, *NMR Biomed*., 2006, **19**, 855.
149. U. Eliav and G. Navon, *J. Am. Chem. Soc*., 2002, **124**, 3125.
150. G. Navon and H. Shinar, *NMR Biomed*., 2001, **14**, 112.
151. R. Fechete, D. E. Demco, B. Blümich, U. Eliav and G. Navon, *J. Magn. Reson*., 2003, **162**, 166.
152. J. Bella, M. Eaton, B. Brodsky and H. M. Berman, *Science*, 1994, **266**, 75.
153. R. Schulz, S. Höhle, G. Zernia, M. Zscharnack, J. Schiller, A. Bader, K. Arnold and D. Huster, *J. Nanosci. Nanotechnol*., 2006, **6**, 2368.
154. R. Z. Kramer, J. Bella, P. Mayville, B. Brodsky and H. M. Berman, *Nat. Struct. Biol*., 1999, **6**, 454.

This page intentionally left blank

CHAPTER 5

NMR Study of Beverages

J. Kidrič

Contents

Abstract

The available NMR data on analysis of beverages are compiled from 2001 until July 2007. Their key features are highlighted. Recently developed high-resolution NMR methods that have been successfully used in the analysis of beverages are reviewed. The use of SNIF-NMR in the adulteration and authentication of alcoholic and nonalcoholic beverages is presented. An overview of the NMR analysis of the chemical composition of wine, beer, spirits, juices, tea and coffee is given in the context of the authentication of beverages.

Keywords: NMR; beverages; authentication; chemical composition

1. INTRODUCTION

Alcoholic and nonalcoholic beverages are complex mixtures of different classes of compounds in solution present in a broad range of concentrations. Alcoholic beverages contain varying amounts of alcohol (ethanol) in contrast to nonalcoholic beverages. Besides alcohol, water is the dominant component of beverages. High-resolution NMR has become the preferable technique for analyzing beverages at the molecular level due to the development of high-field (500–900 MHz) NMR spectrometers, the possibility of recording two- and multi-dimensional spectra, the use of pulse sequences for the suppression of strong signals and availability of special probes like nano probe for μl quantities of samples and the cryogenic probe, up to four times more sensitive than the

National Institute of Chemistry, Hajdrihova 19, 1000 Ljubljana, Slovenia

Annual Reports on NMR Spectroscopy, Volume 64
ISSN 0066-4103, DOI 10.1016/S0066-4103(08)00005-7

room temperature one. With very crowded NMR spectra and overlapping signals, the use of NMR hyphenation with HPLC and MS spectrometry may solve the problem. Diffusion-ordered spectroscopy (DOSY)[1] and its improved versions, two-dimensional *J*-resolved internal DOSY (2DJ-IDOSY)[2] and correlated spectroscopy-internal DOSY (COSY-IDOSY),[3] can also help in solving problems of spectral overlap. NMR sensitivity may be further improved by combining hyphenated techniques with cryoprobe and by the incorporation of an on line post-column solid-phase extraction (SPE) system for on line preconcentration of analytes prior to transfer to NMR tubes.[4–6]

The possibility of detecting ^{2}H at natural abundance gave rise to the method called site-specific natural fractionation (SNIF-NMR)[7] which became the basis for the quality control of alcoholic and nonalcoholic beverages. Starting with wine, nowadays SNIF-NMR is widely used for the quality control of alcoholic and nonalcoholic beverages. SNIF-NMR is backed up by the isotope ratio mass spectrometry (IRMS) method.[8]

This review treats alcoholic beverages made by fermentation including wine and beer, distilled spirits requiring fermentation and distillation like whisky, tequila, Cypriot spirit zivania, Japanese sake and shochu; nonalcoholic beverages juices and beverages made by infusion, such as tea and coffee.

This report reviews the literature on the application of NMR to the characterization of the chemical composition of beverages and the use of NMR for the quality and authenticity control of beverages from 2001 until July 2007.

2. NOVEL METHODS FOR THE ANALYSIS OF BEVERAGES

The problems connected with NMR analysis of beverages are their chemical complexity, signal overlap, low resolution for larger components and low abundance of numerous components.

In the last few years efforts have been directed towards the improvement of spectral resolution and sensitivity enhancement. Noninvasive mixture analysis by NMR is possible using DOSY[1] where differential translational diffusion permits identification of the components. An exploratory application of DOSY to complex liquid foods has been presented.[9] The usefulness of this technique is shown mainly for aliphatic and aromatic compounds found in juices and beer. However, the full potential of DOSY applied to complex mixtures is hindered by the effects of strong signal overlap. DOSY can be further improved by incorporating the diffusion encoding in an existing 2D experiment, in an ''Internal DOSY'' (IDOSY) as in the 2DJ-IDOSY sequence demonstrated on a mixture of medium-chain alcohols and port wine.[2] In comparison to 2DJ-DOSY,[10] 2DJ-IDOSY improves the signal to noise ratio by approximately a factor of 2 and reduces minimum experimental time at least four-fold. 2DJ-IDOSY clearly augments the resolving power in the spectral dimensions making high-resolution DOSY data available for a wider range of mixtures. An improved pulse sequence COSY-IDOSY[3] for measuring diffusion-ordered COSY spectra was achieved by incorporating the diffusion encoding directly into the evolution and detection

periods of a gradient enhanced COSY sequence. It gives improved sensitivity and a 32-fold reduction in minimum experimental time.

Efforts have also been reported on reducing the experimental time in isotopic ^{2}H NMR. The reference method, electronic reference to access *in vivo* concentration (ERETIC), first developed for *in vivo* NMR[11] has been proposed as an independent reference in isotopic ^{2}H NMR.[12–14] With ERETIC, the TMU reference, used in SNIF-NMR, is substituted by the electronically generated signal. By using ERETIC the experimental time is reduced by a factor of 4 and the drawbacks of the internal reference TMU are removed.

A method for studying full, intact wine bottles has been developed.[15,16] An experimental set up was devised in order to use a horizontal bore magnetic resonance imaging magnet of 2.01 T to accommodate a full wine bottle.

3. ANALYSIS AND AUTHENTICATION

To date, NMR has assumed an outstanding position in the field of chemical analysis and authentication of food products. NMR is nondestructive, selective and capable of simultaneous detection of a great number of compounds in complex mixtures. Reliable detection of adulteration of beverages is possible using NMR.

3.1 SNIF-NMR

In the last few years stable isotope analysis has been used widely in authenticity control of foods and beverages. SNIF-NMR in combination with IRMS has been the basis for many applications to wine, beer, fruit juices, tea, coffee, olive oil and some other foods. It has also been extended to alcoholic beverages like whisky, tequila, sake and spirits made from rice. By now, SNIF-NMR and IRMS have entered the field of official regulation and control.[17,18]

Rossmann has published an extensive review on determination and use of stable isotope analysis in food analysis.[19] The scope and limits of the analysis of stable isotope ratio in assessing the quality and determining the origin are demonstrated for fruit juice, wine, spirits and beer.

The application of NMR to food science from 1995 to March 2001 was reviewed.[20] It includes the application of stable isotope analysis to wine, spirits, brandies and fruit juices.

Determination of the authenticity of beverages by NMR and MS methods, including SNIF-NMR and IRMS has been presented.[21]

Calderone et al. have published an overview of isotopic analysis for the control of alcoholic drinks and spirits.[22] In this review the use of the EU Wine-Data Bank for detection of adulterations of wine, rums and a case of fake tequila is presented.

A comprehensive study on SNIF-NMR in four parts has been presented. In Part 1, the principles of SNIF-NMR are outlined.[23] In Part 2, the isotope ratios are presented as tracers of chemical and biochemical mechanistic pathways.[24] In Part 3,

the authors illustrate how isotopic profiles of natural or chemical products can be interpreted in terms of the mechanistic routes of their elaboration.[25] Part 4 presents the applications of SNIF-NMR in an economic context using the examples of wines, spirits and juices.[26]

SNIF-NMR, IRMS and chemometric methods have been applied to wines produced in three wine-growing regions of Slovenia.[27,28] Although a small country, it is pedologically and climatically diverse. The isotopic ratios of discrimination between coastal and continental regions are (D/H)II and $\delta^{13}C$ values. By also including $\delta^{18}O$ values in the PCA and LDA it is possible to distinguish between the two continental regions of Drava and Sava rivers. In the review article[29] by Ogrinc et al., emphasis is placed on the complementary use of SNIF-NMR and IRMS in association with chemometric methods for detecting the adulteration of wine, fruit juices and olive oil, all of them being important products of the Mediterranean Basin.

Using isotopic methods different wine-producing areas in Switzerland could be approximately separated.[30] Very good separation was achieved when isotopic, elemental and classical variables were combined using linear discriminant analysis (LDA).[31]

It has been shown that SNIF-NMR and pyrolysis-IRMS can be used for the detection of exogenous citric acid in fruit juices, the addition of which is strictly limited in Europe.[32]

GC, SNIF-NMR and IRMS have been used to differentiate between tequila derived from 100% agave (*Agave tequilana* Weber var. Azul) and tequila produced with other fermentable sugars ('mixed' tequila).[33]

The origin of edible alcohol in Taiwanese rice-spirits has been identified by SNIF-NMR.[34] In order to increase production and decrease cost, manufacturers often add edible alcohol made from cane molasses declaring it as 'pure rice-spirit'. The authors have found that (D/H)I is an index for the identification of pure rice-spirits mixed with ethanol originating from molasses.

3.2 High-resolution NMR

The purpose of high-resolution NMR studies of beverages lies in the detection and identification of as many compounds as possible, including minor components, in order to obtain a compositional overview and also allowing unexpected compounds to be detected in adulteration, contamination and biochemical studies.

With the development of new techniques, presented in Section 2, more detailed characterization of the chemical composition of beverages has become possible.[35–37] In this section the studies of alcoholic (wine, beer, spirits) and nonalcoholic (juices, tea, coffee) beverages will briefly be presented.

3.2.1 Wine

The acetic acid content in intact wine bottles has been measured down to $0.5\,g\,1^{-1}$, more than half of the accepted limit in normal wine.[15] Full intact wine bottles of a series of Cabernet Sauvignons have been investigated by high-resolution

^{1}H NMR and ^{13}C NMR Spectroscopy.[16] The application of full bottle NMR in the measurement of acetic acid content, the detection of complex sugars, phenols and trace elements in wine is discussed. A rapid throughput method for the quantitation of the oxidation level of intact full bottles of wine has been described and an application to the detection of wine spoilage in more than century old wine has been provided.[38]

The use of 1D and 2D homo- and hetero-NMR experiments and WET suppression technique of strong signals enabled the assignment of ^{1}H and ^{13}C resonances of some organic acids and alcohols, present in higher amounts in wines, as well as ^{1}H and ^{13}C signals of 17 amino acids and of gamma-aminobutyric acid.[39] A good separation of Slovenian wines according to the vine variety has been obtained using ^{1}H signal intensities of amino acids in chemometric analysis.[40] By also adding the signal intensities of glycerol, butylene glycol and succinic acid, Slovenian wines can be distinguished according to their geographical origin.

White wine mannoproteins, *Saccharomyces cervisiae* yeast polysaccharides, that play a major role in wine processing and characteristics have been characterized in terms of chemical composition and molecular structure using two-dimensional ^{1}H and ^{13}C NMR techniques.[41]

A classification study of Italian red wines from different geographical locations in the Apulia (southern Italy) involved the comparison of multivariate analysis of ^{1}H NMR spectra with that of data obtained by alternative methods, including high performance ion chromatography (HPIC), high performance ion chromatography exclusion (HPICE) and coupled plasma emission spectroscopy (ICP-OES).[42] Wines of different geographical origin could be distinguished on the basis of amino acid composition determined by NMR and on the basis of the heavy metal composition determined by alternative methods.

A similar approach has been applied to a group of wine samples from Apulia and Slovenia.[43] It is shown that the best prediction of the country of origin is achieved by multivariate analysis of the NMR data.

Marker signals in the high-resolution ^{1}H spectra of some Romanian wines have been used for the identification and quantitative measurements of minor compounds.[44]

LC-NMR/MS combination has been used for the detection of phenolics such as catechin, epicatechin, *trans*-resveratrol, tyrosol and caffeic acid in the wine extracts.[45]

NMR technique has been used for the first time to accurately determine the diffusion coefficient D of CO_2 dissolved molecules in various carbonated beverages including champagne and sparkling wines.[46] It has been demonstrated that an imaging spectrometer with the ^{13}C Magnetic Resonance Spectroscopy is perfectly adapted to determine the amount of CO_2 dissolved in a closed bottle of Champagne or sparkling wine[47]. The diffusion rate of CO_2 was also determined in this matrix.

The use of high-resolution NMR and DOSY for the characterization of selected Port wine samples of different ages has been described with the aim to identify changes in their chemical composition.[48] It is found that Port wines of

different ages differ mainly in their content of organic acids, some amino acids, an unidentified possible disaccharide and large aromatic species.

The results of different preparation methods of wine samples such as direct analysis, freeze-drying and nitrogen-flow concentration have been presented in the ^{1}H NMR characterization of Brazilian Chardonnay wine composition.[49] It was concluded that the direct analysis is of limited capacity for detecting minor compounds. A low quantity of ethanol remained in the lyophilisate when freeze-drying was used. This process also revealed restrictions concerning long-time consumption and poor reproducibility. Nitrogen-flow concentration has shown advantages in the identification of minor compounds with less time consumption.

The discrimination of wines based on 2D NMR spectra has been performed using the learning vector quantization (LVQ) neural network with orthogonal signal correction (OSC), proposed as a data preprocessing method that removes from X information not correlated to Y.[50] The partial least squares discriminant analysis (PLS-DA) method has also been used with the same data set. OSC-LVQ neural networks method gave slightly better prediction results than OSC-PLS-DA.

It has been demonstrated that using a combination of ^{1}H NMR and PCA it is possible to achieve an excellent classification of the type and production location of wines, produced by three subsidiary companies, located in Shacheng (continental region) and Yantai and Changli (both in the coastal region), China.[51]

3.2.2 Beer

NMR has been used for the characterization of water-soluble arabinoxylanes from barley and barley malt[52] and a novel flavanol glucoside from barley and malt.[53]

High-resolution NMR spectroscopy and multivariate analysis have been used for the characterization of beer.[54] It was found that although some distinction is achieved on the basis of the aliphatic and sugar compositions, clearer separation between ales and lagers is obtained by PCA of the aromatic profiles alone.

Hyphenated NMR (LC-NMR/MS) has been applied for the direct identification of carbohydrates in beer.[55] Dextrins with polymerization degree up to nine monomers were identified in 1–2 h. Two beer samples were found to have significantly different oligosaccharide compositions, reflecting the different production conditions employed.

LC-NMR/MS has also been used to identify 2-phenylethanol, tyrosol and tryptophol in beer.[45]

The multivariate analysis of NMR and FTIR data has been used as a potential tool for the quality control of beer.[56] While PCA of FTIR data resulted in separation of beers mainly according to their alcoholic content, PCA of ^{1}H NMR spectra resulted in the separation of samples into four groups. Most ales, lagers and alcohol-free samples could be distinguished on the basis of their aromatic composition.

Nord et al. have demonstrated the quantification of organic and amino acids in beer using ^{1}H NMR spectroscopy.[57]

Lachenmeier et al. have introduced high-resolution NMR spectroscopy for the quality control and authenticity assessment of beer in official food control.[58]

PCA of ^{1}H NMR spectra of beer has been described in order to obtain information on composition variability.[59] Interpretation of compositional differences is discussed in terms of biochemistry taking place during brewing. The possible application of the method in brewing process control is envisaged.

Two-dimensional *J*-resolved NMR spectroscopy has been successfully applied to differentiation of six brands of pilsner beer.[60] The compounds responsible for differentiation were identified by 2D NMR techniques. They are: nucleic acids derivatives, tyrosine and proline, succinic and lactic acid, tyrosol and *iso*propranol, cholines and carbohydrates.

The relationship between structurally similar compounds and their physico-chemical properties, such as acidity, has been analysed using ^{13}C NMR, UV-spectroscopy and semiempirical calculations.[61] It was found that logarithms of stability constants are essentially linear functions of the NMR chemical shift. The established relation can estimate the aqueous solubility and stability of humulones and their derivatives enabling an effective control of production processes in the brewing industry.

3.2.3 Spirits

The hydrogen-bonding structure of water–ethanol in whisky has been studied.[62] The OH-proton chemical shifts were measured for 32 malt whisky distillery samples aged from 0 to 23 years in five different types of cask. It was concluded that the strength of the hydrogen bonding in aged whiskies was directly predominated by acidic and phenolic components gained in oak wood casks and not dependent just on the aging time.

On the basis of Raman OH stretching spectra and ^{1}H NMR chemical shifts it has been concluded that the strength of the hydrogen bond of water–ethanol in Japanese sake products correlate with the total concentration of organic and amino acids.[63] It has also been shown that the hydrogen-bonding structure in shochu, a Japanese distilled spirit containing some acids differs from that of water–ethanol mixture with corresponding ethanol content.[64] Nose and Hojo have investigated the properties of the hydrogen-bonding structure of water–ethanol in alcoholic beverages using ^{1}H NMR chemical shifts and the Raman OH stretching spectra.[65] On the basis of the results of their studies the authors believe that organic acids or poly(phenols) (proton donors) and conjugate base anions of weak acids (proton acceptors) are the main components to reduce the organoleptical stimulation of alcoholic beverages as a consequence of the change of the hydrogen-bonding structure of water–ethanol.

Two papers considering Cypriot spirit zivania have been published.[66,67] In the paper by Petrakis et al., ^{1}H NMR is combined with statistical analysis for the study of the authenticity of zivania.[66] NMR spectroscopy gave a satisfactory degree of prediction and classification between zivanias and other distillates. In the paper by Kokkinofta and Theocharis, the results using multivariate chemometric techniques and variables determined by ^{1}H NMR, HPLC, GC and ICP spectroscopy are presented.[67] Nearly correct classification for zivania is achieved.

3.2.4 Juices

Tomato juices and pulp have been characterized by liquid and magic angle spinning NMR.[68] A comprehensive assignment of proton spectra of both juice and pulp was obtained. The comparison between the juice and pulp spectra shows that essentially all water-soluble substances in the pulp are extracted in the juice. HR-MAS NMR was able to detect some insoluble compounds such as lipids.

Using LC-NMR/MS several cinnamic acids (*p*-coumaric, *trans*-coutaric and *trans*-caftaric) have been identified in grape juice.[45]

NMR spectroscopy, hyphenated NMR and DOSY have been applied to characterize mango juice.[69] The compositional changes as a function of ripening were followed and selected metabolites were quantified by integration of the corresponding NMR peaks. This enabled the study of the biochemical mechanisms involved in the ripening process. High-resolution ^{1}H NMR spectroscopy has also been used to study natural mango juice spoilage and microbial contamination with *Penicillium expansum*.[70]

^{1}H NMR spectroscopy has been applied to the quantitative determination of malic and citric acids in apple, apricot, pear, kiwi, orange, strawberry and pineapple juices.[71] The results obtained were compared to those obtained by enzymatic methods and they were in close agreement.

^{1}H NMR spectra have been used in the characterization and chemometric differentiation of 52 apple juices obtained from cider apple varieties.[72] The most discriminant variables correspond to polyphenols, (−)-epicatechin, phloridizin-phloretin, and *p*-cumaric, chlorogenic and malic acids.

^{1}H NMR quantitative determination of chlorogenic acid, (−)-epicatechin and formic acid in apple juices has been reported.[73–75]

3.2.5 Tea

Solid-state^{13}C CP-MAS spectra of green and black tea have been obtained and assigned.[76] Contributions of catechin derivatives, carbohydrate, alkaloid and terpenoid constituents are present. The observed peak patterns provide a means to distinguish between both teas.

The analysis of 176 kinds of tea infusions (green, black, oolong and others) by ^{1}H NMR spectroscopy has been reported.[77] Each spectrum pattern was analysed by a multivariate statistical pattern-recognition method where PCA was used in combination with soft independent modelling of class analogy (SIMCA). SIMCA effectively selected variables that contribute to tea categorization. The final PCA resulted in clear classification reflecting the fermentation and processing of each tea, and revealed marker variables that include catechin and theanin peaks.

3.2.6 Coffee

^{1}H NMR and multivariate statistics have been applied for analyzing the quality and authenticity of instant coffees obtained from three different producers.[78] The samples from the three manufacturers were successfully identified.

Quantitative analysis of caffeine using ^{1}H NMR and the identification of the major components in commercial coffee samples have been reported.[79] In this study 1D and 2D NMR techniques were used without any sample pre-treatment.

REFERENCES

1. K. F. Morris and C. S. Johnson, *J. Am. Chem. Soc.*, 1992, **114**, 3139.
2. M. Nilsson, A. M. Gil, I. Delgadillo and G. A. Morris, *Anal. Chem.*, 2004, **76**, 5418.
3. M. Nilsson, A. M. Gil, I. Delagadillo and G. A. Morris, *Chem. Comm.*, 2005, 1737.
4. O. Corcoran, P. S. Wilkinson, M. Godejohann, U. Braumann, M. Hofmann and M. Spraul, *Am. Lab.*, 2002, **34**, 18.
5. J. W. Jaroszewski, *Planta Med.*, 2005, **71**, 795.
6. A. J. Alexander, F. Xu and C. Bernard, *Magn. Reson. Chem.*, 2006, **44**, 1.
7. G. J. Martin and M. L. Martin, *Tetrahedron Lett.*, 1981, **22**, 3525.
8. A. Rossmann, H. L. Schmidt, F. Reniero, G. Versini, I. Moussa and M. H. Merle, *Z. Lebensm.-Unters. Forsch.*, 1996, **203**, 293–301.
9. A. M. Gil, I. Duarte, E. Cabrita, B. J. Goodfellow, M. Spraul and R. Kerssebaum, *Anal. Chim. Acta*, 2004, **506**, 215.
10. L. H. Lucas, W. H. Otto and C. K. Larive, *J. Magn. Reson.*, 2002, **156**, 138.
11. L. Barantin, S. Akoka and A. L. Pape, *Innov. Techn. Biol. Med.*, 1996, **17**, 373.
12. I. Billault, R. Robins and S. Akoka, *Anal. Chem.*, 2002, **74**, 5902.
13. F. Le Grand, G. George and S. Akoka, *J. Magn. Reson.*, 2005, **174**, 171.
14. G. S. Remaud, V. Silvestre and S. Akoka, *Accredit. Qual. Assur.*, 2005, **10**, 415.
15. A. J. Weekley, P. Bruins and M. P. Augustine, *Am. J. Enol. Vitic.*, 2002, **53**, 318.
16. A. J. Weekley, P. Bruins, M. Sisto and M. P. Augustine, *J. Magn. Reson.*, 2003, **161**, 91.
17. E.C. Regulation number 2676/90, *Off. J. Eur. Communities*, 1990, L272, **33**, 64.
18. E. C. Regulation number 440/2003 amending E. C. Regulation number 2676/90 determining Community methods for the analysis of wine.
19. A. Rossmann, *Food Rev. Int.*, 2001, **17**, 347.
20. E. Alberti, P. S. Belton and A. M. Gil, in: *Annu. Rep. NMR Spectrosc.*, G. A. Webb, ed., Elsevier, Amsterdam, 2002, p. 109.
21. N. Ogrinc, I. J. Kosir and J. Kidric, *Res. Adv. Agric. Food Chem.* (Global research network series 3), R. Mohan, ed., 2002, 1.
22. G. Calderone, M. Holland, F. Reniero and C. Guillou, *Eur. Food Res. Technol.*, 2005, 1.
23. G. J. Martin, S. Akoka and M. L. Martin, in: *Modern Magnetic Resonance, Part III*, G. A. Webb, ed., Springer, Dordrecht, The Netherlands, 2006, p. 1629.
24. M. L. Martin, B. Zhang and G. J. Martin, in: *Modern Magnetic Resonance, Part III*, G. A. Webb, ed., Springer, Dordrecht, The Netherlands, 2006, p. 1637.
25. G. J. Martin, M. L. Martin and G. S. Remaud, in: *Modern Magnetic Resonance, Part III*, G. A. Webb, ed., Springer, Dordrecht, the Netherlands, 2006, p. 1647.
26. E. Jamin and G. J. Martin, in: *Modern Magnetic Resonance, Part III*, G. A. Webb, ed., Springer, Dordrecht, The Netherlands, 2006, p. 1659.
27. N. Ogrinc, I. J. Kosir, M. Kocjancic and J. Kidric, *J. Agric. Food Chem.*, 2001, **49**, 1432.
28. I. J. Kosir, M. Kocjancic, N. Ogrinc and J. Kidric, *Anal. Chim. Acta*, 2001, **429**, 195.
29. N. Ogrinc, I. J. Kosir, J. E. Spangenberg and J. Kidric, *Anal. Bioanal. Chem.*, 2003, **376**, 424.
30. G. Gremaud, E. Pfammatter and U. Piantini, *Mitt. Lebensm. Hyg.*, 2002, **93**, 44.
31. G. Gremaud, S. Quaile, U. Piantini, E. Pfammatter and C. Corvi, *Eur. Food Res. Technol.*, 2004, **219**, 97.
32. E. Jamin, F. Martin, R. Santamaria-Fernandez and M. Lees, *J. Agric. Food Chem.*, 2005, **53**, 5130.
33. C. Bauer-Christoph, N. Christoph, B. O. Aguilar-Cisneros, M. G. Lopez, E. Richling, A. Rossmann and P. Schreier, *Eur. Food Res. Technol.*, 2003, **217**, 438.
34. C. W. Hsieh, H. J. Wang, C. M. Chang and W. C. Ko, *J. Food Drug Anal.*, 2005, **13**, 251.

35. J. Kidric and I. J. Kosir, in: *Modern Magnetic Resonance, Part 3*, G. A. Webb, ed., Springer, Dordrecht, The Netherlands, 2006, p. 1575.
36. A. M. Gil and I. F. Duarte, in: *Modern Magnetic Resonance, Part 3*, G. A. Webb, ed., Springer, Dordrecht, The Netherlands, 2006, p. 1667.
37. A. M. Gil and J. Rodrigues, in: *Magnetic Resonance in Food Science*, I. A. Farhat, P. S. Belton and G. A. Webb, eds., RSC, Cambridge, 2007, p. 96.
38. D. N. Sobieski, G. Mulvihill, J. S. Broz and M. P. Augustine, *Solid State Nucl. Mag.*, 2006, **29**, 191.
39. I. J. Kosir and J. Kidric, *J. Agric. Food Chem.*, 2001, **49**, 50.
40. I. J. Kosir and J. Kidric, *Anal. Chim. Acta*, 2002, **458**, 77.
41. F. Goncalves, A. Heyraud, M. N. De Pinho and M. Rinaudo, *J. Agric. Food Chem.*, 2002, **50**, 6097.
42. M. A. Brescia, V. Caldarola, A. De Giglio, D. Benedetti, F. P. Fanizzi and A. Sacco, *Anal. Chim. Acta*, 2002, **458**, 177.
43. M. A. Brescia, I. J. Kosir, V. Caldarola, J. Kidric and A. Sacco, *J. Agric. Food Chem.*, 2003, **51**, 21.
44. M. C. Buzas, N. Chira, C. Deleanu and S. Rosca, *Rev. Chim. Bucharest*, 2003, **54**, 831.
45. A. M. Gil, I. F. Le Duarte, M. Godejohann, U. Braumann, M. Maraschin and M. Spraul, *Anal. Chim. Acta*, 2003, **488**, 35.
46. G. Liger-Belair, E. Prost, M. Parmentier, P. Jeandet and J. M. Nuzillard, *J. Agric. Food Chem.*, 2003, **51**, 7560.
47. G. Autret, G. Liger-Belair, J. M. Nuzillard, M. Parmentier, A. D. de Montreynaud, P. Jeandet, B. T. Doan and J. C. Beloeil, *Anal. Chim. Acta*, 2005, **535**, 73.
48. M. Nilsson, I. F. Duarte, C. Almeida, I. Delgadillo, B. J. Goodfellow, A. M. Gil and G. A. Morris, *J. Agric. Food Chem.*, 2004, **52**, 3736.
49. F. M. Amaral and M. S. B. Caro, *Food Chem.*, 2005, **93**, 507.
50. S. Masoum, D. J. R. Bouveresse, J. Vercauteren, M. Jalali-Heravi and D. N. Rutledge, *Anal. Chim. Acta*, 2006, **558**, 144–149.
51. D. Yuan-Yuan, B. Guo-Yun, Z. Xu and L. Mai-Li, *Chin. J. Chem.*, 2007, **25**, 930.
52. G. Dervilly, C. Leclercq, D. Zimmermann, C. Roue, J. F. Thibault and L. Saulnier, *Carbohydr. Polym.*, 2002, **47**, 143.
53. W. Friedrich and R. Galensa, *Eur. Food Res. Technol.*, 2002, **214**, 388.
54. I. Duarte, A. Barros, P. S. Belton, R. Righelato, M. Spraul, E. Humpfer and A. M. Gil, *J. Agric. Food Chem.*, 2002, **50**, 2475–2481.
55. I. F. Duarte, M. Godejohann, U. Braumann, M. Spraul and A. M. Gil, *J. Agric. Food Chem.*, 2003, **51**, 4847.
56. I. F. Duarte, A. Barros, C. Almeida, M. Spraul and A. M. Gil, *J. Agric. Food Chem.*, 2004, **52**, 1031.
57. L. I. Nord, P. Vaag and J. O. Duus, *Anal. Chem.*, 2004, **76**, 4790.
58. D. W. Lachenmeier, W. Frank, E. Humpfer, H. Schafer, S. Keller, M. Mortter and M. Spraul, *Eur. Food Res. Technol.*, 2005, **220**, 215.
59. C. Almeida, I. F. Duarte, A. Barros, J. Rodrigues, M. Spraul and A. M. Gil, *J. Agric. Food Chem.*, 2006, **54**, 700.
60. A. Khatib, E. G. Wilson, H. K. Kim, A. W. M. Lefeber, C. Erkelens, Y. H. Choi and R. Verpoorte, *Anal. Chim. Acta*, 2006, **559**, 264–270.
61. C. A. Blanco, A. Rojas, P. A. Caballero, F. Ronda, M. Gomez and I. Caballero, *Trends Food Sci. Tech.*, 2006, **17**, 373.
62. A. Nose, M. Hojo, M. Suzuki and T. Ueda, *J. Agric. Food Chem.*, 2004, **52**, 5359.
63. A. Nose, M. Myojin, M. Hojo, T. Ueda and T. Okuda, *J. Biosci. Bioeng.*, 2005, **99**, 493.
64. A. Nose, T. Hamasaki, M. Hojo, R. Kato, K. Uehara and T. Ueda, *J. Agric. Food Chem.*, 2005, **53**, 7074.
65. A. Nose and M. Hojo, *J. Biosci. Bioeng.*, 2006, **102**, 269.
66. P. Petrakis, I. Touris, M. Liouni, M. Zervou, I. Kyrikou, R. Kokkinofta, C. R. Theocharis and T. M. Mavromoustakos, *J. Agric. Food Chem.*, 2005, **53**, 5293.
67. R. I. Kokkinofta and C. R. Theocharis, *J. Agric. Food Chem.*, 2005, **53**, 5067.
68. A. P. Sobolev, A. Segre and R. Lamanna, *Magn. Reson. Chem.*, 2003, **41**, 237.
69. I. F. Duarte, B. J. Goodfellow, A. M. Gil and I. Delgadillo, *Spectrosc. Lett.*, 2005, **38**, 319.
70. I. F. Duarte, I. Delgadillo and A. M. Gil, *Food Chem.*, 2006, **96**, 313.

71. G. del Campo, I. Berregi, R. Caracena and J. I. Santos, *Anal. Chim. Acta*, 2006, **556**, 462.
72. G. Del Campo, J. I. Santos, N. Iturriza, I. Berregi and A. Munduate, *J. Agric. Food Chem.*, 2006, **54**, 3095.
73. I. Berregi, J. I. Santos, G. del Campo, J. I. Miranda and J. M. Azipurua, *Anal. Chim. Acta*, 2003, **486**, 269.
74. I. Berregi, J. I. Santos, G. del Campo and J. I. Miranda, *Talanta*, 2003, **61**, 139.
75. I. Berregi, G. del Campo, R. Caracena and J. I. Miranda, *Talanta*, 2007, **72**, 1049.
76. A. Martinez-Richa and P. Joseph-Nathan, *Solid State Nucl. Mag.*, 2003, **23**, 119.
77. M. Fujiwara, I. Ando and K. Arifuku, *Anal. Sci.*, 2006, **22**, 1307.
78. A. J. Charlton, W. H. H. Farrington and P. Brereton, *J. Agric. Food Chem.*, 2002, **50**, 3098.
79. L. A. Tavares and A. G. Ferreira, *Quim. Nova*, 2006, **29**, 911.

This page intentionally left blank

CHAPTER 6

Contribution of NMR Spectroscopy to Flavour Release and Perception

L. Tavel, E. Guichard and **C. Moreau**

Contents

Abstract

The control of flavouring of a food product as well as the flavour perception during consumption is a great challenge for improving food quality. However, the various ingredient composition and the different textural properties of foods can significantly affect the release of aroma compounds or sapid molecules. It is thus of major importance to determine physico-chemical factors that govern diffusion and binding phenomena of these small solutes in food products. In this way, NMR spectroscopy is an efficient tool to characterize these mechanisms at a molecular scale. Diffusion rates of small solutes in aqueous, viscous and gel solutions can be extracted from relaxation or diffusion NMR experiments. PFG-NMR experiments are particularly valuable methods to investigate aroma compound self-diffusion and gel microstructure in a non-invasive way. A wide range of methods based on chemical shift, relaxation or diffusion rate changes also provide unique and direct information on binding events of aroma compounds with food macromolecules. Binding site localization, affinity constant and spatial conformation of complexes can be achieved using conventional 1D- and 2D-NMR spectroscopy.

Keywords: NMR diffusion; ligand binding; flavour molecules; food systems

UMR1129 FLAVIC, ENESAD, INRA, Université de Bourgogne, 17 rue Sully, B.P. 86510, 21065 Dijon, France

Annual Reports on NMR Spectroscopy, Volume 64
ISSN 0066-4103, DOI 10.1016/S0066-4103(08)00006-9

1. INTRODUCTION

From all the indicators of a 'good' product, flavour is considered as one of the most important quality attributes determining the acceptability of food by the consumer. The perception of food flavour is occurring when flavour compounds, (aroma compounds and sapid molecules), are released from a food matrix and transported through the liquid and gas phases to the flavour receptors in the mouth and nose. However, the enormous variety of food differing strongly by their ingredient composition and their textural properties makes the control of the release mechanism difficult. For example, gelling agents or thickeners such as carrageenan or pectin polysaccharides not only modified textural properties but often reduced intensities of taste and flavour.[1] Moreover protein ingredients can reduce the perceived impact of desirable flavours and may transmit undesirable off-flavours. Beside these considerations, small solutes such as water molecules and ions, for example sodium or potassium ions, also play an important role in these systems. Water influences mechanical and textural properties of foods and acts as a solvation medium. Cation species by promoting cross-linking of polymer chains such as carrageenan, pectin or dextran, could influence the structural arrangement of the food networks. To develop a full understanding of food flavour release, it is thus necessary to determine to what extent composition and textural properties of food affect the binding, entrapment, diffusion and release of flavour compounds. Transport phenomena and release of aroma from foods are influenced by diffusion processes, which in turn are governed by the physical properties of the diffusing solute and its surroundings.[2] Two main factors could impact on the diffusion processes: (i) obstructions or entrapment effects due to macromolecule nature and structural organization and (ii) the strength and the nature of specific interactions (chemical or non-chemical such as hydrogen-bonding) between small solutes, including water molecules and ions, and large food molecules.

The development of rapid and accurate analytical methods, with the ability to account for a range of compounds as comprehensive as possible, would be of significant importance for the understanding of diffusion and small solute–food macromolecule interaction mechanisms. NMR spectroscopy has an outstanding position in the field of chemical analysis of food products because of its non-destructive aspect. It enables detailed compositional, structural and dynamic studies of individual components in the pure state or in mixtures. Several reviews have underlined the enormous potential of the NMR technique for investigations of complex food systems.[3,4] Over the last decade, high-resolution nuclear magnetic resonance (HR-NMR) spectroscopy combined with statistical treatment of NMR data has been increasingly used for the authenticity of food products.[5–7] Indeed NMR spectral profile may be a good indicator of food quality and origin. The so-called site-specific natural isotope fractionation (SNIF)-NMR has been successfully used in the characterization of flavour origin and authenticity.[8] The large range of HR 1D- and 2D-NMR experiments allows the detection and the identification of a great number of low molecular weight components in beverages, wines, fruits or cheeses components.[5,9–11] Moreover, high-resolution

pulsed field-gradient (PFG)-NMR method has become the method of choice to separate each component of a mixture based on their molecular size and gives additional aid for the identification of ambiguous assignments.[12–15]

Nevertheless, even if all these works show the enormous potential of these NMR methods for the determination of food authenticity, no information is given on the characterization of food products based on their organoleptic properties. Understanding at a molecular scale the mechanisms which influence flavour binding or release behaviour of flavour compounds from the food matrix is of major significance for improving flavour quality.[16] Numerous qualitative and quantitative NMR data are available on small solutes–macromolecule complex, particularly in chemical, biological and pharmacological research. However, lesser NMR studies have been applied on aroma compounds–food macromolecule interactions. The aim of this review is to show how NMR spectroscopy can help in understanding flavour release from food product. Among the various NMR methods used to investigate biopolymer–water systems, the determination of relaxation rates and/or self-diffusion coefficients is particularly valuable in examining mobility of small solutes in simple aqueous systems such as water or sugar–water solutions or in model food systems composed of polysaccharides. Besides these insights, several 1D- and 2D-NMR methods based on change of NMR parameters such as chemical shifts, relaxation rates, diffusion coefficient or NOE, provide a rapid and direct characterization on molecular binding events between aroma compounds and food macromolecules.[17–21] Since all these NMR parameters are sensitive to the surrounding medium (viscosity, pH, temperature, ionic strength) and to structural properties of the observed molecular species such as nature, weight, size, and shape, the transport mechanisms of small solutes with microscopic insight into food gel structure and binding affinity or spatial conformation of the complex can be investigated.

2. NMR DIFFUSION OF SMALL SOLUTES

The random reorientation of molecules in simple liquids, such as water, can be divided into rotational and translational motions. These motions, known as Brownian motions, can be probed by diffusion and/or relaxation rates measurements using low-field (LF) and HR NMR spectroscopy.

Two main relaxation processes exist according to their source of origin: spin–lattice ($R_1 = 1/T_1$) and spin–spin ($R_2 = 1/T_2$) relaxation rates which are measurements of the interaction of a spin with its surroundings and the mobility of a spin, respectively.[22,23] T_2 relaxation is referred to the measured translational diffusion rate, also named self-diffusion. The most common methods to determine T_1 and T_2 relaxation times are the inversion-recovery and the CPMG (Carr–Purcell–Meiboom–Gill) experiments, respectively. Relaxometry studies at LF-NMR have been particularly performed in low-water food products to investigate water properties of pure samples and mixtures.[24,25] Different populations of water molecules are distinguished according to their mobility: 'free' water molecules with slow relaxation rates and water molecules with

restricted motion as they are associated or bound to solutes/macromolecules and with fast relaxation time. The translational self-diffusion coefficient, D, of solutes in liquids or gel systems can be probed using PFG-NMR method that applies magnetic gradient pulses to the sample in addition to the static magnetic field (for more details, see excellent reviews [26–29]). In the simplest case, a PFG-NMR experiment is based on the measurement of a series of spin echo spectra with incremented values of the gradient strength resulting in signal decaying at rates determined by diffusion properties of investigated molecules. The intensity (I) of each resonance signal in the spectrum decays exponentially with the square of the gradient amplitude, g, according to:

$$I = I_0 \exp\left[-D(g\delta\gamma)^2\left(\Delta - \frac{\delta}{3}\right)\right] \quad (1)$$

where I and I_0 are, respectively, the intensity of the NMR signal in the presence and absence of external magnetic gradient pulses, δ the duration of the magnetic gradient pulse, γ the gyromagnetic ratio of the observed nucleus and Δ defines the diffusion time scale (from ms to s). A variety of pulse sequences exists for measuring self-diffusion coefficients – one of the simplest sequence being the stimulated spin echo, STE-depending on the investigated systems (molecule size, relaxation times, convection phenomena…).[26,30] PFG-NMR spectroscopy has the advantage to be a rapid and accurate method for measuring self-diffusion coefficient in simple and complex systems. Moreover, diffusion-ordered spectroscopy (DOSY) is a particular convenient means of displaying diffusion data set in 2D-dimensional matrix with diffusion coefficients plotted along one axis.[31,32]

According to the Stokes–Einstein relation, $D_0 = kT/6\pi\eta R_H$, self-diffusion coefficient of small solute depends on the temperature, the viscosity of the solvent, η, and on the hydrodynamic radius of the diffusing solute, R_H. Thus, the D/D_0 ratio, where D is the self-diffusion coefficient of the solute in viscous/gel system and D_0 the onset of pure water, gives information on the impact of solute size and nature, medium viscosity, the presence of macromolecules on diffusion process. Moreover, the average displacement r of a small solute with a self-diffusion coefficient of D during the diffusion time t is given by $\langle r\rangle = (2Dt)^{1/2}$.

2.1 NMR diffusion of small solutes in simple aqueous systems

2.1.1 Diffusion in water solution

In order to understand diffusion process of small aroma compounds in food product, their diffusion in water solutions can provide important information on the impact of their nature. Different techniques have been used to determine diffusion coefficients of small solutes in water solution. The rotating diffusion cell method is designed hydrodynamically so that stationary diffusion layers of known thickeners are created on each side of an oil layer.[33] It enables the calculation of diffusion coefficients in different liquid phases and of the mass transfer coefficients of solutes.[34] Recently, self-diffusion coefficients of aroma compounds at around 500 µM concentration in D_2O solution were measured at 30°C using STE bipolar pulse experiments at 500 MHz.[35] Aroma molecules are

Table 1 Main physicochemical characteristics of aroma compounds

Name	Molar mass ($g\,mol^{-1}$)	log*P*	Solubility in water, 25°C ($g\,L^{-1}$)	Diffusion at 30°C ($\mu m^2\,s^{-1}$)[35]	Vapour/water partition coefficient × 1,000 at 30°C[36]
Ethyl acetate	88.10	0.73	82	1,053 (21)	16.2
Ethyl butyrate	116.16	1.85	5.6–5.75	881 (14)	18.3
Ethyl hexanoate	144.22	2.82	0.46–0.52	856 (25)	30.2
Linalool	154.25	3.38	2.60	679 (7)	3.87
Hexanal	100.16	1.80	1.78	878 (40)	11.6

Note: Values in parentheses indicate 95% confidence intervals.

small volatile compounds which can be characterized by specific physicochemical properties, such as hydrophobic properties, described by the log*P* value, solubility in water or vapour/water partition coefficient (Table 1).[36] Self-diffusion coefficient values of three esters (ethyl acetate, ethyl butyrate and ethyl hexanoate), one alcohol (linalool) and one aldehyde (hexanal) measured with variation coefficient smaller than 5% are shown in Table 1. A general trend is observed between self-diffusion coefficients of aroma compounds and their physicochemical characteristics. The larger and the more hydrophobic (higher log*P* values) the molecules are, the lower the self-diffusion coefficients are. The measured diffusion coefficients only partly explain the vapour–water partition coefficients,[36] and no strictly linear relationship is found between these properties and the hydrophobicity of the molecule. Other parameters such as the chemical or structural functionality (linear or branched molecules, presence of double bonds, hydroxyl groups, rings…) have to be taken into account since they can lead to different spatial arrangements of the solute in water and/or to different water hydration states. Carrying a quantitative–structure–property relationship approach on vapour/water partition coefficients, Chana et al. found that other descriptors than log*P* values were involved in the aroma retention.[37] For example, in the case of esters and ketones, a globular form or the presence of ramifications within the molecule induced a lower retention in water or a higher release.

Other works deal with self-diffusion of small solutes in D_2O solution using PFG-NMR method and showed that for a specific system at a given temperature, the relation between small solute diffusion and solute sizes was verified. Lundberg and Kuchel reported a similar relation between molecular weights and the self-diffusion coefficients of glycine (132 mM), alanine (114 mM), lactate (103 mM) and glucose (122 mM) in D_2O at 37°C measured at 400 MHz.[38] Kwak and Lafleur investigated self-diffusion of small solutes and large micellar systems composed of surfactants in D_2O solution at 37°C using a 2.5 imaging microprobe at 300 MHz.[39] As expected, small organic molecules (alcohols, diols and ketones) diffuse more rapidly than micellar systems due to their sizes and medium viscosity. However, the authors showed that if the Stokes–Einstein relation accounts for self-diffusion of micellar systems described by its hydrodynamic

radius, the relation is not valid for small solutes and that their diffusion process is better described by their van der Waals radii (R_W).

2.1.2 Diffusion in water–sugar solutions

Diffusion of sugars in water–sugar systems has been the subject of several works as it has been shown that the perceived sweetness varies according to the sugar nature and concentration and thus, water molecule availability can be a key factor of this perception.[40,41] Information on NMR mobility of water–sucrose systems is available through longitudinal and transverse relaxation rates or self-diffusion coefficient measurements performed by LF-NMR.[42–44] Three distinct regions of decreasing water mobility with increasing sugar concentration can be observed: (i) at low sugar concentration (<20% w/w), water mobility is slightly decreased principally due to the medium viscosity; (ii) at intermediate concentration (between 20 and 35% w/w), in the addition of viscosity effect, the hydration water increases (increase of relaxation rates or decrease of self-diffusion coefficients) due to proton exchange between water molecules and sugar hydroxyl groups through hydrogen bonding but at this point, the global water mobility is dominated by the bulk water and (iii) at very high sucrose concentration (>35–40% w/w), interactions between water–water, water–sugar and sugar–sugar molecules are predominant leading to the dramatic decrease of the water and sugar mobility.

In the study of Savary et al., the self-diffusion of five aroma compounds (three esters, one aldehyde and one alcohol; Table 1) in 35% w/w sucrose solutions was investigated using DOSY NMR method.[35] As expected, a strong decrease of self-diffusion coefficients for all aroma compounds was observed in 35% w/w sucrose solution compared to D_2O solution ($D/D_0 = 0.33$). Moreover, the magnitude of the self-diffusion decreased in 35% w/w sucrose solutions appears to be independent of the aroma nature, strongly suggesting that the viscosity effect was the main factor and that no specific chemical interaction occurred. As shown in Figure 1, the self-diffusion of ethyl butyrate markedly decreased between 20 and 35% w/w sucrose. Moreover, a good correlation is found between D/D_0 ratio and sucrose solution viscosities ($R^2 = 0.97$) and assuming an averaged 2 Å radius for ethyl butyrate, the Stokes–Einstein relation was valid with these measured self-diffusion coefficients. As self-diffusion coefficients of water and sucrose molecules also dramatically decreased above 20% w/w sucrose, the authors hypothesized that water molecules which are in strong exchange with sugar molecules are not enough to enhance aroma diffusion through solvation. In this work, it was shown that the measured self-diffusion coefficient of residual water was in accordance with the measured water activity showing that DOSY NMR method is a powerful method to obtain complete information on all components of the investigated system in one experiment.

Though sugar–water systems have been the subject of several analytical studies, only one study, to our mind, combined diffusion data obtained at molecular scale with sensorial analysis. In order to validate the hypothesis that ''at equal molar concentrations, the higher the perceived sweetness of a sugar, the more mobile is the water associated with sugar'', Mahawanich and Schmidt

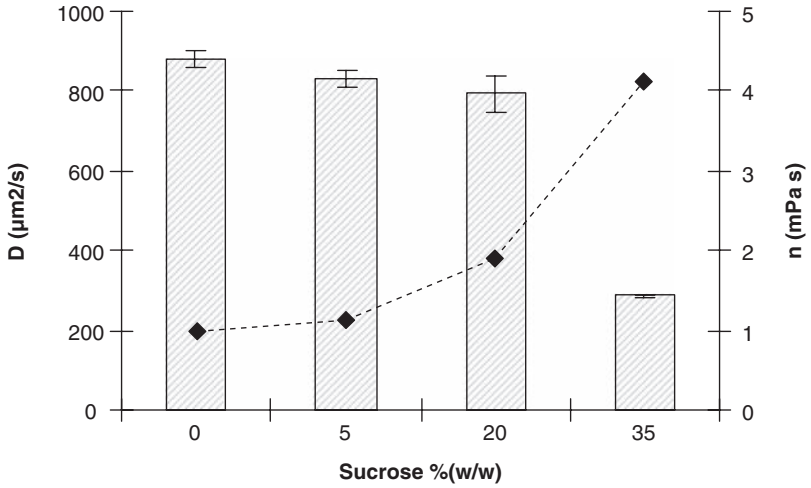

Figure 1 Self-diffusion coefficients of ethyl butanoate at 500 µM in D_2O and sucrose solutions at 30°C. Viscosity values of D_2O and sucrose solutions are also taken.

compared ^{1}H and ^{17}O NMR relaxation rates and ^{1}H self-diffusion coefficient values of water and three different sugars, fructose (180.1 g mol^{-1}), glucose (180.1 g mol^{-1}) and sucrose (342.3 g mol^{-1}) at different concentrations (from 0 to 3.50 mol L^{-1}).[45] Authors showed that if the rotational mobility of water and sugar molecules was slower with the larger sugar molecule, this observation was not valid for the translational mobility: D(fructose) > D(sucrose) > D(glucose) and the same trend was observed for water molecules. Thus, the diffusion process in these systems was not dependent on the nature of sugar and, although no viscosity measurement was done, this parameter had probably a slight impact on water and sugar translational mobility. The same water–sugar solutions were evaluated by the time-intensity (TI) method with a sensory panel composed of 13 persons. For all investigated sugar solutions the I_{max} parameter, corresponding to the maximum sugar intensity perceived, has the same trend as the translational mobility of the water molecules with fructose > sucrose > glucose.

All these works strongly suggested that viscosity was not the only parameter to explain diffusion process and that water availability seemed to be a key factor in flavour perception in such systems.

2.2 NMR diffusion of small solutes in polyoside systems

Polyosides, such as galactomannans, carrageenans, pectin, dextran or agarose are widely used as textural agents in the food industry due to their gelling or thickening properties.[46–49] However, aroma release can be modified in preparations containing such polysaccharides depending on polymer nature and concentration.[50,51] The presence of macromolecules limits the exchange between the various phases: liquid or solid and vapour. In a gelled system, this limitation

was explained by the formation of a three-dimensional network which generated the reduction of the diffusivity of the volatile compounds, slowing down their migration to the matrix–air interface.[52] Not so many values on aroma compound diffusivity in such systems are available in the literature. In gel systems, the diffusivity can be calculated using the method of the concentration profile[53] and was experimented to understand the effect on texturant of aroma diffusivity in sodium caseinate gels[54] or in pectin gels.[52] However this method is time consuming. In the case of specific molecules, rotational diffusivity can be measured by electron spin resonance and translational diffusivity by fluorescence recovery after photobleaching.[55] PFG-NMR method had also been applied to investigate self-diffusion of small solutes in polysaccharide solutions or gels. From all these works, different parameters have been pointed out to explain the observed diffusion process.

2.2.1 Viscosity effect

In their study, Lundberg and Kuchel showed that translational mobility of glycine, alanine, lactate and glucose decreased by about 25–30% in 2.4% w/v agarose solution compared to that in pure solvent.[38] Kwak and Lafleur found an expected reduced diffusion of small solutes and large micellar systems in 20% (w/w) dextran solutions compared to that in D_2O with a more pronounced effect for larger molecules than the smaller ones.[39] In another study, Kwak and Lafleur observed a systematic decrease in self-diffusion coefficient of polyethylene glycol (PEG 1000 and 3500) whatever the investigated temperature as the curdlan concentration increased from 0 to 10% w/w.[56] Rondeau-Mouro et al. showed that translational mobility of 4-ethyl guaicol at 25°C, is decreased by 1.7 order of magnitude in 1% w/w ι-carrageenan solution ('viscous' solution) compared to D_2O solutions.[57] All these works strongly suggest that, whatever the solute and hydrocolloid concentration and nature, no specific interaction occurs and that diffusion process is mainly governed by the medium viscosity.

Others works have also investigated the impact of sugar molecules on solute mobility by measuring self-diffusion coefficients at LF- and HR-NMR. Using DOSY NMR method, Savary et al. investigated the self-diffusion of ethyl butyrate in model fruit preparations – frequently used in dairy product to flavour plain yogurt – composed of 35% w/w sucrose, 1.4% w/w starch and 0.8% w/w λ-carrageenan.[35] As the self-diffusion of ethyl butyrate dramatically decreased (by 84%) in this gelled system compared to aqueous solution, the impact of sucrose and starch–carrageenan content on aroma self-diffusion was separately studied. Authors showed that the presence of sucrose molecules affected the aroma diffusion more strongly than the presence of λ-carrageenan. Brosio et al. showed that in pectin–sucrose systems at 5% pectin, a substantial reduction of water mobility was observed with increasing sugar concentration from 0 to 40% w/w although no restricted water diffusion was evidenced.[58] In this system, the formation of the gel network is dependent on the sucrose concentration. Götz et al. observed the same expected effect by added sucrose in λ-, ι- and κ-carrageenan gels and showed that solute self-diffusion was smaller in sugar–carrageenan preparations than in pure solutions with or without salts.[59] From

these results, the observed diffusion decrease seems to be more affected by the increase of viscosity due to sucrose than the formation of the gel network.

2.2.2 Gel micro-structure

Aroma release and perception studies are often correlated to rheological parameters of the diffusing food systems, particularly in systems containing polysaccharide. Depending on experimental conditions (temperature, polymer concentration and nature, ionic strength), polysaccharides can adopt different structural organization leading to rheological changes and to different textural properties.[60] Three kinds of systems can be generated from a rheological point of view: macromolecular solutions (sol state) for which the solvated chains move freely and are highly entangled, and gel state with a denser structure for which 'weak' and 'strong' structure is distinguished. Strong gels are generally assumed to retain solute molecules more than soft gels or viscous solutions.

PFG-NMR spectroscopy has been widely used to investigate at a micro-scale the structural organization of polysaccharide solutions by measuring water or small solute diffusion. However, some NMR investigations on water mobility in such systems are not in agreement with the rheological measurements. Brosio et al. showed that, in guar galactomannan solutions (from 2.5 to 5.0% w/w), water self-diffusion values were independent of polymer concentration despite a strong thickening of the solution.[58] Götz et al. used PFG-STE-NMR experiments to characterize gelling behaviour of λ-, ι-, κ-carrageenan.[59] Water diffusion coefficients in κ-carrageenan (gelling agent) and λ-carrageenan (viscosity-increasing) at 2% concentration were measured between 5 and 50°C. No characteristic of gel-like behaviour could be discerned for κ-carrageenan and λ-carrageenan/water systems for all investigated temperatures in contrast to rheological observations. Authors concluded that NMR gave information on gel micro-structure and that classification of gel structure depended on the technique used. Rheological measurements give information on the global organization of gels while NMR spectroscopy gives information at a micrometer scale.

The relation between viscosity/textural parameters and solute diffusion measured by NMR spectroscopy depends on the composition of the investigated system. Moreover, it is worth noticing that, depending on the experimental diffusion time scale, more detailed information on the size and shape of the gel microstructure can be obtained. For example, Farhat et al. reported restricted diffusional phenomenon of water in starch gels with increasing experimental diffusion time.[42] Indeed, D/D_0 of water decreased with increasing Δ showing that physical obstructions and/or specific interactions act on water mobility in such systems. The authors estimated the 'pore' size at 36 μm. On the contrary, Rondeau-Mouro et al. did not observe restricted diffusion of aroma compounds in their carrageenan systems.[57]

2.2.3 Impact of cations

Polysaccharides are well-known to be sensitive to cations such as K^+, Na^+ or Ca^{2+}.[61–63] For example, low-methoxy pectin forms gels in the presence of

divalent cations such as Ca^{2+} ions. The gelation of ι-carrageenan takes place through a conformational transition from a disordered state (coil) to an ordered conformation (helix) and this transition is controlled by the ionic content of the medium. The impact on gel formation occurring upon salt addition on the flavour release has been the subject of some investigations using different techniques.[64–66] The NMR diffusion measurements of small solutes in these systems at different salt contents provide information on the structural organization of polysaccharide chains at a micro-scale.

Using PGSE-LED sequences at high field, Gostan et al. investigated self-diffusion of ethyl butyrate in 1% w/w ι-carrageenan in the presence of different contents of sodium salt at 30°C.[31] As unexpected, the diffusion of ethyl butyrate increased with the ionic strength from 0.1% NaCl to 0.5% NaCl despite the gel strength increase. A similar trend was observed for the self-diffusion of 4-ethyl guaicol in purified 2% w/w ι-carrageenan at 25°C.[57] When investigating ethyl butyrate self-diffusion in D_2O, no impact on aroma self-diffusion coefficient was found with increasing salt content showing that sodium salt has an indirect impact on aroma mobility (Figure 2). Similar observations on salt impact have been done in other systems. The presence of KCl in dextran gels strongly influences the bulk water diffusion.[67] In the presence of $CaCl_2$ or KCl, water self-diffusion in ι-carrageenan decreases compared to the pure hydrocolloid while for κ- and λ-carrageenan an increase of self-diffusion coefficients can be observed.[59]

All these NMR investigations showed that cations act on polysaccharide chain organization leading to a change in diffusion medium. Two main environments can be defined in these systems to explain the observed diffusion phenomena. (i) A macro- environment formed by highly entangled polymer chains (sol state) in which small solutes diffuse freely but slower than in pure water due to viscosity or obstruction effect. In the presence of cations, at a specific ions/

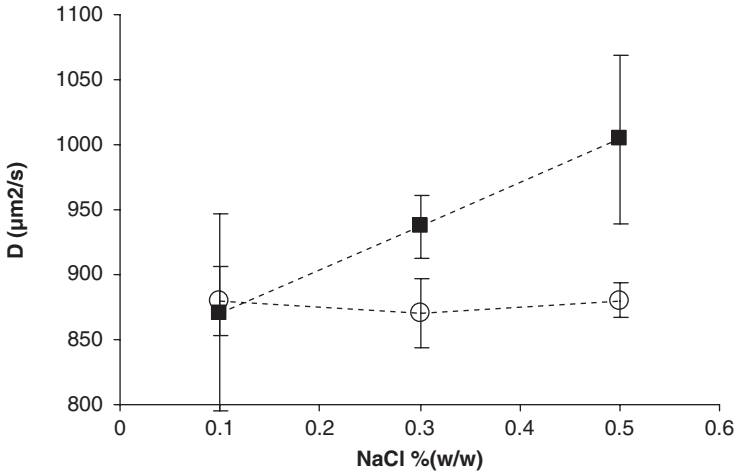

Figure 2 Self-diffusion coefficients of 50 µm ethyl butyrate in D_2O in function of NaCl content (% w/v) in absence (circles) or presence (squares) of *i*-carrageenan at 30°C.

polymer ratio, a gel network is induced by ion cross-linkage with polysaccharide chains. (ii) A micro-environment is thus formed by a more ordered gel network forming very large 'pores' composed of water in which solutes move freely. In this case, an enhancement of diffusion process, sometimes in restricted spaces, can be observed. However, NMR diffusion experiments do not give detailed information on molecular interactions, such as hydrogen bonding or proton exchange. Indeed, when a decrease of diffusion is observed, no direct evidence on potential binding sites is done and further experiments are required.

3. AROMA–MACROMOLECULE INTERACTIONS USING NMR SPECTROSCOPY

High-resolution NMR spectroscopy has been widely used for the investigation of macromolecule–ligand interaction, especially in pharmaceutical or chemical research. There are many strategies to determine binding site localization and/or binding affinity using conventional homo- and hetero-nuclear 1D- or 2D-NMR spectroscopy.[17–21,68] The most common and the most used methods are based on the observation of changes in NMR parameters between spectra of the free macromolecule (or ligand) and the ligand–macromolecule complex in solution. Chemical shifts, relaxation rates and diffusion coefficients are sensitive to binding events. From titration experiments for which the protein concentration is often kept constant while ligand concentration increases, it is possible to extract dissociation constants.[17,68] As diffusion coefficient is related to molecule sizes, dynamic exchange between ligands and macromolecules can also be assessed using PFG-NMR methods.[69] Associated to conventional 2D-NMR experiments such as COSY, TOCSY or HMQC sequences, the binding site localization and affinity of a ligand for a macromolecule can be determined. In this case, the assignment of the macromolecule and ligand resonances is needed. Moreover, the bound ligand conformation can be deduced from the measurement of intermolecular Nuclear OverHauser effect (NOE) through 1D or 2D-experiments.[70,71] Diffusion- and relaxation-edited methods are also considered as powerful tools to perform rapid screening and identification of compounds.[72–75] More particularly, the NOE pumping method introduced by Chen and Chapiro is a diffusion-edited experiment which filtered out signals from non-binding ligands based on their diffusion behaviour.[72]

Since food macromolecules could influence flavour release by interacting or entrapping aroma compounds, the knowledge of interaction mechanisms between aroma compounds and these macromolecules is essential to optimize formulation in food processing.[16] Several NMR works reported the study of the binding/entrapment of aroma compounds to model food systems.

3.1 Aroma–protein/polyphenol interactions

The different abilities of individual aroma molecules to interact with macromolecules, particularly with food proteins, can have significant effects on

the overall aroma perception. It is thus of importance to understand how physico-chemical properties of aroma compounds and food molecules can influence binding mechanisms. The bovine serum albumin (BSA) and the milk β-lactoglobulin (β-LG) proteins are both widely present in foods and are known to have binding affinities with aroma compounds.[76–78] Wine polyphenols are also well-known to influence organoleptic properties of wines either by a direct impact on taste perception[79] or by an indirect effect on aroma perception due to molecular interactions.[80] These two types of macromolecules have been used as simple model food to investigate the binding mechanism of different aroma compounds by NMR spectroscopy.

The binding affinity of different aroma compounds in the presence of wine polyphenols has been probed using titration methods based on chemical shift changes from ^{1}H 1D and 2D NMR spectra. From the magnitude of the up-field shift, $\Delta\delta$, the dissociation constant, K_a, was determined for each complex assuming a 1:1 binding model. Dufour and Bayonove showed that the binding affinity of benzaldehyde to catechin and epicatechin is stronger than 3,5-dimethoxyphenol.[81] Jung et al. showed that 2-methylpyrazine and vanillin interact more strongly with gallic acid and naringin than ethyl hexanoate.[82] These two studies showed that hydrophobic interactions are predominant in these complexes and that complexation is dependent on the nature of small and large molecules. Moreover, with 1D and 2D NOE experiments, Jung et al. proposed a potential structural model for gallic acid and vanillin.[82] However, two experimental limitations have been noticed in these studies: (i) titration experiments are limited by the low solubility of some aroma compounds in water or D_2O and (ii) the use of an organic solvent (DMSO-d_6) to slow down the exchange rate between free and complexed solutes in order to observe NOE peaks.

The localization of binding sites on β-LG for different aroma compounds was investigated using ^{1}H TOCSY and NOESY NMR spectroscopy.[83,84] Chemical shift changes of protein amino acids underlined specific binding regions of the β-LG secondary structure: a groove near the outer surface of protein and the central cavity of the protein. As aroma compounds belong to different chemical classes, this NMR method could help to correlate molecular structure of a large number of these molecules with their binding behaviour with food proteins.

Jung et al. investigated the binding affinity of aroma compounds for BSA and β-LG proteins using NMR methods based on molecule diffusion properties.[73,85] They showed that binding constants and stoichiometry can be extracted from self-diffusion coefficient measurements by PFG-NMR. With titration experiments, the decrease of self-diffusion of four alkenones by increasing the BSA/ligand ratio was observed. The calculated dissociation constant, K_a, increased with the chain length for the 2-alkenones and the binding affinity decreased with the carbonyl group at the 5-position. Predominant hydrophobic interactions and steric hindrances are thus pointed out with these experiments. However, the authors underlined that PFG NMR experiments provide average diffusion coefficients and that protein–protein and/or ligand–ligand interactions as well as

viscosity or temperature changes must be taken into account. The NOE-pumping method was performed on a mixture of four aroma compounds in the presence of the protein.[73] They showed that benzaldehyde and vanillin were selectively bound to BSA, while 2-phenylethanol was a non-binding or weakly binding ligand. The similar experiment was successfully realized with a mixture of three aroma compounds in the presence of cacao bean tannin extract showing a strong binding of ethylbenzoate. Jung and Ebeler used the same method to investigate the binding affinity of α- and β-ionones to β-LG.[85] They confirmed a higher affinity for β-ionone than for α-ionone as already published by Sostman and Guichard.[86] They also investigated the interactions of α- and β-ionones with the β-LG at various ligand/protein molar ratios and different pH. In parallel, the following of the protein conformation changes at different pH was checked using PFG-NMR. They found results similar to Jouenne and Crouzet,[87] i.e., that retention of methyl ketones and methyl esters was the greatest at pH 6 and lowest at pH 11. In these works, the authors underlined the fact that, although NOE-pumping method is a rapid method for screening a mixture of compounds, no detailed information on binding localization is provided.

3.2 Aroma–macromolecule entrapment

A large number of food processes takes advantage of the microencapsulation of aroma compounds by cyclodextrins (CDs), cyclic oligosaccharides composed of 6–8 (1→4)-D-glucosyl residues forming a hydrophobic cavity and a hydrophilic outer wall. To understand the difference of retention of two aroma compounds, benzyl alcohol and 2-methylbutyric acid, by β-cyclodextrins, ^{1}H- and ^{13}C-NMR experiments were performed on free aroma compounds and the corresponding complex in deuterated dimethyl sulfoxide (DMSO) solution.[88] Based on ^{13}C and ^{1}H chemical shift changes of aroma compounds, authors showed that benzyl alcohol seems to include its alcohol function into the β-CD cavity while the carboxylic function of the acid is located near the extremity of the β-CD cavity. The formation of α-CD inclusion complex with aliphatic esters in DMSO was also investigated by 1D ^{1}H NOE experiments and/or by ^{1}H T_1 relaxation measurements.[89,90] Both methods showed that the two groups around the ester bond of ethyl hexanoate were at the narrower side of the CD cavity, while the other protons were within the cavity with a folded structure.

Amylose, a linear fraction of starch, can form complexes with aroma compounds during food processing leading to a decrease of aroma release. According to the nature of the small solute, amylose complex adopts a specific crystalline structure permitting the inclusion of the solute inside or between the amylose helices (inter- or intra-helical associations). The structure of amylose complexes formed with aroma compounds was investigated by solid-state NMR spectroscopy and wide range X-ray diffraction.[91,92] The authors showed that ^{13}C CP-MAS NMR spectra provide important structural features on crystalline type and helical conformation of starch. From ^{13}C chemical shift changes of amylose or aroma compound peaks, inclusion complexes of menthone, butanol, naphtol and linalool between amylose helices were proposed.

4. CONCLUSION

Owing to the large range of methods, NMR spectroscopy is thus a useful and rapid tool to investigate diffusion and interaction mechanisms of aroma compounds in model and complex food systems in a non-invasive way. PFG-NMR methods provide microscopic insights into aroma diffusion process and gel microstructure. Moreover, several NMR methods can give detailed information on binding or entrapment process at a molecular scale. NMR spectroscopy appears to be a very promising technique in the understanding of aroma release mechanism of food products. By combining NMR data to sensorial analysis, the main physicochemical parameters governing aroma release could be determined for a better control of flavour perception.

REFERENCES

1. E. Guichard, S. Issanchou, A. Descourvières and P. Etiévant, *J. Food Sci.*, 1991, **56**, 1621.
2. T. H. Varzakas, G. C. Leach, C. J. Israilides and D. Arapoglou, *Enzyme Microb. Technol.*, 2005, **37**, 29.
3. E. Alberti, P. S. Belton and A. M. Gil, *Annu. Rep. NMR Spectrosc.*, 2002, **47**, 109.
4. L. M. Reid, C. P. O'Donnell and G. Downey, *Trends Food Sci. Technol.*, 2006, **17**, 344.
5. A. M. Gil, I. F. Duarte, M. Godejohann, U. Braumann, M. Maraschin and M. Spraul, *Analytica Chim. Acta*, 2003, **488**, 35.
6. D. W. Lachenmeier, W. Frank, E. Humpfer, H. Schafer, S. Keller, M. Mortter and M. Spraul, *Eur. Food Res. Technol.*, 2005, **220**, 215.
7. N. Ogrinc, I. J. IKošir, J. E. Spangenberg and J. Kidric, *Anal. Bioanal. Chem.*, 2003, **376**, 424.
8. G. Martin, G. Remaud and G. J. Martin, *Flavour Fragrance J.*, 2006, **8**, 97.
9. I. Duarte, A. Barros, P. S. Belton, R. Righelato, M. Spraul, E. Humpfer and A. M. Gil, *J. Agric. Food Chem.*, 2002, **50**, 2475.
10. L. Shintu and S. Caldarelli, *J. Agric. Food Chem.*, 2005, **53**, 4026.
11. A. P. Sobolev, A. Segre and R. Lamanna, *Magn. Reson. Chem.*, 2003, **41**, 237.
12. I. F. Duarte, B. J. Goodfellow and A. M. Gil, *Spectrosc. Lett.*, 2005, **38**, 319.
13. A. M. Gil, I. Duarte, E. Cabrita, B. J. Goodfellow, M. Spraul and R. Kerssebaum, *Anal. Chem. Acta*, 2004, **506**, 215.
14. M. Nilsson, I. F. Duarte, C. Almeida, I. Delgadillo, B. J. Goodfellow, A. M. Gil and G. A. Morris, *J. Agric. Food Chem.*, 2004, **52**, 3736.
15. A. Raffo, R. Gianferri, R. Barbieri and E. Brosio, *Food Chem.*, 2005, **89**, 149.
16. E. Guichard, *Food Rev. Int.*, 2002, **18**, 49.
17. L. Fielding, *Curr. Topics Med. Chem.*, 2003, **3**, 39.
18. L. Fielding, *Prog. Nucl. Magn. Reson. Spectrosc.* 2007, **51**, 219.
19. C. Moreau and E. Guichard, *Modern Magnetic Resonance*, Springer, Netherland, 2006, p. 1589.
20. M. Pellecchia, *Chem. Biol.*, 2005, **12**, 961.
21. E. R. Zartler, J. Yan, H. Mo, A. D. Kline and M. J. Shapiro, *Curr. Topics Med. Chem.*, 2003, **3**, 25.
22. J. Keeler, *Understanding NMR Spectroscopy*, Wiley, England, 2005, p. 245.
23. D. D. Traficante, *Encyclopedia of Nuclear Magnetic Resonance*, Wiley, New York, NY, 1996, p. 3988.
24. P. S. Belton, *Int. J. Biol. Macromol.*, 1997, **21**, 81.
25. B. P. Hills, *Mol. Phys.*, 1992, **76**, 509.
26. B. Antalek, *Concepts Magn. Reson.*, 2002, **14**, 225.
27. J. C. S. Johnson, *Prog. Nucl. Magn. Reson. Spectrosc.*, 1999, **34**, 203.
28. W. S. Price, *Concepts Magn. Reson.*, 1997, **9**, 299.
29. F. Stallmach and P. Galvosas, *Ann. Rep. NMR Spectrosc.*, 2007, **61**, 51.
30. J. C. Cobas, P. Groves, M. Martin-Pastor and A. De Capua, *Curr. Anal. Chem.*, 2005, **1**, 1.

31. T. Gostan, C. Moreau, A. Juteau, E. Guichard and M. A. Delsuc, *Magn. Reson. Chem.*, 2004, **42**, 496.
32. K. F. Morris and C. S. Johnson, *J. Am. Chem. Soc.*, 1992, **114**, 3139.
33. W. J. Albery, J. F. Burke, E. B. Leffler and J. Hadgraft, *J. Chem. Soc., Faraday Trans. 1*, 1976, **72**, 1618.
34. S. Rogacheva, M. A. Espinosa-Diaz and A. Voilley, *J. Agric. Food Chem.*, 1999, **47**, 259.
35. G. Savary, E. Guichard, J. L. Doublier, N. Cayot and C. Moreau, *J. Agric. Food Chem.*, 2006, **54**, 665.
36. G. Savary, E. Guichard, J. L. Doublier and N. Cayot, *Food Res. Int.*, 2006, **39**, 372.
37. A. Chana, A. Tromelin, I. Andriot and E. Guichard, *J. Agric. Food Chem.*, 2006, **54**, 3679.
38. P. Lundberg and P. W. Kuchel, *Magn. Reson. Med.*, 1997, **37**, 44.
39. S. Kwak and M. Lafleur, *Macromolecules*, 2003, **36**, 3189.
40. A. Hansson, J. Andersson and A. Leufven, *Food Chem.*, 2001, **72**, 363.
41. S. Rabe, U. Krings and R. G. Berger, *J. Agric. Food Chem.*, 2003, **51**, 5058.
42. I. A. Farhat, E. Loisel, P. Saez, W. Derbyshire and J. M. V. Blanshard, *Int. J. Food Sci. Technol.*, 1997, **32**, 377.
43. G. W. Padua and S. J. Schmidt, *J. Agric. Food Chem.*, 1992, **40**, 1524.
44. S. J. Richardson, I. C. Baianu and M. P. Steinberg, *J. Food Sci.*, 1987, **52**, 806.
45. T. Mahawanich and S. J. Schmidt, *Food Chem.*, 2004, **84**, 169.
46. H. Neukom, *Lebensmittel Wissenschaft und Technologie*, 1989, **22**, 41.
47. L. Piculell, *Food Polysaccharides and their Applications*, Marcel Dekker, New York, NY, 1995, p. 205.
48. D. A. Rees, *Adv. Carbohydr. Chem.*, 1969, **24**, 267.
49. D. A. Rees, *Chem. Industry*, 1972, **19**, 630.
50. S. Lubbers and E. Guichard, *Food Chem.*, 2003, **81**, 269.
51. D. D. Roberts, J. S. Elmore, K. R. Langley and J. Bakker, *J. Agric. Food Chem.*, 1996, **44**, 1321.
52. B. Rega, E. Guichard and A. Voilley, *Sci. Aliments*, 2002, **22**, 235.
53. A. Voilley and M. L. Bettenfeld, *J. Food Eng.*, 1985, **4**, 313.
54. P. Landy, K. Farès, D. Lorient and A. Voilley, *J. Agric. Food Chem.*, 1997, **45**, 2649.
55. E. Contreras-Lopez, D. Champion, H. Hervet, G. Blond and M. Le Meste, *J. Agric. Food Chem.*, 2000, **48**, 1009.
56. S. Kwak and M. Lafleur, *Colloids Surf. A: Physicochem. Eng. Aspects*, 2003, **221**, 231.
57. C. Rondeau-Mouro, A. Zykwinska, S. Durand, J. L. Doublier and A. Buléon, *Carbohydr. Polym.*, 2004, **57**, 459.
58. E. Brosio, A. D'Ubaldo and B. Verzegnassi, *Cellular Mol. Biol.*, 1994, **40**, 569.
59. J. Götz, K. Zick, R. Hinrichs and H. Weisser, *Eur. Food Res. Technol.*, 2004, **218**, 323.
60. E. R. Morris, *Food Polysaccharides and their Applications*, Marcel Dekker, New York, NY, 1995, p.517.
61. E. E. Braudo, I. G. Plashchina, M. G. Semenova and V. Yuryev, *Food Hydrocolloids*, 1998, **12**, 253.
62. L. Piculell, J. Borgström, I. S. Chronakis, P.-O. Quist and C. Viebke, *Int. J. Biol. Macromolecules*, 1997, **21**, 141.
63. L. Piculell, S. Nilsson and P. Ström, *Carbohydrate Res.*, 1989, **188**, 121.
64. A. Juteau, N. Cayot, C. Chabanet, J. L. Doublier and E. Guichard, *Trends Food Sci. Technol.*, 2004, **15**, 394.
65. A. Juteau, J. L. Doublier and E. Guichard, *J. Agric. Food Chem.*, 2004, **52**, 1621.
66. A. Juteau, C. Tournier and E. Guichard, *Flavour Fragrance J.*, 2004, **19**, 483.
67. T. Watanabe, A. Ohtsuka, N. Murase, P. Barth and K. Gersonde, *Magn. Reson. Med.*, 1996, **35**, 697.
68. O. Monasterio, *Methods*, 2001, **24**, 97.
69. L. H. Lucas and C. K. Larive, *Concepts Magn. Reson., Part A*, 2004, **20**, 24.
70. H. Mo and T. C. Pochapsky, *Prog. NMR Spectrosc.*, 1997, **30**, 1.
71. S. Ravindranathan, J.-M. Mallet, P. Sinay and G. Bodenhausen, *J. Magn. Reson.*, 2003, **163**, 199.
72. A. Chen and M. J. Shapiro, *J. Am. Chem. Soc.*, 1998, **120**, 10258.
73. D.-M. Jung, J. S. de Ropp and S. E. Ebeler, *J. Agric. Food Chem.*, 2002, **50**, 4262.
74. H. Ponstingl and G. Otting, *J. Biomol. NMR*, 1997, **9**, 441.
75. P. Stilbs, *Prog. NMR Spectrosc.*, 1987, **19**, 1.
76. N. Fischer and S. Widder, *Food Technol.*, 1997, **51**, 68.
77. S. Lubbers, P. Landy and A. Voilley, *Food Technol.*, 1998, **52**, 68.
78. A. Tromelin, I. Andriot and E. Guichard, *Flavour in Food*, Woodhead Publishing Limited, Cambridge, 2006, p. 172.

79. S. Vidal, L. Francis, A. Noble, M. Kwiatkowski, V. Cheynier and E. Waters, *Analytica Chim. Acta*, 2004, **513**, 57.
80. C. Dufour and I. Sauvaire, *J. Agric. Food Chem.*, 2000, **48**, 1784.
81. C. Dufour and C. L. Bayonove, *J. Agric. Food Chem.*, 1999, **47**, 678.
82. D. M. Jung, J. S. deRopp and S. E. Ebeler, *J. Agric. Food Chem.*, 2000, **48**, 407.
83. M. Lübke, E. Guichard, A. Tromelin and J. L. Le Quéré, *J. Agric. Food Chem.*, 2002, **50**, 7094.
84. C. Moreau, L. Tavel, J. L. Le Quéré and E. Guichard, *Flavour Science: Recent Advances and Trends*, Elsevier, Oxford, 2006, pp. 425–428.
85. D.-M. Jung and S. E. Ebeler, *J. Agric. Food Chem.*, 2003, **51**, 1988.
86. K. Sostmann and E. Guichard, *Food Chem.*, 1998, **62**, 509.
87. E. Jouenne and J. Crouzet, *J. Agric. Food Chem.*, 2000, **48**, 1273.
88. I. Goubet, C. Dahout, E. Sémon, E. Guichard, J. L. Le Quéré and A. Voilley, *J. Agric. Food Chem.*, 2001, **49**, 5916.
89. T. Matsui, H. Iwasaki, K. Matsumoto and Y. Osajima, *Biosci. Biotechnol. Biochem.*, 1994, **58**, 1102.
90. K. Tobitsuka, M. Miura and S. Kobayashi, *J. Agric. Food Chem.*, 2005, **53**, 5402.
91. P. Le Bail, C. Rondeau and A. Buléon, *Int. J. Biol. Macromol.*, 2005, **35**, 1.
92. C. Rondeau-Mouro, P. Le Bail and A. Buléon, *Int. J. Biol. Macromol.*, 2004, **34**, 309.

CHAPTER 7

Polymer Blend Miscibility

Jeffery L. White and **Marcin Wachowicz**

Contents

Abstract

The annual worldwide economic impact of polymers exceeds 150 billion USD, and polymer blends represent a significant fraction of that total. Mixing in systems containing dissimilar macromolecules can exhibit deviations from ideal solution behaviour. The final physical properties of materials made from multicomponent polymers are critically determined by such deviations. NMR is an ideal experimental tool to understand the origins of why certain macromolecules mix or phase separate, as well as define the final state of mixing in solid materials whose end-use physical properties are of most practical interest. The dynamic interplay between conformational energies within one polymer chain and molecular interactions between neighboring polymer chains in blends is experimentally accessible using modern magnetic resonance techniques. In this review, very recent examples of relaxation, site-specific vs. bulk dynamic, correlation and spatial NMR methods applied to polymer blends in the solid state are discussed. However, rather than organize the polymer blends simply by the various

Department of Chemistry, Oklahoma State University, Stillwater, Oklahoma 74078

Annual Reports on NMR Spectroscopy, Volume 64
ISSN 0066-4103, DOI 10.1016/S0066-4103(08)00007-0

types of modern solid-state NMR experiment used in their study, particular attention is given to the identification and organization of blends according to their specific chemical structures, pertinent interactions and governing enthalpic or entropic contributions to miscibility.

Keywords: polymer; polymer blends; composites; miscibility macromolecules; biopolymers; nuclear magnetic resonance; solid-state nuclear magnetic resonance; macromolecular thermodynamics; enthalpy; entropy

1. INTRODUCTION

Defining structure and dynamics in complex systems of macromolecules is a common goal for modern research in materials science. Many questions arise naturally from the simple prospect of mixing two dissimilar polymers together. How do macromolecules of varying polarity and functional group density organize themselves at the local chain level? How does this organization change with the creation of a mixed system? Does miscibility, a thermodynamic parameter, imply a certain maximum length scale of homogeneous mixing? How does one best interrogate this characteristic length scale? The fundamental spin interactions in solid-state NMR allow detailed interrogation of length scales ranging from 0.5 to 30 nm; this dimensional range completely encompasses typical chain dimensions of macromolecules, e.g., radii of gyration. Additional key elements of the three-dimensional organization of polymer chains, such as crystallite thickness and differential dynamic structure, must be considered in blends containing crystalline or semicrystalline polymers. Modern solid-state NMR methods can provide quantitative information in each of these areas for amorphous/amorphous, amorphous/crystalline and crystalline/crystalline blend systems, most often without the need for any form of isotopic labelling or probe molecule perturbations to the bulk sample. The advantage solid-state NMR presents to problems in polymer blend science is the combined flexibility and specificity inherent to the multiple time-dependent spin interactions available to the skilled experimentalist, and the potential to interrogate structure and dynamics in the end-use state of the material.

During the last 10 years, several books and book chapters have reviewed modern solid-state NMR experiments for a variety of polymer blends.[1–6] In this contribution, we will survey only the most recent results, acknowledging a previous review contribution published in this journal in 2004.[7] Individual sections are organized by the polymer chemical structure characteristics believed to be most relevant to miscibility. There may be some overlap between polymer categories; common polymer types like polyesters and polyurethanes, for example, are included in the heteroatom sections. Polyphosphazenes are not included in this review, since few NMR-related investigations of their blends have been published recently. However, they do represent an interesting component of emerging biopolymer blends, and NMR promises to provide valuable insights into structure/function/biocompatibility/bioerodibility

characteristics in future work.[8] Much of the recent activity in the polymer blends area involves blends with biocompatible, biodegradable and bioerodable polymer components, as discussed in Section 6. Finally, semicrystalline polymers for purposes of this review do not constitute a polymer blend, even though they are clearly a polymer mixture from a solid-state NMR perspective.

2. RECENT DEVELOPMENTS IN SPIN-DIFFUSION AND POLYMER BLENDS

Spin-diffusion NMR techniques, typically involving abundant homonuclei like ^{1}H and ^{19}F, have historically played an important role in discerning differential morphology in polymer blends. Excellent reviews of this area have been published.[9,10] While the general use of spin-diffusion to probe length scales of mixing in polymer blends, or to determine crystallite dimensions in semicrystalline polymers, is well-established, recent improvements in spin-diffusion experiments that address some long-standing limitations warrant mention here. In general, spin-diffusion techniques require that specific polarization originating from only one component or phase of the sample be generated, or selected, as an initial condition, subsequent redistribution of that magnetization gradient throughout the entire sample during a controlled mixing time, and a final spectroscopic detection step in which the extent of polarization redistribution is quantified as a function of the mixing time. Based on analogies with physical or thermal diffusion models, rate equations describing the diffusion process, along with spin-diffusion coefficient values, may be used to determine mixing length scales (or domain sizes) associated with the diffusion process in a heterogeneous polymer system. Typical dimensions accessible by this static dipole-dipole method range from 1 to 200 nm.

Following publication of the aforementioned reviews, two limiting problems have been recently addressed which increase the applicability of this already successful experimental strategy to a wider range of materials. First, insufficient contrast (either spectroscopic chemical shift contrast or dynamic dipolar-based contrast) between different types of polymers often precludes generation of a polarization gradient and/or detection of its redistribution. In practice, ^{13}C detection of the spin-diffusion process is most attractive in polymeric systems, given the extremely small chemical shift range and large dipolar couplings between abundant ^{1}H spins. While blends containing both rigid and mobile regions can easily be interrogated using ^{13}C-detected Goldman–Shen[11] or dipolar filter methods,[12] blends of polymers with similar molecular dynamics and similar ^{1}H chemical shifts are difficult to interrogate. Building on a previous 2D ^{13}C exchange experiment employing ^{1}H spin-diffusion by Spiess and coworkers,[13] Schmidt-Rohr and coworkers recently described a triple cross-polarization experiment that correlates individual ^{13}C resonances with one another via ^{1}H spin-diffusion.[14] Figure 1 shows the resulting correlation spectra for a blend of polystyrene (PS) and poly(2,6-dimethylphenyleneoxide) (PXE), in which the quantitative extent of spin-diffusion is assessed via extraction of

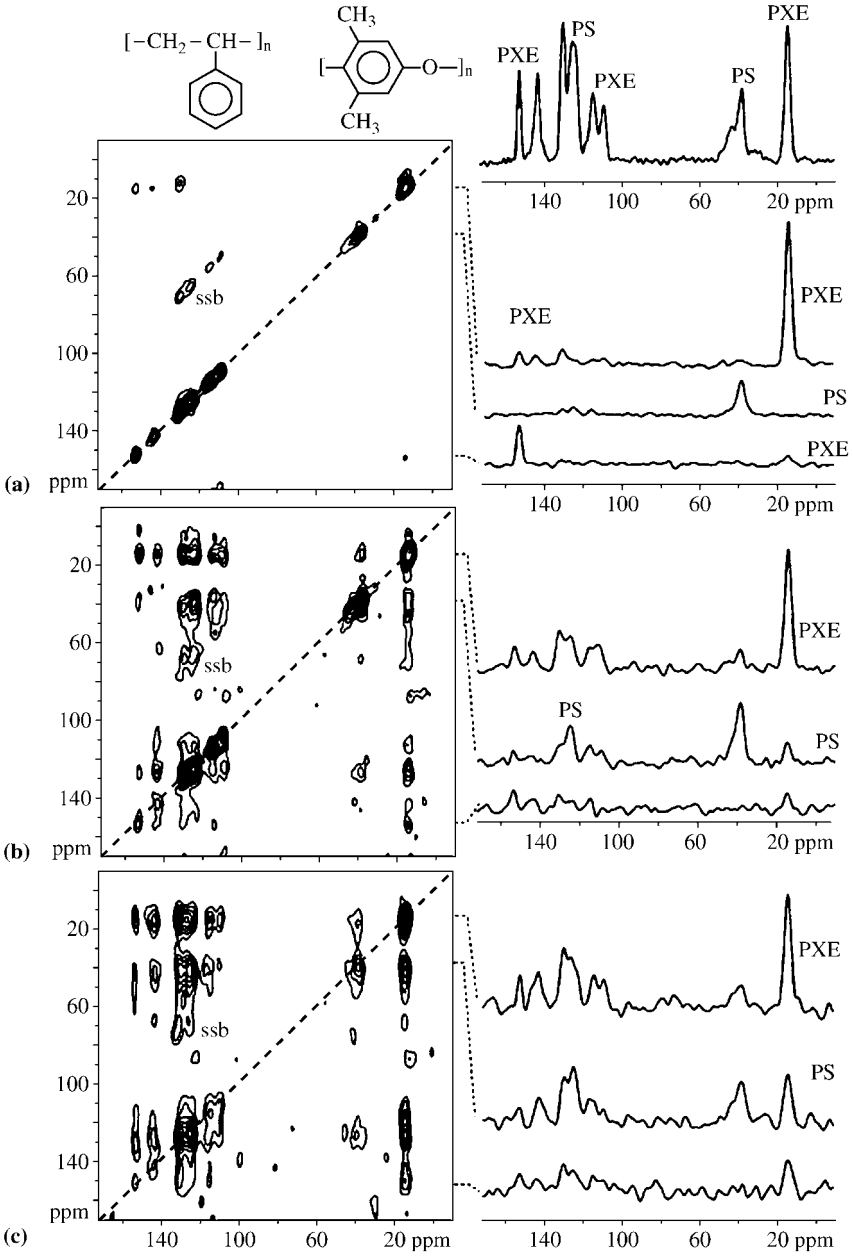

Figure 1 Series of 2D MAD $^{13}C(HH)^{13}C$ spectra and ^{13}C slices of PS/PXE blends as a function of spin-diffusion mixing time equal to (a) 0.01, (b) 0.5 and (c) 2 ms. (Adapted from ref. 14.)

specific rows or columns from the 2D contour plot. The method is attractive since no isotopic labelling is required, and the high-resolution characteristic of ^{13}C spectra is preserved in each dimension. Although sensitivity is improved relative to previous multiple cross-polarization experiments by a factor of 4, the overall efficiency is still quite low. In addition, the technique requires long values of $T_{1\rho H}$ (>5 ms), which potentially excludes many polymer systems of interest.

A second problem that has hindered the application of spin-diffusion methods to a broader range of polymeric materials, and their acceptance by the broader polymer science community, involves the variation in values of spin-diffusion coefficients (D) that have been reported in the literature, and the difficulty with experimentally determining D for any sample of interest. Until recently, the strategy for determination of spin-diffusion coefficients in amorphous polymers involved comparisons of static ^1H linewidths (for rigid polymers) or ^1H T_2 values (for low T_g polymers) to those obtained for well-characterized, model block copolymers.[15] The model block copolymers have either lamellar, cylindrical or spherical morphologies, as measured by SAXS or electron microscopy. By ratioing the measured values of linewidth or T_2 obtained for the sample of interest to similar parameters in the literature for these standards, appropriately scaled values of the spin-diffusion coefficient may be estimated for the sample. While this approach is viable, and provides accurate values for D in many cases, an alternative strategy in which direct measurement of spin-diffusion rates in the polymers of interest, and calculations of D based on that measurement, is attractive. Such an approach would be particularly important for polymer systems in which scattering and microscopy contrast is poor or non-existent, e.g., blends of amorphous polymers with similar chemical structures, for which well-characterized block copolymers of similar structure and molecular dynamics are not available.

White and coworkers have recently described an experimental approach in which intramonomer spin-diffusion is used to quantitatively define upper limits on the value of spin-diffusion coefficients D in mobile and rigid homopolymers, as well as in copolymers and blends.[16–18] The independent determination of the diffusion coefficient using only NMR data would be possible if a unique, invariant reference volume or distance existed in the polymer sample that could be used to quantitatively define the diffusive length scale. In other words, an internal distance calibration on the sample itself would eliminate the need for independent validation of the mixing length scale by scattering or microscopy experiments. White and coworkers reported that the dimensions of the cylinder circumscribing a monomer unit in a chain-extended polymer serves as this reference distance, thereby resulting in calculation of an accurate spin-diffusion coefficient in cases where a polarization gradient may be prepared within the monomer itself. While there are several strategies available for generating an initial ^1H polarization gradient within a monomer, particular attention is devoted to using 2D solid-state heteronuclear correlation (Hetcor) methods for measuring intramonomer spin-diffusion in rigid polymers. The main advantage of this experiment is that naturally occurring ^1H magnetization gradients are exploited. In other words, no special manipulation of the proton spin reservoir is required to generate an initial polarization gradient; all local ^1H magnetization is preserved prior to the

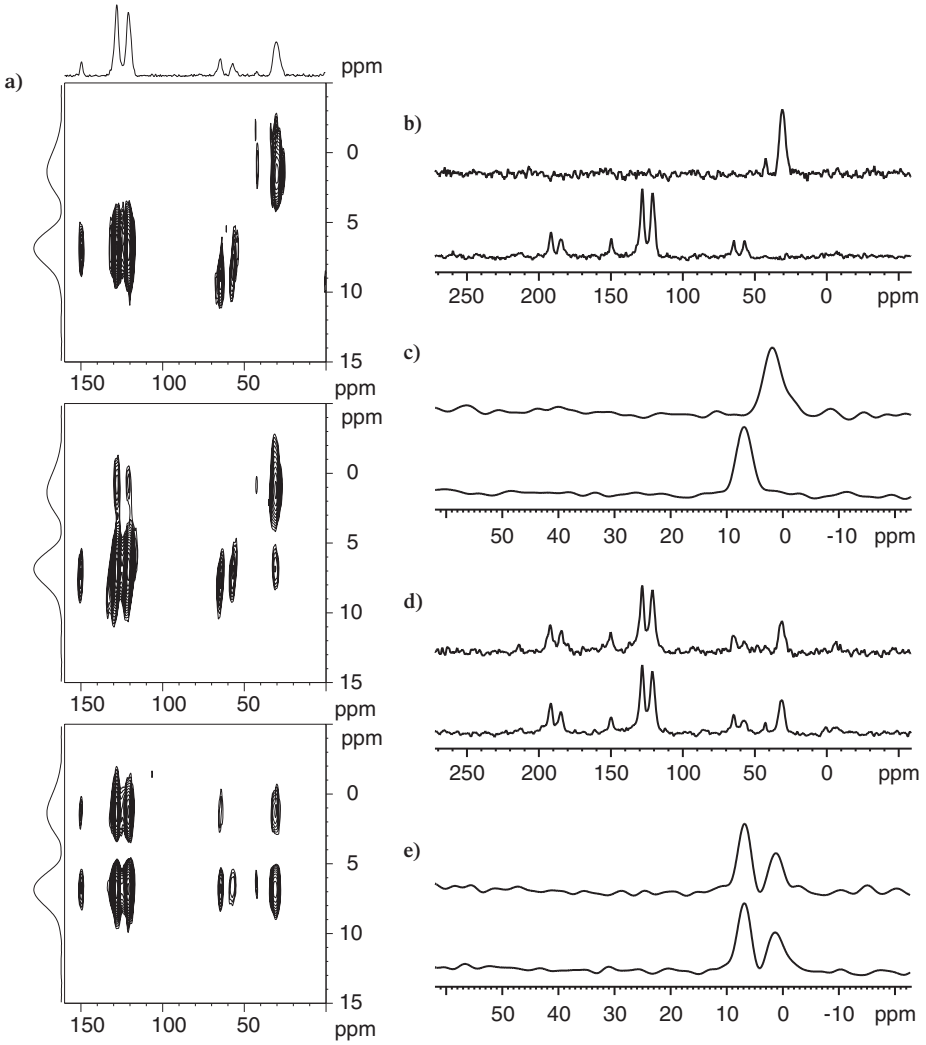

Figure 2 (a) Series of 2D ^{1}H–^{13}C spin-diffusion Hetcor data for polycarbonate at mixing times of (top) 0 ms, (middle) 0.1 ms and (bottom) 2.0 ms. Representative ^{1}H and ^{13}C slices extracted from the Hetcor spin-diffusion data in (a), comparing aliphatic vs aromatic peak positions, for mixing times equal (b, c) 0 ms and (d, e) 1 ms. Note the convergence to identical slice intensities at 1 ms mixing time. Quantitative analysis of this data to extract spin-diffusion coefficients is described in ref. 17. (Adapted from ref. 17.)

spin-diffusion period and therefore one can be confident that the sampled spin-response is representative of the bulk. The benefit of the Hetcor spin-diffusion experiment relative to direct ^{1}H-observe methods is much greater resolution in the ^{1}H dimension due to ^{13}C chemical separation, allowing different polarization-transfer processes (occurring over different length scales) to be detected simultaneously as might occur in blends or block polymers. Figures 2, 3 and 4 show

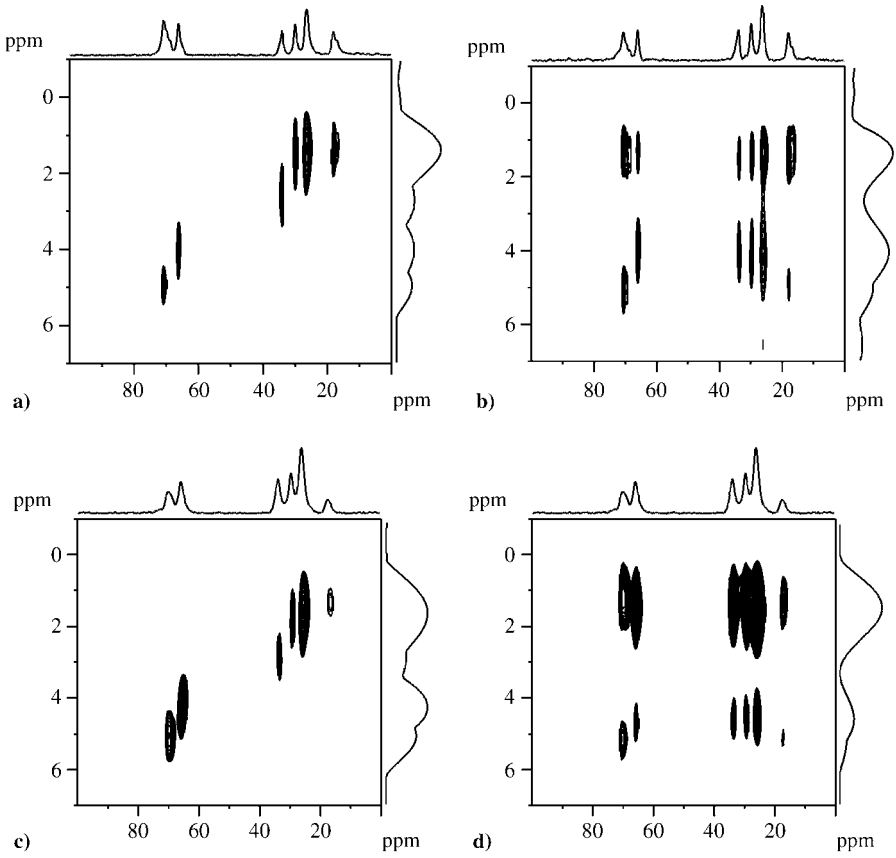

Figure 3 Representative two-dimensional ^{1}H–^{13}C solid-state Hetcor plots of the aliphatic ^{13}C region for: (a) FSLG/LGCP acquisition on the solvent-cast blend with no spin-diffusion time; (b) same as (a), after 1 ms spin-diffusion time; (c) MP/WIM acquisition on the coalesced blend with no spin-diffusion time; (d) same as (c), after 1 ms mixing time. ^{1}H slices were extracted at 19 and 65 ppm for the spin-diffusion analysis. Summed projections from each dimension are shown along the ^{13}C (horizontal) and ^{1}H (vertical) axes. (Adapted from ref. 18.)

example results for pure glassy homopolymers and a biopolymer blend, including slice analysis and curve fitting details.

The two preceding types of experiments directly measure spin-diffusion, i.e., employ a specific mixing time during which spin-diffusion occurs. Several groups have recently employed direct measurement of ^{1}H spin-diffusion to probe domain sizes in blends containing either polar or non-polar polymers, inclusion compounds and composites.[19–24] As shown above, ^{1}H spin-diffusion may be detected via ^{13}C observation; ^{19}F has also been used to follow ^{1}H spin-diffusion in fluoropolymers.[25] The use of homonuclear two-dimensional ^{1}H–^{1}H spin-diffusion correlation experiments has recently been reviewed by Brown;[26] such methods have not yet enjoyed widespread application to polymer blend systems

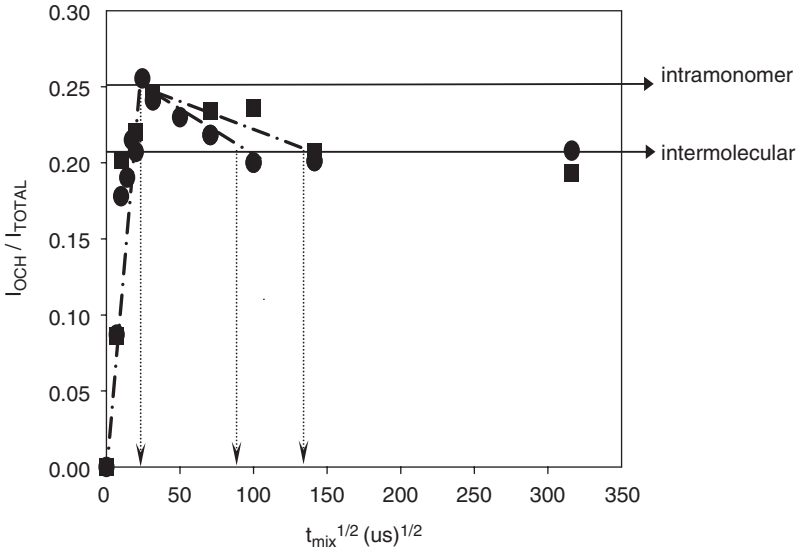

Figure 4 ^{1}H spin-diffusion curves extracted from slices at the PLLA CH_3 signal (19 ppm) for the solution-cast (■) and coalesced (●) PCL/PLLA blends. The horizontal arrows indicate the predicted equilibrium intensity ratios for intramonomer vs. intermolecular (interdomain) spin-diffusion based on the monomer structures. The dashed line in the short time regime is the regression through the first five points of the curve to the intramolecular equilibrium intensity ratio (0.25). From this latter analysis, the equilibration time for intramolecular spin-diffusion was 20 $\mu s^{1/2}$ (τ_{intra} vertical arrow). Additional vertical arrows indicate the equilibration times for intermolecular or interdomain spin-diffusion between PLLA and PCL in the coalesced ($\tau_{coal} = 88\ \mu s^{1/2}$) and solution-cast ($\tau_{sol} = 132\ \mu s^{1/2}$) blends, obtained by regression of the four experimental points between the intramolecular and intermolecular plateaus. (Adapted from ref. 18.)

due to resolution limitations, even in the limit of fast MAS. In general, most researchers still use traditional ^{1}H $T_{1\rho}$ and T_1 measurements to indirectly access the limits of spin-diffusion in an approximate fashion, recent examples of which are mentioned in the following sections for several polymer blend types.

3. BLENDS OF POLYMERS THAT CONTAIN HETEROATOMS

3.1 Weak hydrogen bonding vs. classical hydrogen bonds in polymer blends

Polymer structure can be influenced by through space chemical forces that result in both intrachain (self-association) and interchain associations. Excluding ionic polymers, this most commonly occurs via well-known classical hydrogen bonding interactions, in which the permanent dipole moment from a hydrogen atom covalently bonded to a more electronegative heteroatom (e.g., O, F, Cl, etc.)

interacts with another proximate heteroatom, or in special cases, pi electron density arising from sp or sp^2 carbons. In polymer blends, the most common example is hydrogen bonding between OH or NH group hydrogen atoms and C═O group oxygen atoms. Since these cases are well known both in small molecule chemistry and macromolecular mixing, we shall just cite recent examples in the following relevant sections. However, due to recent experimental NMR evidence that supports previous proposals regarding the role that non-classical or weak hydrogen bonds can play in polymer blend morphology, specific examples will be discussed here.

The acceptance of weak hydrogen bonds, defined here as hydrogen bonds between sp, sp^2 or sp^3 CH hydrogen atoms and proximate electronegative heteroatoms, has occurred more rapidly in the small molecule and biological macromolecule literature than in the polymer blend literature.[27–29] For example, Dixon and Hay discussed the role of hydrogen bonding between backbone glycine CH_2 hydrogen atoms and carbonyl group oxygens, suggesting that this interaction contributed to stabilization of tertiary structure in proteins.[30] In 2005, Zhang and coworkers proposed that methyl group CH hydrogens were weakly hydrogen bonded to carbonyl groups in polylactide stereocomplexes based on peak shifts in infrared data.[31] Recently, the unequivocal assignment of weak hydrogen bonds as the origin of miscibility in amorphous PS/PVME blends has been discussed for the first time by Green and White, based primarily on combined solid-state and solution NOE NMR data.[32] In this contribution, differential solid-state Overhauser effects for *meta*/*para* aromatic ring hydrogens on the PS blend component clearly demonstrated a preferred arrangement of aromatic CH bonds and the PVME oxygen atom.[33] PS/PVME is a long-standing 'classical' polymer blend, well studied in the polymer science community by many methods over several decades. That the fundamental contribution of weak C–H to O hydrogen bonds to miscibility went unrecognized for so long can be attributed to the lack of a molecular emphasis in discussions of negative χ parameters in the general polymer science literature. The contributions of solid-state NMR to the understanding of miscibility in polymer blends in general, and the PS/PVME case in particular, stem primarily from its unique molecular perspective.[34–40] Based on this recent example from the polymer literature, and other recent publications,[26,41] the role that solid-state NMR will continue to play in understanding weak C–H to O hydrogen bonding in polymer blends appears promising. For example, the unusual miscibility of PS with poly(cyclohexyl methacrylate) or poly(1,4-dimethyl-*p*-phenylene oxide) (PPO) could be attributable to weak hydrogen bonding interactions of the type discussed for PS/PVME above, even though in general PS is immiscible with most polymers as recently discussed.[42,43]

3.2 Blends composed of polymer component containing an oxygen atom, and hydrogen bonds

Classical hydrogen bonding interactions between dissimilar chains in polymer mixtures drive miscibility in a variety of blends over wide composition ranges, but with mixing length scales often defined by an interplay of self-association

and interchain bonding as has been discussed extensively over the years by Painter and Coleman.[44] Common hydrogen bonding pairs are C=O oxygens and OH hydrogens from acrylate, phenolic, vinyl acetate and vinyl alcohol polymers. Like FTIR stretching frequencies, carbonyl chemical shifts in CP/MAS experiments can indicate hydrogen bonding, as recently discussed by Chang and coworkers for PMMA/phenolic and PVAc/phenolic blends.[45,46] Interestingly, combined chemical shift and $T_{1\rho H}$ experiments indicated that four-arm star PMMA mixes more intimately with phenolic resin than linear PMMA, with a minimum length scale of mixing of 1–2 nm in the amorphous phase over all blend compositions.[46] Additional comparisons between chemically similar binary blends vs. copolymers can lead to additional insights into the roles of hydrogen bonding in intrachain self-association vs. interchain bonding, as is common for hydroxyl-containing polymers. Recently, Chang and coworkers compared miscible PMMA/PMAA blends to PMMA-co-PMAA using solid-state $T_{1\rho H}$ experiments and determined that the length scale of mixing in the blends exceeded that from the random copolymer, even though the authors claim the blend was intimately mixed over all compositions.[47] ^{1}H and ^{13}C relaxation, lineshape analysis and spin-diffusion experiments were used by Asano et al. to determine a maximum domain size of 2.5 nm for equimolar PMAA/PVAc blends; PMAA-rich blends showed microphase separation.[48] Again, hydrogen bonding between carbonyl group oxygens in PVAc and carboxylate group hydroxyls in PMAA were responsible for mixing.

In the study of polymer blends, it is common to infer miscibility based on a single glass transition temperature T_g. However, the routine use of T_{1H} vs. $T_{1\rho H}$ experiments often reveals that the polymer components are not intimately mixed when a single T_g is observed. Yi and Goh have recently reported such a case, in that length scales of mixing in PPMA/PVA (poly(propylmethacrylate)/poly (vinyl alcohol)) blends were intermediate between 2 and 20 nm.[49] Similarly, Wang et al. used these relaxation methods to measure intermediate miscibility (>2–4 nm) in PCL/PVPh (polycaprolactone/poly-4-vinyl phenol) blends, even though single T_g's were measured for the purely amorphous components of the blend.[50] Shifts in the carbonyl carbon peak position, up to 1 ppm, were taken as indicative of a specific hydrogen bonding interaction; FTIR experiments supported this assignment. Essentially identical conclusions were reached by Zheng et al. for PCL blends with cross-linked epoxy resins, suggesting that for blends containing a single hydroxyl-containing component, self-association limits the degree to which homogeneous intermolecular mixing may be achieved.[51] In contrast, Kuo et al. examined blends of PVPh and poly(hydroxyl-ether of Bisphenol A), both of which contain hydroxyl groups, and found more favourable interchain vs. self-association interactions.[52] In their work, the upfield vs. downfield ^{13}C shifts of specific hydroxyl group carbons was used to identify the electron donor vs. acceptor components in the blend. The specific introduction of dilute (<3 mole%) amounts of hydroxyl group donors into engineered copolymer blends can be used to create effective compatibilizers for normally immiscible pairs via hydrogen bonding; such is the case for a recently reported PS/polyacrylate copolymer system employing routine CP/MAS and

^{1}H relaxation studies to determine microscopic structure/macroscopic property relationships.[53]

Blends of semicrystalline poly(ethylene oxide) (PEO) with PMMA potentially exhibit the additional complication of PEO crystallinity in blends that exceed *ca*. 30 wt% PEO fraction. PEO/PMMA blends are intriguing due to the large difference in T_g of the two polymer components. Recent reports by several authors on the well-studied blend have avoided this complication by limiting PEO concentrations to less than 30 wt%.[54–56] An interesting series of PFG NMR diffusion and lineshape analysis experiments by Jones and coworkers revealed that dynamic heterogeneities provided a reasonable pathway for small molecule diffusion in the blend, presumably favouring PEO-rich regions or diffusion along PEO chains.[54,55] Studies of this type demonstrate a unique advantage of NMR-based methods, in that specific responses from bulk chain dynamics and morphology, both in the absence and presence of probe molecules, can be correlated with the selective response from an appropriate series of probe molecules. In an report of PEO blended with the sodium form of poly(glutamate), Schmidt-Rohr and coworkers used static double-quantum (DOQSY) NMR to show that PEO crystallinity was undisturbed by blending, refuting earlier claims that ionic interactions with Na altered PEO conformational distributions in the blend.[57] When PEO was blended with poly(butylenes succinate), which is also a semicrystalline polymer, solid-state NMR relaxation studies indicate that mixed miscibility exists in the amorphous phases, and that interesting morphologies across the entire composition range may exist when one component is dilute, including fractional PEO crystallization.[58] Indeed, Inoue and coworkers demonstrated that confinement effects in semicrystalline polymer blends can contribute to unique fractional crystallizations if amorphous phase miscibility exists.[58]

3.3 Blends composed of a component containing N, S, Cl or F atoms

Blends containing nitrogen heteroatoms are often considered for their ability to act as a proton acceptor. During this review period, poly(vinylpyridine) and poly(vinyl pyrolidone) were most commonly investigated as components in blends with other, more commonly used polymers. For example, Tavares et al. used CP/MAS based relaxation methods to investigate the miscibility of poly(vinyl pyrolidone) with both PMMA and PEO; while indirect evidence for some specific interactions between each blend component was discussed, the response of the individual relaxation parameters for each pure component upon blend formation suggested that intimate chain contact on the $<$2–3 nm length scale did not occur.[59,60] Zheng and Mi used shifts in the carbon spectrum of specific functional carbon resonances and identical $T_{1\rho H}$ values to identify molecular level mixing in blends of poly(4-vinyl pyridine) and phenoxy (poly hydroxyether of bisphenol A).[61] In this case, miscibility was attributed to specific hydrogen bonding between ring N atoms in the former component, and hydroxyl groups of the latter. Essentially identical conclusions regarding the importance of hydrogen bonding were proposed by Li and Goh in the case where the small molecule bisphenol A (4,4′-isopropylidene diphenol) was used a compatibilizing

agent for the binary blend of poly(2-vinylpyridine) and poly(*N*-vinyl-2-pyrolidone); bisphenol A provides the necessary hydrogen bonding 'bridge'.[62] Based on the convergence of the $T_{1\rho H}$ values as a function of bisphenol A concentration, a 'miscibility' window was identified based on equal number of donor hydroxyl groups and acceptor N atoms on each polymer chain. Using the standard CP/MAS and $T_{1\rho H}$ approach discussed in the preceding examples, Kuo et al. reported a series of experiments detailing the use of A–B/C copolymer/homopolymer blends containing pydrine and pyrrolidone functionality, in which the specific composition of the diblock was used to achieve miscibility on the 2 nm length scale with acrylate or phenol type polymer components.[63–65] Similarly, Lee et al. used the A–B/C blend approach to create miscibility, albeit demonstrated on a longer length scale (common T_{1H}), in poly(2-vinyl pyridine)-block-PEO blends with poly(4-vinyl phenol).[66] Direct observation of the CP/MAS ^{15}N signal from natural abundance Nylon 6 blended with polypropylene oxide was used by Tavares to detect plasticization, suggesting an intimate mixing of the two chain types.[67]

Intermediate miscibility, as defined by common DSC and T_{1H} but unique $T_{1\rho H}$ values, was detected for blends of PVA and the sulphur-containing polymer poly(methylthiomethyl methacrylate), or PMTMA.[68] In this report, hydrogen bonding between PVA hydroxyl groups and the thioether sulphur atom of PMTMA was identified as the interaction driving miscibility, based on sulphur XPS data. In experiments targeted toward identifying membranes for use in direct methanol fuel cells, Wu et al. reported complimentary $T_{1\rho H}$ and DSC studies on blends of PES (poly(ether sulphone)) and SPEEK (sulphonated poly(ether ketone)).[69] Intimate molecular level mixing, as detected by homogeneous T_{1H} and $T_{1\rho H}$ experimental results, was observed by Gelan and coworkers for the blend of two sulphur-containing polymers; poly(3,4-ethylenedioxythiophene) and polystyrenesulphonic acid blends formed active charge transfer complexes with improved conductivity properties.[70] Structurally variant polyarylates, containing sulphonyl backbone linkages, formed blends of varying length scales of mixing, including complete phase separation, with PVC.[71] Domain sizes intermediate between 3 and 30 nm were measured via CP/MAS relaxation techniques for poly(epichlorohydrin)/poly(vinyl acetate) blends.[72] Finally, Oshima et al. used ^{19}F MAS NMR chemical shift data to identify cross-linking chemistry between blends of PTFE and other fluorinated polymer derivatives as a function of electron beam irradiation.[73]

4. BINARY BLENDS OF POLYMERS CONTAINING ONLY SP^3 CARBONS: POLYOLEFINS

Following the high level of activity in metallocene polymerization catalysis in the 1990s, many groups have investigated a variety of polyolefin based polymer blend systems in the last 5 years. In contrast to the preceding discussion on functional polymers, and the role that either weak or classical hydrogen bonding plays in their blends, polyolefins obviously contain no heteroatoms.

Indeed, polyolefin blends do not even have olefinic or styrenic moeties that make many vinyl polymers functional, in that even though the constituent atoms are all carbon or hydrogen, large electron density gradients exist within the macromolecule based on the differential amounts of sp, sp^2 and sp^3 carbons. Consequently, their appreciable polarizability gives rise to induced dipole interactions that again drive mixing via an enthalpic contribution. Therefore, one might ask what happens when the constituent polymers are both chemically and electronically homogeneous, e.g., in completely saturated hydrocarbon polymers? Does one's intuition regarding enthalpic and entropic contributions to the overall free energy of mixing still serve as a useful guide?

Polyolefins are the most ubiquitous of polymer families. It is surprising that such architecturally simple/similar polymers, devoid of any functional groups, exhibit fairly complex phase behaviours. That polypropylene and polyethylene are immiscible at the chain level is by now well known; the reason why is still a controversial subject. The absence of polar functional groups in polyolefins essentially eliminates any significant enthalpic contributions to the free energy of mixing. Such 'heats of mixing', typically represented by the enthalpic interaction term χ in Flory–Huggins theory, are commonly regarded as the driving force for miscibility. Dispersive forces via weak van der Waals interactions are possible, and may be significant for large molecular weight molecules. Entropic contributions to miscibility in polymer blends are usually discounted in the polymer blend literature, since molecular weights are large and Flory–Huggins theory scales combinatorial entropies of mixing according to the inverse of the degree of polymerization. The question remains as to how mutual solubility in polyolefin blends depends on polymeric microstructure, tacticity, comonomer incorporation and chain dynamics, and further, how each of these architectural and physical characteristics contributes to the interplay between enthalpy and entropy. Clearly, one would expect that the details of interchain packing and reorientation would be critically dependent on the aforementioned structural details, and recent activity using solid-state NMR methods have attempted to address these fundamental questions.

White and coworkers have been most active in the area of using solid-state NMR methods to understand polyolefin miscibility. In a series of papers from 2002 to 2007, they have shown that positive configurational entropies of mixing exist in polyolefin blends in which PIB (poly*iso*butylene) is one component.[74–79] Specifically, using a combination of 2D MAS exchange, spin-diffusion, ^{129}Xe MAS NMR, ^{2}H lineshape analysis, CODEX exchange techniques and supporting simulations to fit the data, calculable increases in the total entropy of miscible polyolefin blends (PIB/poly(ethylene-co-butene) and PIB/head-to-head polypropylene) were described for the first time. Indeed, a key component of their work focused on the relationship between very slow-chain dynamics and length scales of mixing using Adams–Gibbs theory. Through direct measurement of polarization transfer, and chain backbone dynamics as a function of mixing, all in the absence of any isotopic labels, enthalpic contributions to miscibility for these specific polyolefin blends could be excluded as a driving force. The types of experiments listed above cover a wide range of mixing length scales and

dynamic time scales, fully exploiting the well-known advantages of modern solid-state NMR methods.[1–6] For the first time, direct inspection of backbone conformational dynamics, with polymer specificity as afforded by distinct ^{13}C peaks for blend components, revealed positive configurational entropies of mixing and negative deviations from Fox or Gordon–Taylor mixing rules. Indeed, a key result from CODEX investigations of the PIB/hhPP blend system was the preservation of local chain activation barriers and correlation time distribution widths upon formation of the miscible blend, even though maximum slow-chain (frequency scale of 10–100 Hz) conformational exchange intensities converged to an identical temperature (see Figure 5).[78] Similar conclusions regarding miscibility have recently been reached for blends of atactic PP and poly(ethylene-co-butene), as shown in Figure 6.[80, 107]

Jones and coworkers have also published detailed investigations on differential dynamics in PIB and hhPP miscible blends.[81] The particular focus

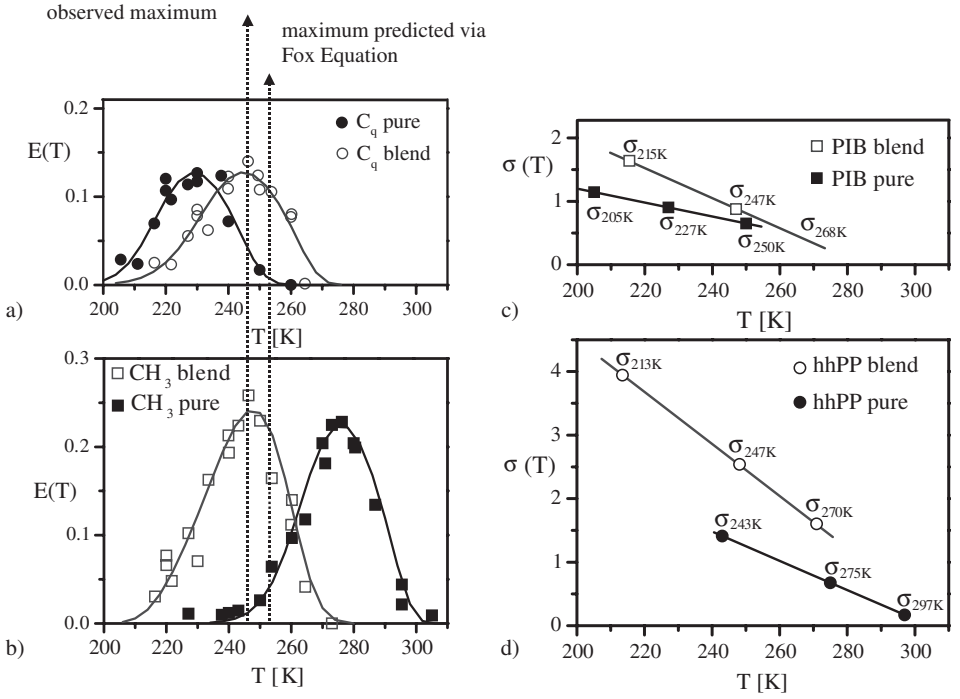

Figure 5 Normalized CODEX exchange intensities $E(T)$ at $t_m = 100$ ms for (a) pure PIB (●) and PIB in the blend (○), and (b) pure hhPP (■) and hhPP in the blend (□). Note the common exchange maximum temperature $T = 246$ K for each polymer in the blend (left arrow) and the Fox equation prediction (right arrow). The smooth lines are fits to the data as described in detail in ref. 78, and were used to extract temperature-dependent correlation time distribution widths for (c) pure PIB and PIB in the hhPP blend, and (d) pure hhPP and hhPP in the blend. (Adapted from ref. 78.)

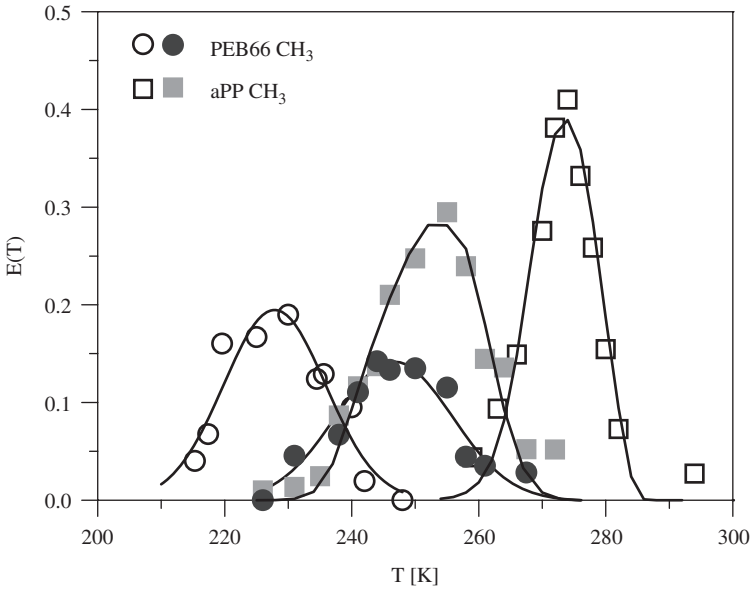

Figure 6 Normalized CODEX exchange intensities $E(T)$ at $t_m = 100$ ms for pure poly(ethylene-co-butene) containing 66 wt% butene comonomer (PEB66), denoted by (○), and PEB66 in the 50/50 blend with atactic PP (●), vs. pure aPP (□) and aPP in the blend with PEB66 (■). While CH_3 group signals are shown here, identical results were obtained using backbone methylene group signals for each pure polymer. Note that in contrast to Figure 5, the two curves denoted by the filled symbols for each polymer in the blend do not converge to the same temperature.[107]

of this work was to discern how well recently discussed models for predicting polymer dynamics, e.g., the Lodge–McLeish model,[82] predicted individual segmental dynamics. Indeed, one of the more active research areas in polymer science at the moment involves miscible blend dynamics.[78,81,82,102–106] The authors used NMR spin-lattice relaxation methods for ^{13}C and ^{2}H to probe this question, finding that the Lodge–McLeish model did not accurately describe component dynamics after blending. However, it should be noted that the very high frequencies probed by NMR relaxation methods might not be adequate to probe this question, and indeed, the authors provided supporting dielectric spectroscopy data to address this point.[81] Finally, Filip and Aluas have used detailed numerical analysis of CP/MAS polarization-transfer build-up (T_{CH}) curves in PP/EPDM blends to help define the active morphology in thermoplastic vulcanizates.[83]

5. BLENDS CONTAINING VINYL OR DIENE POLYMER COMPONENTS

In a recent report, Wang et al. employed ^{1}H observed dipolar filter methods at 25 kHz MAS to monitor the time/concentration dependent interpenetration of

fully protonated PS chains with perdeuterated PS film cast from dilute solution mixtures.[84] Since no spin-diffusion mixing periods were used in the pulse sequence, the authors used this particular isotopically mixed system to demonstrate the general utility of probing heterosegmental mixing on the 0.5 nm length scale via the highly sensitive ^{1}H direct observation. Of course, the technique does require complete deuteration of one polymer component in the blend, but would nicely compliment studies with parallel neutron scattering experiments in which labelling was required to establish scattering contrast. Building on the miscibility of varying styrene-based polymers, Chang et al. compared length scales of mixing in ternary PS/poly(alpha-methyl styrene, and poly(4-methyl styrene) blends as determined by calorimetry (T_g's too close to differentiate), microscopy and ^{1}H solid-state NMR relaxation methods.[85] Since binary blends of these PS's are known to exhibit complex UCST behaviour, the authors suggest that homogeneous mixing does occur at the chain level when sufficiently high concentrations of poly(alpha-methyl styrene) are present to solubilize the other two chain types.

Historically, blends of PS and PB (polybutadiene), and their copolymers, have attracted attention for their improved physical properties as impact polymers and elastomers. Joseph and coworkers, using solid-state ^{1}H relaxation methods in conjunction with electron microscopy, have shown that both random and blocky PS–PB terpolymers more effectively compatibilize blends of the two homopolymers than just the PS–PB diblocks alone.[86] Woo et al. have reported LCST miscible phase behaviour for poly(alpha-methyl styrene) blended with poly(phenylene oxide) (PPO) based on combined solid-state ^{1}H relaxation and FTIR methods, even though PPO/PS blends are known to exhibit UCST behaviour.[87] Using supercritical CO_2 as a mixing solvent, Thurecht and coworkers have shown *ca.* 4-nm length scale mixing for PS/LLDPE (linear low-density polyethylene) blends via $T_{1\rho H}$ relaxation measurements of the solid blend.[88] Interestingly, the authors determined via ^{13}C MAS data that the PS only incorporated within the amorphous regions of the semicrystalline LLDPE, based on differential monomer diffusion in the synthesis. By comparison, domain sizes for normal 1-atm polymer blend preparation exceeded 100 nm.

6. BIOPOLYMER BLENDS

Trends in polymer science reflect broader trends in science, specifically reflected by the growing interest in creating new materials with good physical properties, while at the same time allowing either bioremediation/biodegradation or some form of biocompatibility. Biopolymers as a class of research materials now have several research journals specifically devoted to their study (e.g., *Biomacromolecules, Biopolymers, Biomaterials*, etc.), and recent solid-state NMR investigations have been published dealing with blends in which at least one component is a biopolymer with either biodegradation or biocompatibility potential. Since many pure biopolymers often exhibit a fairly narrow range of physical, mechanical and barrier properties, blending with synthetic polymers can offer the best of both

worlds. Polysaccharides, such as cellulose and cellulose derivatives, have been studied in their blends with several vinyl polymers using solid-state NMR methods. Ohno et al. reported that specific hydrogen bonding interactions between hydroxyl groups in cellulose acetate and poly(*N*-vinyl pyrrolidone-co-vinyl acetate) (PVP-co-VAc) carbonyl groups were responsible for homogeneous structure formation in their blends.[89] Carbonyl ^{13}C chemical shift values varied according to the composition of the blend, and similar results were obtained for other cellulose alkyl esters in the PVP, PVAc or PVP-co-PVAc blends, including cellulose butyrates and cellulose acetate butyrate.[90,91] Even though common DSC T_g values were obtained for many of the cellulose acetate blends, solid-state ^1H relaxation measurements detected heterogeneity on the sub-10 nm length scale in some of the blend compositions. Spevacek and coworkers used T_{1H}, $T_{1\rho H}$ and T_{1C} measurements to evaluate length scales of mixing in native wheat starch blends with PCL (polycaprolactone), an important biopolyester, finding heterogeneous concentration distributions even on the 20 nm length scale.[92] However, formylation of starch to starch formate increased miscibility to homogeneous length scales less than 20 nm; the authors suggest inclusion of PCL chains to form nanodomains within the amorphous channel structure of starch is enhanced via starch formylation. Miscibility and enzymatic biodegradability of PCL/poly(propylene succinate) blends were analyzed over a wide composition range by Bikiaris and coworkers.[93] Due to the semicrystalline nature of each polymer blend component, and largely different crystallization kinetics, phase separation occurred.

Length scales of mixing in amorphous blends of solid PCL (polycaprolactone) and PLLA (poly-l-lactic acid) were investigated as a function of preparation method by White and coworkers, using recently reported two-dimensional heteronuclear correlation (Hetcor) spin-diffusion techniques with intramonomer calibration of spin-diffusion coefficients.[17,18] The rates for intrapolymer polarization transfer vs. interchain/interdomain polarization equilibration were easily differentiated using the 2D technique for either blend. As a result, spin-diffusion coefficients and miscibility length scales could be calculated by direct measurement on the blend constituents, while more traditional methods involving NMR relaxation proved inconclusive. The spin-diffusion methods unequivocally showed that inclusion compound methods for the preparation of blends from normally incompatible polymers, as discussed by Tonelli and coworkers, can enhance mixing.[94] Blends of PLLA with chitosan were investigated by Chen et al. using solid-state CP/MAS, relaxation, and FTIR techniques.[95] The authors observed crystallinity decreases with increases in the chitosan composition in the blend, and attributed the changes to hydrogen bonding between the PLLA carbonyl groups and amine groups in chitosan. Zhao and coworkers reached similar conclusions for PLLA blends with bovine gelatin.[96]

Blends and copolymers based on poly(hydroxyalkanoates) have achieved commercial success as biodegradable thermoplastics. Poly(hydroxybutyrate) (PHB) and its derivatives in particular continue to receive attention for new material design due to its favourable bacterial synthesis and enzymatic degradation routes, and solid-state NMR investigations of morphology in their

blends has been reported recently.[97–100] Na and coworkers, using CP/MAS based relaxation methods in combination with DSC found heterogeneous mixing (>30 nm) in the amorphous phase of poly(3-hydroxybutyrate)/PEO and poly(3-hydroxypropianate)/PEO blends.[97] Crystallization kinetics play a key role in the final morphology of poly(hydroxyalkanoates), as Yoshie and coworkers described in a comparative CP/MAS study with selective ^{13}C enrichment of poly(hydroxybutyrate-co-hydroxyvalerate) (PHB-co-PHV) co-polymers vs. their binary blend.[98] This specific blend showed complete co-crystallization of the blend components across the entire composition range. Hill and coworkers investigated the miscibility of PHB-co-PHV copolymers with PVAc using ^{1}H and ^{13}C CP/MAS methods.[99] Spin-diffusion measurements within and between the different polymer components suggested that the PVAc reside within the inter-lamellar spacing of the PHB chains.

The specific interaction of small molecules with polymers can guide the formation of miscible blends, and also has implications in drug delivery/pharmaceutical chemistry. PHB blends with the small molecule 4-*tert*-butylphenol were investigated by Chen and coworkers using combined CP/MAS and FTIR methods.[100] The authors found specific hydrogen bonding between the hydroxyl groups of the small molecule and PHB carbonyl groups for those polymer chains in the amorphous phase only, and indeed the small molecule would disrupt chain crystallization. Solid-state Bloch decay and CP/MAS revealed that specific hydrogen bonding also existed in PEO blends with the small drug molecule ketoprofen.[101]

7. CONCLUSIONS

Solid-state NMR methods continue to contribute to the understanding of miscibility in polymers, with particular capability in quantifying length scales of mixing below that accessible using traditional calorimetry methods, and in identifying the intermolecular interactions or differential dynamics which accompany miscibility. Currently, the area of understanding miscible blend dynamics is particularly attractive to many NMR-based investigators, and one which could easily be the subject of another review.[76,78,81,82,101–106] In particular, the dependence of individual chain dynamics in intimately mixed mixtures as a function of concentration, and the inherent concentration fluctuations in amorphous macromolecules, as well as predictive models to treat them, will continue to attract attention as more selective NMR-based experiments probing a much wider range of motional timescales, and in particular, very slow-chain motions, become accessible.

REFERENCES

1. I. Ando and T. Asakura, *Solid State NMR of Polymers*, Elsevier, New York, NY, 1998.
2. A. Asano, in: *Modern Magnetic Resonance*, G. Webb, ed., Vol. 1, Springer, The Netherlands, 2006, p. 627.

3. J. L. White, in: *Modern Magnetic Resonance*, G. Webb, ed., Vol. 1, Springer, The Netherlands, 2006, p. 633.
4. P. A. Mirau, *A Practical Guide to Understanding the NMR of Polymers*, Wiley, Hoboken, NJ, 2005.
5. H. W. Spiess and K. Schmidt-Rohr, *Multidimensional Solid-State NMR and Polymers*, Academic Press, San Diego, CA, 1994.
6. A. E. Tonelli and J. L. White, *Physical Properties of Polymers Handbook*, J. E. Mark, ed., Springer, New York, NY, 2006, p. 359.
7. H. Kurosu and Q. Chen, Structural studies of polymer blends by solid-state NMR, *Ann. Rep. NMR Spectrosc.*, 2004, **52**, 167.
8. N. R. Krogman, A. Singh, L. S. Nair, C. T. Laurencin and H. R. Allcock, *Biomacromolecules*, 2007, **8**, 1306.
9. D. L. VanderHart and G. M. McFadden, *Solid State NMR*, 1996, **7**, 45.
10. J. Clauss, K. Schmidt-Rohr and H. W. Spiess, *Acta Polymer.*, 1993, **44**, 1.
11. M. Goldman and L. Shen, *Phys. Rev.*, 1966, **144**, 321.
12. N. Egger, K. S. Schmidt-Rohr, B. Blumich, W. D. Domke and B. Stapp, *J. Appl. Polym. Sci.*, 1992, **44**, 289.
13. M. Wilhelm, H. Feng, U. Tracht and H. W. Spiess, *J. Magn. Reson.*, 1998, **134**, 255.
14. S. S. Hou, Q. Chen and K. Schmidt-Rohr, *Macromolecules*, 2004, **37**, 1999.
15. F. Mellinger, M. Wilhelm and H. W. Spiess, *Macromolecules*, 1999, **32**, 4686.
16. X. Wang and J. L. White, *Macromolecules*, 2002, **35**, 3795.
17. X. Jia, J. Wolak, X. Wang and J. L. White, *Macromolecules*, 2003, **36**, 712.
18. X. Jia, X. Wang, A. E. Tonelli and J. L. White, *Macromolecules*, 2005, **38**, 2775.
19. K. Beshah and L. K. Molnar, *Macromolecules*, 2000, **33**, 1036.
20. T. M. Werkhoven, F. M. Mulder, C. Zune, R. Jerome and H. J. M. de Groot, *Macromol. Chem. Phys.*, 2003, **204**, 46.
21. W. G. Hu and K. Schmidt-Rohr, *Polymer*, 2000, **41**, 2979.
22. K. Landfester, V. L. Dimonie and M. S. El-Aasser, *Macromol. Chem. Phys.*, 2002, **203**, 1772.
23. P. A. Mirau, S. A. Heffner and M. Schilling, *Solid State NMR*, 2000, **16**, 47.
24. A. Buda, D. E. Demco, M. Bertmer, B. Blumich, B. Reining, H. Keul and H. Hocker, *Solid State NMR*, 2003, **24**, 39.
25. P. Holstein, G. A. Monti and R. K. Harris, *Phys. Chem. Chem. Phys.*, 1999, **1**, 3549.
26. S. P. Brown, *Prog. NMR Spectrosc.*, 2007, **50**, 199.
27. G. R. Desiraju and T. Steiner, *The Weak Hydrogen Bond in Structural Chemistry and Biology*, Oxford Science Publications, Oxford, 1999.
28. R. Taylor and O. Kennard, *J. Am. Chem. Soc.*, 1982, **104**, 5063.
29. X. B. Wang, H. K. Woo, B. Kiran and L. S. Wang, *Angew. Chem. Int. Ed.*, 2005, **44**, 4968.
30. R. Vargas, J. Garza, D. Dixon and B. P. Hay, *J. Am. Chem. Soc.*, 2000, **122**, 4750.
31. J. Zhang, H. Sato, J. Tsuji, I. Noda and Y. Ozaki, *Macromolecules*, 2005, **38**, 1822.
32. M. M. Green, J. L. White, P. A. Mirau and M. H. Scheinfeld, *Macromolecules*, 2006, **39**, 5971.
33. J. L. White and P. A. Mirau, *Macromolecules*, 1993, **26**, 3049.
34. P. Caravatti, P. Neunschwander and R. R. Ernst, *Macromolecules*, 1985, **18**, 119.
35. J. L. White, *Solid State NMR*, 1997, **10**, 79.
36. S. P. Brown and H. W. Spiess, *Chem. Rev.*, 2001, **101**, 4125.
37. A. Samoson, T. Tuherm, J. Past, A. Rheinhold, T. Anupold and N. Heinmaa, *New Techniques in Solid-State NMR*, Springer-Verlag, Berlin, 2005.
38. K. Saalwachter, *Prog. NMR Spectrosc.*, 2007, **51**, 1.
39. T. Wagler, P. L. Rinaldi, C. D. Han and H. Chun, *Macromolecules*, 2000, **33**, 1778.
40. X. Qiue and P. A. Mirau, *J. Magn. Reson.*, 2000, **142**, 183.
41. I. L. Karle, P. Venkateshwarlu and S. Ranganathan, *Biopolymers*, 2006, **84**, 502.
42. R. R. Wu, H. M. Kao, J. C. Chiang and E. M. Woo, *Polymer*, 2002, **43**, 171.
43. L. L. Chang and E. M. Woo, *J. Polym. Sci. Part B: Polym. Phys.*, 2003, **41**, 772.
44. M. M. Coleman, J. F. Graf and P. C. Painter, *Specific Interactions and Miscibility of Polymer Blends*, Technomic Publishing, Lancaster, PA, 1991.

45. C. F. Huang, S. W. Kuo, H. C. Lin, J. K. Chen, Y. K. Chen, H. Y. Xu and F. C. Chang, *Polymer*, 2004, **45**, 5913.
46. M. W. Huang, S. W. Kuo, H. D. Wu, F. C. Chang and S. Y. Fang, *Polymer*, 2002, **43**, 2479.
47. C. F. Huang and F. C. Chang, *Polymer*, 2003, **44**, 2965.
48. A. Asano, M. Eguchi, M. Shimizu and T. Kurotsu, *Macromolecules*, 2002, **35**, 8819.
49. J. Z. Yi and S. H. Goh, *Polymer*, 2005, **46**, 9170.
50. J. Wang, M. K. Cheung and Y. L. Mi, *Polymer*, 2002, **43**, 1357.
51. S. X. Zheng, Q. P. Guo and C. M. Chan, *J. Polym. Sci. Part B: Polym. Phys.*, 2003, **41**, 1099.
52. S. W. Kuo, C. L. Lin, H. D. Wu and F. C. Chang, *J. Polym. Res. Taiwan*, 2003, **10**, 87.
53. I. A. Van Casteren, R. A. M. Van Trier, J. G. P. Goossens, H. E. H. Meijer and P. J. Lemstra, *J. Polym. Sci. Part B: Polym. Phys.*, 2004, **42**, 2137.
54. H. H. Cao, G. X. Lin and A. A. Jones, *J. Polym. Sci. Part B: Polym. Phys.*, 2004, **42**, 1053.
55. H. H. Cao, G. X. Lin and A. A. Jones, *J. Polym. Sci. Part B: Polym. Phys.*, 2005, **43**, 2433.
56. T. M. F. F. Diniz and M. I. B. Tavares, *J. Appl. Polym. Sci.*, 2003, **90**, 2955.
57. D. J. Harris, T. J. Bonagamba and K. Schmidt-Rohr, *Macromolecules*, 2002, **35**, 5724.
58. Y. He, B. Zhu, W. H. Kai and Y. Inoue, *Macromolecules*, 2004, **37**, 3337.
59. T. M. F. F. Diniz and M. I. B. Tavares, *J. Appl. Polym. Sci.*, 2004, **93**, 372.
60. T. M. F. F. Diniz and M. I. B. Tavares, *J. Appl. Polym. Sci.*, 2002, **85**, 2820.
61. S. X. Zheng and Y. L. Mi, *Polymer*, 2003, **44**, 1067.
62. X. D. Li and S. H. Goh, *J. Polym. Sci. Part B: Polym. Phys.*, 2002, **40**, 1125.
63. H. F. Lee, S. W. Kuo, C. F. Huang, J. S. Lu, S. C. Chan, C. F. Wang and F. C. Chang, *Macromolecules*, 2006, **39**, 5458.
64. S. W. Kuo, P. H. Tung and F. C. Chang, *Macromolecules*, 2006, **39**, 9388.
65. C. F. Huang, S. W. Kuo, F. J. Lin, C. F. Wang, C. J. Hung and F. C. Chang, *Polymer*, 2006, **47**, 7060.
66. L. T. Lee, E. M. Woo, S. S. Hou and S. Forster, *Polymer*, 2006, **47**, 8350.
67. M. I. B. Tavares and C. M. G. de Souza, *J. Appl. Polym. Sci.*, 2003, **90**, 3872.
68. J. Z. Yi and S. H. Goh, *Polymer*, 2003, **44**, 1973.
69. H. L. Wu, C. C. M. Ma, F. Y. Liu, C. Y. Chen, S. J. Lee and C. L. Chiang, *Eur. Polym. J.*, 2006, **42**, 1688.
70. (a) P. Adriaensens, R. Carleer, L. Storme, D. Vanderzande and J. Gelan, *Polymer*, 2002, **43**, 7003; (b) P. Adriaensens, L. Storme, R. Carler and J. Gelan, *Macromolecules*, 2002, **35**, 3965.
71. S. Y. Kwak, S. H. Kim and T. Suzuki, *Polymer*, 2004, **45**, 8153.
72. M. K. Cheung, J. Wang, S. Zheng and Y. Mi, *Polymer*, 2000, **41**, 1469.
73. A. Oshima, F. Mutou, T. Hyuga, S. Asano, S. Ichizuri, J. Y. Li, T. Miura and M. Washio, *Nucl. Instrum. Methods Phys. Res. Sect. B*, 2005, **236**, 172.
74. J. Wolak, X. Jia, H. Gracz, E. O. Stejskal, J. L. White, M. Wachowicz and S. Jurga, *Macromolecules*, 2003, **36**, 4844.
75. J. E. Wolak, X. Jia and J. L. White, *J. Am. Chem. Soc.*, 2003, **125**, 13660.
76. M. Wachowicz, J. Wolak, H. Gracz, E. O. Stejskal, S. Jurga, E. F. McCord and J. L. White, *Macromolecules*, 2004, **37**, 4573.
77. J. E. Wolak and J. L. White, *Macromolecules*, 2005, **38**, 10466.
78. M. Wachowicz and J. L. White, *Macromolecules*, 2007, **40**, 5433.
79. X. Wang and J. L. White, *Macromolecules*, 2002, **35**, 3795.
80. Y. Thomann, J. Suhm, R. Thomann, G. Bar, R. D. Maier and R. Mulhaupt, *Macromolecules*, 1998, **31**, 10466.
81. E. Krygier, G. Lin, J. Mendes, G. Mukandela, D. Azar, A. Jones, G. Floudas, R. Krishnamoorti and R. Faust, *Macromolecules*, 2005, **38**, 7721.
82. T. Lodge and T. C. B. McLeish, *Macromolecules*, 2000, **33**, 5278.
83. M. Aluas and C. Filip, *Solid State Nucl. Magn. Reson.*, 2005, **27**, 165.
84. X. L. Wang, F. F. Tao, P. C. Sun, D. S. Zhou, Z. Q. Wang, Q. Gu, J. L. Hu and G. Xue, *Macromolecules*, 2007, **40**, 4736.
85. L. L. Chang, E. M. Woo and H. L. Liu, *Polymer*, 2004, **45**, 6909.
86. S. Joseph, F. Laupretre, C. Negrell and S. Thomas, *Polymer*, 2005, **46**, 9385.
87. E. M. Woo, I. C. Chou, L. L. Chang and H. M. Kao, *Polym. J.*, 2003, **35**, 372.

88. K. J. Thurecht, D. J. T. Hill, C. M. L. Preston, L. Rintoul, J. W. White and A. K. Whittaker, *Macromolecules*, 2004, **37**, 6019.
89. T. Ohno, S. Yoshizawa, Y. Miyashita and Y. Nishio, *Cellulose*, 2005, **12**, 281.
90. T. Ohno and Y. Nishio, *Cellulose*, 2006, **13**, 245.
91. T. Ohno and Y. Nishio, *Macromol. Chem. Phys.*, 2007, **208**, 622.
92. J. Spevacek, J. Brus, T. Divers and Y. Grohens, *Eur. Polym. J.*, 2007, **43**, 1866.
93. D. N. Bikiaris, G. Z. Papageourgiou, D. S. Achilias, E. Pavlidou and A. Stergiou, *Eur. Polym. J.*, 2007, **43**, 2491.
94. C. C. Rusa, M. Wei, X. Shuai, T. A. Bullions, X. Wang, M. Rusa and A. E. Tonelli, *J. Polym. Sci. Part B: Polym. Phys.*, 2004, **42**, 4207.
95. C. Chen, L. Dong and M. K. Cheung, *Eur. Polym. J.*, 2005, **41**, 958.
96. X. D. Zhao, W. G. Liu and K. D. Yao, *J. Appl. Polym. Sci.*, 2006, **101**, 269.
97. Y. H. Na, Y. He, N. Asakawa, N. Yoshie and Y. Inoue, *Macromolecules*, 2002, **35**, 727.
98. N. Yoshie, M. Saito and Y. Inoue, *Polymer*, 2004, **45**, 1903.
99. D. J. Hill, M. Markotsis, A. K. Whittaker and K. W. Wong, *Polym. Int.*, 2003, **52**, 1780.
100. C. Chen, P. H. F. Yu and M. K. Cheung, *J. Appl. Polym. Sci.*, 2005, **98**, 736.
101. D. M. Schacter, J. Xiong and G. C. Tirol, *Int. J. Pharmaceutics*, 2004, **281**, 89.
102. T. R. Lutz, Y. He and M. D. Ediger, *Macromolecules*, 2005, **38**, 9826.
103. T. R. Lutz, Y. He and M. D. Ediger, *Macromolecules*, 2004, **37**, 6440.
104. Y. He, T. R. Lutz and M. D. Ediger, *Macromolecules*, 2004, **37**, 9889.
105. T. R. Lutz, Y. He, M. D. Ediger, H. Cao, G. Lin and A. A. Jones, *Macromolecules*, 2003, **36**, 1724.
106. K. L. Ngai and C. M. Roland, *Macromolecules*, 2004, **37**, 2817.
107. M. Wachowicz, L. Gill and J. L. White, *Macromolecules*, 2008, **41**, 2832.

This page intentionally left blank

SUBJECT INDEX